Coupling of Underexpanded Twin-Jets

Graham William Bell

A thesis submitted in partial fulfilment for the award of

Doctor of Philosophy (Engineering)

Monash Graduate Research School

Laboratory for Turbulence Research in Aerospace and Combustion
Department of Mechanical and Aerospace Engineering
Monash University
Melbourne, Australia

MONASH University

Coupling of Underexpanded Twin-Jets

Abstract

This thesis documents an experimental investigation into the coupling phenomena of circular supersonic twin-jets. The supersonic engine exhaust, called a jet in laboratory terminology, produced by an aircraft engine has a high capacity for noise generation. Part of the high capacity is due to the jet's affinity to aeroacoustic feedback processes such as screech. Screech is a synchronisation of the downstream convecting vortical structures produced at the nozzle lip of the jet, and upstream travelling acoustic waves that are produced by fluid interactions within the jet. A dominant feature of screech is an intense acoustic tone at the resonating feedback frequency. Twin-engines are often used in high speed aircraft for practical reasons. The proximity of the twin exhausting jets can enable them to strongly interact. The interaction can synchronise the screech feedback processes of the jets, which causes them to become acoustically and hydrodynamically coupled. The coupling significantly contributes to the jet's total noise production and has caused structural fatigue failure of the empennage surfaces of twin-engined aircraft. The coupling phenomena is also present in laboratory scale jets, where it is more easily studied.

Laboratory scale twin-jets have been studied to characterise the conditions under which they couple. Different modes of coupling have been observed in the parameter space examining jet pressure and nozzle spacing. The symmetric and anti-symmetric modes dominate, which describe the jet's oscillation about a symmetry plane. Studies have also identified coupling in certain regions of the parameter space is complex and not straightforward to characterise qualitatively. Despite being complex and unclassified by mode shape, the jets still produced an intense tone. This complex coupling has been shown to make up approximately half of the parameter space. A small number of studies have examined these regions using rectangular jets and identified that non-linear interactions of the jet coupling processes may be the cause. The physics of these interactions and the hydrodynamic relationship between the jets in these regions are examined in this work.

The complexity of the resonating aeroacoustic flow suggested an experimental approach. Three facilities were used to examine the acoustic, density gradient, and velocity fields of the flow. The complementing information obtained from these fields allowed the complex relationship between the jets to be understood. Facility one examined the acoustic phase between the jets. Opposing microphones were used to extract the phase position of each jet. The phase was examined using stationary and non-stationary statistical techniques. This allowed the mean and transient phase between the jet plume oscillations to be examined. Ultra high speed schlieren was also taken and used to provide an assessment of the qualitative structure of the jet coupling. Facility two examined the velocity field of the jets via particle image velocimetry. Ensemble statistics of the instantaneous velocity were used to provide a quantitative dataset of the flow. Correlation analysis and a reduced order model of the flow were used to examine the dominant hydrodynamic structures. Facility three used a multi-directional microphone array to examine the azimuthal mode structure of the individual jets during coupling. The jets within the microphone array were subject to forcing via nozzle mounted plasma actuators to observe the acoustic response under forced conditions. Trends relating to the stability of certain modes and the feedback pathway were deduced.

The complex coupling had been previously investigated in rectangular twin-jets. Evidence had not yet been provided to identify whether it was also a phenomenon in circular twin-jets. A characterisation study was performed to classify the coupling for different pressure ratios and nozzle spacings. It was found that complex coupling made up approximately half of the parameter space when examined over a similar parameter range ($s/D = 3, 6$ and $2.0 \leq \text{NPR} \leq 5.5$). The regions of clear coupling were found to match the existing initial studies. Additionally, screech wavelength prediction models were applied to different coupling modes to determine the predictive fit. It was found that the models cannot predict the frequencies from jet coupling and more complex mechanisms must be at work such as change in the upstream acoustic closure mechanism or sound source location. The differences in the velocity fields between a clear and complex coupling region were examined on facility two using particle image velocimetry. Differences in the velocity statistics of the shear-layer were found. The complex coupling produced slightly greater growth rates than that of the clear coupling. Unique features of the twin-jet flow were also quantified. It was found that mixing between the jets takes place much further downstream than previously proposed (greater than 10 jet diameters). This was due to the lower velocity gradients when the jets meet only a few nozzle diameters downstream. Velocity correlation maps revealed little information about the dominant modal structure during the complex coupling. The clear region showed a similar structure to those interpreted from the characterisation study using schlieren photography.

Time resolved acoustic analysis of phase was used to examine the phase between the jets undergoing complex coupling. It was found that the individual jets experienced unsteadiness and interruptions to their screech tones. The unsteadiness did not occur simultaneously between the jets, which resulted in the jets becoming uncoupled from one another. Reduced order modelling using proper orthogonal decomposition of the full velocity field resulted in no clear coupled structure despite the existence of strong screech tones. The unsteadiness of acoustic signal prompted the use of the proper orthogonal decomposition on the individual jets to capture their individual modal structures. A single hydrodynamic mode pair was found for each jet. The distribution of the mode energy for each particle image velocimetry snapshot revealed that the jet could have been in either a symmetric coupling mode, an anti-symmetric coupling mode, or neither coupling mode. Thus the symmetric and anti-symmetric coupling modes were deemed to be in competition with a portion of the velocity snapshots exhibiting incoherent oscillations when neither was selected. The symmetric and anti-symmetric coupling modes were associated with a tone encountered at high and low jet nozzle pressure respectively. The two tones had a slightly different frequency and overlapped when examined as a function of sound pressure level vs. jet pressure. Therefore it is deduced that it is the mechanism in which they couple together that produces two coupling modes of different frequencies for a fixed jet hydrodynamic wavelength.

The azimuthal structure of the coupled jets and the acoustic amplification in response to different coupling modes was examined. Two toroidal, a helical, and a 2SS mode were deduced. The 2SS mode was symmetric in-plane but also contained a strong out-of-plane flapping component. In previous studies, it has been observed as a mode with a high instability growth rate determined from stability analysis. The jets were forced in the four different modes found in the mode staging parameter space but outside of where they are naturally encountered as a function of jet pressure. Strong amplification of these modes was observed in the acoustic spectra, which rolled off further away from their natural positions in the parameter space. The amplification of foreign modes not present in the natural spectra

was not as significant. Thus the response to forcing indicated the hydrodynamic instability was shown to have been a factor in the selection of the coupling mode despite the (potentially dominating) presence of upstream acoustic forcing. Lastly, the forcing of only one of the two-jets was examined. It was found that the adjacent unforced jet adopted the forced mode of the forced jet. Thus it was shown that the feedback loop between the jets must have relied on an acoustic pathway in the internozzle-region between the jets.

List of Publications

Bell, G., Soria, J., Honnery, D., & Edgington-Mitchell, D. (2016, December). PIV analysis of coupled supersonic twin-jets. In *20th Australasian fluid mechanics conference* (pp. 5-8).

Bell, G., Soria, J., Honnery, D., & Edgington-Mitchell, D. (2017). Particle image velocimetry analysis of the twin supersonic jet structure and standing-wave. In *23rd AIAA/CEAS aeroacoustics conference* (p. 3517).

Knast, T., Bell, G., Wong, M., Leb, C. M., Soria, J., Honnery, D. R., & Edgington-Mitchell, D. (2018). Coupling modes of an underexpanded twin axisymmetric jet. *AIAA Journal*, 56(9), 3524-3535.

Bell, G., Soria, J., Honnery, D., & Edgington-Mitchell, D. (2018). An experimental investigation of coupled underexpanded supersonic twin-jets. Experiments in Fluids, 59(9), 139.

Bell, G., Cluts, J, Samimy, M., Soria, J., & Edgington-Mitchell, D. Mode Selection and Stability in Coupled Underexpanded Twin-Jets. Journal of Fluid Mechanics (currently under-review).

Declaration

I hereby declare that this thesis contains no material which has been accepted for the award of any other degree or diploma at any university or equivalent institution and that, to the best of my knowledge and belief, this thesis contains no material previously published or written by another person, except where due reference is made in the text of the thesis.

This thesis includes two original papers published in peer-reviewed journals, one currently under review, and two original papers published in conferences. The core theme of the thesis is centred on the analysis of resonance between circular twin supersonic jet plumes. The ideas, development and writing up of all the papers in the thesis were the principal responsibility of myself, the student, working within the Department of Mechanical & Aerospace Engineering under the joint supervision of Dr. Daniel Edgington-Mitchell and Professor Damon Honnery.

The inclusion of co-authors reflects the fact that the work came from active collaboration between researchers and acknowledges input into team-based research.

In the case of Chapters 5, 6 and appendix A, my contribution to the work involved the following:

Title	Status	Student contribution	Co-authors (contribution)	Monash University student
Chapter 5				
An experimental investigation of coupled underexpanded supersonic twin-jets.	Published	60 %, Experiment design, data collection, and analysis. Data analysis, figure preparation, and manuscript writing.	1. Soria, J. (10 %: Input into manuscript.) 2. Honnery, D. (10 %: Input into manuscript) 3. Edgington-Mitchell, D. (20 %: Input into manuscript)	1. No 2. No 3. No
Appendix A				
Coupling modes of an underexpanded twin axisymmetric jet.	Published	8 %, Data analysis and interpretation. Manuscript writing.	1. Knast, T. (51 %: First author.) 2. Wong, M. (8 %: Data collection.) 3. Leb, C. (5 %: Data collection.) 4. Soria, J. (5 %: Input into manuscript.) 5. Honnery, D. (8 %: Input into manuscript) 6. Edgington-Mitchell, D. (15 %: Input into manuscript)	1. Yes 2. Yes 3. Yes 4. No 5. No 6. No

Candidate's signature: Date: 05/11/2019

Graham Bell

The undersigned hereby certify that the above declaration correctly reflects the nature and extent of the student's and co-authors' contributions to this work. In instances where I am not the responsible author I have consulted with the responsible author to agree on the respective contributions of the authors.

Main Supervisor signature: Date: 05/11/2019

Dr. Daniel Edgington-Mitchell

x

Acknowledgements

I feel genuinely privileged to have had the opportunity to engage in my passion for science and engineering in a doctorate at Monash University with the Laboratory for Turbulence Research in Aerospace and Combustion (LTRAC). My appreciation is especially directed towards Dr. Daniel Edgington-Mitchell who very generously provided the opportunity. I would like to thank both my supervisors, Dr Daniel Edgington-Mitchell and Professor Damon Honnery, for their support in providing me a platform to experience a first-class graduate education. The experience has challenged me and provided significant opportunity for self-improvement. Above all, it has provided me the confidence as an engineer and researcher to forge a path rather than to follow one.

Among the many opportunities for growth and experience during the doctorate, I would like to especially thank Daniel for the opportunity to participate in conferences and study tours. The trips to Colorado and Ohio were particularly memorable. For the scientific collaboration with The Ohio State University in 2018, I would like to thank Professor Mo Samimy, Dr. Jordan Cluts, and Dr. Nathan Webb for the support that made the experience a success.

The research students and culture within a laboratory are the catalyst that turns a post-graduate experience into many fantastic memories through the bond of shared experience. In particular I would like to extend my appreciation to the company on the front-line: Nick, Dom, Joel, Tom, and Mike. I would also like to send my thanks to the younger students who have taken the culture to new heights: Marcus, Harry, AJ, Sean, Bhav, Jess, and Rhiannon.

I'd like to thank my family that clearly instilled an attitude of restless curiosity at an early age that has carried through to today. I'd like to thank my Dad for bringing engineering close to our home and for providing a shed to tinker in. My deepest appreciation goes to my Mum. Your courage to speak out, get involved, put your hand up, and confront issues left me slightly embarrassed as a kid, but in awe as an adult. Shortly before this experience, your life was cut tragically short by cancer. I miss you terribly. Grieving for you has lit a flame inside of me that cannot be put out: a sense of resilience, bravery, and an appreciation for the finite nature of life. You never thought you were smart and frankly neither did I. But thanks to you I'm now standing at the doorway to completing a PhD in one of the most challenging fields in engineering. That is more than I could have dreamed for. To have your spirit inside of me is the greatest gift. You are my hero.

Lastly, to the other prominent woman in my life, I wish to thank my partner Zoe for her compassion, patience, and support. You are my greatest supporter and the enabler of dreams. I will be forever grateful.

Contents

List of Figures

List of Tables

Chapter 1

Introduction

High-speed engine exhausts (referred to simply as jets in scientific/laboratory terminology) exhibit a tremendous capacity for noise generation. The gas propelled from the high-speed exhausts is typically supersonic. Air and spacecraft use multiple engines clustered together for practical reasons. Multiple smaller engines offer resistance to total engine failure, reduced frontal area drag, and greater total thrust.

The plumes of parallel supersonic jets can strongly interact producing potentially undesirable acoustic resonance. Berndt (1984) first reported the acoustic resonance between the exhausts of twin-engine aircraft. It was found the exhaust plumes of the B-1B aircraft (shown in figure 1.1) were interacting with sufficient intensity to cause empennage component failure via fatigue. The constant operation of the engines resulted in fatigue failure well before the expected life of the components.

Figure 1.1: The first prototype Rockwell B-1A Lancer, 74-0158, takes off at AF Plant 42, Palmdale, California, on its first flight on 23 December 1974. Rockwell International later merged with Boeing. Source unknown.

The acoustic resonance of parallel supersonic jets is also observed at the laboratory scale where it is more easily studied. Seiner *et al.* (1986) investigated models of the F-15 exhausts after similar interaction

problems to the B-1B were encountered. The analysis used schlieren photography to reveal the link between the resonance problem observed in the B1-B and F-15 to the aeroacoustic phenomenon of screech. Screech is an aeroacoustic feedback phenomenon that is found in shock containing supersonic single jets (Powell, 1954; Tanna, 1977; Norum, 1983; Tam *et al.*, 1986). Screech organises the production of downstream convecting coherent vortical structures (CVS) with upstream travelling acoustic waves. A characteristic feature of screech is an intense discrete tone present in the acoustic spectra of the jet (Tam & Seiner, 1987; Seiner *et al.*, 1986). The screech tone intensity present in the F-15 experiments was shown to be greater than the sum of two screeching single-jets (Seiner *et al.*, 1986). Studies exploring different jet spacings and pressure ratios have shown that it is up to 20 dB greater (Shaw, 1990).

The screech interaction produces coupling between the jet plumes. A representation of the coupling is shown in figure 1.2. The jets are coupled anti-symmetrically about the centreline. The spacing between the jets is non-dimensionalised between the jets by the jet diameter, i.e s/D. Shock features are labelled and will be introduced in chapter 2. The jet coupling is a function of nozzle pressure ratio (NPR), nozzle spacing (s/D), boundary-layer thickness, shear-layer growth-rate, nozzle geometry, and the acoustic environment (Wlezien, 1989; Morris, 1990; Shaw, 1990; Alkislar *et al.*, 2005). NPR is the ratio of nozzle stagnation pressure at the nozzle exit (p_0) to ambient pressure in the exhaust region.

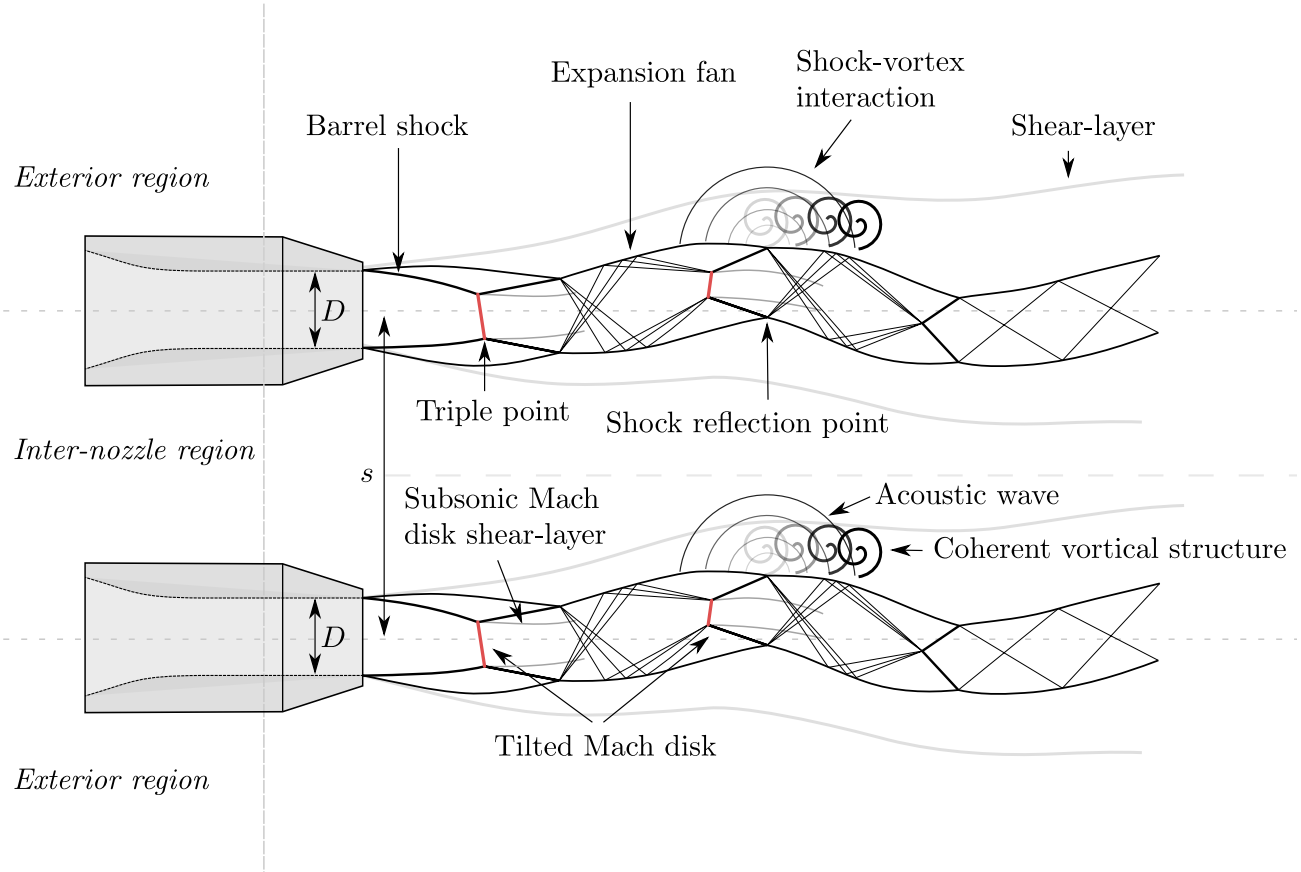

Figure 1.2: A schematical representation of the supersonic coupled twin-jet interaction.

Early studies examined the coupling parameter space to identify different coupling modes and their acoustic amplitudes (Seiner *et al.*, 1986; Wlezien, 1989; Shaw, 1990). Although clear resonance is generally encountered within the parameter space, more complex resonant behaviour has been found under certain jet configurations (Wlezien, 1989; Srinivasan *et al.*, 2009). Studies have identified multi-

modal screech tones corresponding to coupling modes of different amplitudes (Wlezien, 1989; Seiner *et al.*, 1986). Rectangular jet configurations are known to exhibit complex coupling that has resisted description of its mode shape (Raman, 1998; Panickar *et al.*, 2004). Non-linear interactions between the jets have been identified that suggest widely used signal processing methods are unsuitable to analyse these flows (Panickar *et al.*, 2005; Srinivasan *et al.*, 2009; Raman *et al.*, 2012). An explanation for the flow physics in these configurations is lacking and investigations on the prevalence of these configurations in circular jets have not been carried out. More studies are needed to understand the jet coupling in these configurations.

The present work seeks to find an explanation for the complex coupled regions encountered in circular twin-jets. The complex shock-laden flow is most readily investigated experimentally. Chapter 4 presents a joint initial scoping and classification investigation using schlieren photography from facility one (described in chapter 3), where the author played a supporting investigative role. Different modes are classified using schlieren photography and the corresponding phase relationship between the jets is linked to their acoustic signal.

Part of the investigative challenge of the complex interaction between certain modes in the twin-jet is the lack of quantitative data in different configurations (and coupling modes). Chapter 3 outlines three facilities and techniques used in this thesis to obtain quantitative information on the flow. Facility one uses schlieren photography and phase analysis via opposing microphones to allow broad sweeps and modal analysis of the parameter space. Facility two uses a particle image velocimetry (PIV) facility to provide instantaneous velocity fields for the examination of flow statistics and the production of reduced order models. Facility three uses a microphone array and nozzles capable of actuated forcing to investigate the structure of coupling modes and observe their response to forcing.

Chapter 5 describes an experimental approach to provide quantitative data to facilitate deeper investigation of the flow physics by examining PIV data derived from facility two. The dataset comprises two distinct coupling modes (clear and weakly coupled) such that features of the twin-jet flow can be compared. The jet merge-point, mixing in the inter-nozzle region, and the shear-layer growth asymmetry due to the adjacent jet are quantified and compared between modes. The fullfield velocity is decomposed within the clear and weakly coupled regions to examine the hydrodynamic structure of the flow.

Chapter 6 investigates the weakly coupled hydrodynamic and acoustic interactions between the jets. New approaches are developed to deduce the acoustic behaviour of the individual jets. The acoustic behaviour is used to inform different decompositions of the velocity field so that hydrodynamic interaction between the jets can be determined.

Chapter 7 uses facility three to identify the three-dimensional structure of the various coupling modes and the jet's response to forcing. Actuation and acoustic amplification is used as a proxy to assess the stability margins of the modes. Lastly, the enhancement of the coupled mode when only a neighbouring jet is actuated is investigated. Some final comments about the pathway of the coupled feedback loop are included.

Chapter 2

Background

2.1 Screech and Aeroacoustic Resonance

An intense sound produced by screeching jets has been studied for more than 70 years by engineers and scientists. Alan Powell was a pioneer in developing the description of intense acoustic sound produced by imperfectly expanded supersonic jets. His seminal work describes the aeroacoustic feedback loop within free-jets (jet screech, (Powell, 1953*b*,*c*)) and the interaction between a jet and a plate-edge (edge tones, (Powell, 1953*a*, 1961)). The subsequent investigative effort into the screech resonance phenomena has been significant and forms an integral part of the field of aeroacoustics.

The jet screech feedback loop is schematically shown in figure 2.1. The feedback loop is characterized by the following processes (adapted from Edgington-Mitchell (2019)):

- The downstream propagation of energy, typically in the form of a hydrodynamic perturbation (hereafter called the downstream process).
- A mechanism by which energy associated with the downstream-propagating perturbation is converted into an upstream-propagating disturbance. This mechanism is also typically responsible for the generation of acoustic tones (hereafter called the generation process).
- The upstream propagation of this disturbance to a point where the base flow is sensitive to perturbation (hereafter called the upstream process).
- The forcing of this sensitive point in the flow by the upstream-propagating disturbance resulting in the production of a new downstream-propagating hydrodynamic disturbance (hereafter called the receptivity process).

Powell proposed two criteria that must be satisfied to close the screech feedback loop based on phase and amplitude.

The first criterion is one based on the phase of the receptivity and generation processes. The frequency of the resonance model is selected such that the feedback loop becomes self-reinforcing. The feedback loop consists of upstream-propagating fluctuations that perturb the thin jet shear-layer in the region of the nozzle lip. The fluctuations occur at a frequency, f. Instability mechanisms within the thin

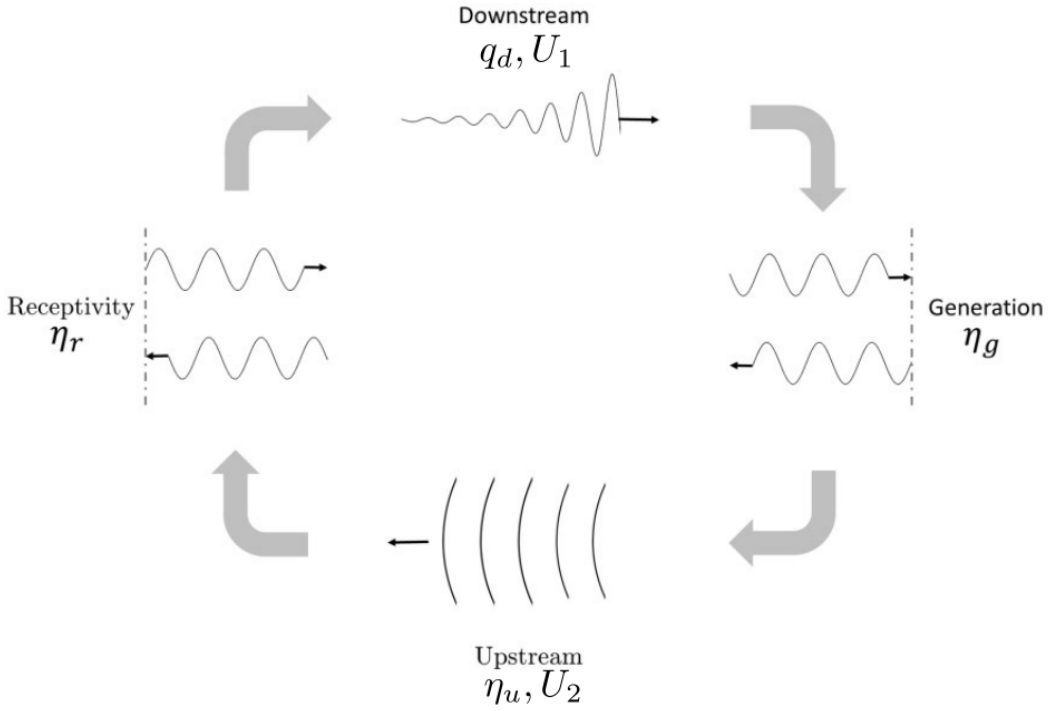

Figure 2.1: Screech processes. Adapted from of Edgington-Mitchell (2019)

shear-layer lead to downstream-propagating hydrodynamic perturbations. These advect downstream with an average velocity of U_1. The downstream-propagating hydrodynamic perturbations interact with shock-cell reflection points within the core of the jet. A dominant emission of sound is produced a nominal distance h downstream. The emission of sound forms the upstream-propagating component and travels with an average speed of U_2. The upstream-propagating component completes the feedback loop.

Powell proposed the relationship between f, h, U_1, and U_2 to be expressed as shown in equation 2.1.

$$\frac{N}{f} = \frac{h}{U_1} + \frac{h}{U_2} + \phi \tag{2.1}$$

where, ϕ contains an observed delay in the receptivity process near the nozzle-lip and the production of acoustic sound downstream. N is the integer value of the number of simultaneous upstream and downstream propagating cycles in the flow at any point in time.

The second criterion for feedback resonance is concerned with the amplitude, gains, and receptivity of the individual processes. The combined process gains of the steady-state resonant-processes should be equal to one and greater than one during transient growth such that

$$q_d \eta_g \eta_u \eta_r \geq 1. \tag{2.2}$$

Where q_d is the gain associated with the downstream process, η_g represents the conversion efficiency of downstream-propagating energy into upstream-propagating energy, η_u is a transmission efficiency for the upstream-propagating disturbances, η_r is the efficiency of the receptivity process that takes place at the nozzle lip.

2.1.1 Staging Behaviour

The feedback criteria are satisfied under a number of different configurations within the jet system. For example, h could be considered to originate from the fourth or the fifth shock-cell. Therefore, different configurations of the feedback loop parameters can give rise to different screech peak frequencies at the same operating condition.

The modifications of the parameters typically correspond to changes in operating conditions of the jet. The dominant operating conditions include the nozzle pressure ratio (NPR) in single jets and additionally the jet spacing in twin-jets. The jet spacing defined by the ratio of spacing between the nozzle centrelines to exit diameter (s/D). The frequency selection behaviour as a function of the operating conditions is coined the staging behaviour (Seiner, 1984; Tam, 1991). It is exhibited within the stacked power spectral density plots shown in figure 2.2. A single power spectral density response is shown in figure 2.2a. This frequency response is typical of screech as it shows sharp discrete peaks of high intensity, corresponding to the selected jet screech frequency. Harmonics are observed at multiples of the fundamental screech frequency. The high-amplitude narrow-band screech frequencies form continuous lines when stacked as a function of NPR as shown in figure 2.2b. These lines discontinuously change as the NPR is increased. This allows certain screech peak frequencies to exist within discrete NPR or s/D regions. Staging behaviour occurs in many different types of jet configurations such as single, elliptical, rectangular, impinging, twin-jets, and twin-impinging.

The different peak frequencies in the acoustic spectra corresponded to different observed jet modes (Powell, 1954). The modes are described by their apparent shape in order of which they appear when increasing NPR in a single jet. A representation of single jet mode staging is shown in figure 2.3. At low levels of under-expansion A1 and A2 toroidal modes are observed. Precessing flapping (B and D) or helical (C) modes are often observed at higher NPR (Davis & Oldfield, 1962; Norum, 1983; Powell *et al.*, 1992; Edgington-Mitchell *et al.*, 2015). The modes for axisymmetric jets can be linked to azimuthal mode-number of order m. The A1 and A2 modes are associated with the $m = 0$ mode. The helical C mode corresponds to $m = +1$ or -1. The flapping B and flapping-precessing (mode D) modes are produced by the superposition of a $m = \pm 1$ mode with a fixed phase relation. These produce an apparent flapping motion.

The sensitivity of mode staging to boundary conditions is significant (Edgington-Mitchell, 2019). This sensitivity often results from facility specific behaviour. While the typical progression of A1, A2, B,... modes is agreed on by jet-aeroacoustic community, the presentation of modes in practice is often facility dependent.

Models have been proposed to explain the staging in the feedback loop. One model considers the ratio of simultaneous waves to the distance to receptivity of the screech sound source in the feedback loop (Gao & Li, 2010). A computational study was used to determine the number of concurrent upstream and downstream propagating waves (screech cycles) n_{cycles}. The numerical study revealed five concurrent propagating waves for a flapping mode and six for a helical mode. This was compared with an effective noise source originating from shock cell n related by the shock-cell spacing, L is the shock-cell spacing provided by the Pack-Prandtl relation (Pack, 1950) shown in equation 2.3 to estimate the distance h (from equation 2.1) where the upstream process is generated.

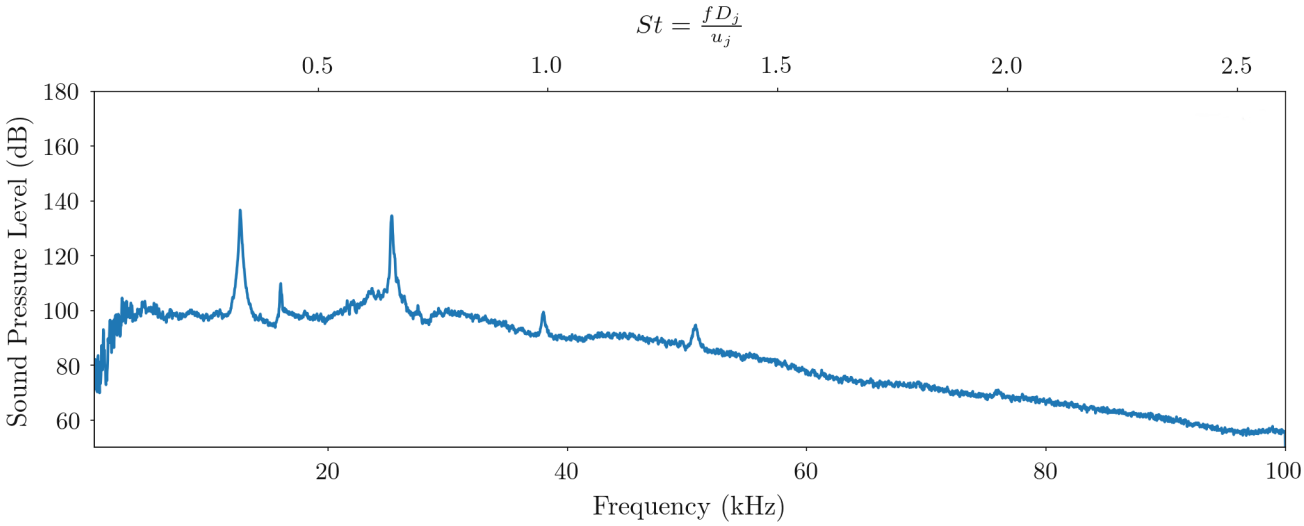

(a) Single Power Spectral Density estimation at NPR = 3.0 for $s/D = 3$.

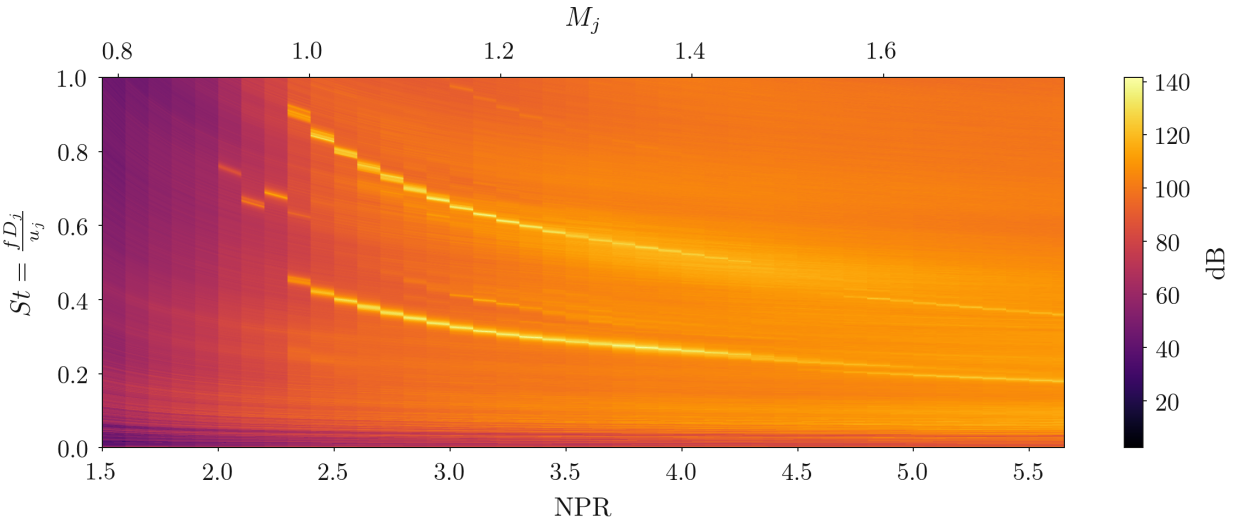

(b) Power Spectral Density estimation waterfall across NPR values.

Figure 2.2: Illustrative acoustic spectra for an underexpanded twin-jet and spacing $s/D = 3$. Produced using acoustic data from facility two discussed in chapter 3.

$$\frac{L}{D} = k\sqrt{M_j^2 - 1} \tag{2.3}$$

Where L is the length of the shock spacing, D is the diameter of the circular jet, and M_j is the ideally expanded Mach number. k is a constant derived analytically to be equal to 1.306. In later experiments k is determined to be closer to 1.26 as the effects of viscosity were not considered in the original formulation (Gao & Li, 2010).

The velocity of downstream convecting structures is represented by the convective Mach number, M_c. Frequency prediction is performed by relating the ratio of simultaneous waves to source length via a timing argument. The timing argument enabled the development of the frequency/wavelength prediction formula shown in equation 2.4.

$$\lambda_s = \frac{nL}{n_{\text{cycles}}} \frac{1 + M_c}{M_c} \tag{2.4}$$

The predictions have been compared to experimental observations of screech frequency. Good agreement with the observed frequency can be achieved assuming the ratios of n_{cycles}, n, L, and M_c can be determined. The measurement of these parameters, however, is not experimentally trivial. n_{cycles} was measured within the original study using a trace of pressure. Pressure traces in high-speed flows are challenging to obtain and obtrusive techniques (such as a pitot tube) disrupt the flow path, which potentially changes the feedback pathway. Large pressure fluctuations within the jet make determination of n_{cycles} challenging to resolve. The determination of the emanating shock-cell has evaded experimental researchers through its observed facility dependence; Thus n cannot be confidently known a priori (Davis & Oldfield, 1962; Norum & Seiner, 1982; Panda & Seasholtz, 1999; Gao & Li, 2010; Mercier *et al.*, 2017). The convective Mach number, M_c, also has as history of variability depending on the experiment. Jet mode, Reynolds number, and jet boundary conditions are known to affect the measurement and a comparison of different result is included in Gao & Li (2010). When the values of M and nL are greater than approximately five, the difference between integer values produces small changes to the fraction $\frac{nL}{M}$. Therefore consideration must be taken in its application considering the challenges of experimentally verifying each variable so that it is not used empirically.

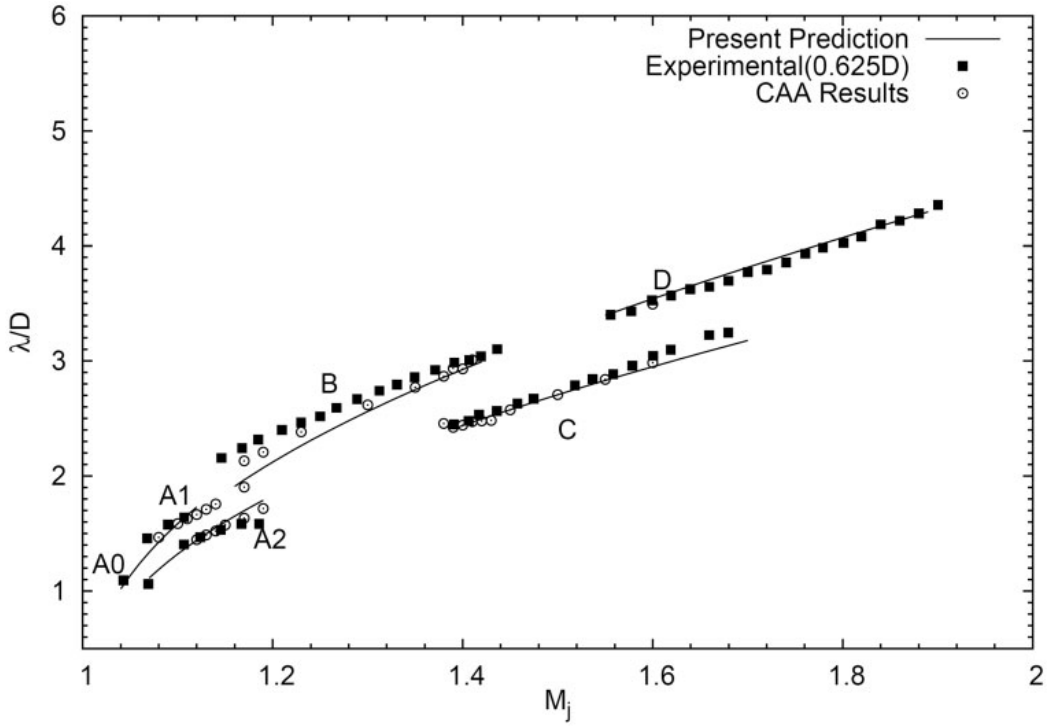

Figure 2.3: Staging behaviour prediction capability using the model of Gao & Li (2010). Figure from of Gao & Li (2010). Different combinations of M, n, L, and M_c are used in conjunction with equation 2.4 to make frequency predictions, which can be selected to have a close match with experimental results. The experimental results are from a single jet (Ponton *et al.*, 1997).

2.1.2 Standing-Wave

The interaction between downstream convecting coherent vortical structures and upstream propagating acoustic waves forms a standing-wave pattern in the near-field pressure (Westley & Woolley, 1969).

Common usage of the term 'standing-wave' implies that the resulting interference pattern between two waves is spatially fixed stationary to an observer. The standing-wave interference pattern in this instance translates spatially. This is due to the difference in propagation speeds of the downstream convecting CVS and upstream propagating acoustic waves. Therefore an ensemble mean performed on the schlieren images containing an expected standing-wave reveals no banded structure; The feature is blurred out by the apparent translation of the interaction. As the frequency between the two propagating waves is equal (as it is locked to the screech frequency), the standing-wave is one based on fluctuation amplitude. This fluctuating pressure amplitude is stationary and observable in schlieren visualisations, which measure path-integrated density-gradient. To observe fluctuating density gradient amplitude, the ensemble variance or standard deviation of the schlieren is calculated. Example figures of this technique are shown in figure 2.4.

The interference of the pressure fluctuations of the two opposite upstream and downstream moving phenomena produces a banded pattern in the pressure field of screeching jets. This banded pattern is visible in the ensemble standard deviation of schlieren images, shown in figure 2.4. The standing wavelength has been proposed as a characteristic length-scale for screech (Panda, 1999). Historically, the shock cell spacing has also been used as a characteristic length scale. Recent work has suggested that a match or mismatch between these length scales is linked to different acoustic feedback mechanisms (Edgington-Mitchell *et al.*, 2015; Bogey & Gojon, 2017).

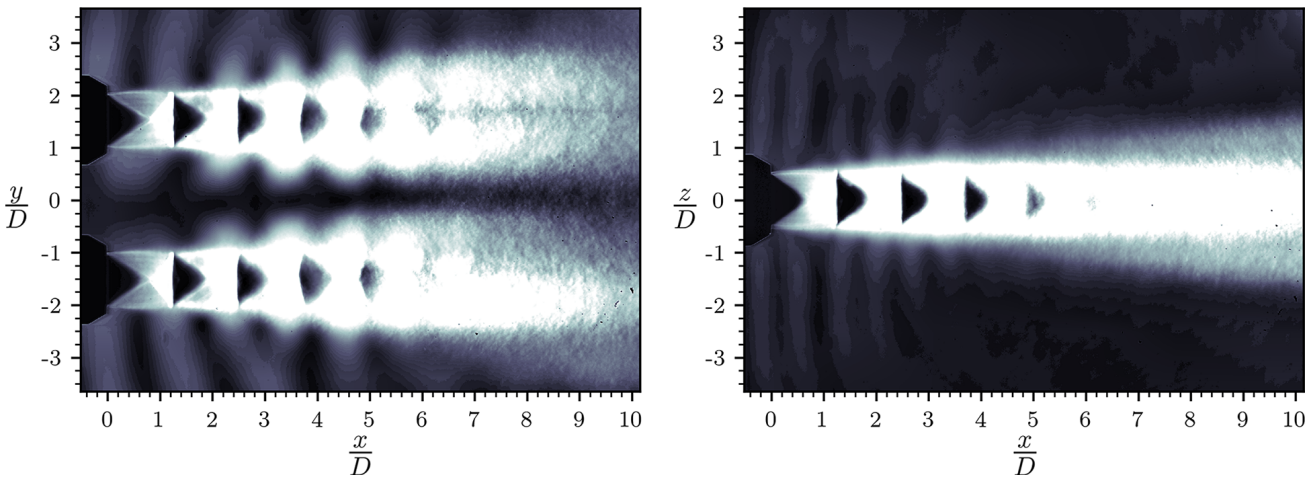

Figure 2.4: Standard deviation of the ensemble of randomly sampled schlieren images of an underexpanded $s/D = 3$ twin-jet. From Knast *et al.* (2018). The standard deviation shows the existence of a stationary standing-wave exterior to the jet core. It is caused by the superposition of upstream and downstream interacting acoustic waves.

2.2 The Introduction of a Parallel Adjacent Jet in Close Proximity

The introduction of a second supersonic jet can cause the coupling and enhancement of the feedback mechanisms typically observed in a single jet (Raman *et al.*, 2012). The conventions for the dominant symmetry planes for the twin-jet are shown in figure 2.5. The conventions that are used to discuss the different in-plane features are shown in figure 2.6. The inter-nozzle region represents the fluid between the jets outside of the shear-layer. There is significant acoustic intensity in this region during the coupled interaction (Raman, 1998; Seiner *et al.*, 1986). The shear-layers experience different boundary conditions depending on their azimuthal position. In chapter 5, the two extremes of this boundary condition will be considered. The shear-layer at the inter-nozzle azimuthal position is denoted **I** and the other that faces externally is denoted **E**.

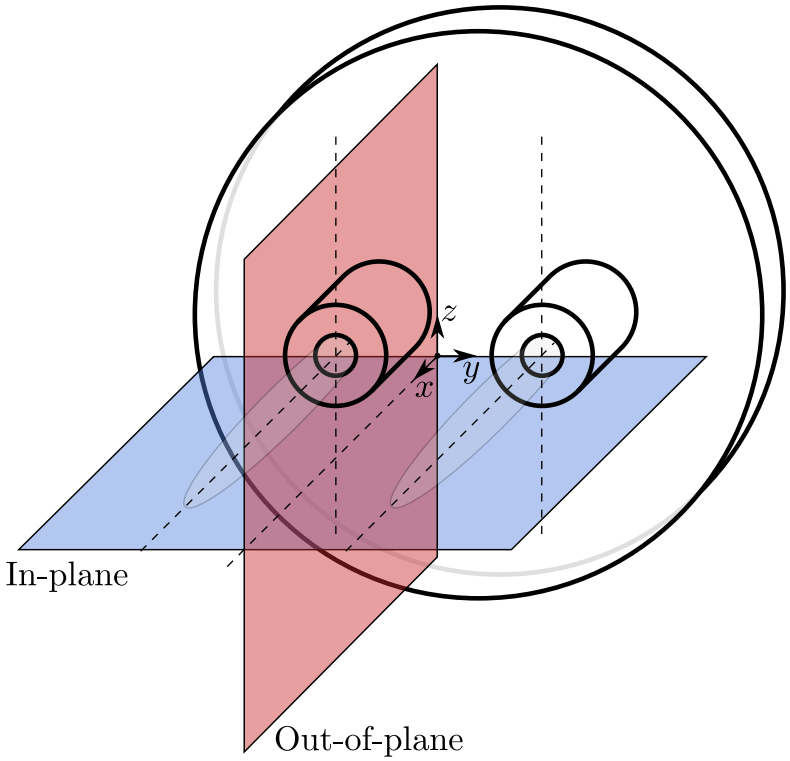

Figure 2.5: Symmetry plane definitions of the twin-jet.

Figure 2.7a shows coupling between the jets via schlieren photography for a twin-jet with a spacing of $s/D = 3$ at NPR = 3.2 and 4.4. Two different coupling modes are shown. At NPR = 3.2 the jets are found to couple strongly in an anti-symmetric mode about the symmetry-plane between the jets. A symmetric coupling mode is observed at NPR = 4.4.

Figure 2.7b shows the time-averaged schlieren images for the jet at the condition NPR = 3.0. Beyond the forth shock-cell, the shock-waves experience significant motion-blur from the passage of CVS that cause the translation of shock structures. The edge-on (out-of-plane) image in Figure 2.7b shows that the shock cells remain sharper until approximately the fifth shock-cell in this orientation. Therefore the translation of the shock structures and hence CVS is primarily in in-plane at this configuration.

The spacing to diameter ratio between between the jets, s/D, strongly affects the observed resonance behaviour in addition to the NPR. The spacing is measured from nozzle centre-centre as shown in

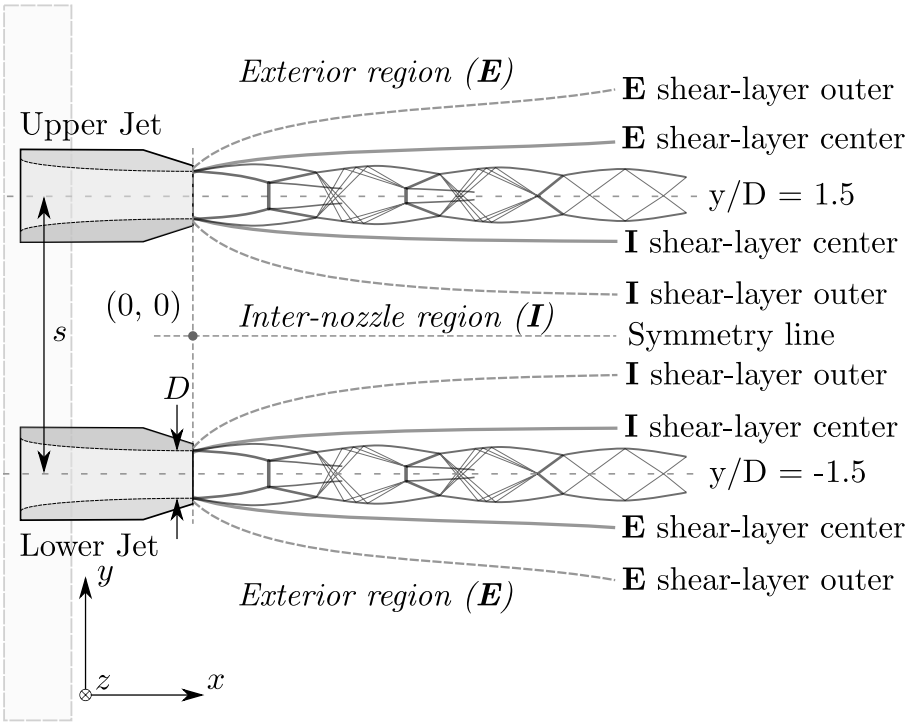

Figure 2.6: Schematic showing coordinate, line, and region definitions definitions used in this thesis for an s/D = 3.0 twin-jet.

figure 2.6. Coupling has been shown to occur whether the jets are very close together or are further apart (Raman, 1998; Wlezien, 1989; Moustafa, 1994). The merging and hydrodynamic interaction of the plumes occurs at a short distance downstream for closely spaced jets (s/D < 3.0) (Seiner *et al.*, 1986). Spacings of s/D = 15 have reported coupling (Raman, 1998). Therefore acoustic information propagates between the jets without hydrodynamic interaction completing part of the feedback loop (Raman *et al.*, 2012).

2.2.1 The Twin-Jet Parameter Space

Berndt (1984) and Seiner *et al.* (1986) provided practical insight into the coupling phenomenon and its impact on high-speed aircraft. A summary of the initial work by Berndt (1984) is included in appendix E. Seiner *et al.* (1986) assessed the twin-jet resonance using techniques and frameworks for experimentally investigating screech. This includes phase-locked schlieren, microphone power spectral density (PSD), multiple microphone coherence analysis, axial pressure measurements, and azimuthal mode classification. Since the relevant application aircraft was the F-15, a 1/40$^{\text{th}}$ scale model was used for experimentation. The scale nozzles consisted of a diameter D = 15.7 mm, and inter-nozzle spacing s/D = 1.9. The baseline experiment was performed at a NPR = 2.85 corresponding to an ideally expanded Mach number of M_j = 1.32. They presented the first set of laboratory twin-jet measurements (reproduced in the collective figure 2.8), which allowed the visualisation and quantification of the resonance problem affecting aircraft for the first time. The PSD measurements (figure 2.8b) show a very strong peak at 7.82 kHz.

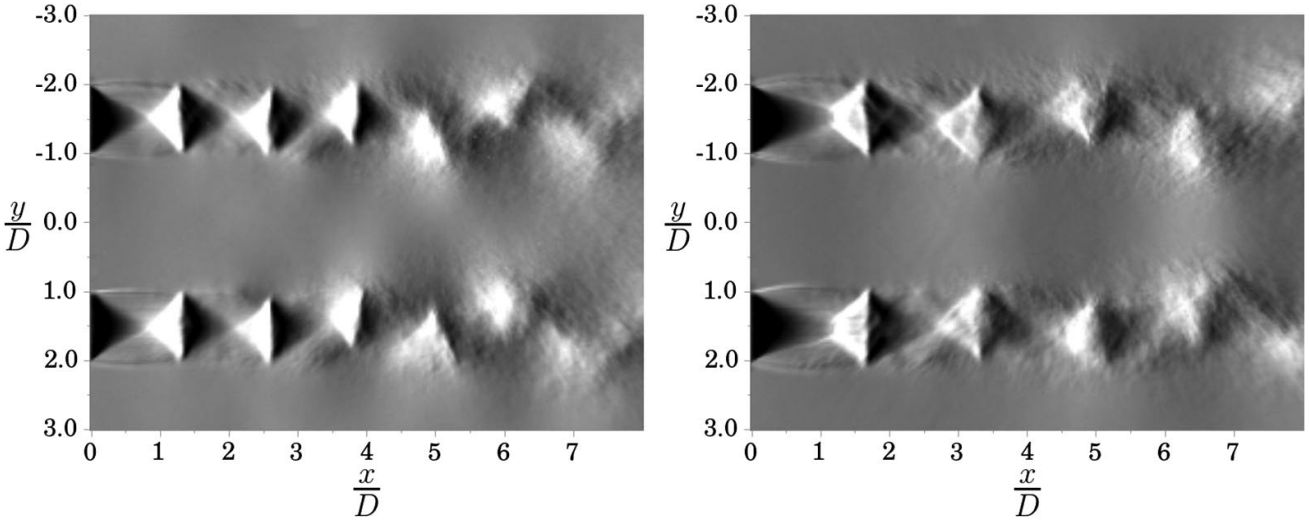

(a) Instantaneous schlieren image from Knast *et al.* (2018) showing two common coupling mode shapes of the twin-jet. Left shows an anti-symmetric oscillation occurring at NPR = 3.2 and right shows a symmetric oscillation at NPR = 4.4

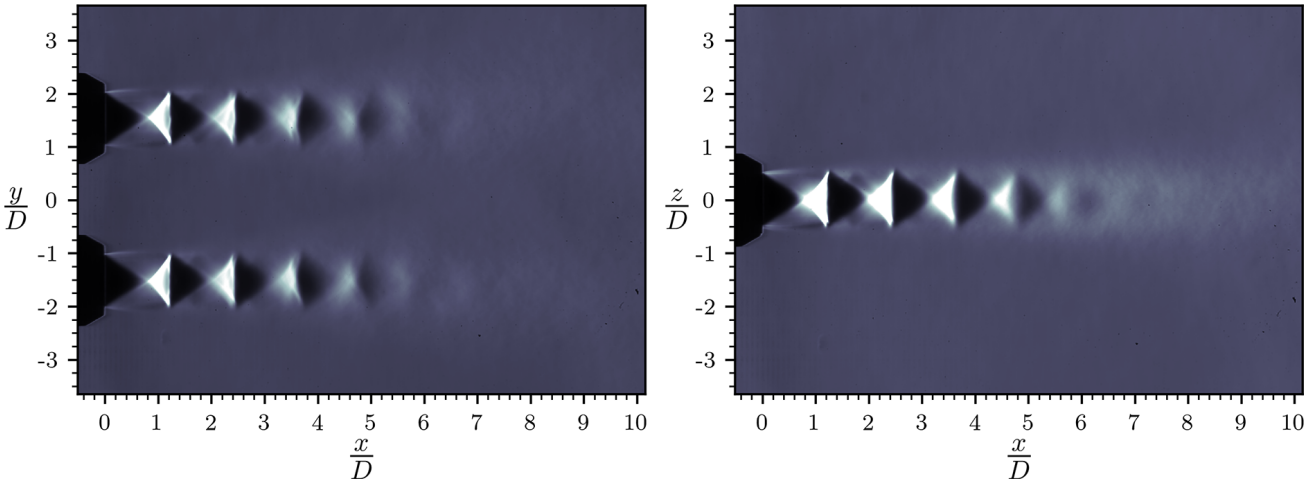

(b) Randomly sampled ensemble mean schlieren image from Knast *et al.* (2018) showing the interaction between the jets, NPR = 3.0, s/D = 3.0. Left: jets normal to camera (in-plane), Right: jets edge on to camera (out-of-plane).

Figure 2.7: Examples of the supersonic twin-jet flow field captured experimentally using schlieren photography.

The phase and coherence of the PSD peak were evaluated using opposing microphones placed in-plane either side of the jets. It was assumed that the acoustic waves being received by separate microphones originate from the nearest jet. Phase and coherence were calculated via cross power spectral density (CPSD) and are shown in figures 2.8d and 2.8c respectively. Figure 2.8c shows a coherence value close to 1.0 at the dominant resonant frequency selected from the PSD spectra. It was inferred that the jets are coupled as the acoustic frequencies produced by the jets are essentially coherent. The coupling consists of feedback cycles that are phase-locked. The coherent frequencies correspond to a frequency band of zero degrees surrounding the resonant tone. This is shown in figure 2.8d. Therefore the phase relation between the feedback cycles can be determined.

The mode shape was also examined by a schlieren visualisation system that was phase-locked to the dominant coherent frequency. The phase-locking was achieved by triggering the schlieren light source (in this case a strobe light) on the rise of the acoustic waveform. Figures 2.8e and 2.8f show the result of averaging the schlieren images at different phase positions. Clear synchronisation and coupling of the jet structure and emanating waves are observed. The shock-cells are observed to oscillate and turn with passing CVSs in a symmetric way about a mid-plane between the jets. It was concluded that the jets are flapping in-plane.

The acoustic intensity of the upstream travelling acoustic waves was also compared to that of a single jet. Figure 2.9 shows the comparison for the dominant tone (indicated by the B mode) between a single and a twin-jet measured in the inter-nozzle region adjacent to the nozzle-lip. The fluctuation of pressure on the vertical-axis shows the twin-jet producing approximately four times the intensity of pressure fluctuation compared to that of the single jet.

Experiments by Wlezien (1989) have mapped the parameter space for coupling modes and acoustic amplitudes. Twin circular converging-diverging nozzles were used with a throat diameter of 25.4 mm and an exit area ratio of 1.15. The parameter space was examined between $1.8 \leq s/D \leq 3.2$ and $1.89 \leq \text{NPR} \leq 4.25$ ($1 \leq M_j \leq 1.6$). The results are shown in figure 2.10. The mode shapes were determined using a phase-locked schlieren system. A microphone frequency spectrum analyser was used to measure the peak sound pressure level within the acoustic spectra. A set of toroidal modes A1 and A2, a central B mode (flapping), and a C mode (helical) were found consistently for each of the spacings analysed: $s/D = 1.8, 2.0, 2.2, 2.4, 2.6, 2.8, 3.0, 3.2$. The observed mode staging was proposed to be linked to changes in shock-cell spacing and shear-layer instability growth-rate. Mode classification using the phase-locked schlieren system was challenging in certain regions of the parameter space. Although the tone was clearly identified, obtaining a phase lock to trigger the schlieren flash was not possible. Small changes in nozzle geometry were found to have a large impact on the observed resonance. This parameter space study is one of the most comprehensive for circular supersonic twin-jets to date.

In-plane and out-of-plane flapping modes were reported to exist in low-aspect ratio rectangular twin-jets (Zilz & Wlezien, 1990). Figure 2.11 shows a schematic of the four jet flapping configurations that were reported to be observed using a phase-locked schlieren system. The schlieren system examined the phase relations between the jets normal to the in and out-of-plane directions. The bright and dark patterns were used to infer the jet flapping configuration, and Zilz & Wlezien (1990) proposes that all four configurations were observed. The available article of Zilz & Wlezien (1990) has since aged

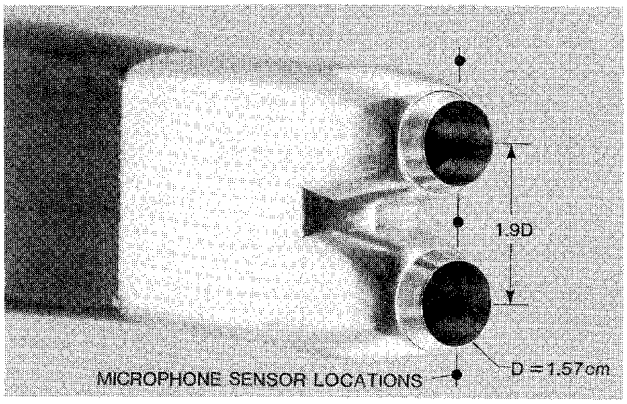

(a) Nozzle geometry and setup.

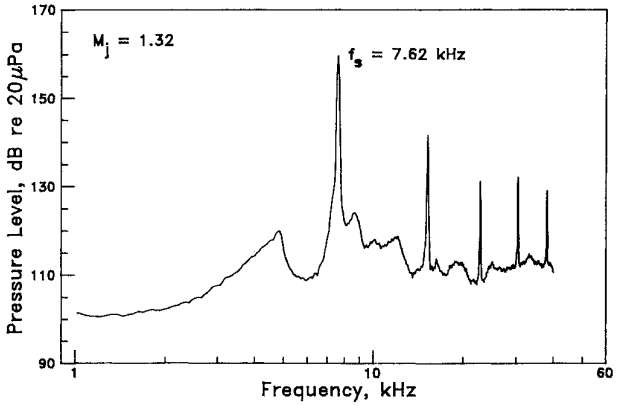

(b) Inter-nozzle microphone PSD.

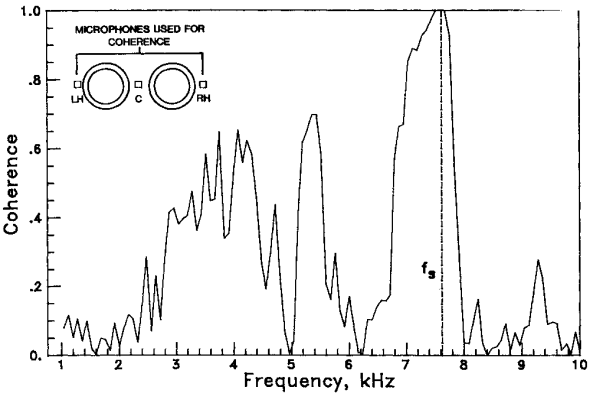

(c) CPSD-coherence between exterior microphones.

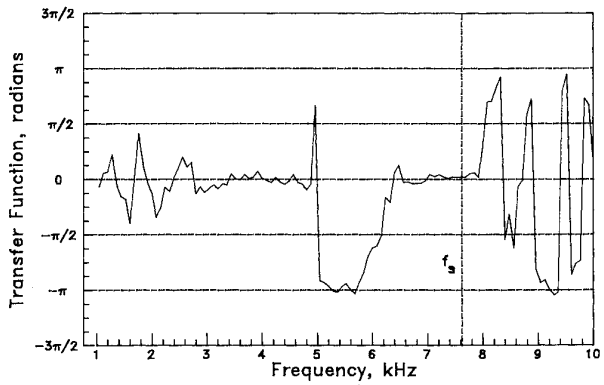

(d) CPSD-phase between exterior microphones.

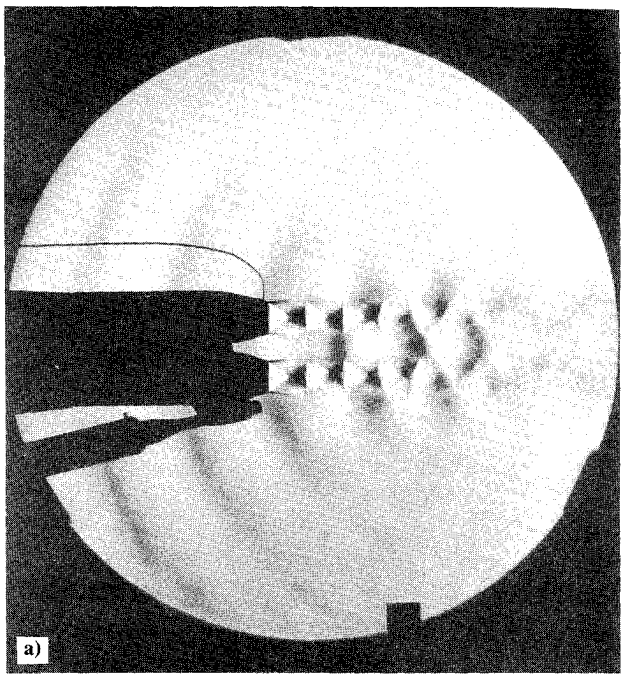

(e) Phase averaged schlieren image at $\theta = 0$.

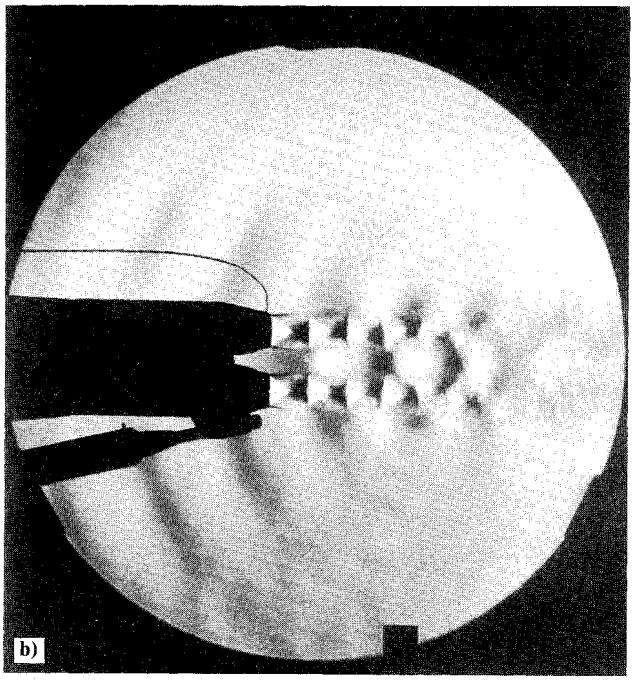

(f) Phase averaged schlieren image at $\theta = \pi$.

Figure 2.8: Figures from Seiner *et al.* (1986). The first laboratory setup and study of the twin-jet resonance problem affecting aircraft at the time.

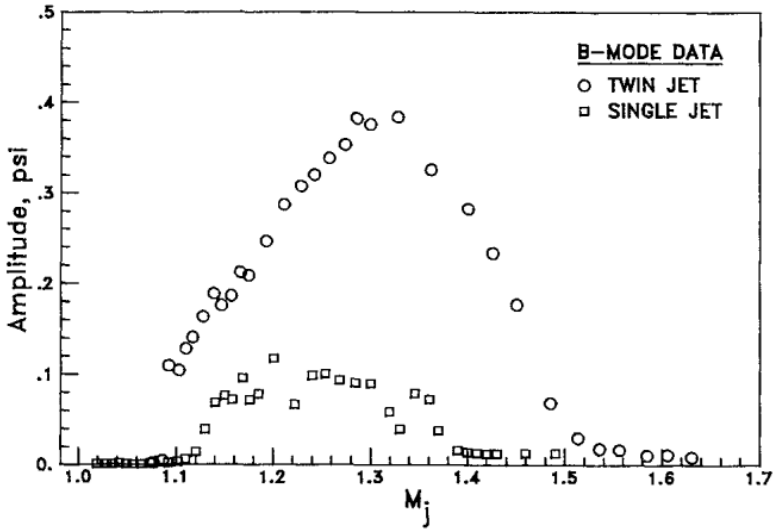

Fig. 12 Comparison of B-type helical mode amplitude behavior between single and twin jets.

Figure 2.9: Comparison between single and interacting twin-jet acoustic fluctuation levels measured adjacent to the nozzle lip (in the inter-nozzle region for the twin-jet case). From Seiner *et al.* (1986).

and the clarity of the phase-locked figures used to support the finding are presently unclear. In making the observational claims, the path-integrated nature of the schlieren technique in the out-of-plane direction was not considered. The path-integration renders the ability to determine the phase of each jet in the out-of-plane direction as speculative. This is because it is not possible to determine which jet the schlieren pattern belongs to - *it is path integrated across both jets*. More experimental investigative work is required to validate these findings.

Shaw (1990) investigated the ability to suppress twin-jet resonance via changing jet spacing, changing axial jet positioning, tabs inside the nozzle lip, and secondary jet injection. The experiments were performed using circular converging-diverging nozzles with a design Mach number of 1.47 (based on the F-15). Screech tone amplitudes of up to 162 dB were measured, which was reported to be 20 dB greater than that of the equivalent single-jet. Tabs and jet injection were found to be very effective noise suppressors. Axial spacing between the jets resulted in effectively no suppression. Lateral jet spacing was shown to change the position of the maximum intensity, but not necessarily suppress it. The sensitivity of the coupling phenomena to boundary conditions was also investigated. It was found that changing the air supply-hose length altered the observed acoustic intensity and mode-switch location. It was concluded that the additional hose alters the nozzle boundary-layer. The boundary-layer exiting from the nozzle has a strong effect on initial shear-layer thickness and hence the receptivity process.

2.2.2 Twin-Jet Resonance

As discussed in section 2.1, the screech resonant feedback loop consists of four processes. The upstream and downstream processes translate energy in the axial direction of the jet. The generation and receptivity processes involve the conversion of the energy into the upstream or downstream processes respectively. The downstream process draws energy from the jet and the conversion of this energy

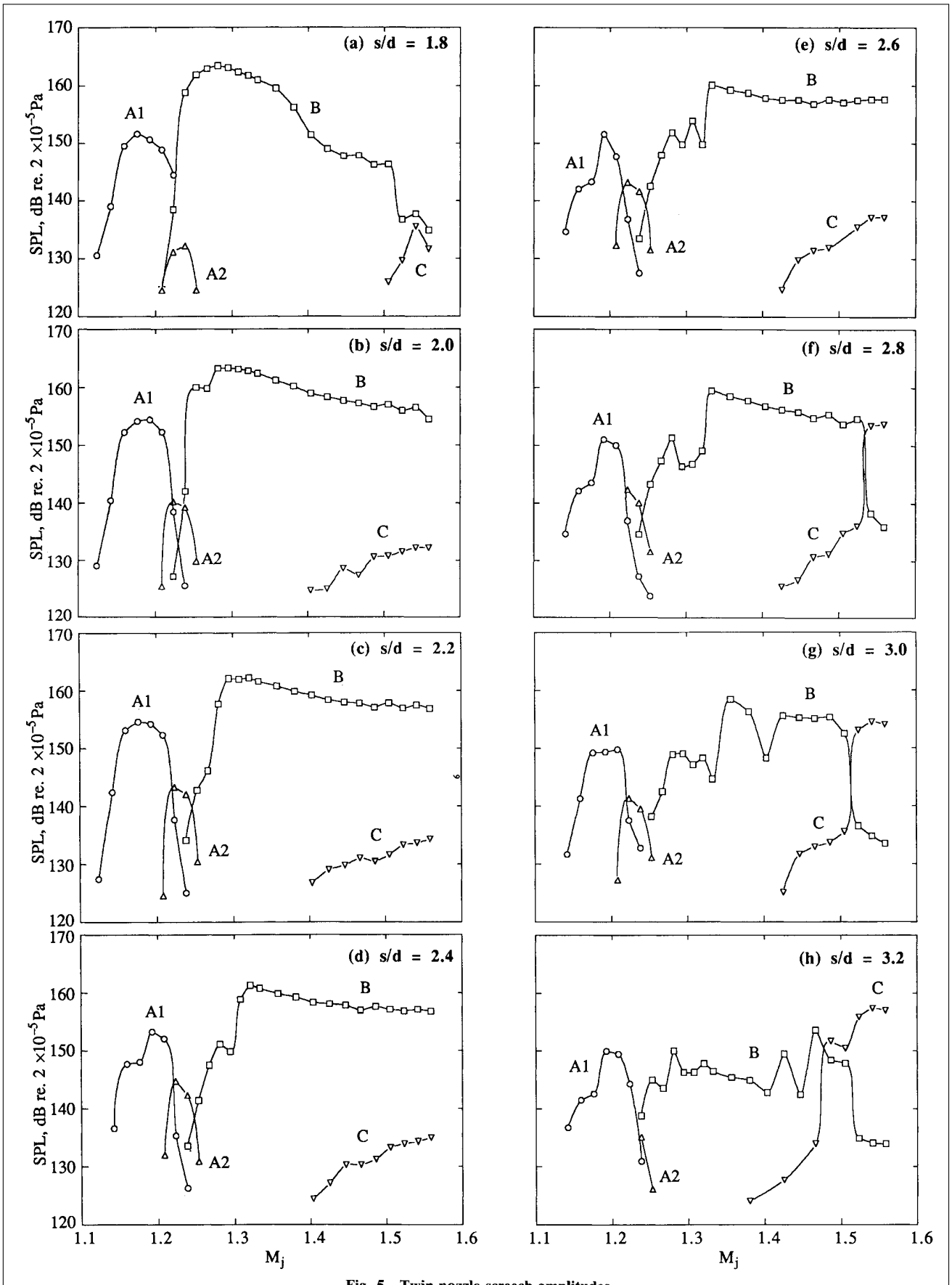

Figure 2.10: Screech tone parameter space results from Wlezien (1989). Nozzles are circular converging-diverging. Parameter space was investigated using a microphone, frequency spectrum-analyser, and a phase-locked schlieren system.

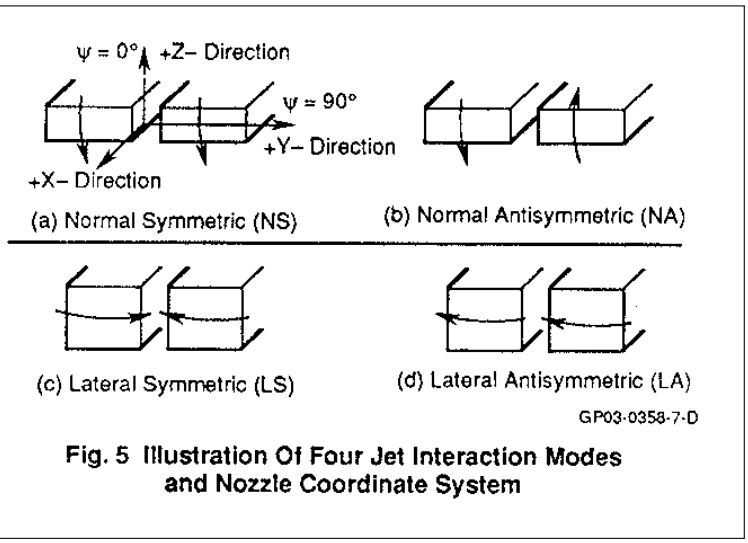

Figure 2.11: Observed modes from a rectangular jet from Zilz & Wlezien (1990)

.

drives the processes of the feedback loop (Tam & Ahuja, 1990). Therefore the downstream process functions as a gain term in equation 2.2 and its value must be greater than one. The other processes function as energy efficiency conversion terms. The gain of a downstream process is linked to the rate at which it grows as it advects in the shear-layer of the jet. The growth of structures in the shear-layer are driven by the Kelvin-Helmholz instability (Michalke, 1984). The Kelvin-Helmholz instability in supersonic (and subsonic) jets has been extensively studied using different forms of stability analysis (Morris, 2010). Therefore stability analysis of the Kelvin-Helmholtz instability provides a mechanism to investigate a significant component of resonance sensitivity, amplification, and selection in a supersonic jet.

Locally parallel linear stability analysis (LSA) provides one of the most direct routes to assessing the flow stability. LSA in supersonic single jets has provided the following conclusions (Morris, 2010):

- The spatial growth rate of the instability modes decreases with increasing Mach number.
- The most unstable mode frequency decreases with increasing Mach number.
- The axisymmetric $m = 0$ mode is the most unstable at low supersonic Mach numbers.
- The helical $m = \pm 1$ mode is the most unstable at higher Mach numbers.
- Increasing shear-layer thickness reduces both the spatial growth rate and the most unstable mode frequency.

The phenomenon of mode staging in single jets is therefore a strong function of the jet instability. At different jet operating conditions the presentation of different Mach numbers and shear layer thicknesses present sensitivity to different instability modes. These different modes are selected for resonance based on their instability growth-rate and enhanced through Powell's phase and amplitude criteria.

Despite the assumptions and simplifications of LSA, agreement with the approach and observations have been verified for supersonic jets in its predictions of Mach wave radiation and turbulent mixing

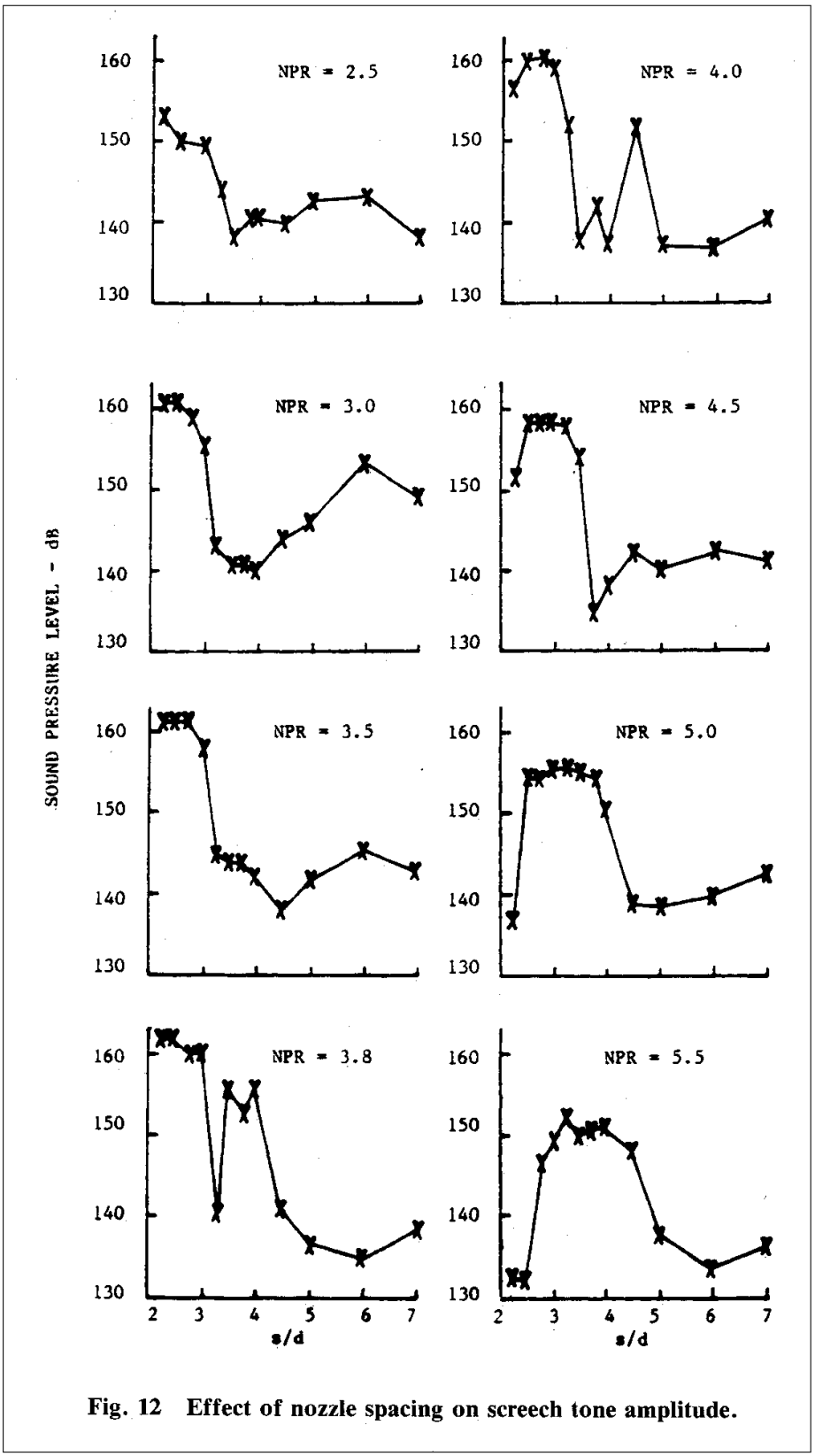

Fig. 12 Effect of nozzle spacing on screech tone amplitude.

Figure 2.12: Overall sound pressure level observed for jets of different pressure ratio and spacing from Shaw (1990). Nozzles are circular converging-diverging with a design Mach number of 1.47 (based on the F-15).

noise (Tam, 1971; Sinha *et al.*, 2014). The application of LSA to examine the instability of twin-jets has been attempted (Tam & Seiner, 1987; Morris, 1990; Du, 1993, 2002). The non-axisymmetric geometry and lack of quantitative base flow data have provided significant challenges for model development and validation (Morris, 1990; Rodríguez *et al.*, 2018). Morris (1990) examined LSA for jets of different spacing and shear-layer thickness. Four modes were considered, which are of the same mode shape as those indicated by figure 2.11 (modes I-IV in Morris (1990) correspond to A-D in Wlezien & Kibens (1988)). The growth rates of different azimuthal modes are shown in figure 2.13. For various azimuthal mode numbers, the different mode shapes show varying growth rates as a function of jet separation. All modes appear to converge to a similar growth rate at a non-dimensionalised jet spacing greater than three indicating equal preference. Mode type III (lateral symmetric) shows maximum instability growth-rate for the azimuthal mode numbers considered.

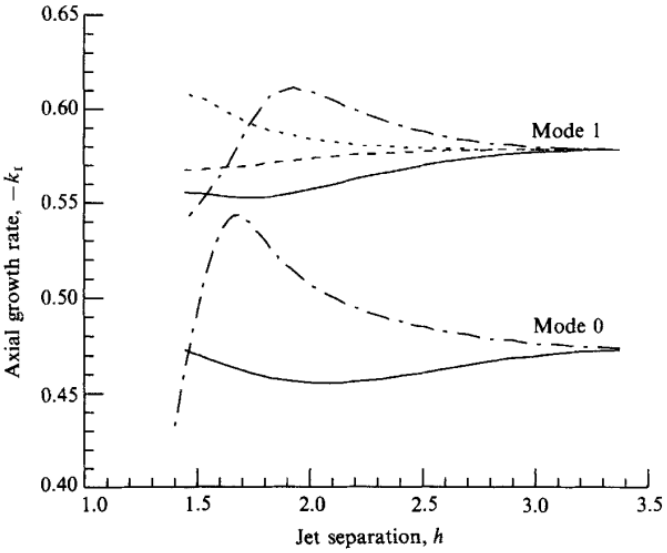

FIGURE 4. Variation of the axial growth rate $-k_i$ with jet spacing. $M_j = 1.32$, $M_d = 1.0$, $St = 0.3$, $b = 0.2$. ——, mode type I; – – – –, type II; — — —, type III; ……, type IV.

Figure 2.13: Figure taken from Morris (1990) showing linear stability analysis results of a twin-jet velocity profile corresponding to $M_j = 1.32$. Corresponding stability of various azimuthal modes is at the non-dimensional frequency of St = 0.3.

The simplifications and assumptions built into linear stability analysis also compromise its application to more complex flows. Non-parallelism of the flow and non-linear effects are not captured by the technique. Additionally inputs to the technique are taken from a base flow rather than from the history of the disturbance and thus the evolution of the instability cannot be evaluated (Herbert, 1997). Parabolized stability equations (PSE) were developed to overcome these restrictions in research and engineering applications (Herbert, 1997). They relax the parallel and linear requirements by substituting a modal solution into the Navier-Stokes equations, rather than a perturbation quantity. A variation on standard PSE has been developed and applied to subsonic twin-jets to assess their hydrodynamic instability and noise generation potential (Rodríguez *et al.*, 2018). Subsonic $M = 0.4$ jets were examined for different spacings. The jet interaction was found to have the potential to stabilise and destabilise the Kelvin-Helmholtz instability compared to an isolated jet. Figure 2.14a shows the calculated wavenumber stability spectra for a single jet (marked by open circles) and a twin-jet at $s/D = 1.5$ (marked by crosses). The twin-jet markers are annotated by azimuthal mode number, fol-

lowed by the representative in-plane and out-of-plane mode (symmetric or anti-symmetric). The axes indicate the complex wavenumber of the particular mode. The real component, α_r, corresponds to the spatial wavenumber of the associated mode, and α_i is the growth-rate. More negative values of α_i correspond to more unstable modes. At the particular frequency of St = 0.5 the modes 2AA, 2SA, 2AS, 2SS are approximately equally unstable with similar growth-rates. Therefore the real-world sensitivity of the flow boundary conditions such as acoustic reflections and facility imperfections such as surface roughness or nozzle lip thickness are significant. Additionally, the lack of preference for a dominant instability mode at a give operating condition means that potentially regions of no preference are encountered - these are considered next.

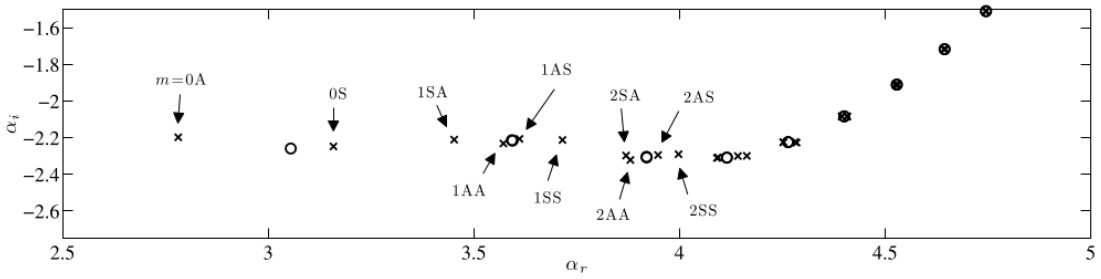

Fig. 3. Locally-parallel stability eigenspectra, for single-jet (circles) and twin-jet configuration with $h = 1.5\,D$ (crosses). $St = 0.5$ and $x = 0.25\,D$.

(a) Mode wavenumber (α) spectra identifying the most unstable mode for a particular configuration.

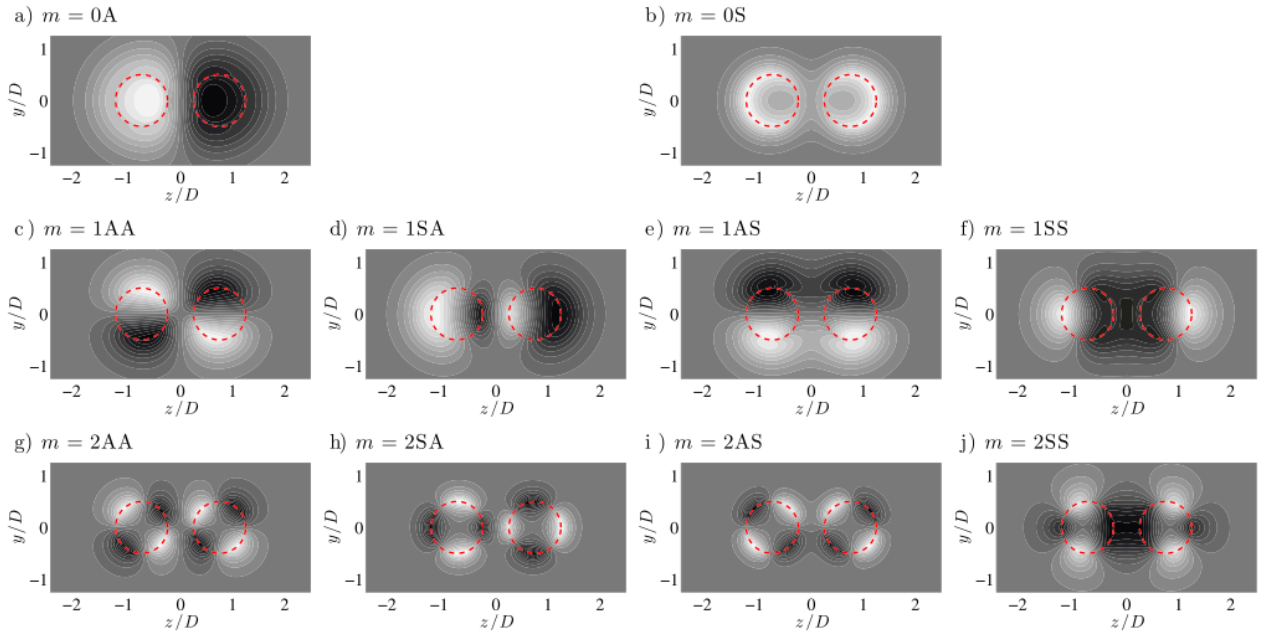

Fig. 5. Pressure eigenfunctions corresponding to Kelvin–Helmholtz modes $m = 0$, $m = 1$ and $m = 2$ for twin jets separated by $h/D = 1.5$. $St = 0.5$, $x = 0.25\,D$.

(b) Mode shapes derived from stability modes.

Figure 2.14: Stability results by Rodríguez *et al.* (2018) for an $M_j = 0.4$ twin-jet with $s/D = 1.5$ spacing.

2.2.3 Complex Coupling Interactions

The mode preference of twin supersonic jets is not always straightforward. Experiments in rectangular twin-jets have demonstrated weak complex interaction, symmetric, and anti-symmetric coupling

regions dependent on parameter space location (Raman, 1998). The study examined high aspect ratio twin rectangular jets (width to height: w/h = 5.0) with an application intended for military aircraft. To avoid a future nomenclature clash, the weak complex interaction is hereby called complex coupling. Figure 2.15 shows the coupling modes that were found. The coupling modes flapped out-of-plane around the major axis of the rectangular nozzle. No minor-axis modes were observed which was reported to be due to the high aspect-ratio (Shaw, 1990). The complex coupling was described as a coupling region where tones in the acoustic spectra are present but phase-locked schlieren or opposing microphone phase analysis are not possible. The steadiness of the observed modes was examined via short windowed Fourier transform (SWFT). The SWFT analysis found no significant instability in the tone. The mode switch locations were examined using the SWFT to determine whether the modes are mutually exclusive. The SWFT shows that the symmetric and anti-symmetric modes are mutually exclusive and the feedback loop is defined by one coupling mode or the other. The exclusivity of the complex coupling cannot be determined. The SWFT limits the ability to resolve the signal spectra on short time-scales. The microphone signal was acquired at 200 kHz and a 2^{10} window was selected for the Fourier transform, thus a 195 Hz minimum time-scale frequency was achieved. With a time/frequency scale of 195 Hz, the SWFT was separated from the screech frequency (approximately 7 kHz) by an order of magnitude. Therefore only mode switches appearing at frequencies lower than the SWFT window frequency could be assessed.

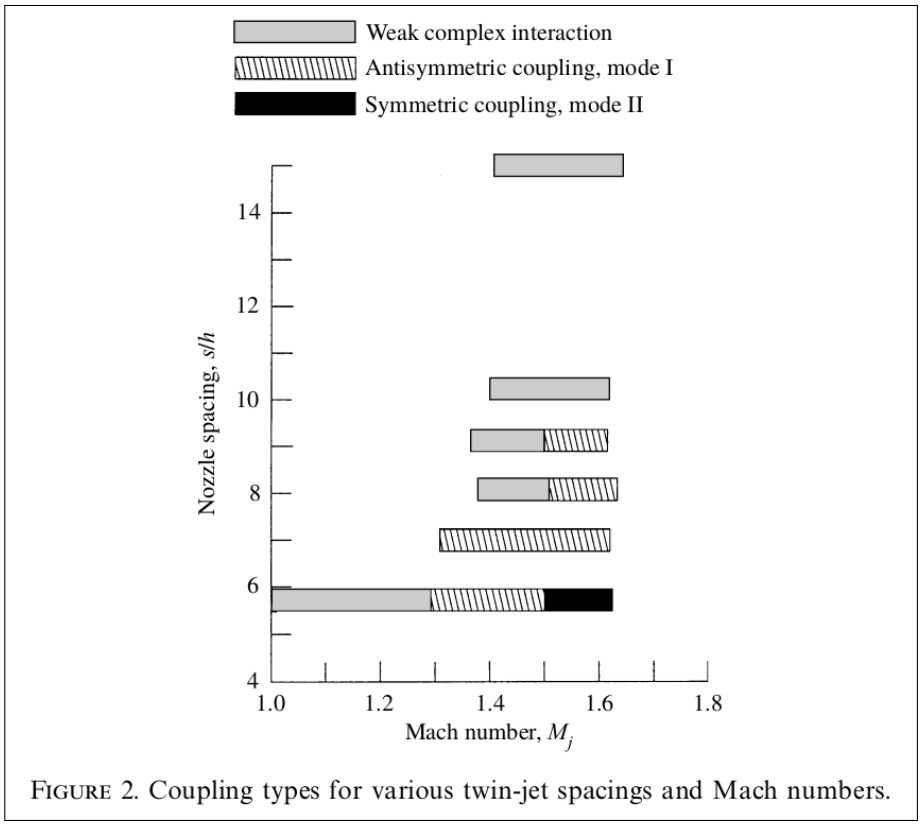

FIGURE 2. Coupling types for various twin-jet spacings and Mach numbers.

Figure 2.15: Classified coupling modes observed within a high aspect-ratio rectangular jet. From Raman (1998).

Additional datasets and analysis techniques were later explored in twin rectangular beveled jets to identify if similar coupling behaviour was encountered (Panickar *et al.*, 2004). Figure 2.16a shows two modes observed: a symmetric and anti-symmetric mode about the major-axis with a switch point of

$M_j \approx 1.4$ similar to the previous rectangular nozzle results (Raman, 1998). The effect of spacing was explored for fixed $M_j = 1.33$ in figure 2.16c. The anti-symmetric mode appeared at $s/h \approx 8.25$ for this pressure ratio. SWFT was again performed to assess the mutual exclusivity of the observed modes. It was found that both tones existed simultaneously in the spectra despite earlier evidence indicating they were mutually exclusive (Raman, 1998). The results for figures 2.16c and 2.16b were produced in a single 50 s recording and the spectra were developed using a SWFT. The SWFT was performed every 50 Hz - approximately three times longer than the previous experiments. The nozzles were mechanically traversed during the recording. Figure 2.16b appears to show the lower anti-symmetric mode continuously translating through frequency as a function of nozzle separation. Therefore the switch point between modes could also be translating as a continuous function of M_j as the nozzles get further apart. It was stated that no clear coupling was found between the jets for $s/h \geq 9.7$. Figure 2.16b shows high amplitude tones for $s/h \geq 9.7$. These were assumed to be the screech tones of the uncoupled individual jets.

An explanation for the mutual inclusivity or exclusivity of the tones was sought. Additionally, the complex coupling regions also presented an unanswered question. Higher-order statistical techniques applied to the acoustic signals were investigated to educe the potential for non-linear interactions in the jet (Srinivasan *et al.*, 2009). It was proposed that the non-linear physical processes in the jet (such as shock-cell structure, shear-layer development, and other flow physics) must require a non-linear/higher-order statistical analysis to explain phenomena like mode-staging. A non-linear spectral analysis technique called the cross bi-spectrum was examined to estimate the interactions between different frequencies in the acoustic spectra. The cross bi-spectrum is a third-order statistic computed from the Fourier transform of the triple correlation of the time signals. It is shown in equation 2.5.

$$S^{(k)}_{YXX}(f_1, f_2) = Y^{(k)}(f_1 + f_2)X^{(k)*}(f_1)X^{(k)*}(f_2) \tag{2.5}$$

$X^{(k)}(f)$ and $Y^{(k)}(f)$ are the Fourier transform of the time-series signals $x(t)$ and $y(t)$ respectively and the asterisk $(*)$ represents the complex conjugate. k windows are used to reduce Fourier transform window edge effects. An average is performed over M ensembles in equation 2.6.

$$S_{YXX}(f_1, f_2) = \frac{1}{M}\sum_{k=1}^{M} S^{(k)}_{YXX}(f_1, f_2) \tag{2.6}$$

Similar to the CPSD, the cross-bispectrum uses coherence as a measure of amplitude similarity as a function of frequencies f_1 and f_2. The cross-bispectrum-coherence (called the cross-bicoherence) is obtained by normalising the complex valued cross-bispectrum by the amplitude of the average power spectra of the two signals shown in equation 2.7.

$$b^2_c(f_1, f_2) = \frac{|S_{YXX}(f_1, f_2)|^2}{\left(\sum_{k=1}^{M} |Y^{(k)}(f_1 + f_2)|\right)\left(\sum_{k=1}^{M} |X^{(k)}(f_1)X^{(k)}(f_2)|^2\right)} \tag{2.7}$$

The technique was used to investigate cross-frequency interactions (peaks of cross-bicoherence) in twin rectangular bevelled jets. This was performed over two publications (Panickar *et al.*, 2005;

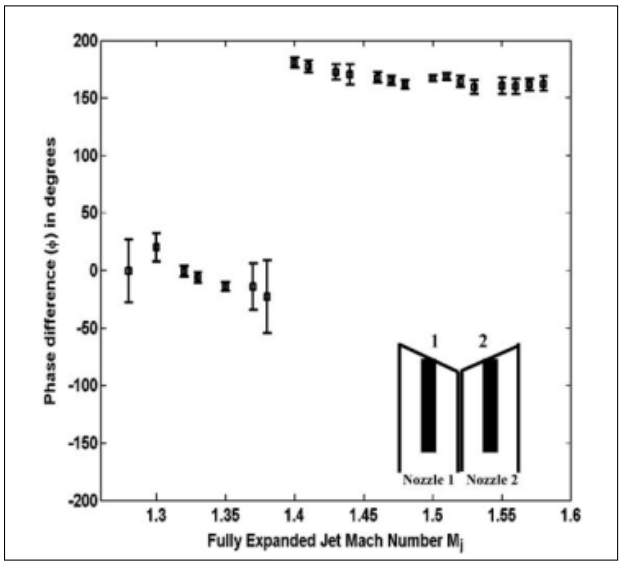

(a) Phase vs M_j for a co-directed beveled supersonic rectangular jet with zero inter-nozzle spacing. From Panickar *et al.* (2004)

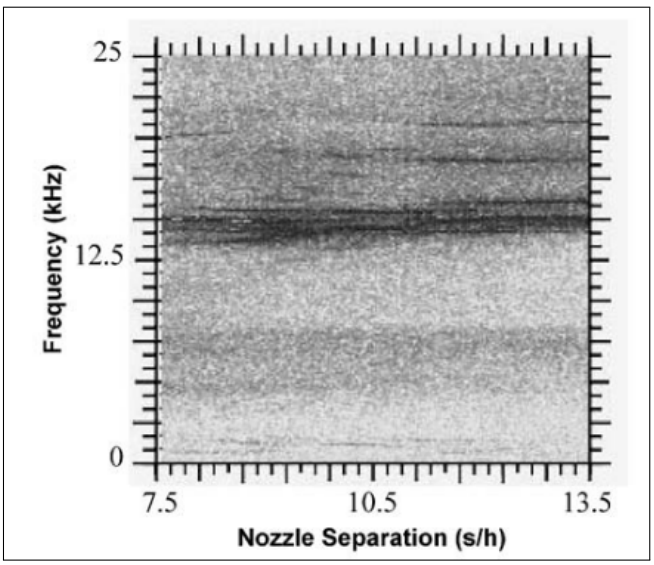

(b) Sound pressure level plotted against spacing between the jets. From Panickar *et al.* (2004)

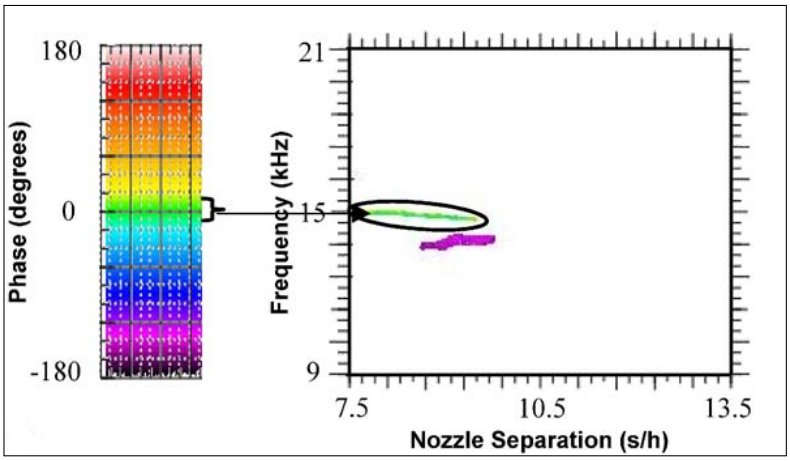

(c) Sound pressure level plotted against spacing between the jets. From Panickar *et al.* (2004)

Figure 2.16: Spectral analysis of twin bevelled co-directed supersonic rectangular jets from Panickar *et al.* (2004).

Srinivasan *et al.*, 2009). The interactions between twin co- and contra-directed beveled jets with no spacing were examined first (Panickar *et al.*, 2005). It was shown that no coupling is observed in the contra-directed configuration. Correspondingly low numbers of frequency interactions were found for this configuration. The co-directed configuration experienced both symmetric and anti-symmetric out-of-plane coupling modes. An increased number of frequency interactions were identified.

The effect of jet spacing between co-directed modes was investigated later (Srinivasan *et al.*, 2009). The results of the cross bi-coherence performed on the co-directed rectangular jets at $M_j = 1.3$ and 1.46 with zero inter-nozzle spacing ($s/h = 7.3$) are shown in figure 2.17. The number of interacting frequencies are indicated by the number of peaks in the frequency-frequency plane. $M_j = 1.3$ and 1.46 were presumably selected as they correspond to two different coupling modes within the parameter space shown in figure 2.16c. A greater number of interacting frequencies were identified for $M_j = 1.3$ than 1.46. Thus it was proposed that interacting frequencies are the effect of more complex non-linear

interactions within the physics of the flow. The number of peaks above a certain threshold was used to determine the 'interaction density' of a given configuration. The scalar metric allowed sweeps of the parameter space to occur that are shown in figures 2.18a and 2.18b. Peaks of interaction were observed surrounding the mode switching locations. Thus it was proposed by the authors that the number of non-linear interactions within the flow are indicators of mode switching locations.

The non-linear interactions could be generated at the mode-switch locations by two mechanisms. Either the modes close to the switch points are mutually inclusive and thus coherent frequencies are observed due to the two tones interacting. This would be expected to be particularly vigorous at the mode-switch locations where both modes will have similar amplitude as per Powell's amplitude criterion. If the modes are mutually exclusive on either side of the mode-switch location, then frequent switching between two modes is expected as there is no preference in feedback amplitude gain. If the modes are switching as a function of time then a mechanism does not exist for those frequencies to interact. Recent research into the cross-bi-spectrum has shown that the technique can return false positives if the input signals are non-stationary (Poloskei *et al.*, 2018). Therefore, the source of the non-linearity could also be the spurious result of the cross-bispectrum. These two scenarios are investigated in chapter 4.

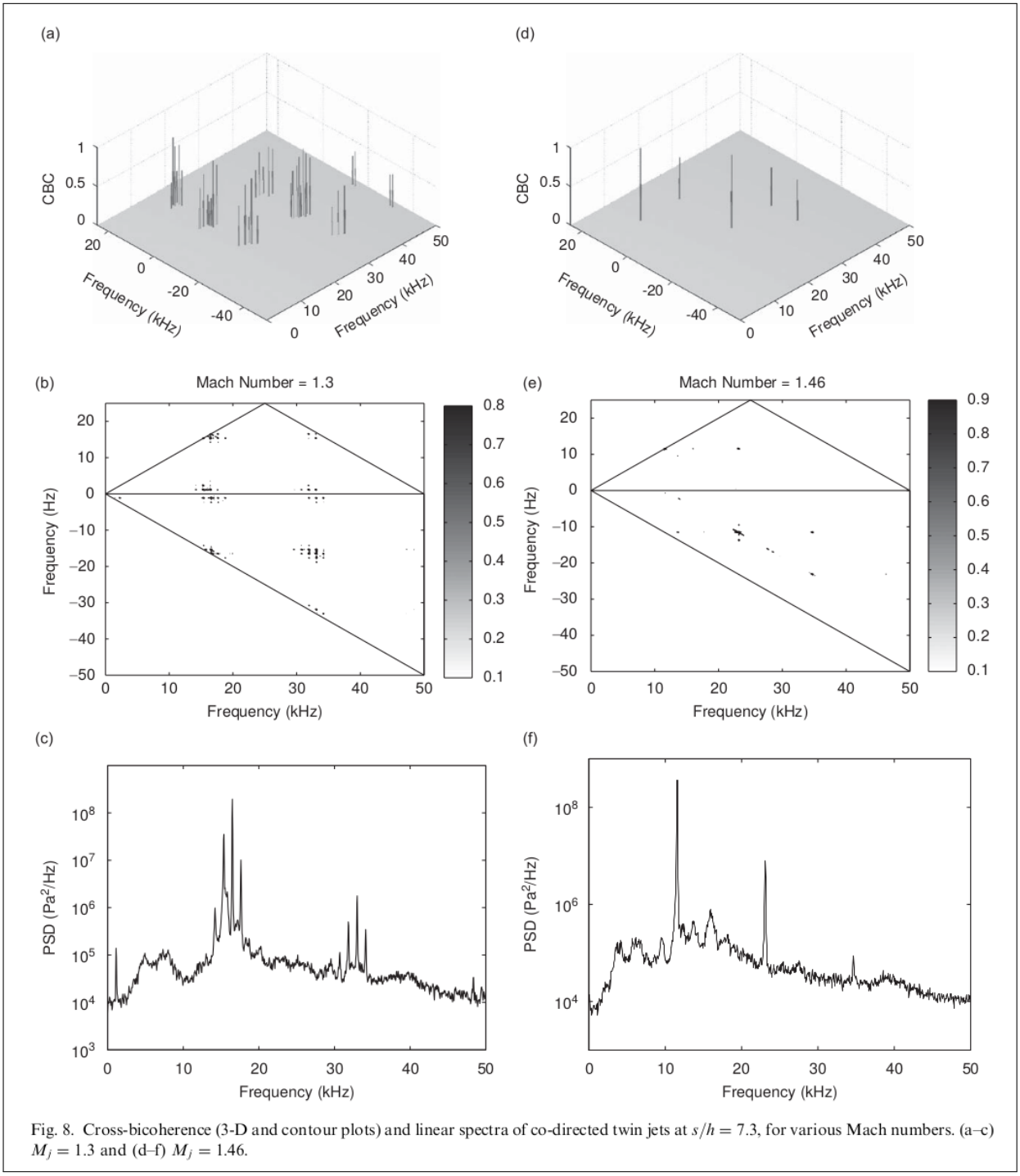

Fig. 8. Cross-bicoherence (3-D and contour plots) and linear spectra of co-directed twin jets at $s/h = 7.3$, for various Mach numbers. (a–c) $M_j = 1.3$ and (d–f) $M_j = 1.46$.

Figure 2.17: Cross-bicoherence results from Srinivasan *et al.* (2009). Experimental results are from Panickar *et al.* (2004).

.

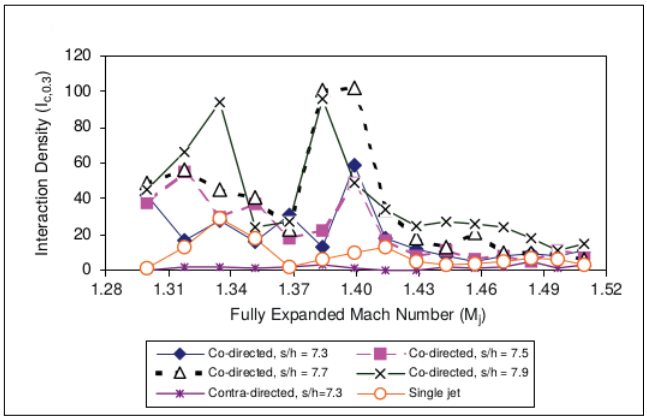

(a) Interaction density estimation from the bicoherence spectra. From Srinivasan *et al.* (2009).

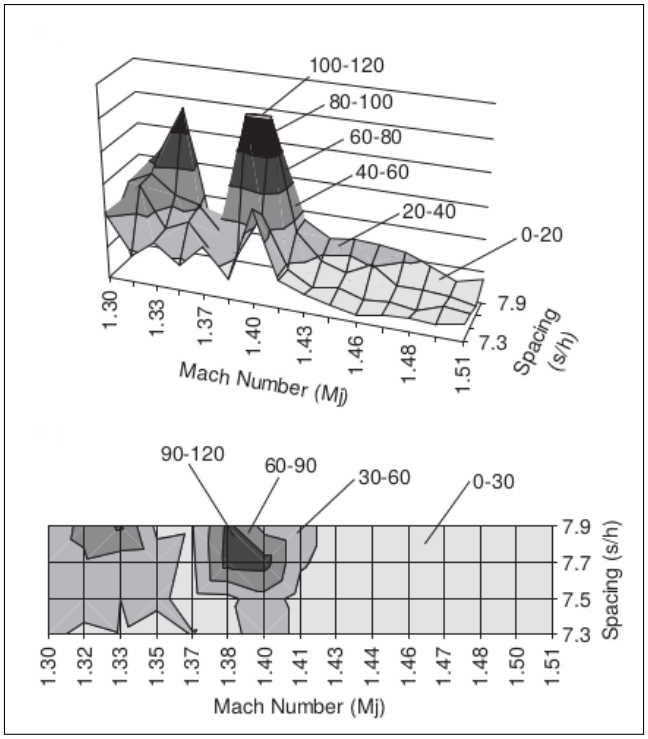

(b) Interaction density estimation surface plot from the bicoherence spectra. From Srinivasan *et al.* (2009).

Figure 2.18: Interaction density estimation the bicoherence spectra examined in Srinivasan *et al.* (2009).

2.2.4 Summary

Effort has been made to explain the coupling modes experienced by twin-jets. The demonstration of interacting frequencies surrounding mode switching locations infers a non-linear interaction of the flow physics (Srinivasan *et al.*, 2009). There is presently no explanation for the physics driving the observed non-linear interaction or evidence illustrating why it occurs more intensely surrounding the mode switching locations. In addition, 50 % of coupling in the parameter space of some coupled jets has been classified as complex (weak complex interactions) despite being away from the mode switch locations (Raman, 1998). No definitive analysis has shown whether the coupling modes are mutually exclusive across mode switch points (Panickar *et al.*, 2004). Circular jet parameter studies have revealed that mode strength and instability growth rate are a functions of the parameter space (Wlezien, 1989; Morris, 1990; Rodríguez *et al.*, 2018). Thus there is a lack of knowledge about the relationship between the jets across coupling modes that enable or prohibit mutual exclusivity.

There exists a need for quantitative examination of these flows to determine the hydrodynamic interactions of twin-jet surrounding mode switch locations. The interactions between different modes have been considered in rectangular twin-jets. Substantially less is known about the existence of these interactions in circular twin-jets. Although rectangular nozzles have a place in military aircraft, circular twin-jets are more prevalent in civil use. Therefore knowledge of the interactions between circular twin-jets contributes scientific and practical value.

The present work examines the modal behaviour of circular twin-jets. It provides an explanation for the coupling between the jets occurring around mode switch locations. A characterisation study of circular twin-jets is considered in chapter 4. In the accompanying study (included in appendix A) schlieren photography is used in different parameter space locations to determine the modal structure of the coupling and the azimuthal structure of the jets. Screech feedback models are also compared to assess their fit in twin-supersonic resonance. In chapter 5 a study of the velocity field is performed to provide a piece-wise description of the flow and to examine quantitative differences between the resonant flows of different coupling modes. In chapter 6 the coupling behaviour between the jets near the mode-switch locations is uncovered by linking the acoustic and hydrodynamic fields. In chapter 7 the stability of the mode selection process is examined and conclusions are drawn about mode staging and the feedback loop.

Chapter 3

Summary of Experimental Facilities and Measurements

Three experimental facilities were used to obtain experimental data. Facility one and two are gas-jet facilities within the Laboratory for Turbulence Research in Aerospace and Combustion (LTRAC) at Monash University. Facility one was used for the collection of acoustic and schlieren photography data that were examined for the development of chapters 4, 5, 6, and appendix A. Facility two was used for the collection of acoustic and PIV data that were examined in the development of chapters 5 and 6. Facility three is an anechoic gas-jet facility with jet actuation capability at the Gas Dynamics and Turbulence Laboratory (GDTL) at the Ohio State University. Facility three is fitted with an orthogonal microphone-array that was used for the collection of acoustic data that were examined in chapter 7. A description of each facility is provided.

3.1 Facility One - Coupling Parameter Sweep

Facility one is a general purpose gas-jet facility suited to schlieren photography and acoustic research. A schematic of the facility is shown in figure 3.1.

Compressed air at 298 ± 2 K was supplied directly to the plenum chamber, which contained a honeycomb section and wire mesh screens that homogenised and conditioned the flow. Compressed air exhausted from twin converging circular nozzles with an exit diameter of $D = 10$ mm, a nozzle-lip thickness of 1.5 mm and a non-dimensionalised spacing of $s/D = 3.0$. The flow at the exit was choked (exit Mach number, $M_e = 1$) with a jet exit velocity $U_e \approx 310$ m/s.

Acoustic measurements were obtained with a pair of G.R.A.S. type 46BE 1/4" preamplified microphone with a frequency range of 20 Hz to 100 kHz. The individual microphone amplitude coefficients were referenced against a G.R.A.S. type 42AB sound level calibration unit. The signal output from the microphones was recorded on a National Instruments DAQ (NI USB-6341 BNC) at a sample rate of 250 kHz to prevent aliasing and a signal resolution of 16 bit. The opposing microphones were positioned $8D$ radially from the closest nozzle lip. Millimetre microphone positional accuracy was

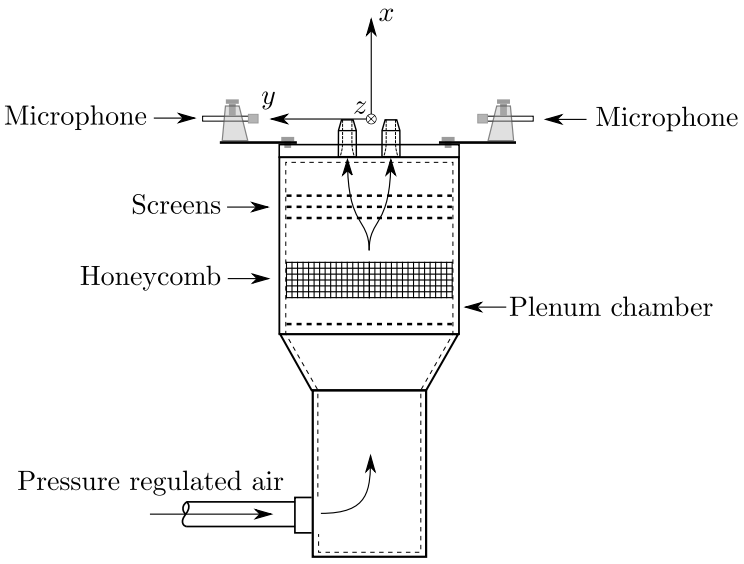

Figure 3.1: Schematic of the acoustic experimental setup, adapted from Knast *et al.* (2018).

achieved, which corresponds to a phase error of approximately ±5 degrees (considering a screech frequency of 15 kHz, 340 m/s ambient speed of sound corresponding to a wavelength on the order of 20 mm). 500 k samples were recorded simultaneously on both microphones and five measurements were combined into an ensemble. The facility is free-standing within the laboratory. Potential reflective acoustic surfaces (walls, cabinets, other facilities, etc,.) are located a distance of between 2-10 m away and as such the facility cannot be considered anechoic.

A Töpler Z-Type schlieren system was used to image the twin supersonic jet (Settles, 2012; Mitchell *et al.*, 2012). Two mirrors, each of focal length 2032 mm, were used to create a collimated light path through the test section. Only the density gradient in the streamwise direction ($\partial\rho/\partial x$) was considered with in the analysis as it provided the greatest contrast to the axial density gradients within the jet. A Shimadzu HPV-1 camera was used to obtain high-speed images of the twin jet. The camera has a resolution of 320×260 pixels and can capture 102 images at an acquisition speed of up to 1 million frames per second at an exposure of 0.25 us. Illumination was provided with a Metz Mecablitz flash. A PCO4000 camera was used to obtain instantaneous high-resolution images of the twin jet. The camera has a resolution of 4008×2672 pixels and was operated at an acquisition rate of 1 Hz with an exposure of 1.6 us. Illumination was provided with a pulsed light-emitting diode (Willert *et al.*, 2012).

3.1.1 Key Results

The facility was used to obtain parameter sweeps of the twin-jet acoustic response at different NPR and spacings. The cases are presented in table 3.1.

PSD and CPSD results between the opposing microphones were used to infer coherence and phase information between the jets. To calculate the PSD estimate, Welch's method (Welch, 1967) was applied: windows of 2^{12} samples with a 25 % overlap were applied to improve spectra averaging, and a Hann window function was applied to minimise edge effects between windows. The resulting frequency

Case	Jet diameter (mm)	Spacing	Pressure Ratio	Reynolds Number ($\times 10^5$)	Chapter
1	10.0	2	2.0 <NPR <5.5	$3.2 \leq Re_j \leq 9.3$	None
2	10.0	3	2.0 <NPR <5.5	$3.2 \leq Re_j \leq 9.3$	4, 6, A
4	10.0	6	2.0 <NPR <5.5	$3.2 \leq Re_j \leq 9.3$	4, A
5	10.0	0 (Single Jet)	2.0 <NPR <5.5	$3.2 \leq Re_j \leq 9.3$	4, A

Table 3.1: Summary of acoustic experiments performed on facility one.

resolution was 24 Hz. As the facility was non-anechoic, the resulting PSD amplitude is potentially biased by echos. However, the spectra are used to identify intense frequencies only. Thus no treatment to calibrate SPL amplitude was necessary for the purposes of this investigation. Two examples that horizontally stack individual spectra results as a function of NPR from $s/D = 3$ are shown in figures 3.2a, 3.2b, and 3.2c.

3.2 Facility Two - Particle Image Velocimetry

Facility two is a gas-jet facility dedicated to capturing velocity fields via the PIV technique. A schematic of the facility is shown in figure 3.3. The purpose of the velocity field measurements was to examine velocity field features of two different coupling modes. The use of these measurements is discussed and presented in chapters 4, 5, and 6.

Air at approximately 298 K was supplied directly to a mixing chamber where the jets were uniformly seeded with smoke particles from a Viscount 1300 smoke generator. Only one smoke source was needed for both jet core and ambient fluid measurements as after a short time the smoke particles completely filled the measurement facility. The mixing chamber was connected to the plenum chamber, which contains a honeycomb section and wire mesh screens to homogenize and condition the flow. The exhausted flow was imaged inside the PIV enclosure, which was $60 \times 60 \times 200$ diameters in size. The walls of the enclosure were not acoustically treated. The nozzle assembly used in facility one was identical with this experimental facility and used in these experiments for consistency.

Single exposure image pairs were acquired using a 12-bit Imperx B6640 camera with a CCD array of 6600×4400 px at a rate of 0.5 Hz. Approximately 9,000 velocity fields were used for the calculation of all statistics. A magnification of 19.9 um/px was achieved using a 200 mm Nikon Micro-Nikkor lens, which resulted in a PIV image plane of 129.3×86.2 mm. The particle field was illuminated using a diverging light sheet of approximately 1 mm in thickness, which was produced by a dual cavity pulsed Nd:YAG laser at 532 nm with a maximum pulse energy of 200 mJ. Within the flowfields shown later, the laser sheet was projected from bottom to top. A multi-grid cross-correlation digital particle image velocimetry algorithm was used to analyze the image pairs (Soria, 1996). As a final method to remove erroneous vectors, a filter based on a Chauvenet criterion of 3 standard deviations was applied to the temporally stacked vector fields. Detected erroneous vectors were interpolated via a cubic function if they contained 3 good neighbours, else were otherwise excluded from statistical representation.

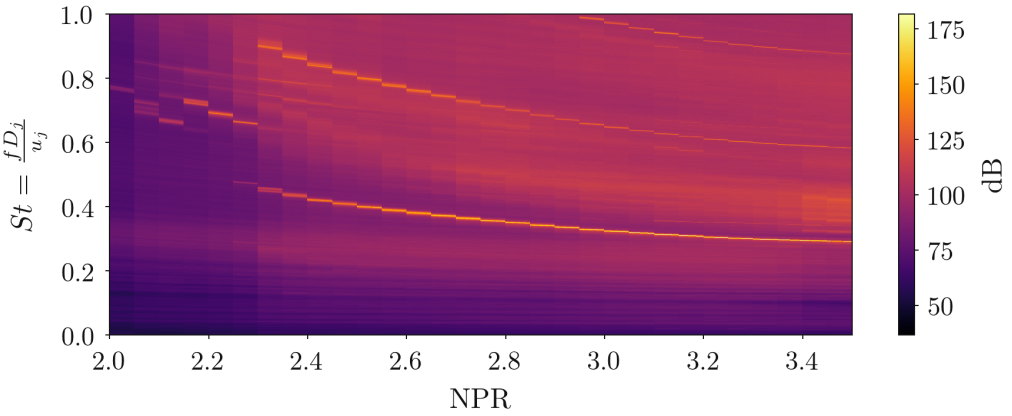

(a) Waterfall plot of individual power spectral density plots of sound pressure level.

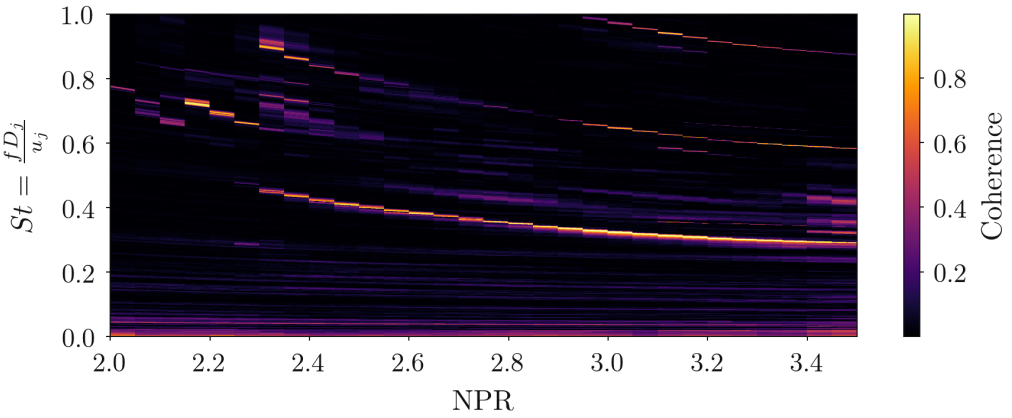

(b) Waterfall plot of individual cross spectral density coherence results.

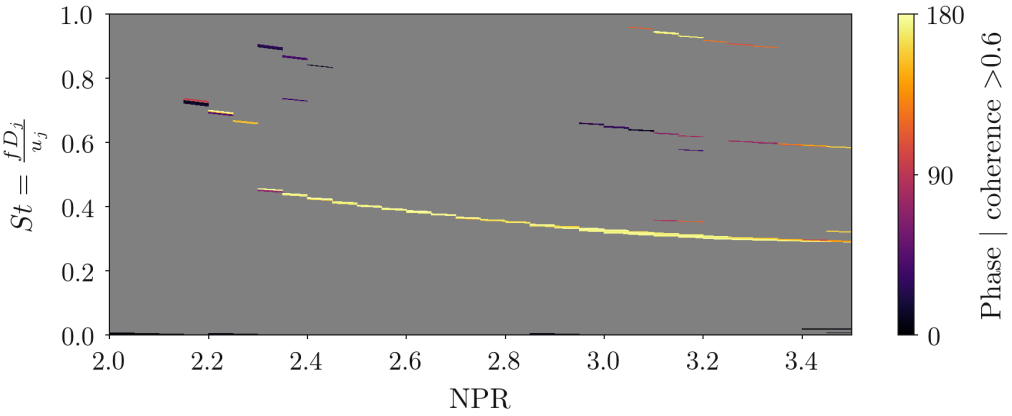

(c) Waterfall plot of individual cross spectral density phase results.

Figure 3.2: Example parameter sweep acoustic spectra from facility one for $s/D = 3$.

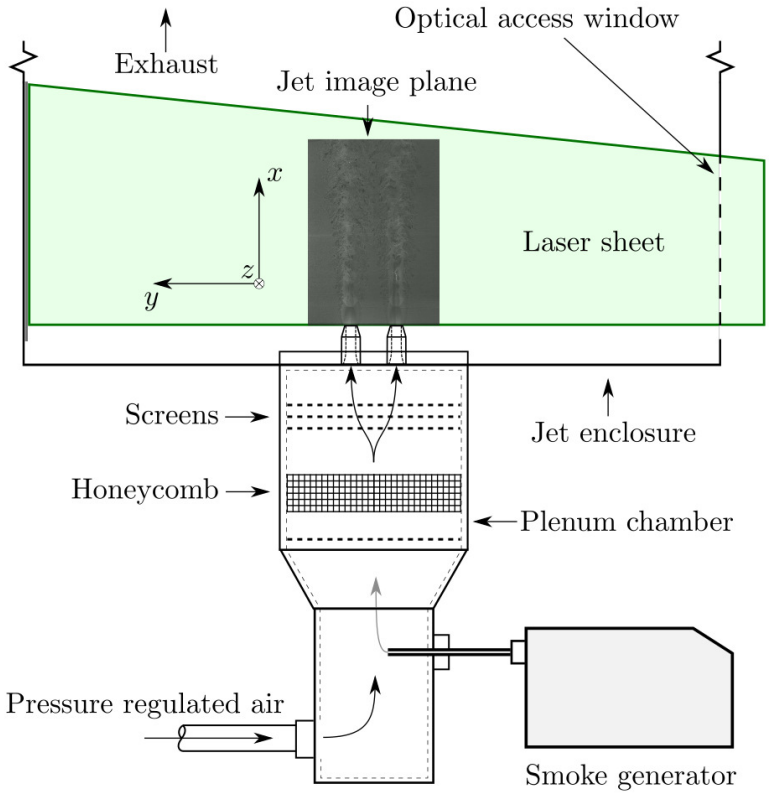

Figure 3.3: Schematic of the particle image velocimetry setup for examining the flow fields of twin-supersonic jets. Located in the Laboratory for Turbulence Research in Aerospace and Combustion (LTRAC) at Monash University.

3.2.1 Dynamic Range

Velocity statistics in the jet core and entrainment field are analysed within chapter 5. Therefore it was critical that the core and entrainment features were measured precisely. Jets present a challenging PIV processing requirement because of the range of velocities (affecting pixel displacement) and the scale of the velocity gradients (affecting required spatial resolution) within the flow. The range of velocity scales may displace particles within the jet core one or two orders of magnitude greater than those in the entrainment field. This requires large PIV processing interrogation windows to ensure that a large portion of the displaced pattern is within in the second image. The velocity gradients within locations such as the jet shear-layer may dictate the use of small interrogation windows so that reliable linear pattern translation between the two snapshots is achieved.

The amount of displacement present in interrogation window is a function of image spatial-resolution, image magnification, interrogation window-size, and inter-frame timing (Raffel *et al.*, 2007; Willert *et al.*, 2008). The image spatial resolution and magnification should be sufficient to allow for approximately a dozen flow particles within an interrogation displacement window. This has been found to provide sufficient texture to provide unambiguous displacement peaks within the cross-correlation function (Willert *et al.*, 2008). The individual particles should be resolved to a size greater than one pixel to prevent peak-locking (integer displacements of the cross-correlation function), which requires sufficient magnification or high image spatial-resolution. Peak-locking binarises the recorded velocity into integer values and biases the flow statistics. Increased magnification occurs at the cost

of field-of-view. In supersonic jet flow, the sonic and potential cores (the central region bounded by Mach lines within the jet that is of relatively constant velocity) extend to approximately 10 to 15 D downstream from the nozzle lip. As a result, imaging a field-of-view extending from the nozzle lip to 10-20 D downstream is a common requirement. Considering the typical field-of-view for jet flow experiments and the compromises of simply increasing magnification, high spatial-resolution is generally preferable to compensation by magnification. Based on typical supersonic jet core velocities of approximately 350 m/s and typical camera inter-frame times of 0.8 µs, jet-core displacements on the order of 30-60 pixels (depending on image-plane magnification) were observed within the jet core. Simultaneously, the near field region (exterior to the jet in the entrainment field) produces displacements of <1 px due to lower velocities and the short inter-frame time. If interrogation windows of >60 px across the entire flow field were used, the resulting vector resolution would be insufficient to make meaningful conclusions about the flow. Conversely, small interrogation windows fail to identify the cross correlation peak for the large displacements. To overcome the large range of displacements, a multi-scale cross-correlation technique is employed (Soria, 1996). The technique repeats the correlation of windowed sections across the image, successively reducing the size and using the previous displacement result as the initial displacement of the following window. This provides a significant boost in achievable vector resolution and precision.

The number of different properties affecting predictable displacement of the vectors and adequate resolution are considerable. The selected PIV parameters (such as inter-frame time, laser energy, and interrogation window size) and specification of the hardware (such as the imaging lens or camera aperture) are presented in chapter 5. A synthetic PIV analysis was performed prior to the experiment to identify the measurement precision error as a function of particle displacement. The minimum expected displacement was below one pixel in the troughs of the standing-wave in the entrainment field and inter-nozzle regions. In the jet core a maximum of 48 px was expected. Synthetic velocity fields were developed using the expected displacement range and a velocity field function was developed that approximated the expected standing-wave velocity distribution. The synthetic velocity field was produced using equation 3.1. Where i, j are the pixel coordinates along the horizontal and vertical axes respectively and λ is the wavelength of the streamwise velocity modulation.

$$u_x(i,j) = 48\left[(0.5\cos\frac{2\pi}{\lambda}i + 0.5)\cos(j)e^{-j}\right] \tag{3.1}$$

Particles were randomly distributed throughout the velocity field. The particle was generated using a Gaussian function over a 7×7 pixel kernel at the seed location to avoid peak-locking. A double exposure (for presentation only) of the particle images is shown in figure 3.4b. The multi-grid cross-correlation PIV algorithm was applied to the images using the same settings that were intended for the experiment. The procedure of random velocity field generation displacement estimation was performed 100 times and the estimated velocity fields were saved. The error between the estimated velocity fields and the true displacement was calculated and used to estimate the standard deviation of the error in pixels. The standard deviation of the error is shown in figure 3.5. The following signal degradation was applied to simulate real-world results: A random displacement between 0-1 px was added to the particles and 10 % of the particles were added or removed on the second image. A log-log scale is used so that both large and small displacement error can be compared. The sub-

pixel standard deviation at 0.2 px displacement was found to be approximately 1 px corresponding to a 95 % confidence interval of 0.2 ± 1.96 px. At 0.5 px displacement the standard deviation of error is approximately 0.3 px corresponding to a 95 % confidence interval of 0.5 ± 0.59 px. Therefore the precision on the displacements at the lower end of the expected displacement range is well captured by the PIV algorithm settings. The higher velocity range plateaus with a error standard deviation of approximately 0.05 px corresponding to a 95 % confidence interval of ±0.098 px. It is unlikely this level of precision can be captured in practice as other sources of error may become significant (Westerweel *et al.*, 2004).

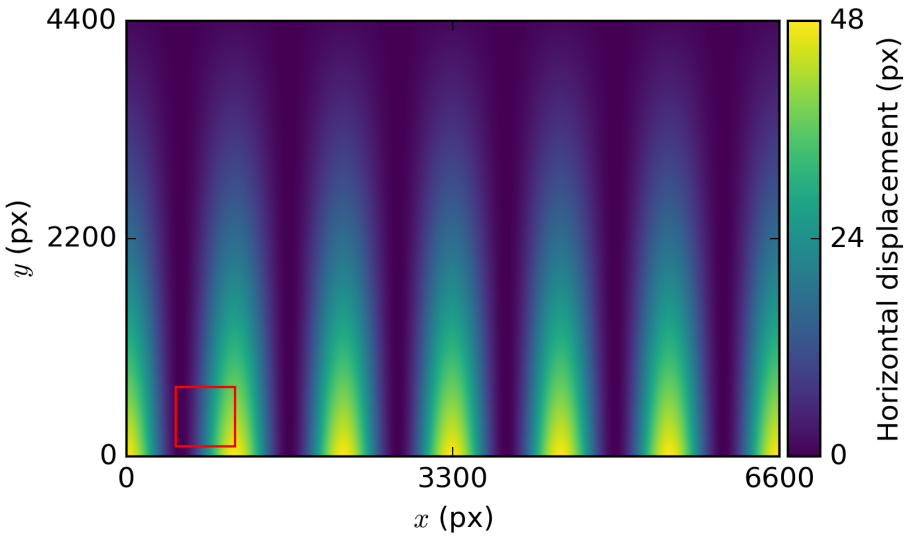

(a) Synthetic displacement contour. Red square corresponds to the synthetic particle translation zoomed section in figure 3.4b.

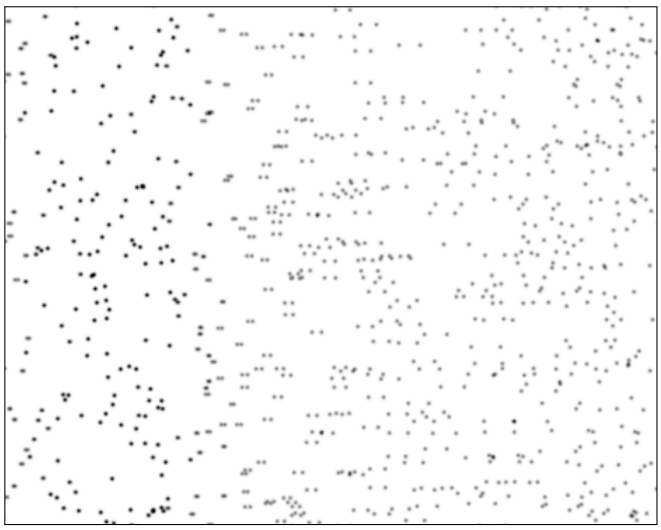

(b) Double exposure of the randomly distributed synthetic particles for PIV precision testing. The figure is a zoomed section corresponding to the red square above.

Figure 3.4: Model used to produce synthetic particles for testing the end displacement precision error under different PIV parameter configurations.

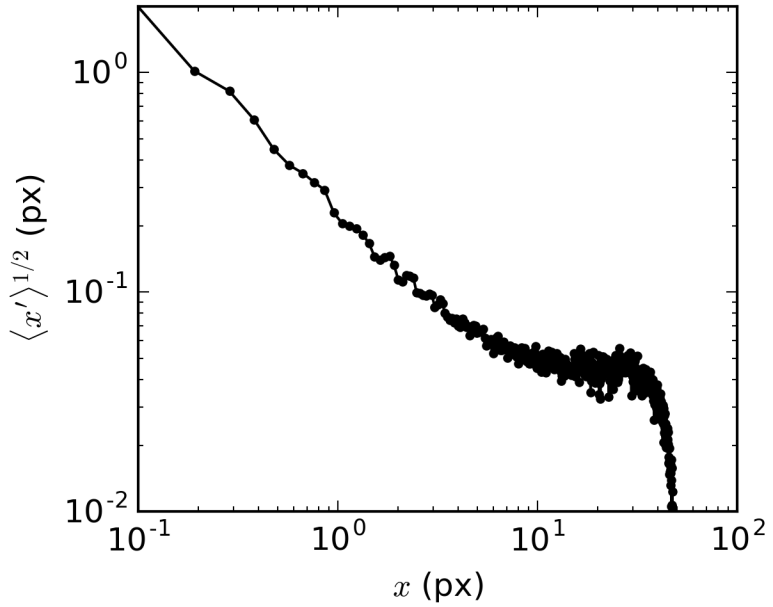

Figure 3.5: Results of a synthetic particle image velocimetry dynamic range analysis. The error in the particle displacement standard deviation is shown as a function of particle displacement.

3.2.2 Key Results

To determine the coupling mode switch NPR, an acoustic measurement was performed. Acoustic measurements were obtained with a G.R.A.S. type 46BE 1/4" preamplified microphone with a frequency range of 20 Hz $\rightarrow$ 100 kHz. The microphone amplitude coefficient was referenced against a G.R.A.S. type 42AB sound level calibration unit. The signal output from the microphone was recorded on a National Instruments DAQ at a sample rate of 250 kHz to prevent aliasing and a signal resolution of 16 bits. The single microphone was placed between the two jets 23 D away at the nozzle lip height in the out-of-plane position using the same reference coordinate system as Kuo et al, $y/D = 23, \theta = 90°, \phi = 90°$ (Kuo *et al.*, 2017*b*). The PIV facility contains potential reflective acoustic surfaces and as such cannot be considered anechoic. The average acoustic spectra were calculated using a 2^{13} sample sliding-window via a Fourier transform. A 25 % window overlap and a Hann window were used to minimize edge effects.

Figure 3.6 shows the acoustic frequency spectra with vertical lines indicating the screech tone. Horizontal axis is strouhal number (St), where f is the measured screech peak frequency, D_j is the calculated ideally expanded jet diameter, and U_j is the ideally expanded jet velocity. The mode switch point was deemed to exist at NPR $\approx$ 4.85. Therefore NPR = 4.6 and 5.0 were selected as they contained different coupling modes.

Table 3.2 summarises the PIV cases recorded on this facility. Cases 1 and 4 represented the two basic distinct coupling modes. 0.9 µs was the shortest possible camera inter-frame time. Multiples of this inter-frame time (cases 2, 3, 5, 6, 7, 8, 9) were included in the event the sub-pixel displacement regions could not be resolved and a greater displacement was needed. 0.9 µs proved sufficient after statistical analysis. An uncertainty analysis is included in chapter 5. The greatest velocity uncertainty

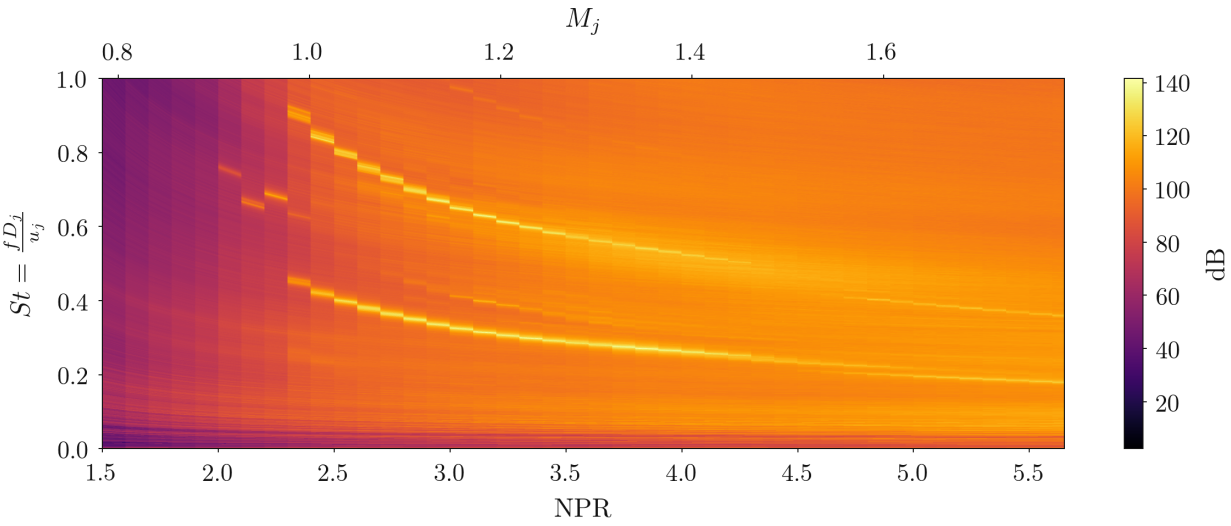

Figure 3.6: Acoustic spectra of the nozzles installed in the PIV facility.

is approximately 5 % in the region exiting the nozzle before the first shock-cell. Cases 6-9 were captured to analyse the external standing-wave. These cases do not form part of the present work.

Case	Pressure Ratio	Inter-frame time (μs)	FOV position	PIV Pairs Recorded	Re_j (10^5)	Chapter
1	4.6	0.9	Both jets	11k	7.76	5, 6
4	5.0	0.9	Both jets	11k	8.46	5, 6

Table 3.2: Summary of PIV cases recorded for analysis. LJ & E represents the field of view of just the lower jet and the entrainment field beyond.

An instantaneous snapshot from case 4 is shown in figure 3.7. The highest velocities occur prior to the Mach disk. A subsonic region occurs immediately downstream of the disk. Strong coupling between the plumes occurs beyond $x/D = 8$. Figure 3.8 shows a comparison between the ensemble mean of case 1 and 4. The top half corresponds to case 4 and the lower to case 1. The white areas are areas that were excluded from the calculation as they contained laser light reflections. The vertical bars indicate the shock-reflection positions.

3.3 Facility Three - Microphone array and jet forcing

The experiments were conducted at the Gas Dynamics and Turbulence Laboratory (GDTL) within the Aerospace Research Center at The Ohio State University (OSU). The jet anechoic chamber facility consists of a $6.2 \times 5.6 \times 3.4$ m room covered with fiberglass wedges with a cut-off frequency of 160 Hz. Images of the anechoic facility, the jet nozzles, and the microphone setup are included in the sub-figures of figure 3.9. The compressed air supply for high-speed jets originates from large cylindrical tanks at 16 MPa, which is regulated down to the desired plenum chamber pressure. During compression, the air is filtered and dried. The nozzles are mounted on the end of the plenum chamber. A an inter-nozzle

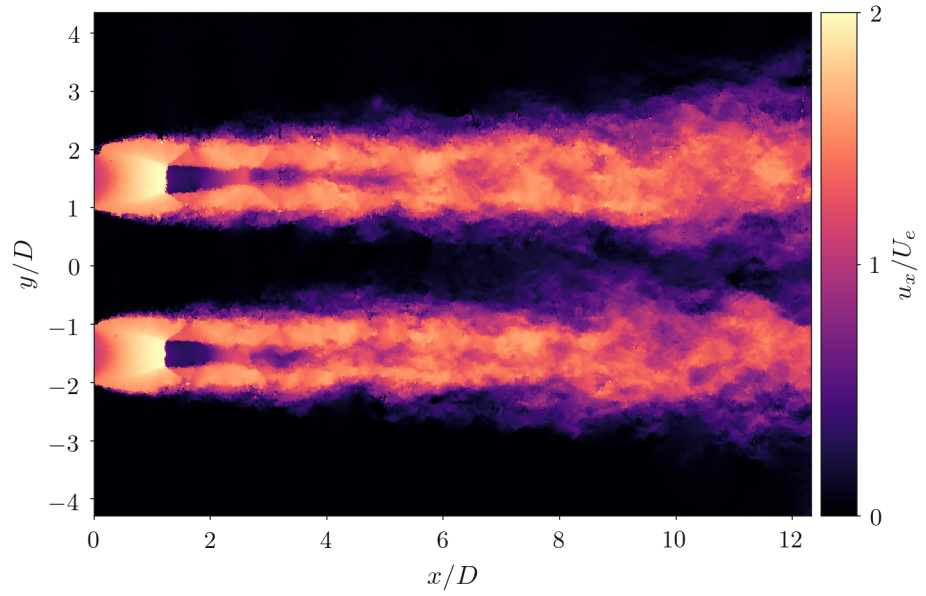

Figure 3.7: Example particle image velocimetry snapshot from case 4, NPR = 5.0. Axial velocity is normalised by the throat velocity.

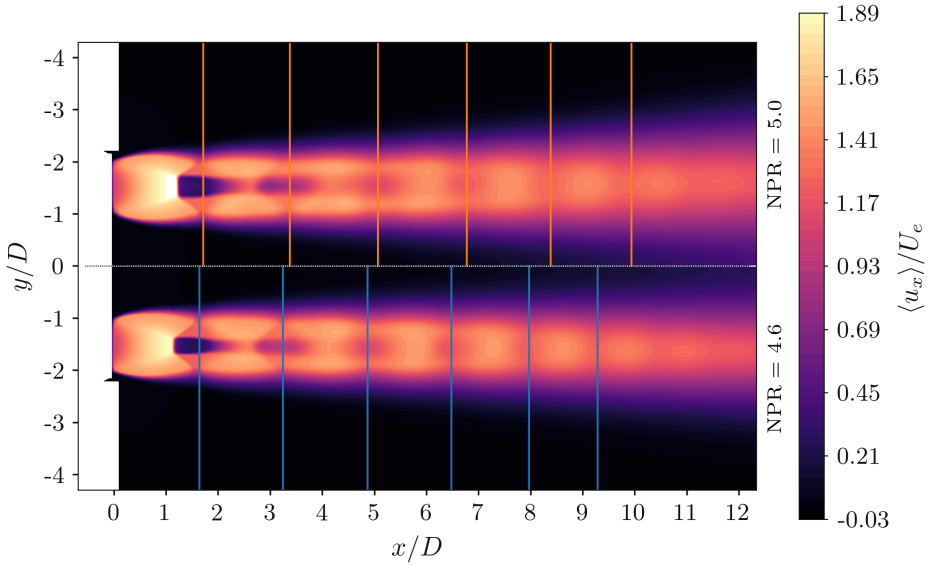

Figure 3.8: Comparison between the ensemble mean of case 1 and 4, which correspond to different coupling modes.

spacing of $s/D = 3$ was examined to align with existing chapters. The nozzles are converging-diverging with a fully expanded Mach number of 1.23 and a nozzle exit diameter of 19.05 mm (3/4"). The nozzle lip thickness is 7.6 mm (0.3 in.), which is significant and can influence screech feedback behaviour (Ponton & Seiner, 1992; Shen & Tam, 2000). The large lip thickness is required accommodate the plasma actuators. Open-cell acoustic foam was applied to all potentially reflective array structure surfaces.

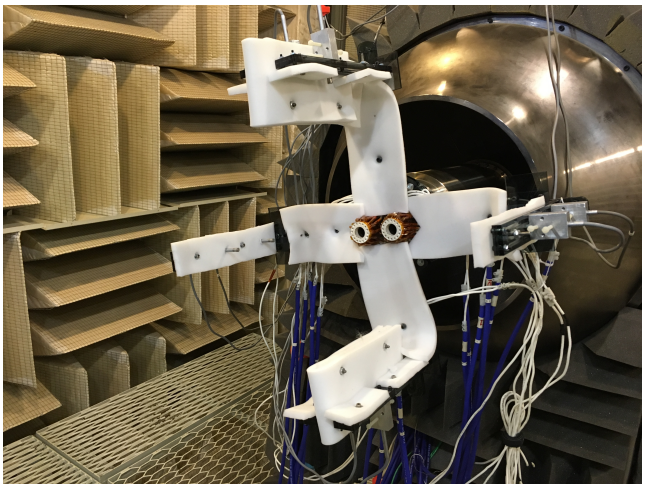

(a) Jet microphone array with applied acoustic foam.

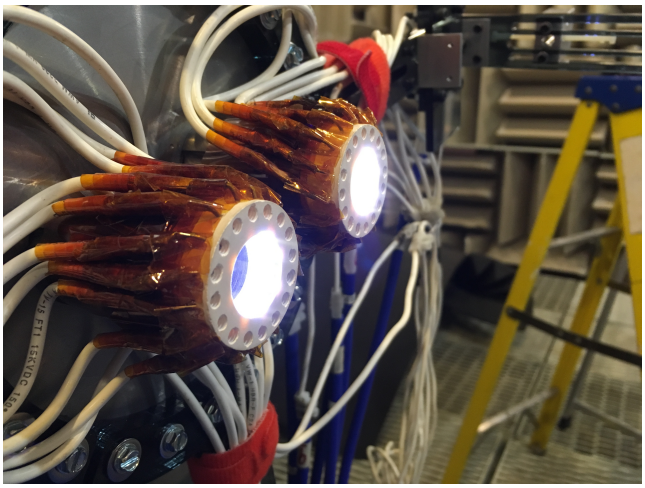

(b) Nozzle installation showing the blue glow produced by plasma actuation.

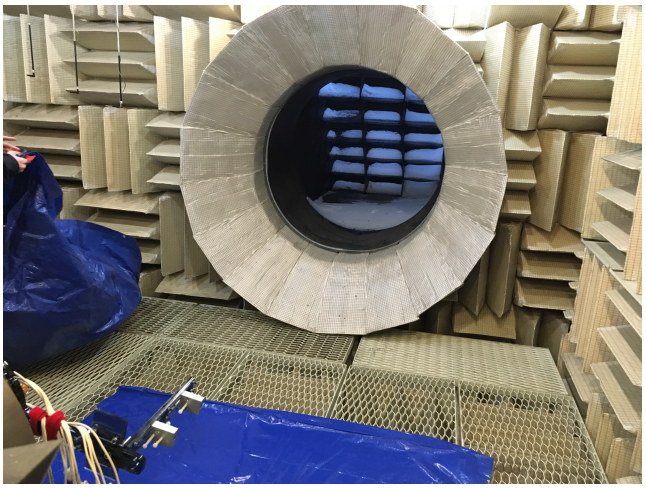

(c) Anechoic chamber exhaust. Jet nozzles are just out of frame on the left-hand side.

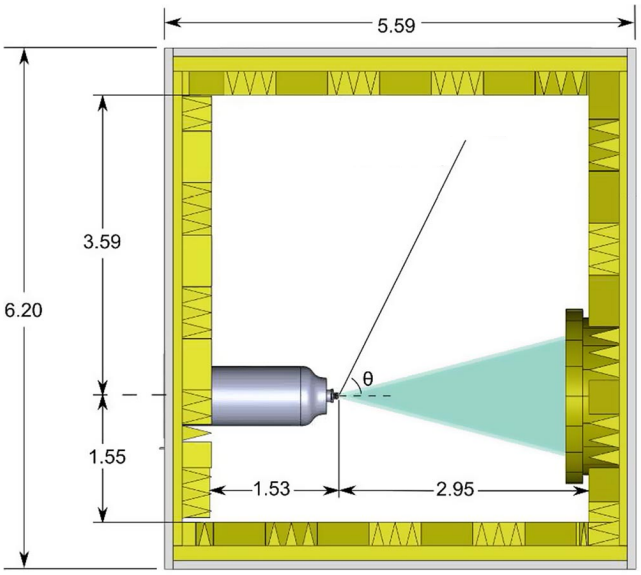

(d) Schematic of the anechoic chamber. Dimensions in m.

Figure 3.9: Images and schematics of the jet-setup and anechoic chamber at the Gas Dynamics and Turbulence Laboratory at The Ohio State University.

3.3.1 Setup and Microphone Array

This acoustic based phase study was performed using a microphone array shown schematically in figure 3.10 and in-situ within figure 3.9a. The microphones were arranged in opposing pairs so that the acoustic phase between the received signals can be evaluated and the underlying mode shape evaluated.

The opposing microphones were carefully positioned so that the tip of each microphone was displaced by the same distance as its opposing counterpart from the same nozzle reference point.

B&K 4939 1/4" microphones were used and were conditioned by B&K Nexus 2690 conditioning amplifiers with a built-in bandpass filter from 20 Hz to 100 kHz. The signals were sampled by National Instruments PXI-6133 DAQs and were archived using LabVIEW software. Microphone calibration was

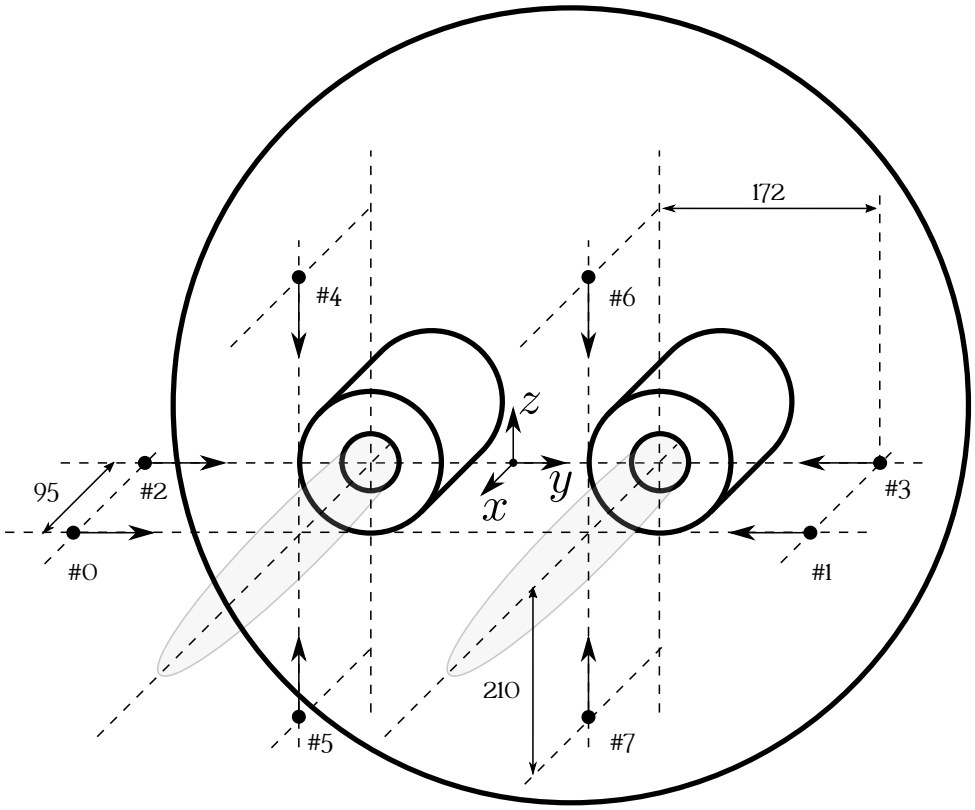

Figure 3.10: Ohio State University opposing microphone configuration layout for the forcing acoustic measurements. Dimensions in mm.

performed with a B&K acoustic calibrator (model 4231), and the microphone calibration constants were recorded to provide the conversion from measured voltage to the equivalent pressure. The sample rate was 200 kHz, and 819,200 data points were collected. The collected data points were split into 8192 data points per segment on the buffer before they were saved as a continuous signal for processing.

The methodology for retrieving phase information from the microphone array is discussed in detail within chapter 6.

3.3.2 Plasma Actuators

Forced mode experiments were conducted with collaboration with the Gas Dynamics and Turbulence Laboratory (GDTL) at The Ohio State University (OSU). GDTL has developed the use of Localised Arc Filament Plasma Actuators (LAFPAs) for controlling the azimuthal mode of high-speed jets.

Each actuator consists of two 1 mm tungsten electrodes. These electrodes are arranged such that their tips are approximately 3 mm apart from one another on the inner surface of the nozzle just upstream (1 mm) of the nozzle exit. Eight pairs of actuators are arranged around the nozzle. The circumferential actuators are fired in patterns to simulate different mode-shapes and azimuthal mode numbers.

The actuators use a spark generated by a pair of high-voltage electrodes to perturb the flow exiting

from the nozzle. The spark is generated when the electric field between the high-voltage electrodes causes the air to ionize. The ionization threshold is set by the breakdown electric field strength of air, which is approximately 7 kV. Spark ionization is classified as a strong ionization. In strong ionization the majority of the molecules within the intense electric field ionize forming a plasma. The plasma is highly conductive and allows electric current to flow. The current rapidly heats the plasma, which expands and generates a small pressure pulse. This pressure pulse provides a pressure perturbation to the flow. Another type of plasma actuator ustilises weak ionization to peturb the flow. Weak ionization partially ionizes the air molecules which accelerate along the electric field lines. The ionized molecules strike non-ionized molecules and transfer momentum to the bulk flow (Corke *et al.*, 2010). Dielectric barrier discharge actuators use this weak ionization working principal.

Figure 3.9b shows an image of the nozzles with plasma actuation. The blue light emanating from inside the nozzle lip is created by the actuator plasma. The actuator electrodes are shown in figure 3.11a. The nozzle is fabricated from ceramic, which provides sufficient insulation/dielectric properties to resist conduction of the electrode voltage. The electrodes are bent into an L-shape and inserted so that they stand slightly proud inside the jet nozzle. The nozzle has a small groove near the exit as shown in figure 3.11b. This provides a small recirculation zone for the stabilisation of the plasma. Additionally, the groove prevents the electrodes from protruding into the flow and acting as streamwise vortex generators. This would significantly alter the shear-layer development and thus the resonance of the jets.

The arrangement of electrodes around the circumference of the nozzle allow the generation of azimuthal modes. The electrode pair polarity is reversed to the adjacent electrode pair, i.e: (+, -) (-, +), (+, -), (+, -), ... This causes the spark to reliably form between the desired electrode pair and not with its neighbour.

The voltage between the actuators is ramped up to 15 kV to reliably produce a spark in the high-speed flow. The low reliability of spark generation at lower voltages means that there is little control over the amplitude of the perturbation. The 15 kW spark provides a fixed strong perturbation to the flow. The frequency of the spark can be precisely controlled. A computer based control system orchestrates the firing of actuators to generate different azimuthal mode shapes as a function of frequency. It was found that the actuation was effective for NPR < 4.0. Beyond this pressure the nozzle exit pressure was sufficient to push the plasma back into the electrode hole.

The effect of the actuators on the jet flow-field has been examined by GDTL over a number of publications utlising PIV, schlieren photography, and acoustic techniques (Kim *et al.*, 2009; Samimy *et al.*, 2012; Cluts *et al.*, 2015*b*,*a*; Kuo *et al.*, 2016*b*,*a*; Cluts *et al.*, 2016; Kuo *et al.*, 2017*b*,*a*; Cluts *et al.*, 2017). Statistical and mechanistic studies on the effect of the actuation on the large-scale structure and jet evolution have been investigated (Kim *et al.*, 2009; Samimy *et al.*, 2012). PIV was used to extract a Galilean decomposition of the forced velocity field. Faithful reproduction of azimuthal modes were observed including toroidal ($m = 0$) and helical combinations ($m = 1, \pm 1$) when the actuators pulse in the range of jet sensitive frequencies. The sensitive frequencies occur over a range of $0.1 \leq \mathrm{St} \leq 0.5$. Within the twin-jet context, Kuo *et al.* (2017*b*) reports that the actuators are able to faithfully reproduce input modes, verified with phase-locked schlieren photography. An example of the different modes and their effect on the flow-field is shown in figure 3.12.

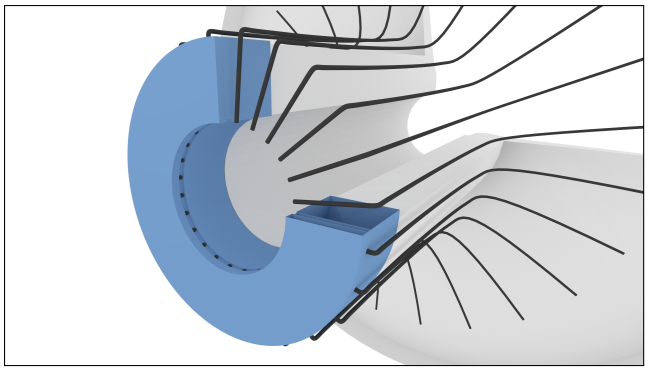

(a) Nozzle cut away showing the electrode positioning.

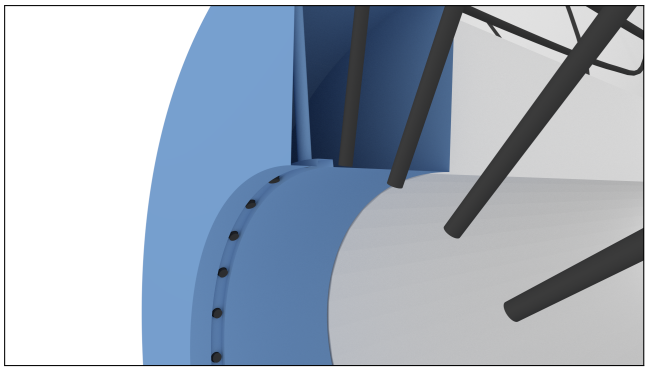

(b) Nozzle cut away showing the electrode plasma generation location.

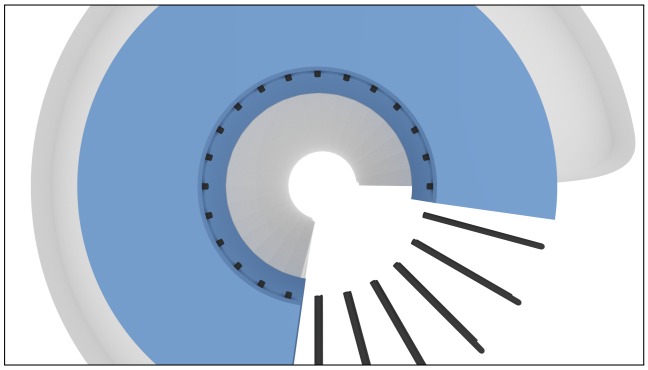

(c) Actuator locations within the nozzle.

Figure 3.11: Diagrams depicting the electrode layout for the jet actuators. Blue indicates the ceramic nozzles. Black indicates the tungsten electrodes.

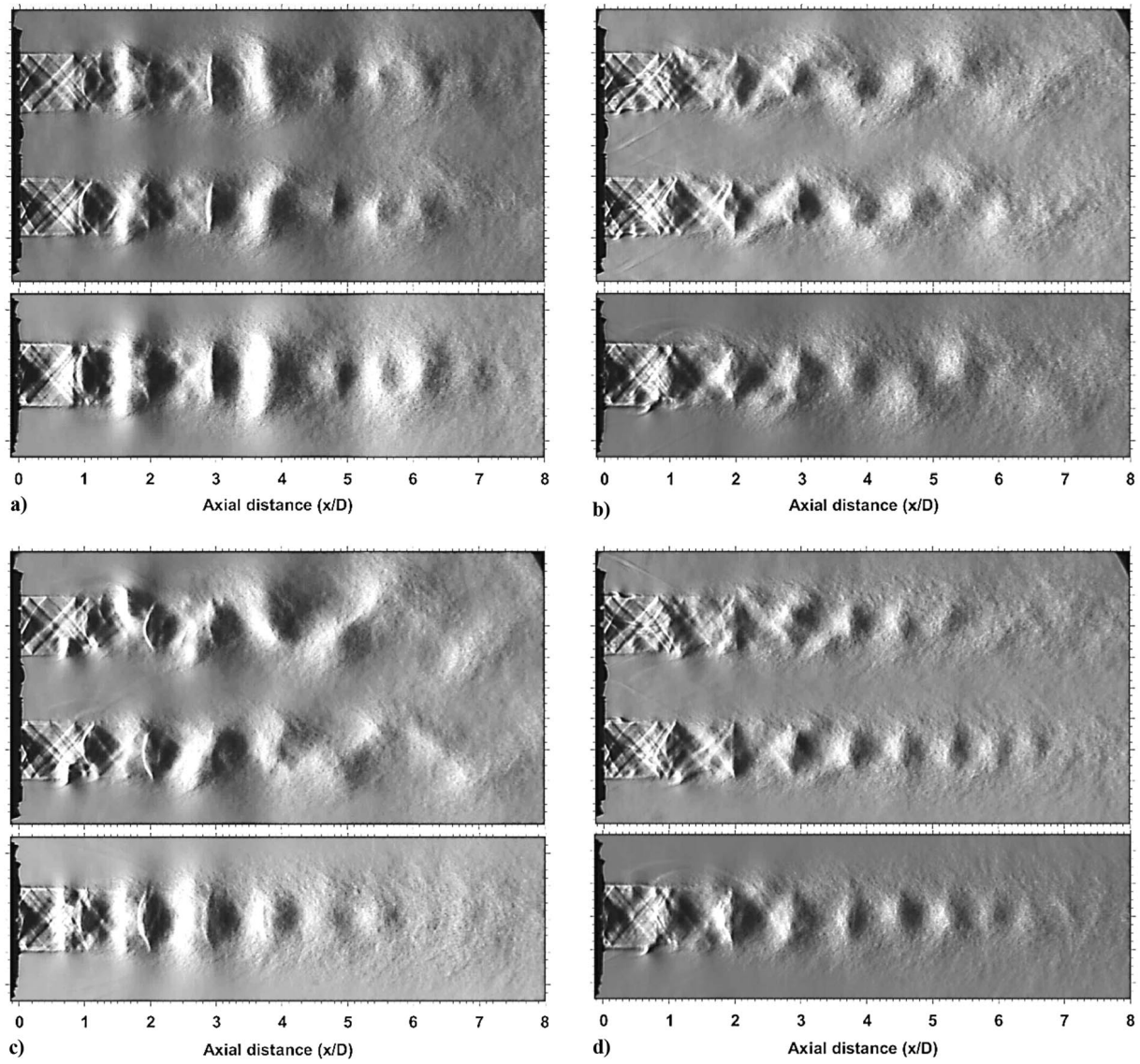

Figure 3.12: Schlieren visualisation of different forced modes on the flow-field. From of Kuo *et al.* (2017*b*). The figure shows phase-averaged schlieren images of twin-jet plumes (on the twin-jet plane on top and normal to the twin-jet plane on bottom) at $M_j = 1.3$ excited at $St_{DF} = 0.3$: a) axisymmetric mode ($m = 0$), b) a helical mode ($m = 1$), c) a flapping mode ($m = \pm 1$), and d) a helical mode ($m = 3$).

3.3.3 Forced Mode Shapes

There are twelve symmetrical $m = 1$ mode combinations about the various symmetry planes for the twin-jet. They vary in initial starting phase (0 or 180 degrees), travelling direction (clockwise or counter-clockwise), and angular offset from a zero reference point (0 or 180 degrees).

The mode convention used within this work is provided in figure 3.13. Starting in columns left to right: *Mode* represents arbitrary labelling of the different modes. *Shape* represents the starting position of the azimuthal precessing instability, *Azimuthal Mode Number* represents the azimuthal wavenumber of the precessing instability and is written in the notation catering for two simultaneous azimuthal instabilities per jet so that counter-rotating instabilities can be represented. Non-counter-rotating instabilities are represented by repeated values. The sign of the mode number identifies its travelling direction, with positive representing clockwise on both jets.

In this format:

- A toroidal mode ($m = 0$) is represented as (0,0) per jet.
- A single helical mode ($m = 1$) is represented as (1,1) per jet.
- A flapping mode is represented as a counter-rotating double helical mode ($m = \pm 1$) and is represented as (-1,1) per jet.

Phase represents the starting phase of the instability and is measured in degrees. *Offset* represents the offset in the number of actuators between one jet to the other. It is similar to phase offset between the two jets and assists with representing the computer algorithms that program the firing sequence. The next column shows the groupings of modes. There are four $m = 1$ flapping modes: C, D, E, and F. There are two co-rotating $m = 1$ helical modes: G and H. There are two counter-rotating $m = 1$ helical modes: I and J. Higher azimuthal wavenumber modes that were included in the study have been labelled as: K, L, and M. The *Observed In-Plane Phase* column identifies the phase difference between the two jets if a opposing microphone study was performed in-plane with the jets. The majority of $m = \pm 1$ and $m = \pm 2$ modes show a zero degree phase offset, which is likened to a symmetric oscillation when the in-plane view of the jets is examined. Modes E, G, and J are the only modes depicted here capable of producing in-plane anti-symmetric oscillatory modes. The *Observed In-Plane Phase* column identifies the phase difference between the two jets if a opposing microphone study was performed out-of-plane aligned with the left or right jet (assuming the superposition of the acoustic waves emanating from each jet is ignored during the phase cycle). Finally, the last column provides groupings to a generic descriptive label, which would describe their appearance to a full-field technique like schlieren photography or PIV. *Sym* and *ASym* denote symmetric and anti-symmetric respectively.

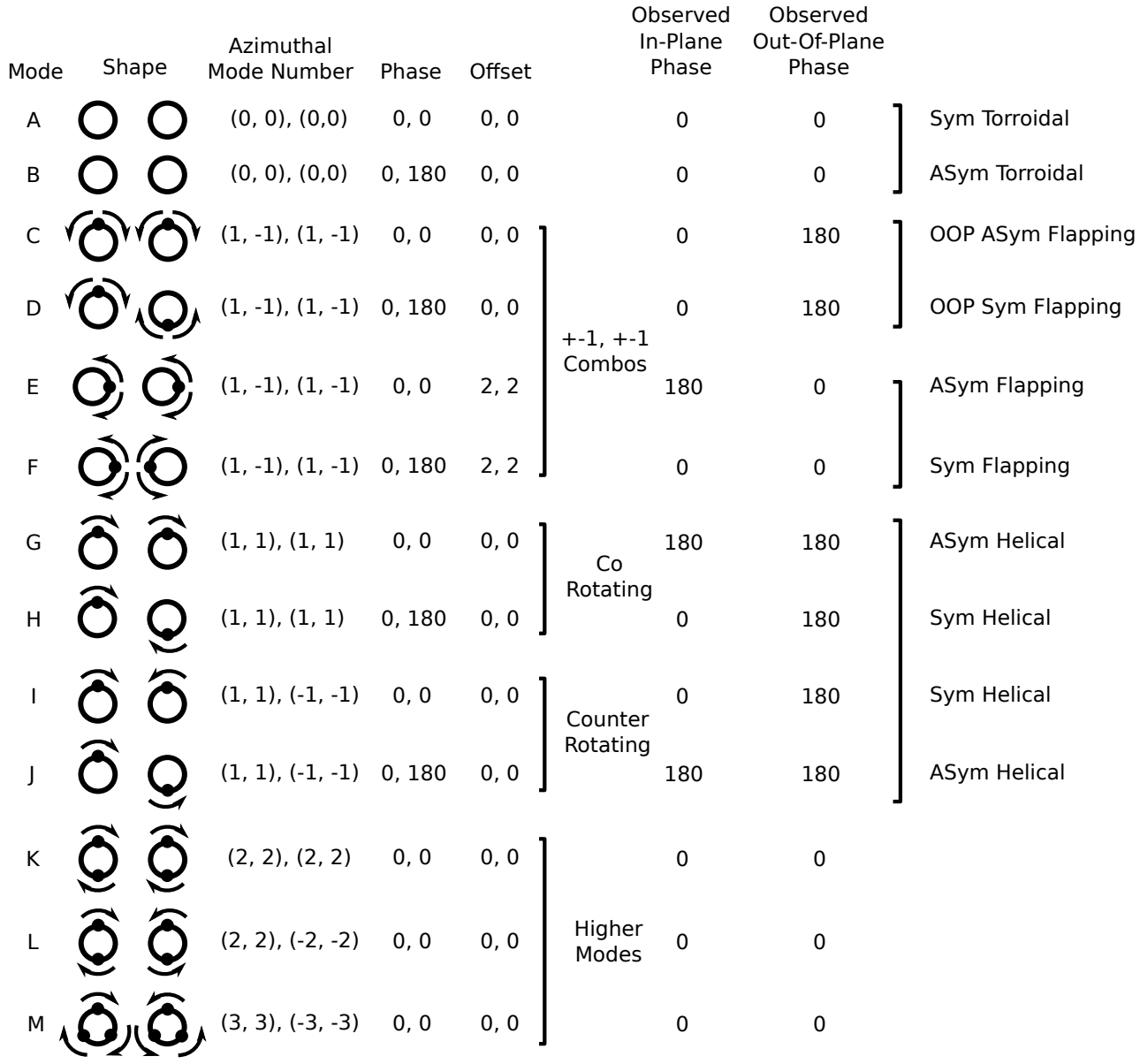

Figure 3.13: Diagrammatic description of the various modes based on azimuthal precessing instabilities of the twin-jet used in this thesis. Column description is provided in the adjoining text.

The forced modes were applied the parameter space $0.1 \leq St \leq 0.8$ in $0.05\,St$ steps and NPR = 2.52, 2.75, 3.0, 3.25, 3.5, 3.75, and 4.0 as shown in figure 3.14. The NPR value was held constant while the range of forcing frequencies and modes were swept through. It was physically observed that for NPR values greater than 4.0, the pressure was significant enough to displace the plasma through the electrode entry hole. Therefore, at NPR > 4.0 the forcing effect is likely to be marginal at best. Hence, the range above this NPR was not explored, despite the existence of potentially scientifically interesting behaviour.

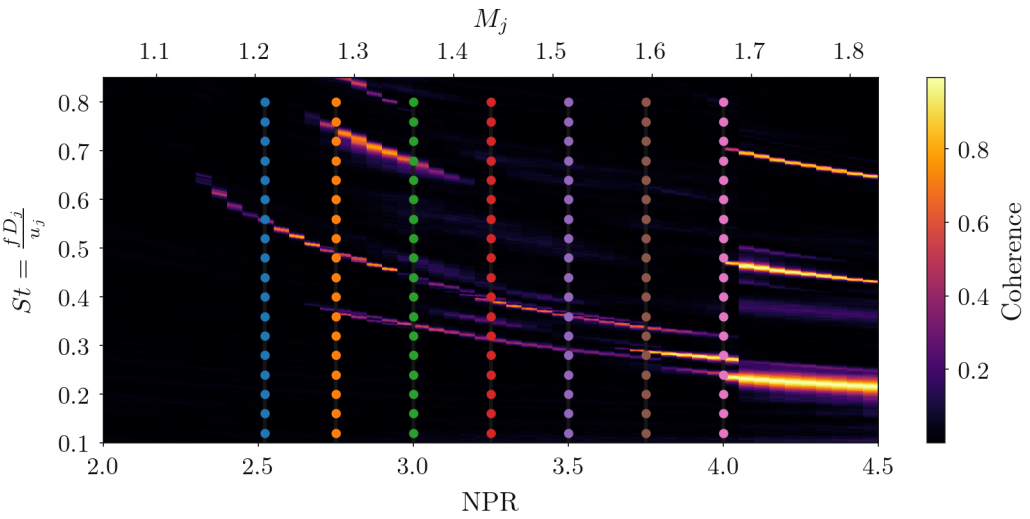

Figure 3.14: Acoustic spectra and overlaid forced parameter space in frequency (Strouhal) and NPR. NPR values are (from left to right) 2.52, 2.75, 3.0, 3.25, 3.5, 3.75, and 4.0.

3.3.4 Cases

Eight cases were recorded and are compared in table 3.3. The unforced case examined $2.0 \leq \text{NPR} \leq 6.0$ using steel polished nozzles with identical geometry to the ceramic nozzle. The Reynolds number based on ideally expanded conditions for this pressure range is is 5.95×10^5 and 1.94×10^6 for NPR = 2.0 and 6.0 respectively. The unforced experiments were performed at NPR = 2.52, 2.75, 3.0, 3.25, 3.50, 3.75, and 4.00. As previously mentioned, pressure ratios greater than 4.0 resulted in poor plasma actuation are not included in the analysis.

Case	Forcing	Nozzle 0	Nozzle 1	Chapter
0	Unforced	Ceramic	Ceramic	7
1	Steady forcing	Ceramic	Ceramic	7
2	Unforced	Steel	Steel	7
4	Unforced	Steel convergent	Steel convergent	5
5	Temporal forcing	Ceramic	Ceramic	7
6	Unforced	Ceramic	Steel	7
7	Single jet forcing	Ceramic	Steel	7

Table 3.3: Cases recorded using facility three. Cases not relevant to the present measurements have been excluded.

Chapter 4

Characterisation Study of Circular Supersonic Twin-Jets

4.0.1 Introduction

Chapter 2 established a need to examine the circular twin-jet parameter space for complex coupling and the mode switch locations. The objective of this study was twofold. Firstly, to classify the dominant coupling modes at different jet spacing as a function of NPR. Secondly, to examine the fit of existing screech models to the twin-jet to extract the parameters of the feedback loop. An opposing microphone technique was used to extract phase between the acoustic signals of the jets. Schlieren photography was also used to assess the mode shapes in the in-plane and out-of-plane directions. The author's role was to assess the phase extraction via the opposing microphone technique. The acoustic and schlieren techniques were performed individually on facility one. This study was published under Knast *et al.* (2018) and is included in appendix A.

4.0.2 Results and discussion

The dominant tones as a function of NPR are shown in figure 4.1. The mode selection appears to be quite stable across NPR for both s/D = 3 and 6. The main mode switch point for s/D = 3 and 6 was NPR = 4.3 and 4.8 respectively. The single nozzle was found to produce a number of different high amplitude screech-tones.

The parameter space mode classification was performed using a spatial correlations of schlieren image intensity and acoustic phase. Schlieren spatial correlation maps for different pressure ratios are shown in figure 4.2. The antisymmetric banding pattern across figure 4.2a indicated an anti-symmetric mode. Symmetric modes were observed for the higher pressure ratios, shown in figures 4.2b and 4.2c. Despite NPR = 3.0 and NPR = 3.6 showing different coupling modes, the screech peaks did not show a clear frequency step indicating a mode-switch point. The reference point location in the shear-layer resulted in strong correlation with the schlieren image intensity changes in the entrainment field. This is due to the downstream convecting processes generating pressures waves that extend into the entrainment field (Westley & Woolley, 1969; Panda, 1999). The correlation between the convecting

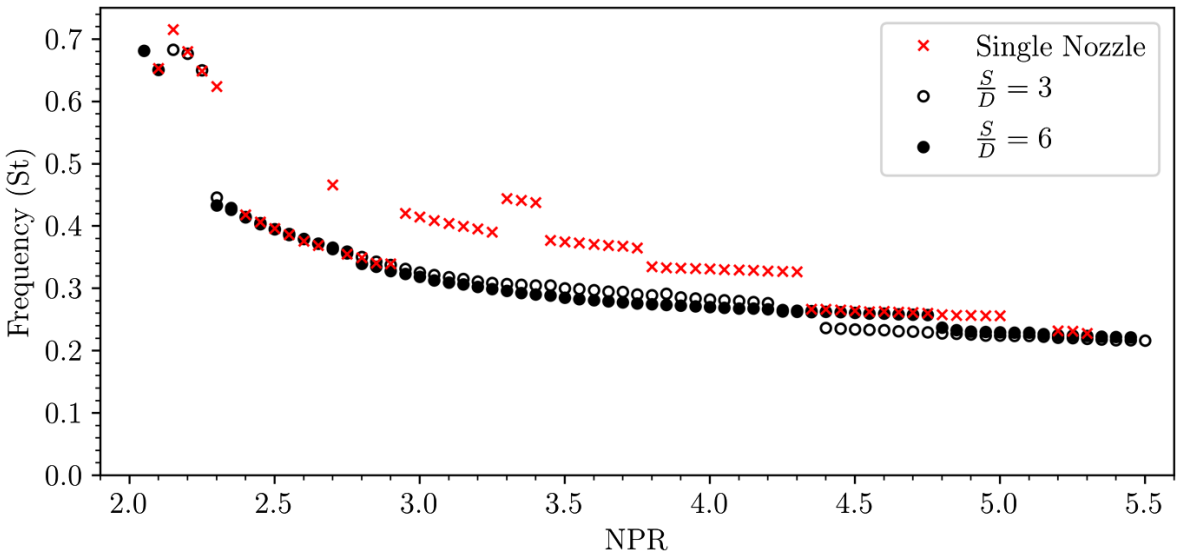

Figure 4.1: Dominant screech tone frequency as a function of NPR. From Knast *et al.* (2018).

structures and the pressure waves means that the wavelength of the correlation field corresponds to the hydrodynamic wavelength of the downstream process. There was a clear change in hydrodynamic wavelength between NPR = 3.6 and NPR = 4.6 and a corresponding frequency step between these pressure ratios in figure 4.1. Therefore, while some changes in modes are indicated by a change in screech frequency, others do not.

CPSD was used to examine the time-averaged phase from the opposing microphones placed either side of the jet. The screech peak (determined by PSD amplitude) provided the screech frequency. The screech frequency was used to examine the corresponding phase value from the CPSD spectra. The acoustic recordings were performed at 0.05 NPR increments. The phase for both spacings is shown in figures 4.3a and 4.3b. The results indicated a different parameter space than what was inferred from the schlieren spatial correlations. The phase for both s/D = 3 and 6 was divided up into regions based on phase value. For s/D = 3, there existed three regions. Region I with approximately zero degree phase difference indicates that the jets are in a symmetric mode about the centreline. Region III shows a 180 degree phase difference indicating an anti-symmetric mode. Region II contained a sporadic phase difference with a wide variation. The repeatability (sample variance) within region II was approximately 30 degrees - the results were generally repeatable and thus not entirely stochastic. The associated jet modes for region I and III were predictable and straightforward to interpret, region II was not. The sporadic phase was also observed within region V of s/D = 6. Region III and V do not correspond to the same mode. Region IV was found to be a unique mode. The high NPR mode within s/D = 6 could not be captured due to camera equipment failure and thus only microphone phase is available. Therefore, it was found that changes in jet coupling mode were not necessarily accompanied by a change in observed screech frequency.

The analysis of cross-bicoherence was not included in the publication but is included here for context and comparison with earlier studies (Raman, 1998; Panickar *et al.*, 2005; Srinivasan *et al.*, 2009). The cross-bicoherence spectra for NPR = 3.0, 3.4, 4.0, 5.0 are shown in figures 4.4a, 4.4b, 4.4c, 4.4d. The spectra were calculated using equation 2.7. The Fourier transform provided a frequency resolution of approximately 48 Hz/bin. The bicoherence spectra peaks are very narrow and predominantly

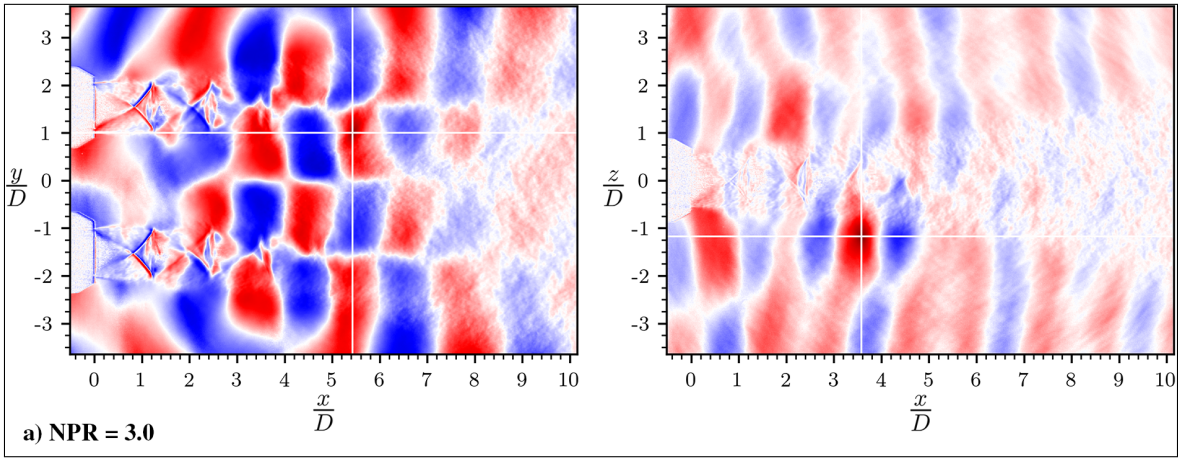

(a) NPR = 3.0, symmetric oscillation pattern.

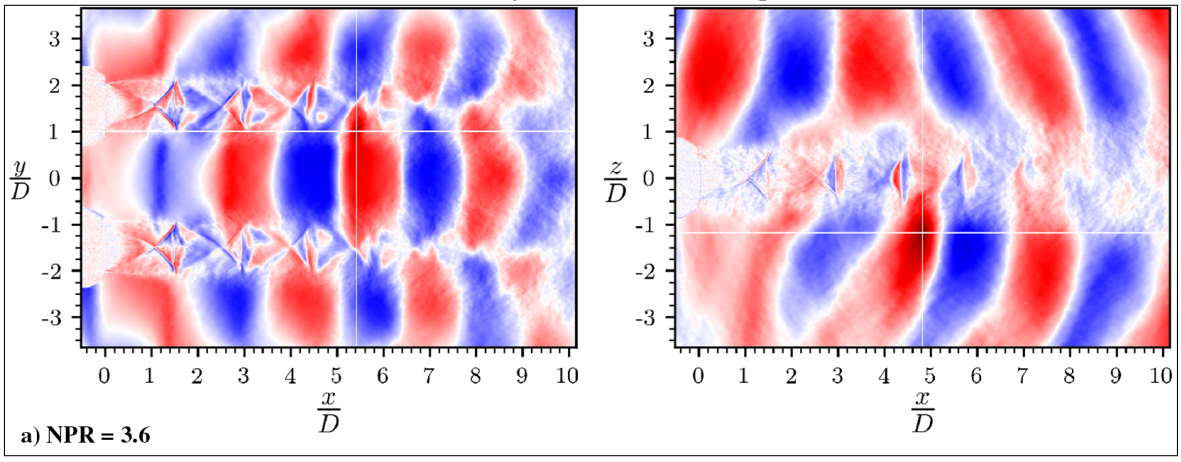

(b) NPR = 3.6, anti-symmetric oscillation pattern.

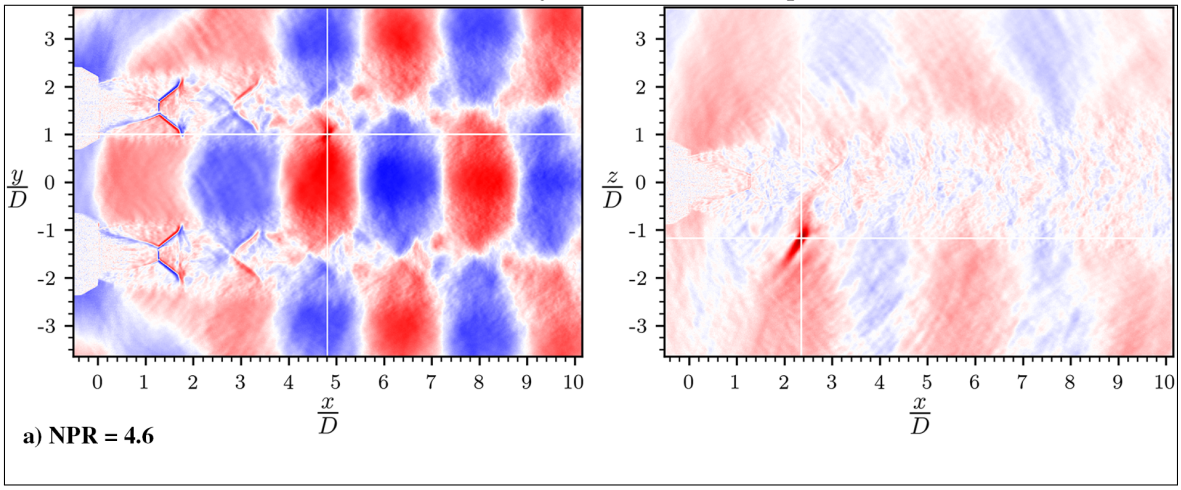

(c) NPR = 4.6, anti-symmetric oscillation pattern.

Figure 4.2: Selected two point correlation maps from Knast *et al.* (2018). Maps are constructed from instantaneous schlieren images for NPRs = 3.0, 3.6, and 4.6 at $s/D = 3$. White line intersection shows correlation reference point. Red indicates correlation of 1, blue indicates correlation of -1. Left figures show jets in-plane. Right figures show jets out-of-plane.

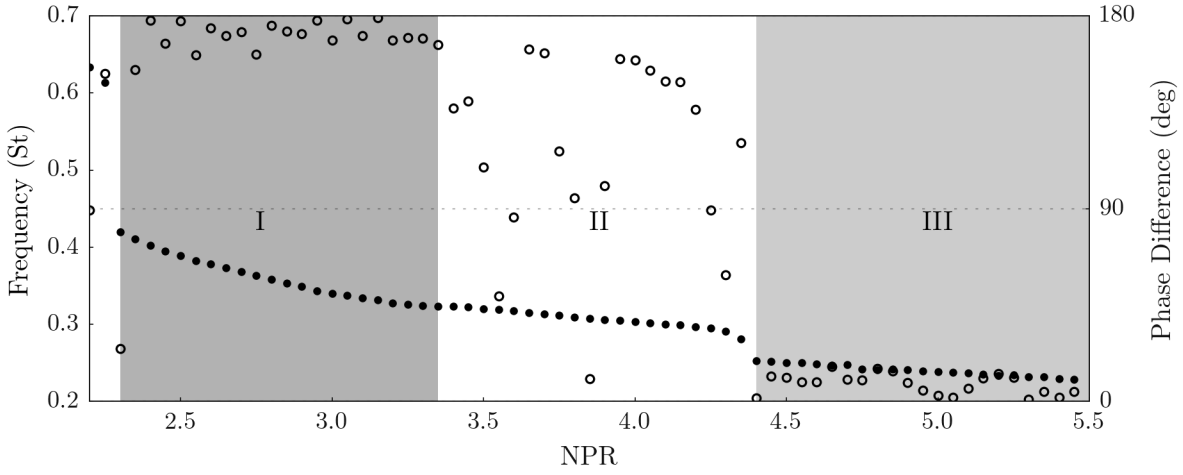

(a) $s/D = 3$

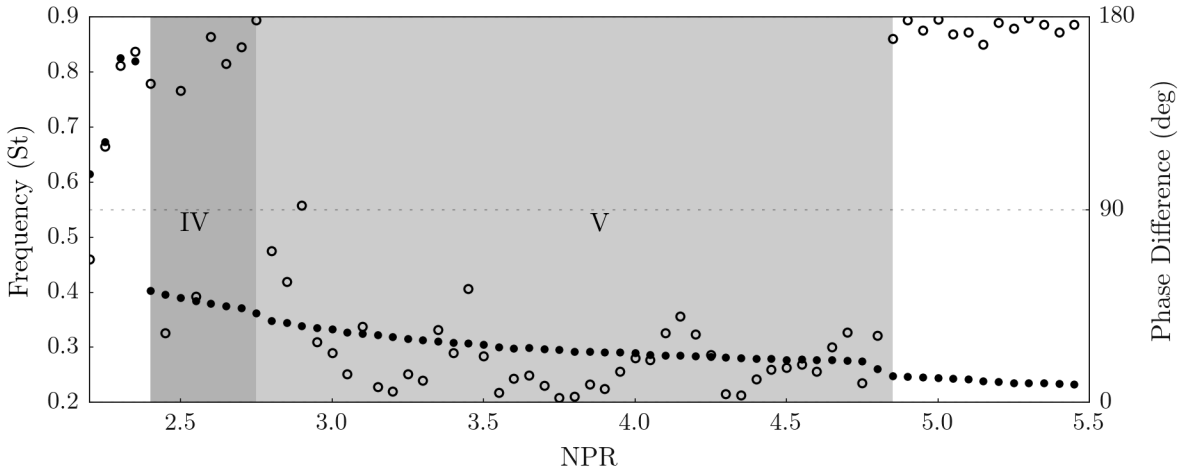

(b) $s/D = 6$

Figure 4.3: Opposing microphone phase and frequency results for non-dimensionalised jet spacings of 3 and 6 against nozzle pressure ratio. Solid dots indicate screech tone frequency election from PSD, open dots indicate phase estimate from CPSD at the solid dot frequency. Region II within figure 4.3a shows the sporadic phase behaviour. Figures from Knast *et al.* (2018).

surrounded by incoherence. The log of the cross-bicoherence value is shown to normalise the changes in magnitude for presentation as the figures are otherwise completely blue. All four figures show similar spectra structure. A peak is observed at the screech tone between the microphones. Orthogonal lines of higher coherence originate from this peak that show the coherence of the screech frequency with other frequencies in the spectra. Harmonic peaks are visible for NPR = 5.0 due to its lower screech frequency. Clustering of peaks is not observed as in previous research (Panickar *et al.*, 2004; Srinivasan *et al.*, 2009).

The interaction density is shown in figure 4.4e and is calculated to estimate the number of peaks where $b_c^2 \geq 0.4$. The interaction density peaks over the range $3.0 \leq \text{NPR} \leq 3.5$. Comparing this region with figure 4.3a indicates that the two do not align with expected signal anomalies. The peak in cross-bicoherence falls within a region of reasonably well defined phase before the region I to region II switch point. Throughout region II the cross-bicoherence value is comparatively low. The cross-bicoherence has thus not demonstrated that the phenomenon in region II can be explained as a non-linear interaction between modes. The mutual inclusivity of both coupling modes (a multi-modal

condition) would generate simultaneous tones that could potentially appear as frequency interactions in the cross-bicoherence. This was shown to be not the case. Alternatively, the modes could be mutually exclusive. At the mode switch points, the tone would fluctuate between the two modes resulting in a non-stationary acoustic signal. Recent research has indicated that applying the cross-bispectrum to non-stationary signals produces false-positive and other spurious results (Poloskei *et al.*, 2018). Therefore, a stalemate on the use of the cross-bicoherence was created. The lack of intensity in the cross-bicoherence measurement indicated no mode mutual inclusivity. Conversely, there existed a possibility for false-positives if the mutual-exclusivity was experienced due to the time-varying signal. Nevertheless, the lack of a consistent phase value was consistent with the description for the complex coupling regions (Raman, 1998; Wlezien, 1989). Therefore the concept of pure non-linear interactions driving this interaction was placed aside and the physics of the coupling modes were further investigated. Region II is hereby described to contain complex coupling produced by multi-modal or mutually exclusive mode behaviour.

The agreement with the screech prediction methodologies developed based on the single jet feedback loop were assessed (Panda, 1999; Gao & Li, 2010). A comparison against the method of Gao & Li (2010) is shown in figure 4.5. Changes in the distance to the upstream process generation source were considered by examining M (which is m in Knast *et al.* (2018) but changed here to avoid a nomenclature clash). M represents the number of simultaneous upstream and downstream waves in equation 2.4 from section 2.1.1). Changes to the number simultaneous waves, m, the emitting shock-cell number, n, and the shock-cell length, L, cannot explain the change in frequency for the symmetric and anti-symmetric mode. Changes in convective velocity of structures in the jet shear-layer were also considered as an explanation. Convective velocity normalised by the jet ideally expanded Mach number was shown to be effectively constant, which is also observed in single jets (Mercier *et al.*, 2017). Therefore it was concluded that shock-cell spacing, standing-wavelength, and convective velocity cannot explain the mode staging behaviour. The remaining possibilities that can explain the small frequency change between the observed frequencies include a modification to h (the downstream distance) to include a diagonal path from one jet to another. This is dependent on the jet spacing. Alternatively, the upstream closure mechanism may not be the free-stream acoustic mechanism that propagates externally of the jet. A new upstream closure mechanism involving a neutrally-stable acoustic mode that travel upstream in the shear-layer of the jet has been shown to exist in single jets (Edgington-Mitchell *et al.*, 2018; Bogey & Gojon, 2017). A phenomenological model for this upstream closure mechanism is yet to be developed.

4.0.3 Conclusions

The study provided a classification of coupled jet modes across two jet spacings ($s/D = 3, 6$). Nozzle spacing was found to play a significant role in coupling mode selection. Discontinuous jumps in dominant screech frequency were found to be insufficient to identify all changes in the coupling modes. Mode staging could not be explained by the existing models for screech (Panda, 1999; Gao & Li, 2010). Additionally convective velocity normalised by the ideally expanded jet velocity was found to be invariant with NPR. Therefore it was also unable to explain mode staging in the twin-jet case and more complex mechanisms must be at work. Possibilities for these mechanisms include a different path-length than the one considered for single jets or a different upstream closure mechanism recently

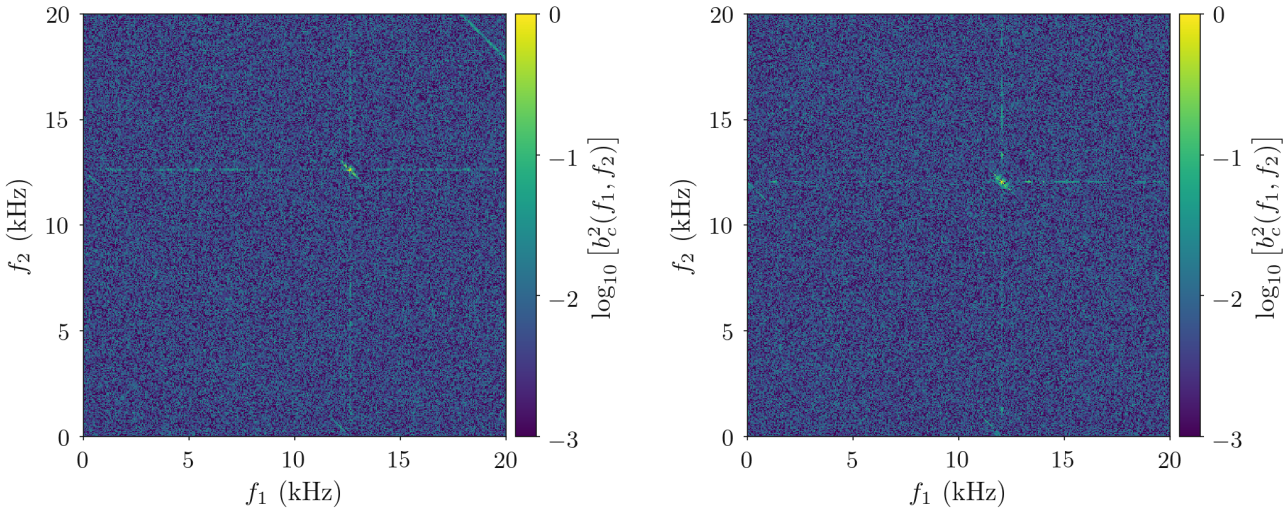

(a) NPR = 3.0

(b) NPR = 3.4

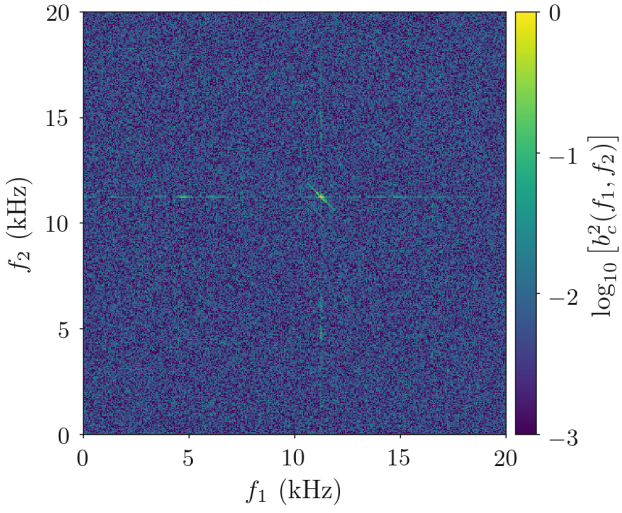

(c) NPR = 4.0

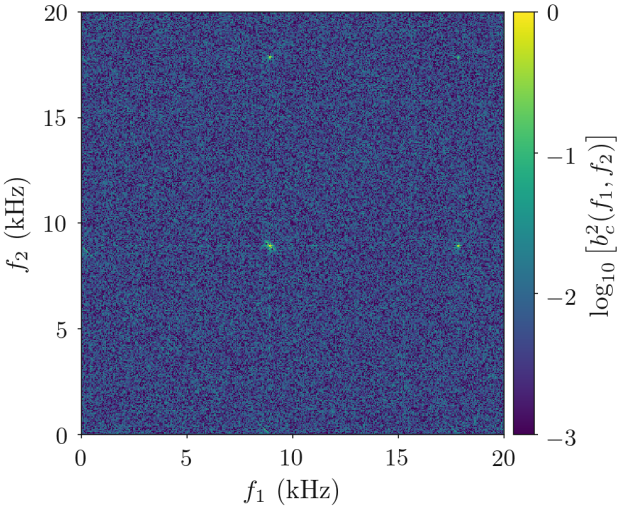

(d) NPR = 5.0

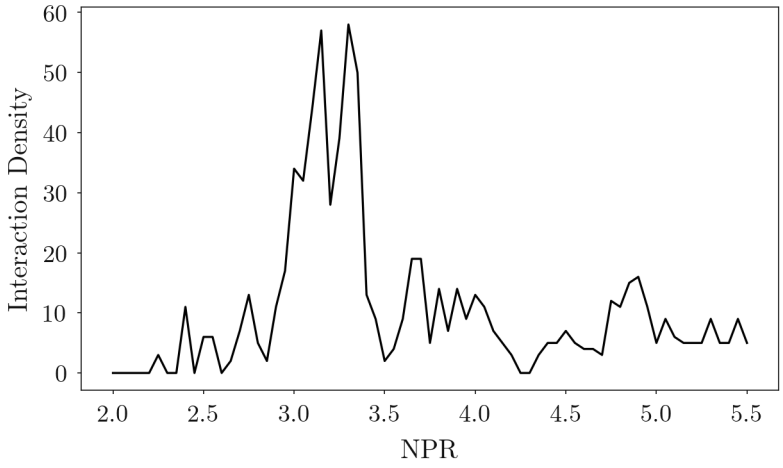

(e) Interaction density of the respective bicoherence spectra.

Figure 4.4: Bicoherence properties for the $s/D = 3$ spacing.

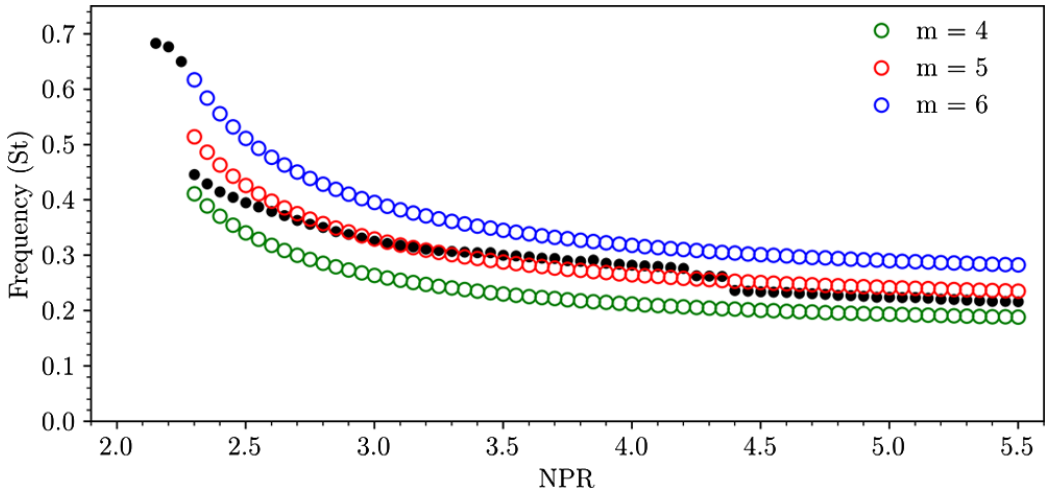

Figure 4.5: Observed screech tone overlaid by a screech tone prediction model for single jets (Gao & Li, 2010). From Knast *et al.* (2018).

observed in single jets.

The acoustic phase between the jets appeared sporadic for the regions between symmetric and anti-symmetric modes for both $s/D = 3, 6$. Potentially this could have been caused by non-linear interactions between the jets (Panickar *et al.*, 2005; Srinivasan *et al.*, 2009). The cross-bicoherence was used to determine the rate of non-linear interactions. High rates of interaction did not correlate to the sporadic phase region or the surrounding mode-switch locations. A stalemate on the use of the cross-bicoherence was encountered. The lack of intensity in the cross-bicoherence measurement indicated no mode mutual inclusivity. Conversely, the existed a possibility for false-positives if the mutual-exclusivity was experienced due to the time-varying signal. The regions' sporadic phase are similar in description to the complex coupling regions observed by earlier works. Therefore the complex coupling behaviour is now considered in the context of multi-modality or mutual exclusivity of adjacent coupling modes and the interactions between them. An investigation into identifying what the coupling within region II contains and how it forms is now the direct subject of investigation spanning both chapters 5 and 6.

The schlieren measurements were used to classify the modes of the parameter space. However, the path-integrated nature of the technique caused interpretation challenges. The path-integration made the interpretation of the out-of-plane direction unclear. Additionally, hydrodynamic structures cannot be directly tracked using schlieren, only inferred from strong density fluctuations. A full-field quantitative analysis comparing different coupling modes was lacking. It was the next logical step for further physical insight. The methodology of the PIV experiment was discussed in chapter 3. Its analysis is presented in chapter 5.

Chapter 5

Quantitative Examination of Coupling Modes

5.1 Introductory Statement

The characterisation study in chapter 4 revealed that the features of complex coupling are also found in circular twin-jets. A strong acoustic tone was observed within these regions of complex coupling despite a sporadic phase relationship between the acoustic signals of the jets.

There existed a clear lack of quantitative velocity field data that examines the differences between twin-jet coupling modes. Additionally, flow features unique to the twin-jet such as the inter-nozzle region and the differences between internal and external facing shear-layers had not been explored. A single study examining the twin-jet velocity field using PIV had been performed (Alkislar *et al.*, 2005). Full-field mean and fluctuation flow statistics at a single pressure ratio were reported. A converging-diverging nozzle and ideally expanded pressure ratio resulted in a shock-free flow where purportedly screech is suppressed. Spanwise velocity statistics were reported so that the velocity profile of the jets could be examined. The exterior facing shear-layer thickness was reported, where it is found that twin-jets experience lower shear-layer growth rates than single jets. Statistics for the base flow were reported but the structure of the coupling mode shape was not examined. Additionally, the under-expanded twin-jet regime remained unexplored from a velocity field perspective.

The objectives of this study were to decompose the flow field to examine different coupling modes to provide a physical description for 'complex coupling' and to acquire a piece-wise description of unique features the twin-jet flow. The quantitative flow description is intended to provide a baseline of flow statistics of the full-field, inter-nozzle region, and shear-layers. The location and velocity characteristics for the supersonic twin-jet merge point have not been quantitatively examined (Seiner *et al.*, 1986). The merge point determines the structure of the interior shear-layers. It is likely the interior shear-layer is within the acoustic feedback pathway and therefore is an integral part of the coupling feedback process.

The dataset examines the $s/D = 3$ spacing for two coupling-modes. The pressure ratios were located

either side of the region II/III acoustic tone switch point when performed on facility two. The location of the region II/III acoustic tone switch point on facility one corresponded to NPR = 4.85. This is higher than for facility one and is possibly due to the reflective walls within the PIV enclosure. Region III was observed to produce a clear symmetric mode on facility one. Comparing the velocity field changes between region II and III coupling modes was the next step to determining the coupling behaviour in the complex region.

This chapter is presented as a journal paper published in Experiments In Fluids (Bell *et al.,* 2018).

Experiments in Fluids (2018) 59:139
https://doi.org/10.1007/s00348-018-2593-1

RESEARCH ARTICLE

An experimental investigation of coupled underexpanded supersonic twin-jets

Graham Bell[1] · Julio Soria[1] · Damon Honnery[1] · Daniel Edgington-Mitchell[1]

Received: 10 February 2018 / Revised: 19 July 2018 / Accepted: 3 August 2018 / Published online: 20 August 2018

Abstract
High-resolution particle image velocimetry measurements of coupled underexpanded twin-jets are presented. Two nozzle pressure ratios are examined, which are selected due to a change in coupled plume mode indicated by a discontinuous jump in screech frequency. Estimates of the turbulent flow statistics, shear-layer thickness, merge point, inter-nozzle mixing, and integral length scales are provided. The higher nozzle pressure ratio case shows a strong standing-wave present in the velocity fluctuation amplitude and integral length scale. The ratios of standing, acoustic, and hydrodynamic wavelength are compared and find a close fit to Panda's relation for screech. This indicates that screech in the twin-jet system operates with similar length-scale and frequency characteristics to single jets and provides evidence to suggest screech is an integral part of the twin-jet coupling process. Second-order spatial velocity correlation maps reveal the larger modal structure. A symmetric mode is found for the higher pressure ratio and a weakly symmetric mode for the lower. Comparison is made between where the standing-wave is present and where it is not. It is found that the standing-wave, not the shock structure, is the driver of turbulence coherence modulation near the jet. In regions that are affected only by the standing-wave, it is found that it contributes to both the turbulence intensity and coherence modulation.

1 Introduction

This work presents an investigation of underexpanded circular twin-jets. The twin-engine arrangement is common in high speed air and spacecraft. Supersonic exhaust from this configuration can produce intense acoustic radiation that has led to nozzle and empennage structure fatigue damage in some high speed aircraft (Berndt 1984), including the F-15 (Seiner et al. 1986).

One major source of acoustic radiation is a self-reinforcing aeroacoustic feedback process called jet screech (Powell 1954; Tam 1995). Screech occurs in shock containing supersonic jets as a result of the interaction between coherent vortical structures (CVS) produced at the nozzle lip, and downstream shock cells. This shock–vortex interaction produces intense acoustic waves that propagate most strongly in the upstream direction. The arrival of these waves at the nozzle lip perturbs the shear layer, producing new CVSs and completing the feedback process (Edgington-Mitchell et al. 2014). A summary of the knowledge on screech is provided by (Raman 1998). Screech has been observed in many single jet configurations. It has also been observed in twin and multi jet-configurations, where its acoustic signature is significantly stronger than the superposition of two single jets would imply (Shaw 1990).

The screeching jet process produces distinct modal behavior within the jet plume (Powell 1954; Davis and Oldfield 1962; Powell et al. 1992). For a single screeching jet, the modal behavior can be attributed to the flow instability, the phase velocity of returning acoustic waves, and the number of screech periods within the feedback loop (Mercier et al. 2017; Gojon and Bogey 2017). In the twin-jet configuration, the screech cycle is modified by the presence of the adjacent jet and causes the jet plumes to become coupled (Raman et al. 2012; Kuo et al. 2017a, b). Toroidal, helical, and flapping modes within the jet shear-layer have been observed (Kuo et al. 2017b). However, the process of mode selection, transition between modes, and coupling mechanisms are not well understood (Srinivasan et al. 2009; Panickar et al. 2004, 2005). The coupling behavior is a complex function of nozzle spacing, nozzle

✉ Graham Bell
Graham.Bell@Monash.edu

[1] Laboratory for Turbulence Research in Aerospace and Combustion, Department of Mechanical and Aerospace Engineering, Monash University, Melbourne, VIC 3800, Australia

pressure ratio (NPR), jet expansion level, boundary layer thickness, shear-layer growth rate, nozzle symmetry, and the acoustic environment (Alkislar et al. 2005; Wlezien 1989; Morris 1990). NPR is the ratio of nozzle stagnation pressure upstream of the nozzle (p_∞) to ambient pressure in the exhaust region (p_0), (NPR $= p_0/p_\infty$).

The interaction between downstream convecting coherent vortical structures and upstream propagating acoustic waves forms a standing-wave pattern in the near-field pressure (Westley and Woolley 1969). The interference between these two opposite moving phenomena produces a banded pattern that is visible in the pressure fields of screeching jets (Panda 1999). Panda was among the first to provide a quantification for the banded pattern through schlieren photography in measures of ensemble variance. He was able to deduce that these bands were the interference pattern between downstream convecting CVSs and upstream propagating acoustic waves. He described the structure as a 'standing-wave' and the term has remained in usage within the jet aeroacoustics community since. Common usage of the term 'standing-wave' implies that the resulting interference pattern between two waves is fixed and spatially stationary to an observer. Considering the aeroacoustic wave interaction present in a screeching jet, however, the interference pattern consists of structures that have different propagation speeds and hence the resulting interference pattern translates spatially. The two waves do have the same frequency and produce an interference pattern visible in measures of pressure or velocity fluctuation amplitude. The standing wavelength has been proposed as a characteristic length-scale for screech (Panda 1999). Historically, the shock cell spacing has also been used as a characteristic length scale. Recent work has suggested that a match or mismatch between these length scales is linked to different acoustic feedback mechanisms (Edgington-Mitchell et al. 2015; Bogey and Gojon 2017).

Few quantitative studies of the twin-jet velocity field exist in literature. Alkislar et al. (2005) focused on obtaining turbulent flow properties of the twin-jet system and experimented with micro-jets surrounding the nozzle lip to disrupt the coupling process. High-resolution full-field measurements in these flows are now possible due to increased camera resolution and sensitivity, and laser timing. This offers new opportunities to study the velocity field dynamics and investigate the coupling behavior. Understanding the twin-jet features such as the full-field modal behavior, standing-wave, and turbulence characteristics are critical to unraveling the fundamental coupling mechanisms. The objective of this paper is thus to provide a quantitative experimental study of twin-jet coupling. High-resolution PIV measurements for two modal configurations of coupling are presented, the effect of the standing-wave on the velocity field is determined, and its link to coupling mode examined. Also presented are full-field velocity correlations and associated length scales, which are provided to quantify modeshape and turbulent mixing.

2 Experimental methodology

2.1 Experimental facility

The experiments were conducted in the Laboratory for Turbulence Research in Aerospace and Combustion (LTRAC) gas jet facility at Monash University. The experimental PIV setup is shown in Fig. 1. Air at approximately 298 K is supplied directly to a mixing chamber where the jets are uniformly seeded with smoke particles from a Viscount 1300 smoke generator. Only one smoke source was needed for both jet core and ambient fluid measurements as after a short time the smoke particles completely filled the measurement facility. The mixing chamber is connected to the plenum chamber, which contains a honeycomb section and wire mesh screens to homogenize and condition the flow. The exhausted flow is imaged inside the PIV enclosure, which is $60 \times 60 \times 200$ diameters in size. The walls of the enclosure are not acoustically treated. The gas jet facility has been previously validated by experimental studies (Weightman et al. 2016, 2017). Compressed air exhausts from twin converging circular nozzles with an exit diameter of $D = 10$ mm and nozzle lip thickness of 1.5 mm. Both nozzles share the same plenum chamber. The converging nozzle section follows an elliptical profile (37 mm semi-major and 4 mm semi-minor) becoming tangent at the exit. As the nozzles

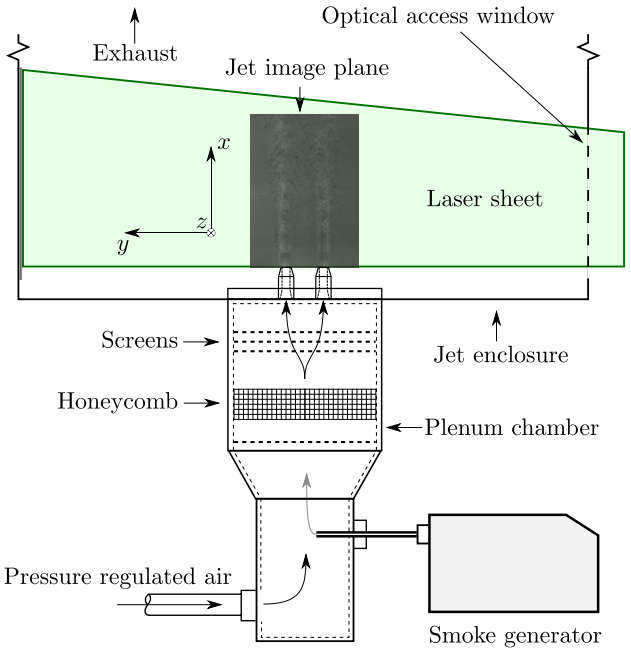

Fig. 1 Experimental PIV setup

are purely converging, the minimum area throat occurs at the nozzle exit. The flow at the exit is choked (exit Mach number, $M_e = 1$) with a jet exit velocity $U_e \approx 310$ m/s. The Reynolds number based on the ideally expanded quantities exiting from the nozzle is approximately 7.8×10^5 for NPR = 4.6 and 8.5×10^5 for NPR = 5.0.

2.2 Acoustic characterization

Previous qualitative studies within the laboratory using the same twin-jet nozzles found that an inter-nozzle spacing (spacing between the jets s, and D is the minimum jet area) $s/D = 3$ in the range NPR $\approx 2.0 \rightarrow 5.4$ produced strong coupling. Acoustic measurement and analysis were performed to characterize the fundamental screech tone peak of the jet pair in the measurement facility as a function of NPR.

Acoustic measurements were obtained with a G.R.A.S. type 46BE 1/4" preamplified microphone with a frequency range of 20 Hz → 100 kHz. The microphone amplitude coefficient was referenced against a G.R.A.S. type 42AB sound level calibration unit. The signal output from the microphone was recorded on a National Instruments DAQ at a sample rate of 250 kHz to prevent aliasing and a signal resolution of 16 bits. The single microphone was placed between the two jets 23 D away at the nozzle lip height in the out-of-plane position using the same reference coordinate system as Kuo et al, $y/D = 23, \theta = 90°, \phi = 90°$ (Kuo et al. 2017b). The PIV facility contains potential reflective acoustic surfaces and as such cannot be considered anechoic. The average acoustic spectra were calculated using a 2^{13} sample sliding-window via a Fourier transform. A 25 % window overlap and a Hann window were used to minimize edge effects. Figure 2 shows the acoustic frequency spectra with vertical lines indicating the screech tone. Horizontal axis is strouhal number (St), where f is the measured screech peak frequency, D_j is the ideally expanded jet diameter, and U_j is the ideally expanded jet velocity.

Figure 3 shows the identified fundamental screech tone as a function of NPR. The abrupt change in screech frequency at NPR = 4.85 was assumed to indicate a transition between coupling modes, as observed in other twin-jet studies (Raman 1999; Alkislar et al. 2003; Raman et al. 2012). The primary objective was to capture different coupling modes and the small change in NPR should result in minimal variation of the base flow.

The large change in strouhal for the lower NPR values (NPR ≈ 2.2) correspond to a region described by Raman as a 'weak complex interaction' and will not form part of this study. Two NPRs on either side of this switch point (NPR = 4.60 and 5.00) were selected for PIV analysis.

2.3 PIV Parameters

Single exposure image pairs were acquired using a 12-bit Imperx B6640 camera with a CCD array of 6600×4400 px at a rate of 0.5 Hz. Approximately 9000 velocity fields are used for the calculation of all statistics. A magnification of 19.9 µm/px is achieved using a 200 mm Nikon Micro-Nikkor lens, which results in a PIV image plane of 129.3×86.2 mm. The particle field is illuminated using a diverging light sheet of approximately 1 mm thickness produced from a dual cavity pulsed Nd:YAG laser at 532 nm with a maximum pulse energy of 200 mJ. Within the flowfields shown later, the laser sheet is projected from bottom to top. A multi-grid cross-correlation digital particle image velocimetry algorithm (Soria 1996) is used to analyze the image pairs. As a final method to remove erroneous vectors, a filter based on a Chauvenet criterion of 3 standard deviations was applied to the temporally stacked vector fields. Detected erroneous vectors were interpolated via a cubic function if they contained 3 good neighbors, else were otherwise excluded from statistical representation. Table 1 describes the specific parameters of the PIV component of this work.

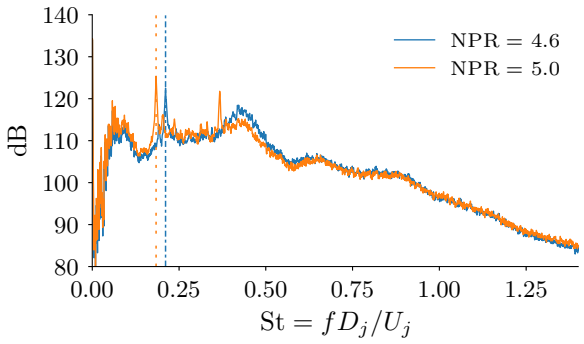

Fig. 2 Acoustic spectra measured for two comparison cases; NPR = 4.6 and NPR = 5.0

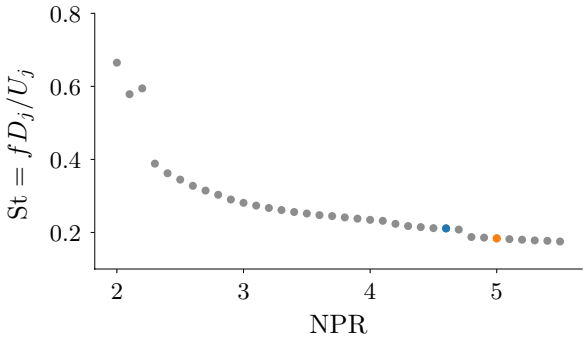

Fig. 3 Fundamental screech tone strouhal number for a variety of NPRs. The two cases examined using PIV are NPR = 4.6 (blue marker) and NPR = 5.0 (orange marker)

Table 1 PIV measurement parameters

Parameter	Value	Non-dimensional value
Field of view ($x \times y$)	129.3 × 86.2 mm	12.9 × 8.6 D
Laser inter-frame delay	0.9 µs	–
Initial PIV window size	128 × 128 px	0.255 × 0.255 D
Final PIV window size	12 × 12 px	0.032 × 0.032 D
Depth of field	0.66 mm	0.066 D
Vector spacing	8 px	0.016 D
Vector overlap	50 %	–
Resulting vector field ($x \times y$)	1092 × 726	–

Flow features in the jet core and surrounding near-field (standing-wave) are measurement objectives. This provided a challenging problem in maintaining a resolvable dynamic range of particle displacements for the PIV algorithm. A conservative estimate for minimum resolvable particle displacement is 0.1 px (Raffel et al. 2007; Willert et al. 2008). An inter-frame timing of 0.9 µs resulted in the smallest velocities in the jet near-field displacing 0.5 px and the largest in the jet core 30 px.

2.4 Uncertainty analysis

To quantify the uncertainty in measurement precision of the presented velocity fields, we apply the bootstrapping resampling technique (Benedict and Gould 1996). A bootstrap resample is implemented by drawing randomly with replacement n velocity fields, where n is the same number of snapshots in the original dataset. The desired statistic is then calculated on the resampled set and stored. The process was repeated $B = 1000$ times, typically $B > 100$ is sufficient. The standard deviation of the bootstrap resamples is examined to generate bounds on a confidence interval. The process is represented mathematically below. $\hat{\theta}_{\text{boot},k}$ is the sampled statistic, where $k = 1, 2, \ldots, B$ and $\hat{\theta}_{\text{boot},k}$ is the statistic of the kth resample. In this case, we examine the precision of the standard deviation estimates of the axial velocity.

$$\langle \hat{\theta}_{\text{boot}} \rangle = \frac{1}{B} \sum_{k=1}^{B} \hat{\theta}_{\text{boot},k} \tag{1}$$

where $\langle\rangle$ signifies the ensemble mean.

$$\text{var}(\hat{\theta})_{\text{boot}} = \frac{1}{B-1} \sum_{k=1}^{B} (\hat{\theta}_{\text{boot},k} - \langle \hat{\theta}_{\text{boot}} \rangle)^2 \tag{2}$$

The 95 % confidence interval is produced by examining $\hat{\theta} \pm 1.96 \left[\text{var}(\hat{\theta}_{\text{boot}})\right]^{\frac{1}{2}}$, where the 1.96 represents the normalized z score corresponding to the 95th percentile.

As arguments presented in Sect. 4 are largely predicated on an analysis of the fluctuating velocities, uncertainty estimates are provided for these quantities here. Figures 4 and 5 show contour maps of relative standard deviation uncertainty. The bootstrap quantity is represented as $\hat{\theta}_{\text{boot},k} = \langle u'_{x,k} u'_{x,k} \rangle^{\frac{1}{2}}$, where u_x is the axial velocity fluctuation quantity, and $\langle\rangle$ signifies the ensemble mean. The largest uncertainties are located in the region prior to the first shock. The external and inter-nozzle nearfield regions, however, indicate diminished uncertainty on the order of ±2%.

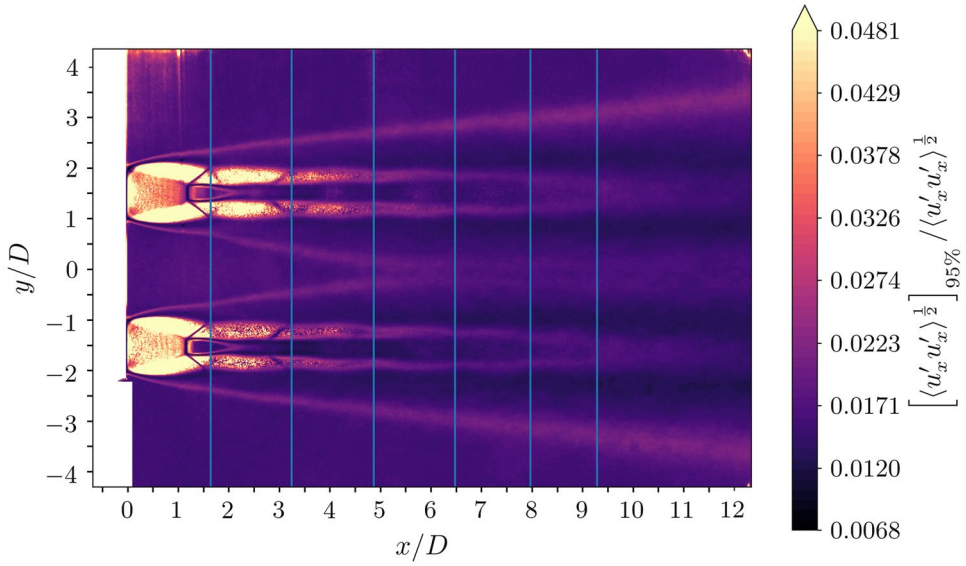

Fig. 4 Normalized 95 % confidence interval of the standard deviation of axial velocity for NPR = 4.6

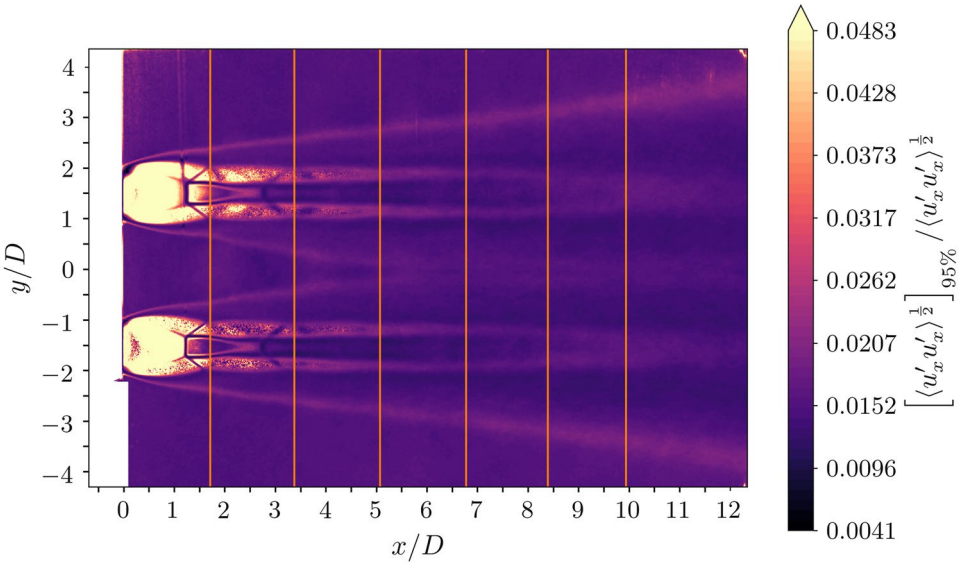

Fig. 5 Normalized 95 % confidence interval of the standard deviation of axial velocity for NPR = 5.0

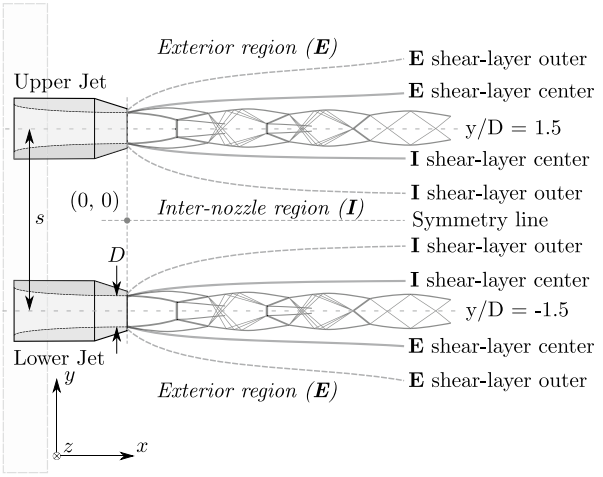

Fig. 6 Twin-jet schematic defining the regions used throughout this paper

3 Results

3.1 Twin-jet regions

Figure 6 shows the region and line convention used to describe quantities throughout this paper. The **I** (internozzle) region is located in the nearfield area between the jets. The **E** (exterior) region is located in the nearfield area outside the jets. The shear-layer center lines are defined by the axial line of maximum variance of velocity fluctuation ($\langle u'u'\rangle$), where u' is the velocity fluctuation vector, and $\langle\rangle$ signifies the ensemble mean. The shear-layer outer lines are defined by the method described surrounding Eq. (4) and is discussed in more detail there. The coordinate origin is located between the jets with the orientation convention in the bottom left corner of Fig. 6.

3.2 Mean flow fields

Mean axial velocity flow fields for jets operating at NPR = 4.6 and 5.0 are provided in Figs. 7 and 8 respectively. Overlaid is the **I** and **E** spatial extent of the shear-layer (calculated as described in Sect. 3.4). The white regions are masked in the analysis as they contained laser light reflections that could not be avoided.

The two cases are separated by a small change in NPR and based on a discrete change in screech acoustic frequency are assumed to correspond to a different coupling mode (Raman 1999; Alkislar et al. 2005). A quantitative examination of the mean axial velocity fields (Figs. 7, 8) reveals similar features between cases: Both flows are characterized by a large Mach disk at the first shock-cell and include a cellular shock-expansion pattern typical of strongly underexpanded jets. In neither case is the jet axial velocity or shock-cell pattern distorted towards each other as reported by Seiner et al. (1986) and Goparaju and Gaitonde (2017). The internozzle spacing was 1.9 in those cases, as opposed to 3.0 here. The maximum axial component of velocity is 1.87 U_e for NPR = 4.6 and 1.92 U_e for NPR = 5.0. The maximum velocities in both cases occur prior to the first shock-cell. Vertical lines indicate the shock reflection point locations, which were determined via changes in sign of the axial velocity gradient plotted at the jet boundary.

Due to the strong Mach disk and the incident grazing angle of the laser sheet, the planar laser sheet is diffracted after passing through the lower jet. A similar phenomenon was found and examined by Yoo et al. (2010). Consequently the upper jet receives less consistent illumination

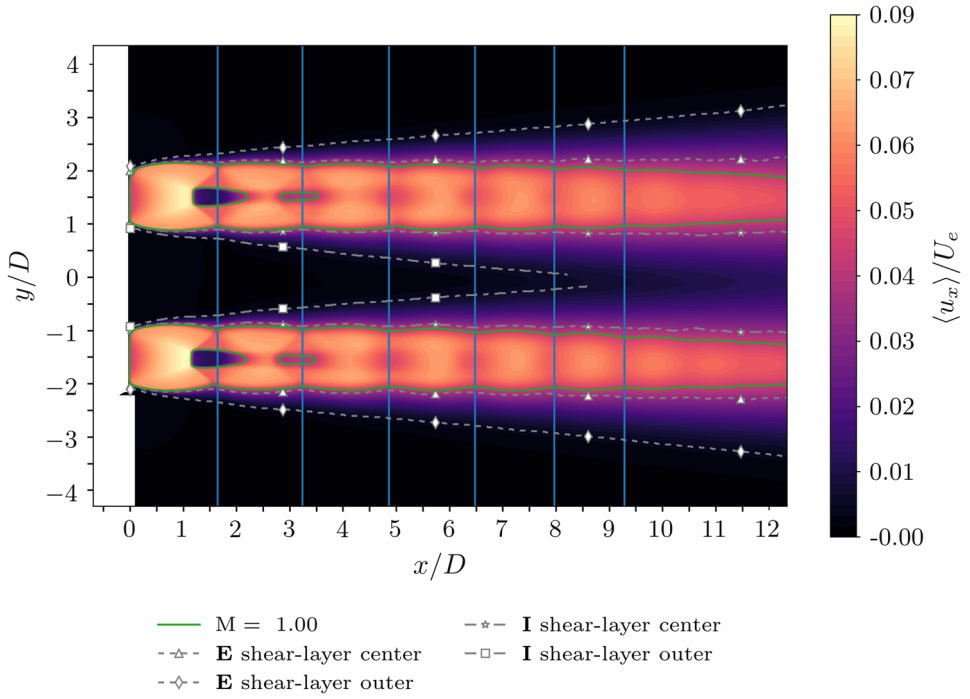

Fig. 7 Mean axial velocity for case NPR = 4.6 with shear layer and M = 1.0 (where the local Mach number is calculated assuming adiabatic dependence on measured velocity) contour overlaid. Vertical lines indicate shock reflection locations

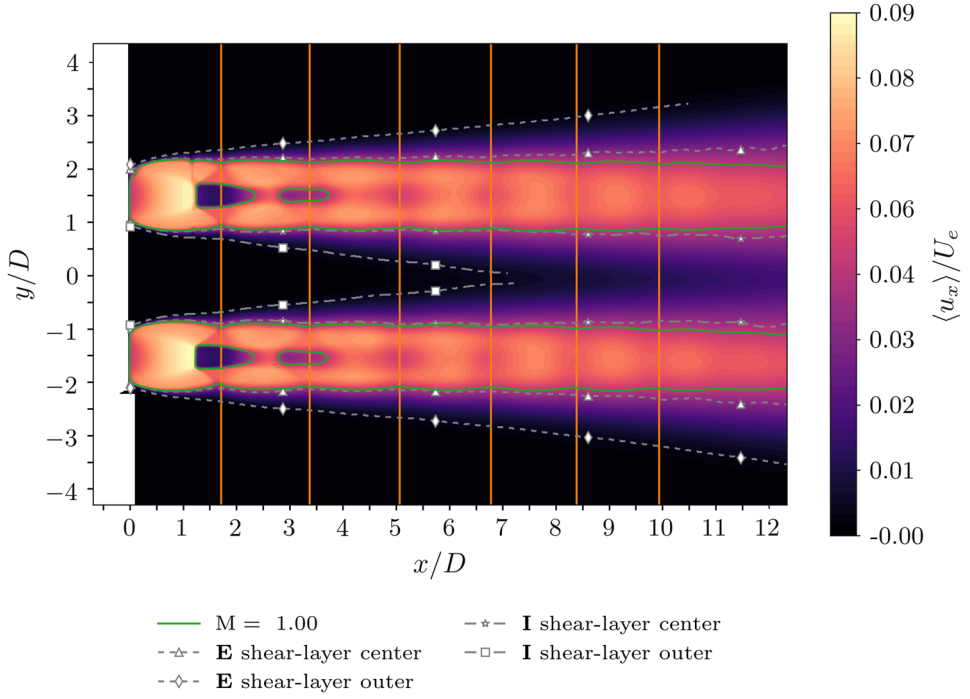

Fig. 8 Mean axial velocity for case NPR = 5.0 with shear layer and M = 1.0

due to the temporal perturbations on the Mach disk, which cause strong density gradients diffracting the light sheet from its intended path. The diffraction amount varies from snapshot to snapshot and produces an unintended inconsistency in measurement plane illumination. The effect of which reveals itself in the higher order statistics that are more susceptible to measurement noise. The flows are visually symmetric about the centerline, which for the purposes of observing differences between the two cases allows the generation of 'half–half' contour plots. The half–half plots consist of the lower jet from each field. To represent the upper half, the NPR = 5.0 case and y-axis are mirrored vertically hence the negative y axis scale in the top half.

The half–half contour of transverse (spanwise) velocity is shown in Fig. 9. The oscillating pattern of positive and negative velocity is the result of the turning angle produced by oblique shocks in the cascading shock structure.

Half–half contours of out-of-plane vorticity (ω_z) are shown in Fig. 10. The sliplines associated with the Mach disks can be observed emanating at the Mach disk edges and continue to extend downstream. The Mach disk diameter is larger in the NPR = 5.0 case. The steep gradient of vorticity along the jet boundary provides a quantitative estimate of the shear-layer extent.

Profiles of axial velocity are provided in Fig. 11. For both cases, the upper and lower jet profiles are nearly identical. The centerline velocity oscillation due to the shock-cell structure has not ended within the measurement domain (greater than $x/D \approx 11$).

The local Mach number has been inferred using the procedure where only velocity information is available (André et al. 2014). The calculation assumes that the total temperature is uniform within the jet and the local Mach number is purely a function of measured velocity. The local Mach number is calculated using Eq. (3).

$$M = \left[\frac{u^2}{\gamma R T_0 - u^2(\gamma - 1)/2}\right]^{\frac{1}{2}} \tag{3}$$

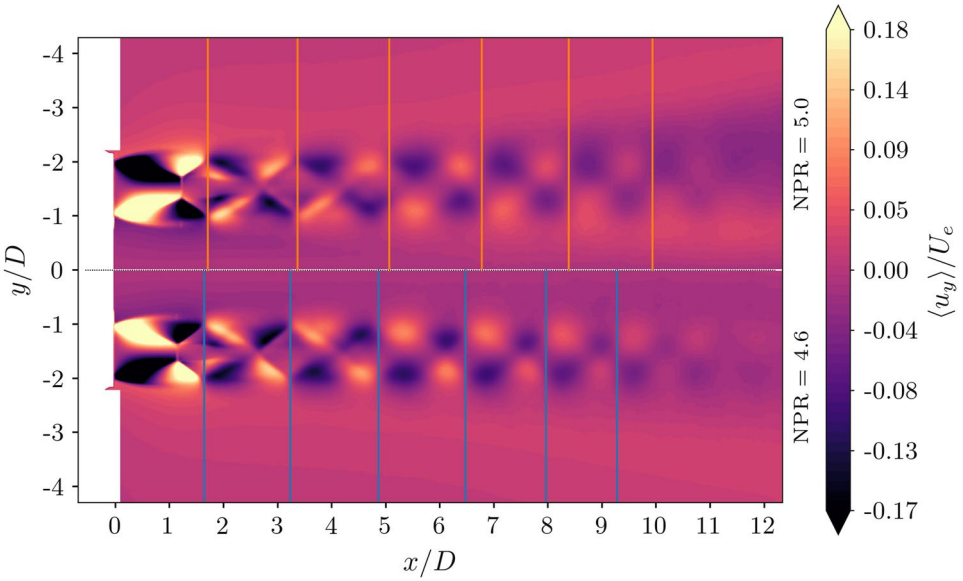

Fig. 9 Mean transverse velocity for case NPR = 4.6 (bottom half) and NPR = 5.0 (top half, reflected vertically). Vertical bars indicate shock reflection locations for each case, respectively

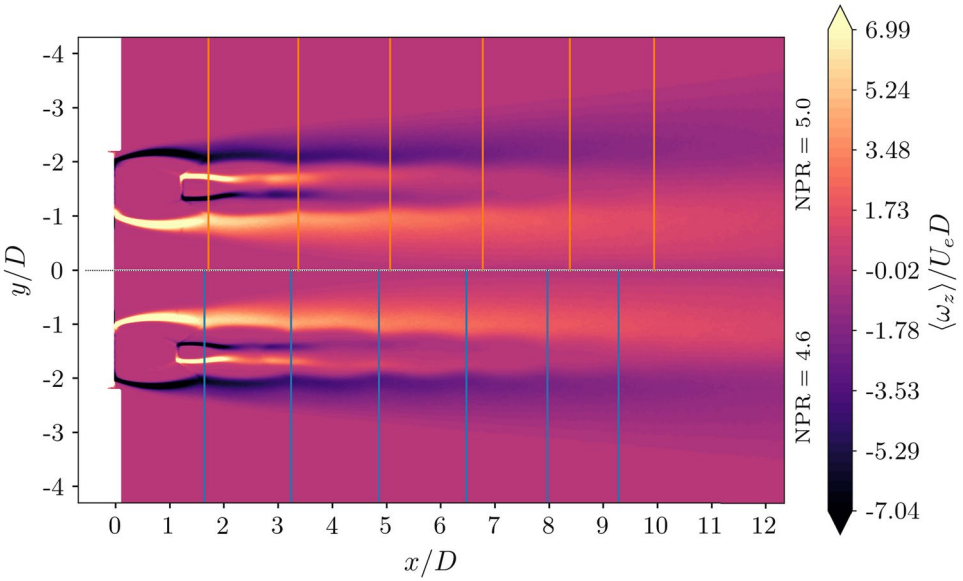

Fig. 10 Mean out-of-plane vorticity for case NPR = 4.6 (bottom half) and NPR = 5.0 (top half). Vertical bars indicate shock reflection locations for each case respectively

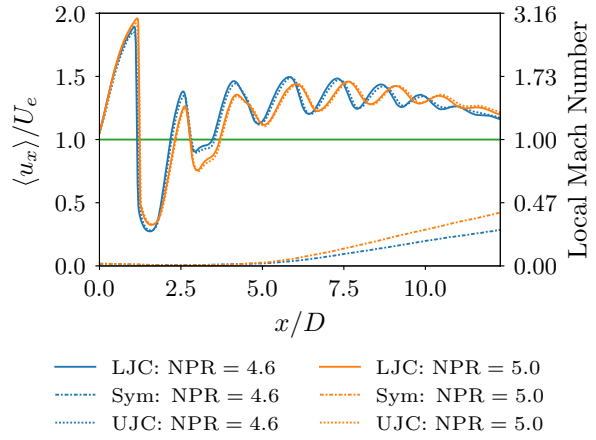

Fig. 11 Mean axial velocity along symmetry and jet-center profiles. LJC, lower jet center; UJC, upper jet center; Sym, sline

where M is the estimated local Mach number, u is the measured velocity, $T_0 = 298$ K is the total temperature, $\gamma = 1.4$, $R = 287.06\,\mathrm{J\,kg^{-1}\,K^{-1}}$.

Within the PIV flowfields, the calculation of the local Mach number allows the separation of subsonic and supersonic components of the flow, such as downstream of Mach disks within the supersonic jet core.

The $M = 1.0$ local Mach number profile is provided in Figs. 7, 8, and 11. The resulting relationship between velocity and local Mach number is strongly non-linear, as demonstrated by the parallel y-axes in Fig. 11.

In both cases, evidence for Mach disks occurring in the first two shock-cells is provided by contours and profiles of local Mach number. Figure 11 shows locally subsonic flow within the supersonic structure at both $x/D \approx 1.8$ and 3.2. The low region of axial velocity at $x/D \approx 3.8$ corresponds to this subsonic flow pocket generated by the second Mach disk.

The standard deviation of the axial velocity fluctuation is provided in Fig. 12. The velocity artifact in the shear layer at $x/D \approx 1.0$, $y/D \approx -1.0$ is the result of laser light diffraction caused by the first Mach disk. Axial fluctuations generated by the shocks are minimal and are only marginally stronger in the transverse direction (not shown here). Similar fluctuations have been shown to be likely non-physical and are a PIV artifact associated with steep and discontinuous velocity gradients (Mitchell et al. 2011). The growth of the shear-layer can be observed at the jet edges via increased fluctuation level downstream.

3.3 Flow field symmetry

Both nozzles receive flow from the same plenum chamber and hence are at an identical NPR. Axial profiles of axial velocity (u_x) in Fig. 11 show that the mean velocity between the two jets' centerlines (upper jet center and lower jet center) show strong symmetry.

Figure 13 shows the axial standard deviation along the respective jet centerlines. In both cases, the centerlines of both jets follow very similar trends. Later in this work cross-plane profiles are examined (e.g., Fig. 16). In those profiles, the jets show different levels of peak standard deviation in the shear-layers. The authors reason that this is due to attenuation of the light sheet, which travels from the bottom of the measurement domain to the top and the effect of strong temporally dependent refractive gradients, which provide less consistent illumination of the upper jet. With confidence of both jet flows being symmetric and the intention

Fig. 12 Standard deviation of axial velocity for lower jet in both cases

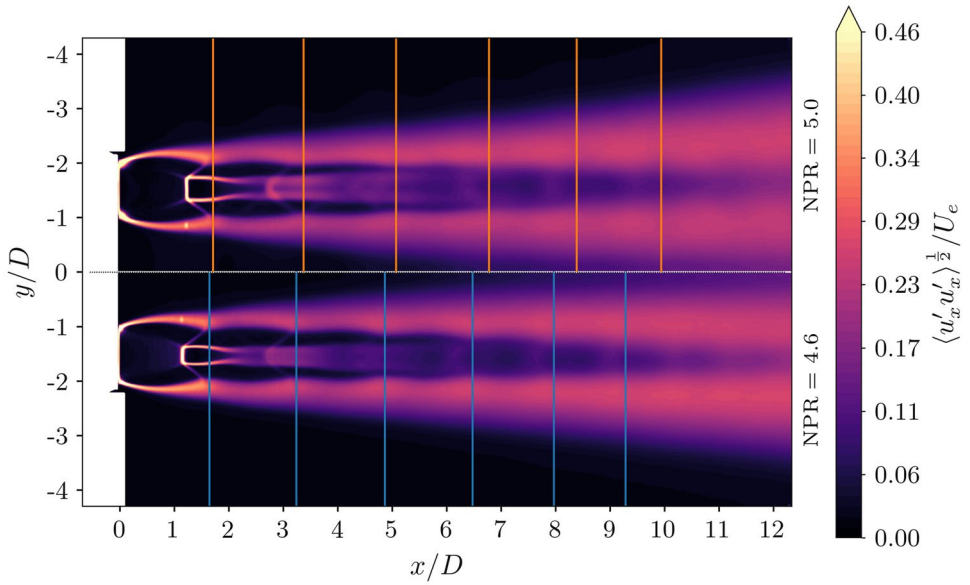

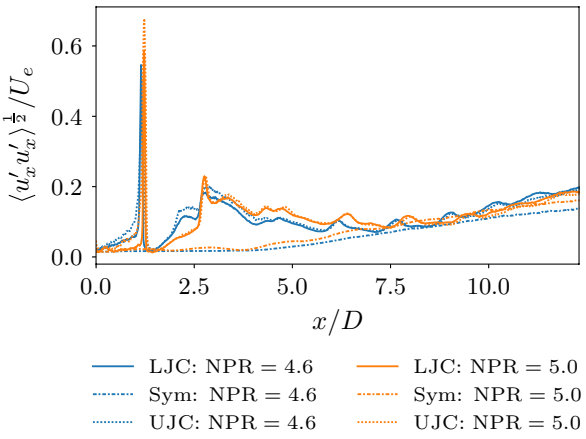

Fig. 13 Standard deviation of axial velocity along the center lines of both jets in both cases. UJC, upper jet centerline; LJC, lower jet centerline; Sym, symmetry line

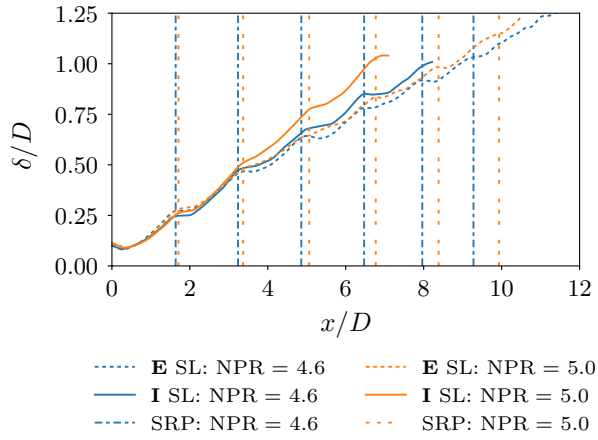

Fig. 14 Averaged shear-layer thickness estimate. δ/D indicates the non-dimensional thickness with respect to nozzle diameter. SL and SRP refer to shear-layer and shock reflection point, respectively

of providing low measurement noise, only statistics relating to the lower jet are presented here on.

3.4 Shear-layer

Shear-layer thickness is calculated for each jet for both shear-layers facing the external jet near-field (denoted as **E** in figures) and the interior inter-nozzle region (denoted **I**). Refer to Fig. 6 for a graphical representation of the respective profiles. Shear-layer thickness is estimated here as a function of axial position. The thickness, defined by Eq. (4), is estimated as the spanwise distance between maximum axial velocity magnitude fluctuation amplitude to a 10 % threshold level of the respective maximum.

$$\delta(x) = y\left(\max\left[\langle u'_x u'_x \rangle^{\frac{1}{2}}\right]\right) - y\left(0.1 \max\left[\langle u'_x u'_x \rangle^{\frac{1}{2}}\right]\right) \quad (4)$$

The velocity magnitude variance forms a profile as a function of axial distance and is denoted as the shear-layer center. The corresponding 10 % threshold level also forms a profile and is denoted as the shear-layer outer. Refer to Figs. 7 and 8 for a graphical representation of the different shear-layer profiles. The 10 % threshold has been used in many other studies as a relative cutoff to determine thickness where only velocity information (as PIV typically lacks density information) is known (Alkislar et al. 2003; Tan et al. 2017; André et al. 2014; Weightman et al. 2016). The two **I** and two **E** external jet shear-layer thicknesses were found to be symmetrical and the average thicknesses (between upper and lower jet) are provided in Fig. 14.

Beyond the second shock reflection point, the growth rates in the **I** regions are larger for both cases. The **E** shear-layer thicknesses follow a more consistent trend with a lower growth rate. Cross-plane velocity profiles are provided in Fig. 15 for reference. Along the nozzle lipline of the jets, both **I** and **E** maximum velocities are similar until $x/D \approx 8$ where the **I** maximum velocity appears to decay slower.

3.5 Jet merge point

Determining where the two jets first interact in the inter-nozzle region may be useful in the deduction of coupling mechanisms. However, the 'first point of interaction' between the individual jets is typically not well defined, therefore, a discussion of different qualitative and quantitative measures are provided here. The merging point is likely to be most dependent on jet spacing (s/D). For jets with a spacing of $s/D = 2$, it has been reported that the merging point occurs between 5 and 15 D downstream depending on jet Mach number (Lin and Sheu 1991; Moustafa 1994; Goparaju and Gaitonde 2017). Using the ensemble statistics, we consider only the mean interaction point here.

3.5.1 Extrapolation of the outer shear-layers

When the **I** shear-layer edge reaches the centerline could be considered a measure of the first point of hydrodynamic interaction. The shear-layer growth in the **I** region follows an approximately linear trend for both cases, shown by Fig. 14, and if extrapolated provides an intersection point of $x/D = 8.5,\ 7.5$ for NPR $= 4.6,\ 5.0$ respectively. The edge of the shear-layer is, however, defined by an arbitrary cutoff, in this case 10 % of the respective axial maximum. Alternative methods for determining the shear-layer edge are explored by (André et al. 2014) but are demonstrated there as means for *relative* comparison.

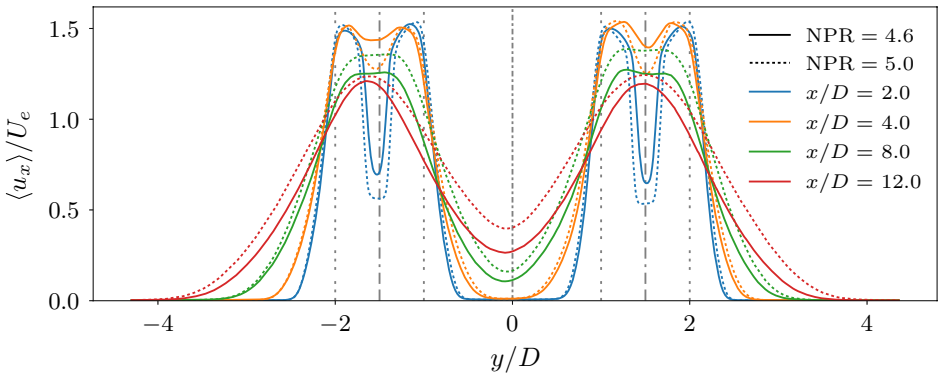

Fig. 15 Axial cross plane mean velocity profiles farther down stream where the shear-layer has become developed. Dash dot dash vertical line indicates symmetry line at $y/D = 0$. Dash dash dot lines indicates nozzle center lines at $y/D = \pm 1.5$. Dot dot dot lines indicates nozzle lip lines at $y/D = -2.0, -1.0, 1.0$, and 2.0

3.5.2 Detection of shear-layer induced velocity fluctuations advancing on the quiescent fluid

Figure 16 shows profiles of spanwise velocity fluctuation amplitude for NPR = 4.6. The flat region of velocity fluctuation within the **I** region (between $y/D \approx \pm 0.5$) is at the background quiescent fluid level for $x/D = 2.0$. Moving downstream, one can observe that the shoulders of the quiescent fluctuation level become enveloped by the shear layer edge. Finally, between $x/D = 4.0$ to 5.0, the expanding velocity fluctuations reach the center ($y/D = 0$) and the local minimum lifts from the quiescent fluid background fluctuation level. The authors suggest that this is a method for determining the interaction location for the hydrodynamic structures.

3.5.3 Detection of the edge of coherent vortical structures

Fluctuation amplitude measures, however, do not consider the coupling modality as a function of time and are in a sense the time-averaged fluctuation level. The time-averaged component does not consider whether the two jets were simultaneously interacting, or simply occupied the spatial location with a turbulent structure at a particular point in time. To shed more light on the first point of hydrodynamic interaction, contours of the skewness of the axial velocity component are calculated and shown in Fig. 17. The skewness metric highlights and provides a qualitative indication of the shear-layer edge with positive value. CVSs that propagate along the jet shear-layer are known to play a major role in supersonic twin-jet coupling (Knast et al. 2018). Positive skewness in the shear-layer has been linked to the periodic passing of faster moving CVSs (Sadr and Klewicki 2003; Bogey et al. 2012; Edgington-Mitchell et al. 2014). Positive skewness in the edge of the **I** shear-layer can be observed in the half–half skewness contour (Fig. 17). The slightly positive region offset but running adjacent to the interior shear-layer propagates away from the respective jet centerline. It strikes and becomes parallel to the symmetry line at $x/D \approx 4$ for NPR = 4.6 ($x/D \approx 4.5$ for NPR = 5.0). The authors suggest that the coherent structures cease to continue spreading once reaching the symmetry line and instead turn and become parallel with the jets. Their growth is inhibited by the low velocity gradient compared to the external quiescent fluid downstream of this point.

3.6 Inter-nozzle mixing

Strong inter-nozzle mixing due to the interaction of the two jets is often observed in twin-jet studies (Alkislar et al. 2003; Goparaju and Gaitonde 2017; Gao et al. 2016; Seiner et al. 1986). Mixing is often measured with reference to scalar transport. As only randomly sampled velocity field snapshots were captured here, the authors will examine turbulent kinetic energy as a proxy to scalar

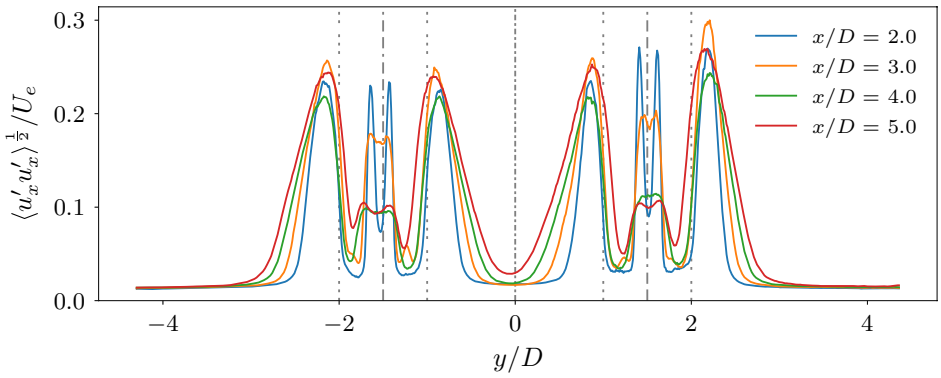

Fig. 16 Axial cross plane fluctuating velocity profiles, NPR = 4.6. Dash dot dash vertical line indicates symmetry plane at $y/D = 0$. Dash dash dot lines indicates nozzle center lines at $y/D = \pm 1.5$. Dot dot dot lines indicates nozzle lip lines at $y/D = -2.0, -1.0, 1.0, 2.0$

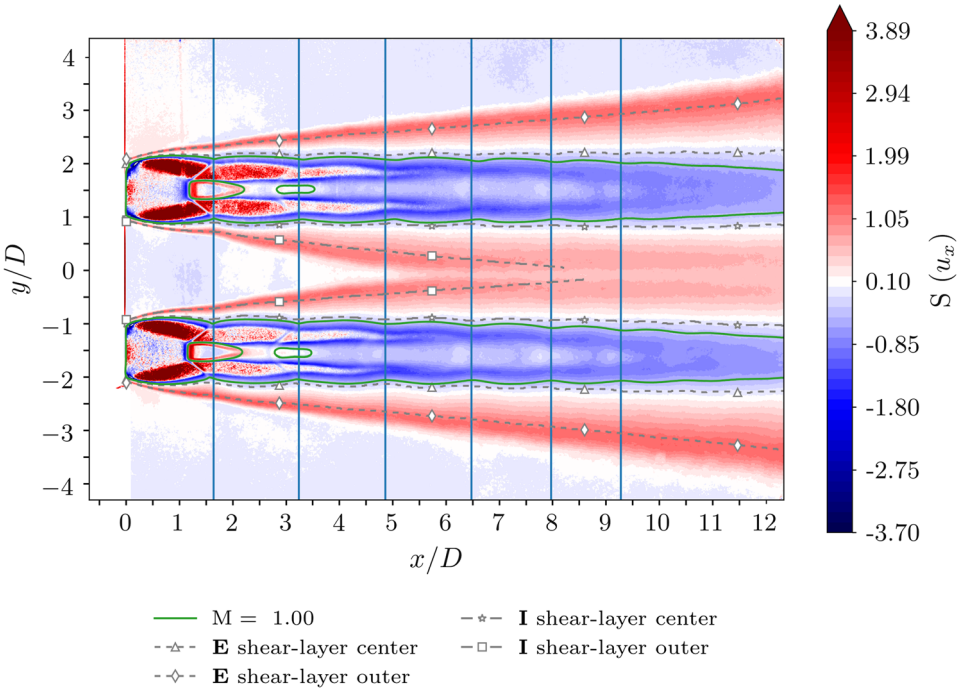

Fig. 17 Skewness contour of axial velocity: NPR = 4.6. Shear-layer edges and sonic line overlaid

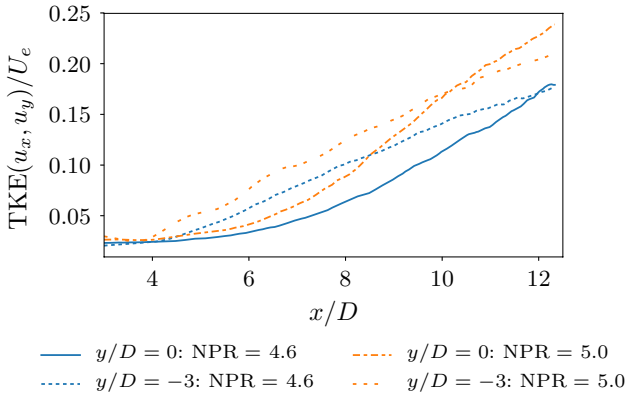

Fig. 18 Equidistant axial profiles of specific turbulent kinetic energy (TKE) for the symmetry line and lower jet exterior. Mildly smoothed for clarity

transport to infer mixing. Figure 18 provides a comparison of the specific turbulent kinetic energy (TKE) for the symmetry line ($y/D = 0$) and an equivalent axial line 1 D from the exterior of the nozzle lip ($y/D = -3$). The figure shows that in both cases the TKE is lower in the inter-nozzle region even after the point of first interaction. At $x/D \approx 10$ the inter-nozzle region surpasses the **E** region, showing a steeper gradient and subsequently higher levels of TKE. The larger levels of TKE downstream is likely linked to strong jet coupling motion, which is well developed by $x/D \approx 10$. The authors suggest that this is due to the lower velocity gradients present in the inter-nozzle shear-layers once the jets have merged, with comparison to the external shear-layers.

3.7 Second-order spatial correlations

3.7.1 Examination of modal behavior in the velocity field

To assess the spatial structure of the coupling modes, second-order spatial correlations of instantaneous velocity fields are performed. The coefficient of the second order spatial velocity correlation is stated in Eq. (5).

$$R_{ij}(\boldsymbol{x}, \xi) = \frac{\langle u_i'(\boldsymbol{x}, t) u_j'(\boldsymbol{x} + \xi, t) \rangle}{\sigma_i(\boldsymbol{x}) \sigma_j(\boldsymbol{x} + \xi)}. \tag{5}$$

The subscripts i and j indicate velocity components and u' signifies the velocity fluctuation quantity, $\boldsymbol{x} = (x, y)$ is the spatial reference point vector, ξ is the spatial separation distance, t is the time/index of the snapshot, σ is the standard deviation. Holding $\boldsymbol{x}$ fixed and varying ξ across the entire field, correlation maps can be made. Within flows that contain a single significant periodic time component, the correlation maps can be used to reveal the large scale modal behavior. Spatial velocity correlations have been examined in other jet configurations, particularly single jets (André et al. 2014; Tan et al. 2017; Fleury et al. 2008).

The axial-axial velocity correlation is represented by R_{11} (Figs. 19, 20) and transverse–transverse velocity represented by R_{22} (Figs. 21, 22). The intersection of the red lines indicates the correlation reference point, $\boldsymbol{x}$. The black

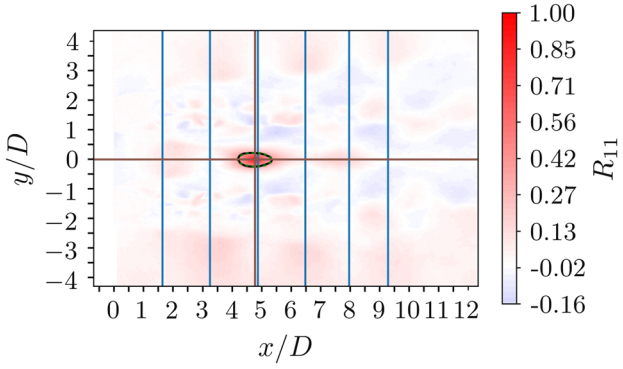

Fig. 19 R_{11}, Axial–axial velocity spatial correlation of NPR = 4.6. Correlation reference point on the symmetry line

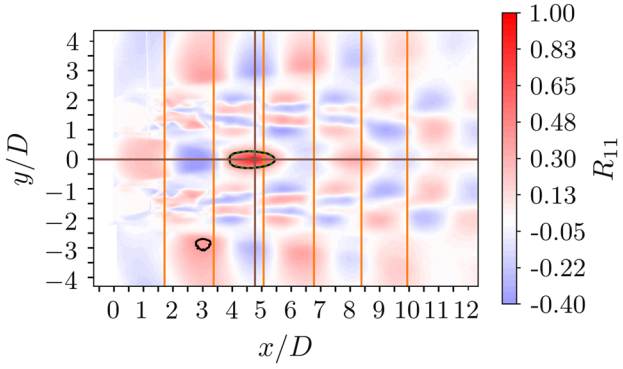

Fig. 20 R_{11}, Axial–axial velocity spatial correlation of NPR = 5.0. Correlation reference point on the symmetry line. Black contour surrounding the selection point shows the 1/e cutoff. In this case there is also a correlated region above 1/e at approximately $x/D, y/D = 3, -3$

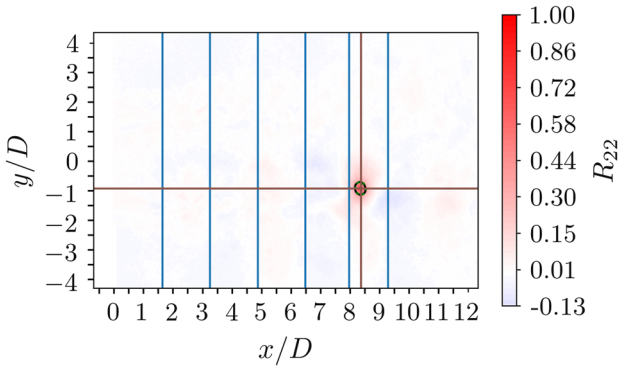

Fig. 21 R_{22}, transverse-transverse velocity spatial correlation of NPR = 4.6. Correlation reference point on the line of maximum velocity fluctuation

contour shows the $1/e \approx 0.368$ cutoff, which was selected as the bound for the integral length scales that are investigated in Sect. 3.8.

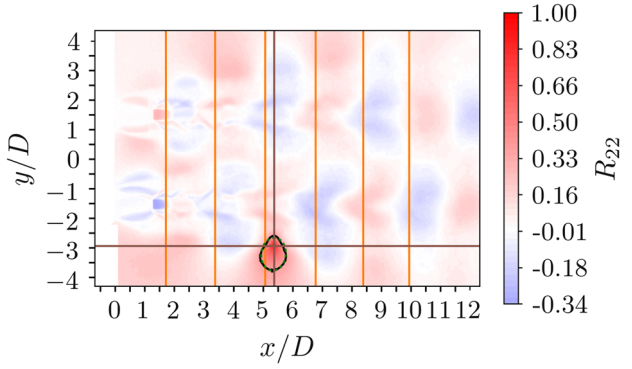

Fig. 22 R_{22} spatial correlation of NPR = 5.0. Correlation reference point on the line of maximum velocity fluctuation

For correlation maps corresponding to R_{11} (Figs. 19, 20), the reference point $(x/D = 4.76, y/D = 0)$ was chosen as it is a location where strong periodic fluctuations are felt. This provides maximum correlation contrast to the rest of the field to indicate the shape of the underlying mode. Correlation reference points along the symmetry line were found to reveal modal structure within the entire field. A variety of other points were examined, which showed the same modal structure, but with less contrast. Weak modal correlation is observed for NPR = 4.6 and stronger correlation is observed for NPR = 5.0 for both R_{11} and R_{22} correlation maps.

The correlation maps for the R_{22} velocity component are presented in Figs. 21 and 22. The opposing banded structure of the NPR = 5.0 R_{22} correlation in Fig. 22 indicates a symmetric coupling mode about the symmetry plane. The R_{22} correlation for NPR = 4.6 in Fig. 21 shows a very weak but similar pattern of streamwise modulation. No other reference point was found that showed greater banding contrast. The R_{11} and R_{22} modulation wavelength was found to be identical.

3.8 Correlation integral length scales

Integral length scales (ILS) have been calculated for the R_{11} and R_{22} correlations. The ILS is evaluated via the following method

$$L_{ij}^{k}(\boldsymbol{x}) = \frac{1}{2}\int_{0}^{\infty} R_{ij}(\boldsymbol{x}, \xi_k)\mathrm{d}\xi_k. \tag{6}$$

L_{ij}^{k} represents the ILS of the correlation R_{ij} and k indicates the ILS direction (x or y). The integral cutoff length is chosen to extend from the reference point location forward to the $R_{ij} = 1/e \approx 0.368$ limit. This level has been found to be a robust limit for the ILS estimation (Nicolaides et al. 2004; Tritton 1977). The 1/e integral length cutoff does consistently lead to underestimation of the true value compared to

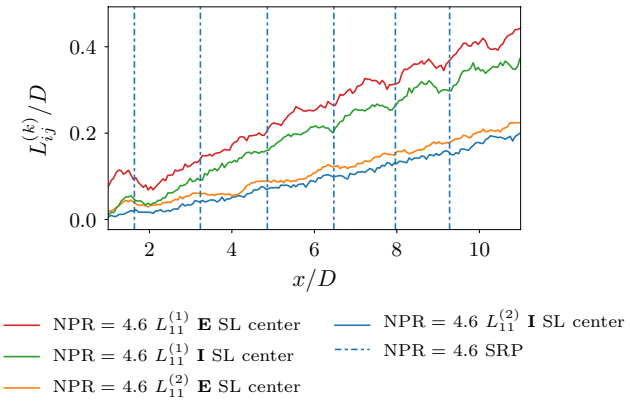

Fig. 23 L_{11} integral length scales. SL, shear-Layer; SRP shock reflection point, indicated by the vertical lines

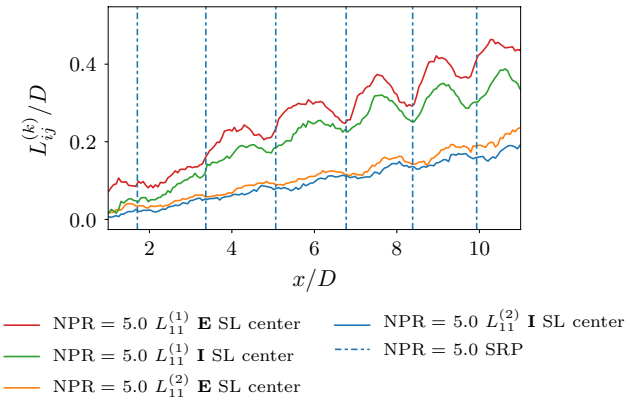

Fig. 24 L_{11} integral length scales. SL, shear-layer, SRP shock reflection point, indicated by the vertical lines

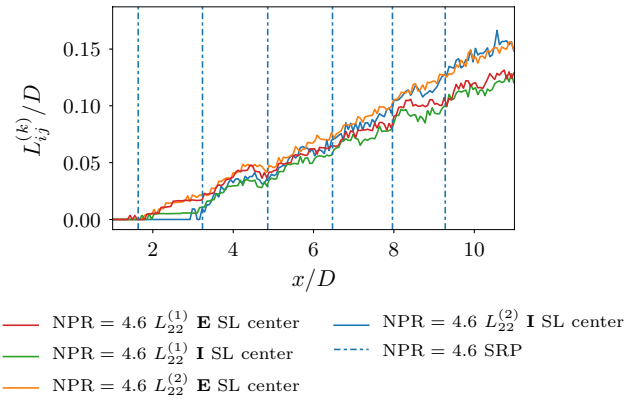

Fig. 25 L_{22} integral length scales. SL, shear-layer, SRP, shock reflection point, indicated by the vertical lines

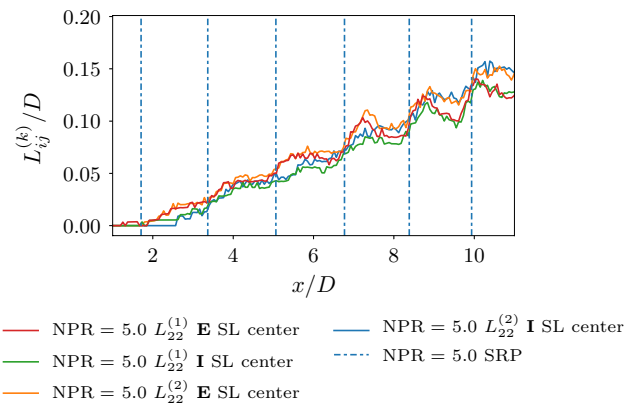

Fig. 26 L_{22} integral length scales. SL, shear-layer, SRP, shock reflection point, indicated by the vertical lines

full domain integration. However, the nature of free-shear flow problems, especially those that contain shocks, do not lend themselves to full domain integration.

The L_{11} ILS along the internal (**I**) and external (**E**) shear-layer center lines are examined first in Figs. 23 and 24. The shear-layer centerline was defined earlier as the axial line of maximum axial velocity fluctuation within the respective jet shear-layer. Figures 23 and 24 shows the ILS value grouped by their directions ($k = 1, k = 2$). Within the L_{11}^1 group, the **I** ILS is consistently larger than **E** for both NPR values. This is consistent with the shear-layer thickness where **I** was larger than **E**. Strong spatial modulation of the ILS in the axial direction is observed in the NPR = 5.0 case. The same modulation is observed only far downstream for the NPR = 4.6 case.

The L_{22} ILS are shown in Figs. 25 and 26 for NPR = 4.6 and 5.0, respectively. The scales are smaller in magnitude compared to the L_{11} components. The correlation contours are a more rounded shape and as a result the $k = 1$ and $k = 2$ contours fall almost on top of one another as the integrated shape and functions are similar. Close inspection reveals that the ILS modulation with varying axial position exists for the NPR = 5.0 case only.

4 Discussion

4.1 Standing-wave

The standing-wave has been measured using traversed microphones (Panda 1999) and schlieren photography (Edgington-Mitchell et al. 2015). However, in the twin-jet flow fields captured here, the standing-wave signature is visible in the velocity data. The standard deviation of axial velocity for both cases was presented in Fig. 12. The same figure, now with a logarithmic scale, is used in Fig. 27 to simultaneously resolve the jet core and smaller fluctuations due to the standing-wave.

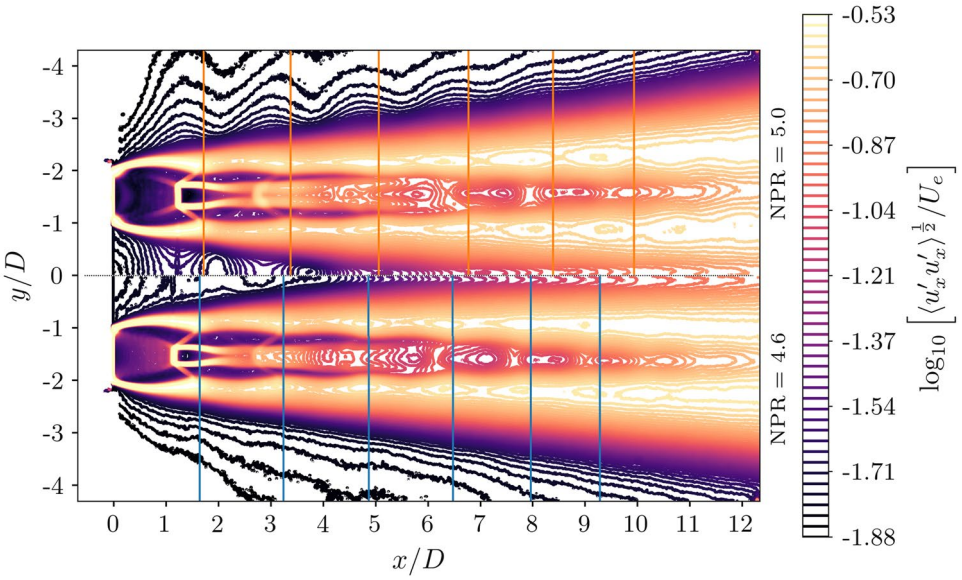

Fig. 27 Half–half contour lines of axial velocity standard deviation with logarithmic scale for visibility purposes. Standing-wave is visible in NPR = 5.0 half only as lobed structures adjacent to the jet

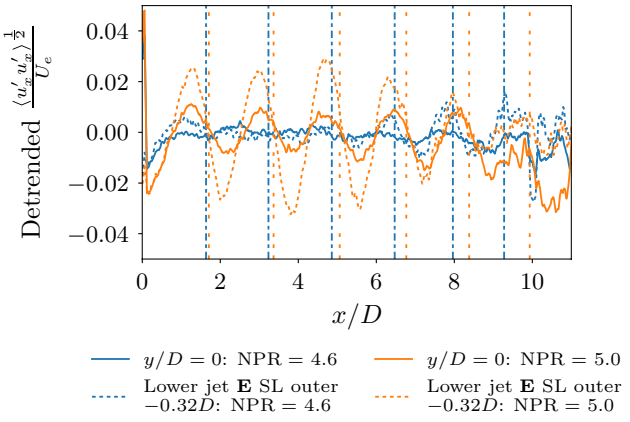

Fig. 28 Detrended standard deviation of axial velocity showing standing-wave modulation. SL, shear-layer. See text for explanation of **E** shear-layer profile and label

The standing-wave structure is observed in the NPR = 5.0 case as lobes of higher fluctuation in axial velocity and is visible in both the **I** and **E** regions. No modulation is apparent in the transverse velocity fluctuations. This implies that the waves generated by hydrodynamic coherent structures and emitted acoustic waves travel predominantly in the axial direction. This provides evidence that the features observed are indeed associated with the standing-wave.

For clarity, Fig. 28 presents axial profiles of fluctuating axial velocity for the jets' symmetry line and **E** regions. These profiles have been detrended to remove the monotonic increase in velocity fluctuations associated with shear-layer growth, which dominated the sinusoidal modulation due to the standing-wave. The detrending was accomplished using a 1D Gaussian filter (mean calculated over 200 samples, standard deviation of 10) which was used to remove the low frequency monotonic rise in the data for clarity. Two profiles are selected to demonstrate the fluctuation modulation; the symmetry line $y/D = 0$ and the lower jet **E** field. For clarity, the **E** shear-layer outer $-0.32D$ is presented as it has lower baseline fluctuations and provides a clear view of the modulated signal.

In the NPR = 5.0 case, the fluctuation modulation pattern produced by the standing-wave is larger in the **I** region. The standing-wave strength is linked to both the amplitude of the upstream propagating acoustic waves and the downstream convecting hydrodynamic waves. It has been previously demonstrated that for symmetric coupling modes, the overall sound pressure level in the interior region was greater than the sum of two non-interacting single jets (Seiner et al. 1986; Shaw 1990). Morris predicted that the increased pressure fluctuations caused by passing hydrodynamic structures drops off exponentially with increasing distance from the shear-layer (Morris 1977). It is suggested in the present work that the amplitude discrepancy between the interior and exterior regions derives from two factors. Firstly, the stronger acoustic field present in the interior region due to the synchronized summation of both jets' acoustic waves should result in a stronger standing-wave as suggested by Seiner (Seiner et al. 1986). Secondly, the difficulty of defining a consistent measurement location between the inner and outer jet edges may hinder direct comparison. Case NPR = 4.6 shows no repeatable standing-wave modulation in the axial velocity.

The standing-wave structure revealed by detrended axial velocity fluctuation (provided earlier) and nodal structure in the inter-nozzle regions of the R_{11} spatial correlation overlap. Several conclusions can be drawn from this finding. Firstly, the modal behavior in the axial direction is associated with the standing-wave and highlights nodes within the **I** and **E**

near-field regions surrounding the jets. Secondly, the standing-wave modulates both the turbulence intensity of the fluctuation amplitude (provided earlier) and the coherence of the turbulence in this region. Thirdly, the R_{11} correlation pattern reveals a clear symmetric mode within the jet near-field for NPR = 5.0 and a weaker symmetric mode for NPR = 4.6. Within the jet cores, however, the NPR = 5.0 shows symmetric coherence, which is considered to be modulated at the hydrodynamic structure length scale. The NPR = 4.6 R_{11} correlation, by contrast, does not show any discernible structure within the jet core.

The analysis has not yet provided a clear indication relating the jump in screech tone to an expected change in modal behavior as observed in other twin-jet studies (Raman 1999; Alkislar et al. 2003; Raman et al. 2012). Both tones have similar screech tone strength (NPR = 4.6: 122.5 dB and 5.0: 125 dB) and similar base flow as shown in the mean velocity fields earlier. It appears that both cases exhibit a symmetric mode, albeit the NPR = 4.6 case seems to be significantly weaker. When examining the standing-wave derived directly from the streamwise velocity fluctuations, a strong modulation was again seen for the NPR = 5.0 case, weak to no modulation was seen for the NPR = 4.6 case. The authors hope to investigate this behavior in the future and leave a number of possible explanations here to prompt further discussion. It may be that NPR = 4.6 is particularly unstable and switches between modes on a temporal basis. This would produce spatial averaging between standing-wave patterns and blur the underlying standing-wave structure. With the temporal switching hypothesis, although no standing-wave is readily observed in the data this does not mean that one (or several) does not exist. Alternatively, the coupling mode could be out-of-plane [as observed by Raman in high aspect ratio rectangular jets (Raman 1998)] and unobservable with the planar PIV technique used here. This could explain the existence of the weak symmetric modal pattern. Perhaps within the twin-jet configuration, screech tone frequency jumps do not necessarily correspond to changes in coupling modes. This could imply that the two happen independently. Or it may be that the NPR = 4.6 case does indeed have a symmetric coupling mode like the higher NPR = 5.0 case and that the change in acoustic tone is caused by a change in screech feedback mechanism. A similar conclusion was explored by Edgington-Mitchell et al. (2015).

4.2 Evidence for a screech based coupling mechanism

The mechanisms that drive the twin-jet coupling are currently unclear (Raman et al. 2012). In supersonic single jets, the screech feedback loop is understood to provide closure and induce strong modal behavior (Raman 1998). Whether coupling of supersonic shock containing twin-jets is driven primarily hydrodynamically by an unstable base flow as demonstrated by Morris (1990), by an analogous screech based mechanism, or a combination of the two, remains unknown. If evidence to demonstrate that screech behavior is present in the flow fields attained here then support for screech based coupling mechanisms can be inferred.

Panda provided the analysis and derivation of a relation that links the standing-wavelength (λ_{sw}), the screech acoustic wavelength (λ_s), and the hydrodynamic wavelength (λ_h) in a screeching single jet (Panda 1999).

$$\frac{1}{\lambda_{sw}} = \frac{1}{\lambda_s} + \frac{1}{\lambda_h} \tag{7}$$

Assuming acoustic propagation speeds are constant in the near-field of the jets, one can calculate approximate Strouhal numbers that can be compared to measured frequencies from acoustic analysis. The relation has been applied to singular axisymmetric (Singh and Chatterjee 2007) and elliptical jets (Edgington-Mitchell et al. 2015), which links jet modality to screech based mechanisms. Here, the authors apply the relation to the twin-jet coupling system.

The average standing wavelength (λ_{sw}) was measured in Sect. 4.1 via averaging the distance between crests of standard deviation axially along the jet edge and symmetry line. It is provided in Table 2. The average hydrodynamic wavelength (λ_h) is measured using the same procedure, but taking crests from the respective R_{11} correlation maps. By substituting the measured λ_{sw} and λ_h into Eq. (7), close agreement of the predicted screech tone to the measured acoustic tone is found for the NPR = 5.0 case.

Table 2 Screech metrics

	NPR	
	4.6	5.0
Screech Strouhal number	0.22	0.19
Screech λ_s, ($a \approx 345$ m/s, $T = 298$ K)	3.4 D	3.9 D
Avg. standing wavelength (λ_{sw}) ($\pm$ 95 % conf.)	–	1.7 ± 0.12 D
Avg. hydrodynamic wavelength (λ_h) ($\pm$ 95 % conf.)	3.0 ± 0.18 D	3.2 ± 0.15 D
Estimated screech wavelength	–	3.7 ± 0.17 D
Nominal $\lambda_{s_{est.}} / \lambda_{s_{meas.}}$ relative error	–	6.1 ± 17.1 %

The close agreement with the predicted acoustic tone provides evidence that Panda's relation for screech is applicable to twin-jets where the coupling mode is in-plane and the standing-wave can be readily measured. It also indicates that it is a screech feedback cycle that is active and is potentially contributing to the coupling behavior.

4.3 Turbulence modulation within the flow

Turbulent fluctuations are major contributors to noise production (Tam 1995). Insight into mechanisms of production is useful for their mitigation. Tan has shown that the ILS adjacent and parallel to the potential core are strongly modulated (Tan et al. 2017). Here, the effect of the shock structure and standing-wave on both the modulation of turbulence intensity and coherence is able to be determined. Turbulence intensity refers to the measure of axial velocity standard deviation, $\langle u'_x u'_x \rangle^{1/2}$. Turbulent coherence has its meaning derived from the velocity correlation function and the associated length scale over which turbulence remains largely similar, evaluated here as the ILS.

Figures 29 presents the case with no standing-wave comparing the detrended axial velocity standard deviation and detrended integral length scales. Figure 30 shows the case where the standing-wave is present. From these figures, in the region where we would expect the standing-wave to dominate the modulation of the turbulent features (**E** shear-layer outer $-0.32\,D$):

- Modulation of the turbulent intensity is observed in the NPR = 5.0 case only.
- Modulation of the turbulent coherence is observed in the NPR = 5.0 case only.

In the region where we would expect the shock structure to dominate the modulation of the turbulent features (**E** shear-layer center):

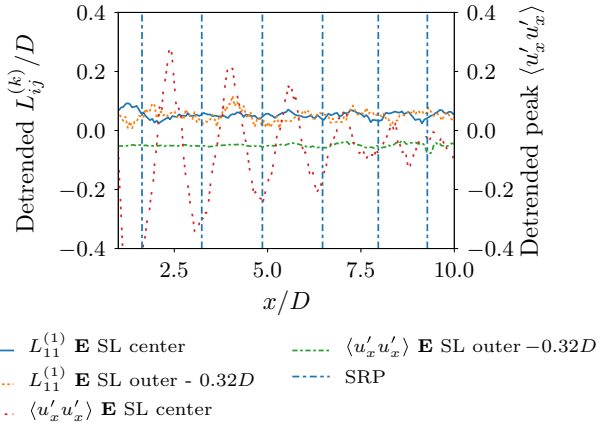

Fig. 29 NPR = 4.6 $L_{11}^{(1)}$ detrended length scales and detrended velocity fluctuations

- Modulation of the turbulent intensity is observed in both cases.
- Modulation of the turbulent coherence is observed in the NPR = 5.0 case only.

From these observations that are summarized in Table 3 and graphically in Fig. 31, we can make conclusions which separate the modulation of turbulence coherence and intensity.

In the case of Tan et al. (2017) the question was posed, *is the modulation of the ILS due to the shock structure or the standing-wave?* We find that when the standing-wave is not present, the ILS modulation is not evident. Hence it can be concluded that the shock structure is a contributor to the turbulent intensity modulation in the nearfield.

Considering regions isolated and acted on only by the standing-wave that are out of range from the shock structure: When the standing-wave is present, it modulates both the

Table 3 Summary of turbulence modulation findings

	Intensity modulation		Coherence modulation	
	NPR			
	4.6 (No SW)	5.0 (SW)	4.6 (No SW)	5.0 (SW)
Shock dominated zone (**E** SL center)	Yes	Yes	No	Yes
SW dominated zone (**E** SL outer)	No	Yes	No	Yes

SW, standing-wave; SL, shear-layer

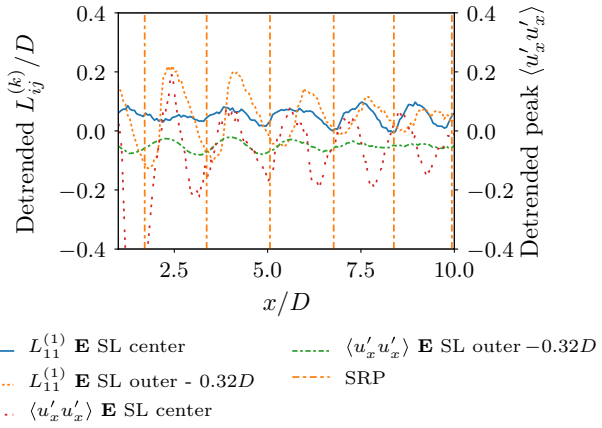

Fig. 30 NPR = 5.0 $L_{11}^{(1)}$ detrended length scales and detrended velocity fluctuations

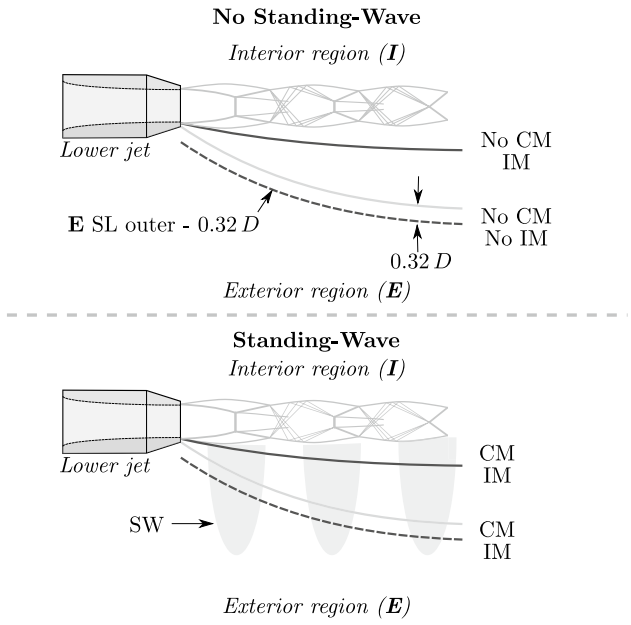

Fig. 31 Graphical representation of turbulence modulation findings. SW, standing-wave; CM, coherence modulation; IM, intensity modulation. Refer to Fig. 6 for line definitions

intensity and coherence. When the standing-wave is not present then neither are modulated. Hence it can be concluded that the standing-wave contributes to both the modulation of intensity and coherence of turbulence in the jet flow, and the modulation of intensity in the NPR = 5.0 case near the jet is the summation of both the effect of the standing-wave and shock structure. Further, as the coherence is modulated only when the standing-wave is present, it can be concluded that it is the standing-wave that drives the coherence modulation near the jet and not the shock-structure.

5 Conclusion

PIV measurements and analysis of closely spaced ($s/D = 3$) twin-jets have been presented. Both the turbulent flow properties and the spatial modality have been investigated. The first point of interaction between the jets was found to be in the range of $x/D = 4$ to 4.5. Mixing has been historically reported to be greater and more vigorous in the inter-nozzle region. Analysis of turbulent kinetic energy indicated that the intense mixing likely takes place much further downstream ($x/D \geq 10$) than previously understood. The authors reason that this is due to the lower velocity gradients present in the inter-nozzle shear-layers once the jets have merged, with comparison to the external shear-layers. The two NPR cases are selected as they are separated by a discontinuous jump in their acoustic screech frequency. The screech frequency jump is understood to be the result of a change in screech feedback mechanism that is accompanied by a change in coupling mode. The base flow and acoustic measured tones for both cases are similar. However, a strong standing-wave is evident in the NPR = 5.0 case only (absent from NPR = 4.6). Panda's relation was demonstrated to retrieve a close match to the measured acoustic tone. Hence the authors inferred that at least where the standing-wave was present, the coupling mechanisms are based in screech. Analysis by second-order spatial correlations of the velocity fields indicated that NPR = 5.0 is characterized by a symmetric coupling mode. NPR = 4.6 also shows a very weak symmetric mode. Integral length scales for the axial and transverse directions have been calculated. Comparison between the two cases where the standing-wave was present allowed the following conclusions to be made:

- the standing-wave, not the shock structure, is the driver of turbulence coherence modulation ($L_{11}^{(1)}$) near the jet, and
- the standing-wave contributes to both the intensity ($\langle u_x' u_x' \rangle$) and coherence modulation ($L_{11}^{(1)}$) of turbulence in the jet flow.

Acknowledgements The authors would like to acknowledge the financial support of the Australian Research Council (ARC) and the computational resources of the Australian National Computational Infrastructure (NCI).

References

Alkislar MB, Krothapalli A, Lourenco LM (2003) Structure of a screeching rectangular jet: A stereoscopic particle image velocimetry study. Journal of Fluid Mechanics 489(489):121–154. https://doi.org/10.1017/S0022112003005032

Alkislar MB, Krothapalli A, Choutapalli I, Lourenco L (2005) Structure of Supersonic Twin Jets. AIAA journal 43(11):2309–2318. https://doi.org/10.2514/1.10431

André B, Castelain T, Bailly C (2014) Investigation of the mixing layer of underexpanded supersonic jets by particle image velocimetry. International Journal of Heat and Fluid Flow 50:188–200. https://doi.org/10.1016/j.ijheatfluidflow.2014.08.004

Benedict LH, Gould RD (1996) Towards better uncertainty estimates for turbulence statistics. Experiments in Fluids 22(2):129–136. https://doi.org/10.1007/s003480050030

Berndt DE (1984) Dynamic Pressure Fluctuations in the Internozzle Region of a Twin-Jet Nacelle. In: SAE Technical Paper, Society of Automotive Engineers, p 10, https://doi.org/10.4271/841540

Bogey C, Gojon R (2017) Feedback loop and upwind-propagating waves in ideally expanded supersonic impinging round jets. Journal of Fluid Mechanics 823:562–591. https://doi.org/10.1017/jfm.2017.334

Bogey C, Marsden O, Bailly C (2012) Influence of initial turbulence level on the flow and sound fields of a subsonic jet at a diameter-based Reynolds number of 105. Journal of Fluid Mechanics 701:352–385. https://doi.org/10.1017/jfm.2012.162

Davis MG, Oldfield DES (1962) Tones from a choked axisymmetric jet. I. Cell structure, eddy velocity and source locations and II. The self excited loop and mode of oscillation. Acustica 12(4):257–277

Edgington-Mitchell D, Oberleithner K, Honnery DR, Soria J (2014) Coherent structure and sound production in the helical mode of a screeching axisymmetric jet. Journal of Fluid Mechanics 748:822–847. https://doi.org/10.1017/jfm.2014.173

Edgington-Mitchell D, Honnery D, Soria J (2015) Staging behaviour in screeching elliptical jets. International Journal of Aeroacoustics 14(7):1005–1024. https://doi.org/10.1260/1475-472X.14.7-8.1005

Fleury V, Bailly C, Jondeau E, Michard M, Juvé D (2008) Space-Time Correlations in Two Subsonic Jets Using Dual Particle Image Velocimetry Measurements. AIAA Journal 46(10):2498–2509. https://doi.org/10.2514/1.35561

Gao J, Xu X, Li X (2016) Numerical Simulation of Supersonic Twin-Jet Noise with High Order Finite Difference Scheme. 22nd AIAA/CEAS Aeroacoustics Conference pp 1–14, https://doi.org/10.2514/6.2016-2938

Gojon R, Bogey C (2017) Numerical study of the flow and the near acoustic fields of an underexpanded round free jet generating two screech tones. International Journal of Aeroacoustics 16(7–8):603–625. https://doi.org/10.1177/1475472X17727606

Goparaju K, Gaitonde DV (2017) Dynamics of Closely Spaced Supersonic Jets. Journal of Propulsion and Power pp 1–13, https://doi.org/10.2514/1.B36648

Knast T, Bell G, Wong M, Leb CM, Soria J, Honnery DR, Edgington-Mitchell D (2018) Coupling Modes of an Underexpanded Twin Axisymmetric Jet. AIAA Journal pp 1–12, https://doi.org/10.2514/1.J056434

Kuo CW, Cluts J, Samimy M (2017a) Effects of excitation around jet preferred mode Strouhal number in high-speed jets. Experiments in Fluids 58(4):35. https://doi.org/10.1007/s00348-017-2329-7

Kuo CW, Cluts J, Samimy M (2017c) Exploring Physics and Control of Twin Supersonic Circular Jets. AIAA Journal 55(1):68–85. https://doi.org/10.2514/1.J054977

Lin YF, Sheu MJ (1991) Interaction of parallel turbulent plane jets. AIAA Journal 29(9):1372–1373. https://doi.org/10.2514/3.10749

Mercier B, Castelain T, Bailly C (2017) Experimental characterisation of the screech feedback loop in underexpanded round jets. Journal of Fluid Mechanics 824:202–229. https://doi.org/10.1017/jfm.2017.336

Mitchell D, Honnery D, Soria J (2011) Particle relaxation and its influence on the particle image velocimetry cross-correlation function. Experiments in Fluids 51(4):933–947. https://doi.org/10.1007/s00348-011-1116-0

Morris PJ (1977) Flow characteristics of the large scale wave-like structure of a supersonic round jet. Journal of Sound and Vibration 53(2):223–244. https://doi.org/10.1016/0022-460X(77)90467-9

Morris PJ (1990) Instability waves in twin supersonic jets. Journal of Fluid Mechanics 220(1):293–307. https://doi.org/10.1017/S0022112090003263

Moustafa GH (1994) Experimental investigation of high-speed twin jets. AIAA journal 32(11):2320–2322. https://doi.org/10.2514/3.12293

Nicolaides D, Honnery DR, Soria J (2004) Autocorrelation Functions and the Determination of Integral Length with Reference to Experimental and Numerical Data. 15th Australasian Fluid Mechanics Conference 1(December):1–4

Panda J (1999) An experimental investigation of screech noise generation. Journal of Fluid Mechanics 378:71–96. https://doi.org/10.1017/S0022112098003383

Panickar P, Srinivasan K, Raman G (2004) Aeroacoustic features of coupled twin jets with spanwise oblique shock-cells. Journal of Sound and Vibration 278(1–2):155–179. https://doi.org/10.1016/j.jsv.2003.10.011

Panickar P, Srinivasan K, Raman G (2005) Nonlinear interactions as precursors to mode jumps in resonant acoustics. Physics of Fluids 17(9):1–18. https://doi.org/10.1063/1.2008995

Powell A (1954) The reduction of choked jet noise. Proceedings of the Physical Society Section B 67(4):313–327. https://doi.org/10.1088/0370-1301/67/4/306

Powell A, Umeda Y, Ishii R (1992) Observations of the oscillation modes of choked circular jets. The Journal of the Acoustical Society of America 92(5):2823–2836. https://doi.org/10.1121/1.404398

Raffel M, Willert CE, Wereley ST, Kompenhans J (2007) Particle Image Velocimetry, A Practical Guide, vol 6, 2nd edn. Springer Berlin Heidelberg, Heidelberg, New York, https://doi.org/10.1097/JTO.0b013e3182370e69, arXiv:1011.1669v3

Raman G (1998) Advances in Understanding Supersonic Jet Screech: Review and Perspective. Progress in Aerospace Sciences 34(1–2):45–106. https://doi.org/10.1016/S0376-0421(98)00002-5

Raman G (1999) Coupling of Twin Supersonic Jets of Complex Geometry. Journal of Fluid Mechanics 36(5):123–146. https://doi.org/10.2514/2.2523

Raman G, Panickar P, Chelliah K (2012) Aeroacoustics of twin supersonic jets: a review. International Journal of Aeroacoustics 11(7):957–984. https://doi.org/10.1260/1475-472X.11.7-8.957

Sadr R, Klewicki JC (2003) An experimental investigation of the near-field flow development in coaxial jets. Physics of Fluids 15(5):1233–1246. https://doi.org/10.1063/1.1566755

Seiner JM, Manning JC, Ponton MK (1986) Dynamic pressure loads associated with twin supersonic plume resonance. AIAA Journal 26(8):954–960. https://doi.org/10.2514/3.9996

Shaw L (1990) Twin-jet screech suppression. Journal of Aircraft 27(8):708–715. https://doi.org/10.2514/3.25344

Singh A, Chatterjee A (2007) Numerical prediction of supersonic jet screech frequency. Shock Waves 17(4):263–272. https://doi.org/10.1007/s00193-007-0110-1

Soria J (1996) An investigation of the near wake of a circular cylinder using a video-based digital cross-correlation particle image velocimetry technique. Experimental Thermal and Fluid Science 12(2):221–233. https://doi.org/10.1016/0894-1777(95)00086-0

Srinivasan K, Panickar P, Raman G, Kim BH, Williams DR (2009) Study of coupled supersonic twin jets of complex geometry using higher-order spectral analysis. Journal of Sound and Vibration 323(3–5):910–931. https://doi.org/10.1016/j.jsv.2009.01.011

Tam CKW (1995) Supersonic Jet Noise. Annu Rev Fluid Mech 27:17–43

Tan DJ, Soria J, Honnery D, Edgington-Mitchell D (2017) Novel Method for Investigating Broadband Velocity Fluctuations in Axisymmetric Screeching Jets. AIAA Journal 55(7):2321–2334. https://doi.org/10.2514/1.J055606

Tritton DJ (1977) Physical Fluid Dynamics. Oxford Science Publ, Clarendon Press, https://doi.org/10.1007/978-94-009-9992-3,arXiv:1011.1669v3

Weightman JL, Amili O, Honnery D, Edgington-Mitchell DM, Soria J (2016) Supersonic Jet Impingement on a Cylindrical Surface. In: 22nd AIAA/CEAS Aeroacoustics Conference, pp 2016–2800, https://doi.org/10.2514/6.2016-2800

Weightman JL, Amili O, Honnery D, Soria J, Edgington-Mitchell D (2017) An explanation for the phase lag in supersonic jet impingement. Journal of Fluid Mechanics 815:815R11–815R111, https://doi.org/10.1017/jfm.2017.37

Westley R, Woolley JH (1969) The near field sound pressures of a choked jet during a screech cycle. In: Agard Cp, American Institute of Aeronautics and Astronautics, Reston, Virigina, vol 42, pp 23.1–23.13, https://doi.org/10.2514/6.1975-479

Willert CE, Stockhausen G, Voges M, Klinner M, Schodl R, Hassa C, Schürmans B, Güthe F (2008) Particle Image Velocimetry:

New Developments and Recent Applications, vol 112, 1st edn. Springer, Berlin Heidelberg

Wlezien R (1989) Nozzle geometry effects on supersonic jet interaction. AIAA Journal 27(10):1361–1367. https://doi.org/10.2514/3.10272

Yoo J, Mitchell D, Davidson DF, Hanson RK (2010) Planar laser-induced fluorescence imaging in shock tube flows. Experiments in Fluids 49(4):751–759. https://doi.org/10.1007/s00348-010-0876-2

5.2 Concluding Statement

The analysis provided a description of the flow for two different coupling modes and a dataset for further examination in chapter 6. The inter-nozzle region was found to contain relatively low velocity flow. The merge point was quantified by the point where shear-layer velocity fluctuations reach the symmetry line between the jets. Under this definition it was found to reside between $x/D = 4$ to 4.5. The mixing in the inter-nozzle region was shown to be lower than previously proposed. Analysis of turbulent kinetic energy found that mixing was suppressed until $x/D \geq 10$ due to the removal of the strong velocity gradient after the merge point. Despite this the shear-layer thickness for the internal shear-layers was found to be larger than the external, although the difference was small and dependent on coupling-mode.

An uncertainty analysis was examined to quantify the error in the measurements using the bootstrapping technique (Benedict & Gould, 1996). A maximum error of approximately ±5 % of the axial standard deviation was observed within the first shock-cell where optical distortion is strongest due to density changes in the flow. Additional error of approximately ±3 % was observed along the shear-layer boundary where the maximum shear and the production of vorticity occur.

Spatial correlations of the full field velocity yielded a clear symmetric coupling mode for region III and an inconclusive result for region II. Regardless of reference point the dominant structure revealed very low overall modal structure and no evidence for a standing-wave in this region. In contrast, the schlieren spatial correlations of chapter 4 revealed a clear symmetric mode for region II and the existence of a standing-wave. Schlieren photography is a path-integrated measurement and it is possible that the in-plane mode could be mixed with out-of-plane density gradient fluctuations.

The lack of a clear dominant modal pattern in the velocity field of region II deepened the challenge of identifying the coupling behaviour between the jets under these operating conditions. There was now a clear drive to use the dataset to further examine the flow in region II and identify its underlying flow structure. This is examined in the next chapter.

Chapter 6

An Explanation for Complex Coupling

6.1 Introductory Statement

The preceding chapter provided a velocity dataset of the complex coupling region but failed to yield a description of the coupling mode in region II. A deeper investigation into this region is examined in this chapter.

Early parametric studies observed simultaneous tones at a given location within the twin-jet parameter space (Seiner *et al.*, 1986; Wlezien, 1989). The behaviour observed in region II is possibly a function of multi-modality. This prompted a more comprehensive modal analysis of the PIV dataset in region II.

Various proper orthogonal decompositions (POD) of the region II velocity field were attempted. These attempts were examined in the conference proceedings included in appendix F. POD of region II did not yield results typical of a screeching jet flow. The POD results did not show a symmetric and/or an anti-symmetric mode. The results showed rather a confusing non-symmetric structure. The flow could not be decomposed into modes that were readily identifiable as coupling of one form or another. If the modes contained symmetric and anti-symmetric mode pairs, then it would indicate that the flow was simply multi-modal. The multi-modal jet would have made it possible for early experimenters to simply change the phase-locked schlieren triggering frequency to resolve the different coupling modes. Instead, it was mentioned that this was not possible (Seiner *et al.*, 1986; Wlezien, 1989; Shaw, 1990; Raman, 1998). Thus it appeared that region II is not simply the superposition or the serialisation of two modes indicating either mutual inclusivity or exclusivity respectively.

The effort to filter and extract coupling mode shapes via POD had not directly identified the coupling modes. The complexity of the interaction necessitated a different approach that could capture the physical relationship between the jets. The acoustic measurements provided another source of information. Some phase variance (approximately 15 degrees) was observed in repeated measurements of pressure ratios within region II. Essentially no variance was observed in the corresponding coherence. Further work examined the uncertainty of the microphone measurement and technique. No significant uncertainty was found that could explain the phase variance in region II. The significant variance of phase in region II thus must lie in the time-dependence of the input signal on a given record.

The CPSD technique is based on a Fourier analysis that assumes a statistically stationary signal. If the mean value of a signal varies it is classified as non-stationary and not suitable for stationary techniques like CPSD (or the cross bi-spectrum). The SWFT is often used as a tool to provide approximate temporal-frequency analysis of time-dependent signals. Previous studies had examined the temporal mutual exclusivity of modes using the SWFT (Raman, 1998; Panickar *et al.*, 2004). The low temporal resolution relative to the time scales of the flow (separated by more than an order of magnitude) potentially prevented further insight. Therefore the SWFT resulted in a trade-off between frequency and temporal resolution insufficient for the present application. Other statistical techniques for examining the microphone signals were examined. Empirical mode decomposition utilising the Hilbert-Huang transform was explored (Huang *et al.*, 1998). The empirical method was successful in providing time-dependent modes. However, these modes could not be guaranteed to contain the vital screech frequency where the coupling was taking place. The Hilbert transform applied to a bandpass filtered region of the acoustic signal provided an effective tool to examine time-dependent behaviour. A narrow bandpass filter was centered on the screech tones. This provided direct access to the amplitude and phase as a function of time where the analysis could begin.

This work is currently (November 2019) under review at the Journal of Fluids Mechanics.

Mode Selection and Stability in Coupled Underexpanded Twin-Jets

G. W. Bell[1]†, J. Cluts[2] M. Samimy[2] J. Soria[1] and D. M. Edgington-Mitchell[1]

[1]Department of Mechanical and Aerospace Engineering, Laboratory of Turbulence Research in Aerospace and Combustion, Monash University, Melbourne, Victoria 3800, Australia

[2]Department of Mechanical and Aerospace Engineering, Gas Dynamics and Turbulence Laboratory, Aerospace Research Center, The Ohio State University, Columbus, Ohio 43235, USA

(Received xx; revised xx; accepted xx)

Twin supersonic jets in close proximity exhibit a range of complex coupling behaviours. Depending on operational parameters (especially nozzle pressure ratio and jet spacing), this coupling involves symmetric or anti-symmetric oscillations about the major twin-jet symmetry plane. Recent works by Knast *et al.* (2018) have indicated the existence of regions of the parameter space exhibiting erratic phase relations between the jets when examined by traditional methods and techniques (e.g., schlieren and second-order cross-correlation, or multiple microphones and cross power spectral density). In this work, the authors analyse these erratic regions, using non-stationary acoustic analysis to provide new insight into the temporal behaviour of the coupling phenomena. The results show that where the phase between the jets is time-varying, the screech tone is characterised by high rates of spontaneous interruption ($\approx 20\,\%$ of signal duration). Depending on the position in the pressure-ratio parameter space, the interruptions are either correlated and experienced by both jets at a time or are anti-correlated and only experienced by one. During the anti-correlated interruption, the uninterrupted jet continues to screech in the manner of an isolated jet. Particle image velocimetry is then used to explore the instantaneous state of the hydrodynamic field for the individual cases where the jets are either uninterrupted or interrupted. The results show that for the majority of snapshots during an acoustic interruption, the jets do not exhibit a coupled oscillation. When the jets are uninterrupted, they are oscillating in either a coupled symmetric or anti-symmetric mode - which the authors propose correspond to different screech tones present in the acoustic spectra.

Key words: To be inserted by the editor.

1. Introduction

This work presents an investigation of the coupling behaviour of underexpanded supersonic circular twin-jets. Supersonic jets produce intense acoustic radiation, which is sometimes further amplified in the twin-jet configuration. The amplified acoustic radiation of twin-jets has led to nozzle and empennage structure fatigue damage in some

† Email address for correspondence: graham.bell@monash.edu

high-speed aircraft with the twin-engine configuration, including the B-1B (Berndt 1984) and the F-15 (Seiner *et al.* 1986).

One major source of acoustic radiation in these jets stems from a self-reinforcing aeroacoustic feedback process called jet screech (Powell 1954; Tam 1995). Screech occurs in shock-containing supersonic jets as a result of the interaction between coherent vortical structures (CVS) produced in the shear-layer of the jet and the jet shock-cells. This interaction produces intense acoustic waves that propagate most strongly in the upstream direction via two known mechanisms (Powell 1954; Gojon *et al.* 2018; Edgington-Mitchell *et al.* 2018). Upon striking the jet nozzle lip, the waves scatter and perturb the thin jet-exit shear-layer. Under certain conditions they produce new CVSs and completing the feedback process (Edgington-Mitchell *et al.* 2014*b*). A summary of the present understanding of jet screech is provided by Edgington-Mitchell (2019).

Screech is associated with periodic oscillation modes of the jet column. Within twin-jet studies, toroidal, helical, and flapping modes of the individual jets have been observed (Seiner *et al.* 1986; Kuo *et al.* 2017*b*), which then couple symmetrically or anti-symmetrically about the symmetry plane of the twin-jet system. Each individual jet and corresponding overall coupling mode are associated with a particular location within the jet spacing and nozzle pressure ratio parameter space. Correspondingly, moving through the parameter space results in the presentation of different coupling modes. Despite numerous studies observing clear coupling in twin-jet systems since the mid 1980s, the process of mode selection, transition between modes, and the coupling mechanisms remain poorly understood (Panickar *et al.* 2004, 2005; Srinivasan *et al.* 2009; Raman *et al.* 2012; Knast *et al.* 2018). The coupling behaviour has been observed to be a function of nozzle pressure ratio (NPR), nozzle spacing, boundary-layer thickness, shear-layer growth-rate, nozzle geometry, and the acoustic environment (Alkislar *et al.* 2005; Wlezien 1989; Morris 1990). NPR is the ratio of nozzle stagnation pressure at the nozzle exit (p_0) to ambient pressure in the exhaust region (p_∞), NPR $= p_0/p_\infty$. The non-dimensional spacing between the jets is represented by s/D, where s is the spacing between the jet centres, and D is the jet exit diameter. The effect of jet temperature ratio on twin-jet coupling remains an open topic for investigation. The addition of heat is generally associated with a suppression of screech in single jets (Shen & Tam 2000), though under certain conditions has also been seen to amplify the acoustic tones (Gojon *et al.* 2017, 2019). Strong coupling associated with the production of screech tones was observed in the two primary full-scale aircraft studies (Berndt 1984; Seiner *et al.* 1986), indicating that in full-scale systems, screech is still present in even heated twin-jet configurations.

Typically, NPR and s/D are the primary independent variables that govern coupling behaviour in twin-jets; within certain NPR and s/D ranges, different coupling modes are observed. The term mode staging is used to describe the discontinuous changes in mode shape and tone frequency at points in the parameter space. Several existing studies have focused on characterising the behaviour and mode staging of twin-jet systems as a function of these parameters (Seiner *et al.* 1986; Wlezien 1989; Raman 1998; Knast *et al.* 2018; Panickar *et al.* 2005; Srinivasan *et al.* 2009). The tendency of the jets to couple about the symmetry plane has facilitated the use of opposing microphones on each side of the twin-jet system to study the coupling behaviour. Acoustic measurements in this style, alongside a range of qualitative optical techniques, have been applied to a wide range of laboratory-scale twin-jet systems (Bell *et al.* 2017; Goparaju & Gaitonde 2017; Cluts *et al.* 2015; Kuo *et al.* 2017*b*,*a*, 2016*b*,*a*; Cluts *et al.* 2017; Alkislar *et al.* 2003; Shaw 1990; Wlezien 1989; Zilz & Wlezien 1990; Umeda & Ishii 2001; Panickar *et al.* 2004). While acoustic measurements are relatively easy to obtain, they are not always easy to interpret, and measurements of the hydrodynamic field are far more difficult to acquire. These

challenges as well as advances in computational capabilities have motivated numerical approaches to the problem (Brès *et al.* 2013; Goparaju & Gaitonde 2017). However, the sensitivity of resonant systems to boundary conditions presents its own set of challenges (Weightman *et al.* 2019). From a mechanistic perspective, the tendency of these jets to couple together has been demonstrated theoretically via vortex-sheet and finite-thickness stability approaches (Morris 1990; Du 1993, 2002), though these studies did not include the upstream-component of the resonance process.

Seiner *et al.* (1986) provided a detailed canonical experimental investigation of axisymmetric supersonic twin-jets. The experimental setup consisted of $1/40^{\text{th}}$ scale F-15 nozzles with a diameter of $D = 1.57\,\text{cm}$, and inter-nozzle spacing of $s/D = 1.9$. They swept the parameter space through $1.89 \leqslant NPR \leqslant 7.8$ ($1.0 \leqslant M_j \leqslant 2.0$) and attempted to identify the coupling shape and azimuthal mode number associated with each high-amplitude acoustic peak. Mode staging (based on peak frequency) reminiscent of an isolated jet was observed, though with fewer stages that extended over larger pressure ranges with much higher amplitudes. The oscillations of the jets were observed to be strongly coupled about the symmetry plane via both a phase-locked schlieren technique, and measurements of coherence from opposing microphones.

Raman (1998) examined the coupling of twin supersonic high-aspect-ratio rectangular jets, with major axes normal to the symmetry plane. Opposing microphones and phase-locked acoustically-triggered schlieren were used to characterise the coupling modes of the system. A parameter sweep was performed across $1.89 \leqslant \text{NPR} \leqslant 4.6$ ($1.0 \leqslant M_j \leqslant 1.65$) and $5.5 \leqslant s/D \leqslant 15$, which identified three distinct coupling modes. With increasing M_j, an anti-symmetric mode followed by a symmetric mode were observed. Unlike axisymmetric jets, both coupling modes involved a flapping of the jet in the symmetry plane direction, driven by the tendency of high-aspect ratio jets to flap about their major-axis plane. For the range of jet spacings considered, as NPR was increased the first coupling mode was described by the authors as a 'weak complex interaction', where multiple strong acoustic tones exist but phase-locking with the schlieren system was not possible.

Panickar *et al.* (2004) further investigated the propensity for twin-jets to couple and the physical interactions that allowed them to do so. They studied rectangular oblique jets, measuring in what portions of the parameter space they coupled and comparing this with stability analysis to find the stability margin required to enable coupling. General agreement was found between stability analysis predictions and the experimental observations. Panickar *et al.* (2005), and Srinivasan *et al.* (2009) sought a quantitative indicator for when a coupled jet might soon switch to another mode. The indicator was based on measuring the number of non-linear interactions between frequencies in the time-averaged acoustic spectra using cross bi-coherence. Non-linear interactions were detected in jet acoustic recordings by computing the cross bi-coherence of two simultaneously recorded microphone signals and measuring the number of peaks and their cluster density in the resulting spectra. General agreement between the number of non-linear interactions and proximity to the mode-switch point was found.

Knast *et al.* (2018) revisited the circular twin-jet in a canonical setup similar to Seiner *et al.* (1986), comparing experimental data to the frequency prediction relations developed by Powell (1953), Shen & Tam (2002), and Panda (1999). Within the study, Knast et al. examined the $s/D = 3$ twin-jet spacing using time-resolved and high-resolution schlieren photography, and opposing microphones. In the initial characterisation of the twin-jet modes, Knast et al. observed parameter space regions of unambiguous symmetric and anti-symmetric coupling from the cross power spectral density (CPSD) measurement of phase between the opposing microphones. Additionally, a region of the NPR space

($3.4 \leqslant \mathrm{NPR} \leqslant 4.4$) between the symmetric and anti-symmetric modes was found to exhibit an erratic phase relation between the jets. Curiously, the region also maintained high coherence between the acoustic signals ($\geqslant 0.7$). High-speed imagery failed to provide further clarity. Spatial correlation maps of high-resolution schlieren images were similarly inconclusive. The erratic phase region was also found to exist at the $s/D = 6$ spacing, where it persisted from $2.75 \leqslant \mathrm{NPR} \leqslant 4.75$ between two symmetric coupling modes.

Bell *et al.* (2018) investigated the velocity field of the $s/D = 3$ circular twin-jet using Particle Image Velocimetry (PIV). Spatial correlations of velocity were used to indicate the dominant coupling mode at conditions with both steady and erratic phase relations between the jets. The velocity correlations exhibited a clear anti-symmetry for the condition with steady acoustic phase, but no clear mode shape in the erratic phase region. Furthermore, the anti-symmetric mode showed a strong standing-wave in the jets' near-field, whereas no standing-wave was observed at the condition with erratic phase relation. Hereafter in this paper the operating range with an erratic phase relation will be termed the "phase anomaly".

The results of Panickar *et al.* (2005) and Srinivasan *et al.* (2009) revealed the signature of potential non-linear interactions at operating conditions adjacent to mode staging points. It remains unclear whether the phase anomaly observed in both Knast *et al.* (2018) and Bell *et al.* (2018) is the signature of non-linear interaction. The region is book-ended by a symmetric coupling at low pressure, and an anti-symmetric coupling at higher pressure ratios. Thus the phase anomaly being the result of a non-linear competition between two coupling modes is plausible. However, as little is presently known about the behaviour of the jets in this region, it is difficult to comment further at this point.

In this paper, the authors provide an explanation for the hydrodynamic and acoustic behaviour that characterises the phase anomaly region. First, the acoustic nearfield of the twin-jet system is interrogated using several methods of analysis applied to acoustic data obtained from a pair of microphones. Then the hydrodynamic field associated with different coupling behaviour of the twin-jet systems is assessed using a modal decomposition and conditional sampling of PIV data.

2. Experiments and Methodology

The results of three separate facility experiments are examined within this work. Two of the three have featured in other publications. The data underpinning the analysis in this paper are drawn from the acoustic measurements of Knast *et al.* (2018) and the velocity data described in Bell *et al.* (2018).

2.1. *Facility One*

2.1.1. *Opposing Microphone Study*

This set of experiments were conducted in the Laboratory for Turbulence Research in Aerospace and Combustion (LTRAC) schlieren jet facility at Monash University. The experimental setup is shown in Figure 1. Compressed air at 298 K ±2 is supplied directly to the plenum chamber, which contains a honeycomb section and wire mesh screens to homogenise and condition the flow. Compressed air exhausts from twin converging circular nozzles with an exit diameter of $D = 10\,\mathrm{mm}$, a nozzle-lip thickness of 1.5 mm and a non-dimensionalised spacing of $s/D = 3.0$. The flow at the exit is choked (exit Mach number, $M_e = 1$) with a jet exit velocity $U_e \approx 310\,\mathrm{m/s}$. The Reynolds number based on the nozzle exit conditions is approximately 7.8×10^5 for NPR = 4.6 and 8.5×10^5 for NPR = 5.0.

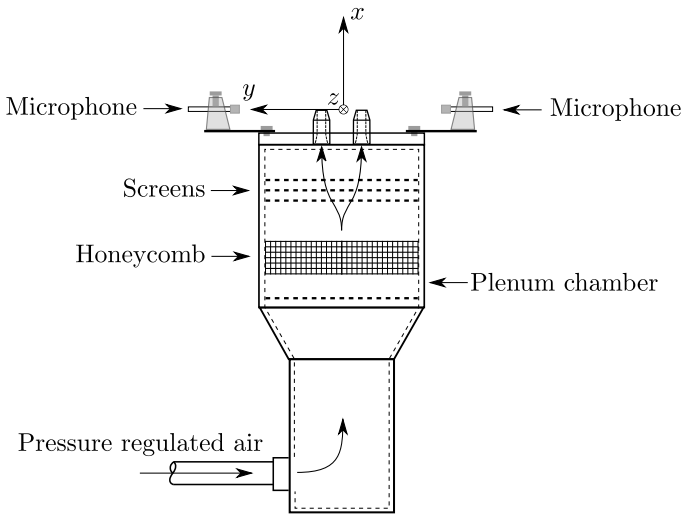

FIGURE 1. Schematic of the acoustic setup, adapted from Knast *et al.* (2018).

Acoustic measurements were obtained with a G.R.A.S. type 46BE 1/4" preamplified microphone with a frequency range of 20 Hz to 100 kHz. The microphone amplitude coefficient was referenced against a G.R.A.S. type 42AB sound level calibration unit. The signal output from the microphone was recorded on a National Instruments DAQ at a sample rate of 250 kHz to prevent aliasing and a signal resolution of 16 bits. The opposing microphones were positioned $8\,D$ radially from the closest nozzle lip and an uncertainty analysis was performed to ensure that microphone positioning error (and thereby phase response) was minimised. Millimetre microphone positional accuracy was achieved that corresponds to a phase error of approximately ± 5 degrees (considering a screech frequency of 15 kHz, 340 m/s ambient speed of sound corresponding to a wavelength on the order of 20 mm). 500 k samples were recorded simultaneously on both microphones and five measurements were combined into an ensemble and presented in this work.

2.1.2. *Schlieren Dataset*

A short comparison with high-speed schlieren photography is presented at the end of this work as a physical reference to confirm the analysis techniques. The examination of its statistics was presented in Knast *et al.* (2018). A Toepler Z-Type schlieren system was used to image the twin supersonic jet, which was not simultaneously recorded with the acoustic recordings mentioned previously. Two mirrors, each of focal length 2032 mm, were used to create a collimated light path through the test section. Only the density gradient in the streamwise direction ($\delta\rho/\delta x$) is presented within this work. A Shimadzu HPV-1 camera was used to obtain high-speed images of the twin-jet. The camera has a resolution of 320×260 pixels and can capture 102 images at an acquisition speed of up to 1 million frames per second at an exposure of 0.25 μs.

2.2. *Facility Two*

2.2.1. *Particle Image Velocimetry*

The experiments were conducted in the Laboratory for Turbulence Research in Aerospace and Combustion (LTRAC) supersonic particle image velocimetry jet facility also at Monash University. The PIV results within this paper were also examined in previous work (Bell *et al.* 2018). The experimental PIV setup is shown in Figure 2. Air at approximately 298 K is supplied directly to a mixing chamber where the jets are uniformly seeded with smoke particles from a Viscount 1300 smoke generator. Only one

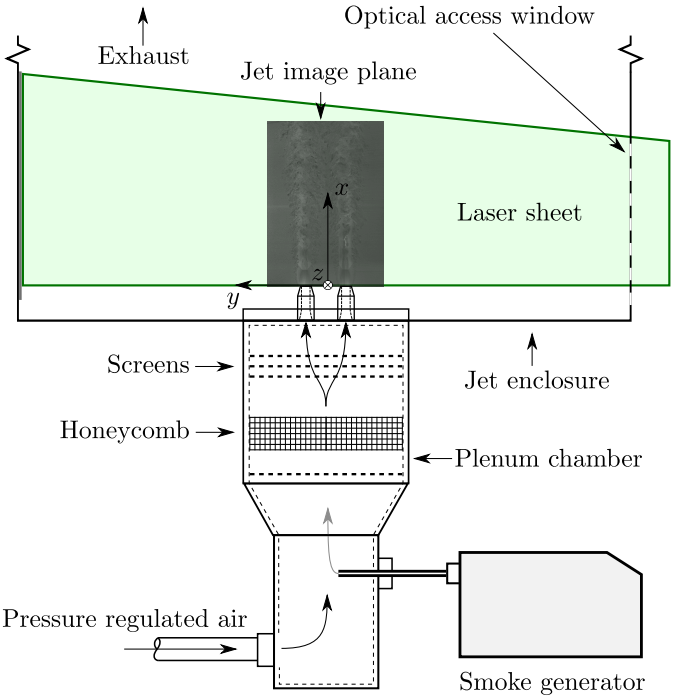

[hbt]

FIGURE 2. Experimental PIV setup.

smoke source was needed for both jet core and ambient fluid measurements as after a short time the smoke particles completely filled the measurement facility. The mixing chamber is connected to the plenum chamber, which contains a honeycomb section and wire mesh screens to homogenize and condition the flow. The exhausted flow is imaged inside the PIV enclosure, which is $60 \times 60 \times 200$ diameters in size. The walls of the enclosure are not acoustically treated. The nozzle assembly used in facility one is compatible with this experimental facility and used for these experiments for consistency.

The LTRAC supersonic schlieren and supersonic PIV jet facilities are similar, but not identical. The same nozzles were used on both facilities, with the same plenum design, but with different boundary conditions for the acoustic field, namely:

- The PIV facility consists of an enclosure surrounding the jet flow to prevent the seeded flow from entering the laboratory. The enclosure measures $60 \times 60 \times 200\,\mathrm{D}$ and has hard perspex walls. These walls are strong acoustic reflectors.
- In the PIV facility the plenum face where the nozzles are mounted sits nearly flush with the base of the enclosure. There is thus also a different upstream reflection condition in this facility; the facility for the acoustic measurements has no such mounting.

A third facility and set of experiments were undertaken to confirm that the observed results are impartial to the facility used. These are described in appendix B.

3. Ensemble-averaged spectral analysis of the acoustic field

Knast *et al.* (2018) extracted the phase difference between screech tones obtained by opposing microphones via Cross Power Spectral Density (CPSD). While many NPR conditions produced a highly coherent phase difference of either 0 or 180 degrees, a high phase variance between $3.4 \leqslant \mathrm{NPR} \leqslant 4.4$ (Figure 7 in Knast *et al.* (2018)) was observed. These results are first reconsidered here, before the application of other analysis techniques.

Figure 3 presents a waterfall plot of individual power spectral density (PSD) amplitudes

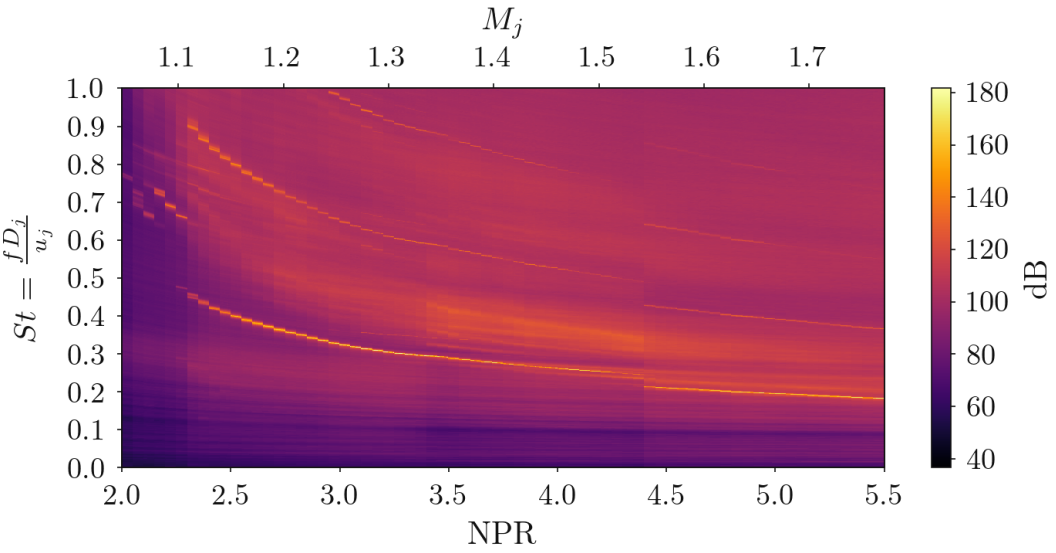

FIGURE 3. Waterfall plot of PSD for $s/D = 3$. Data from (Knast *et al.* 2018). The high-intensity narrow-band lines indicate screech tones. Discontinuous frequency changes in the screech tone indicate a change of twin-jet mode.

stacked as a continuous function of NPR. The vertical axis represents the Strouhal number, which is calculated from the acoustic frequency f, ideally expanded exit diameter D_j, and the ideally expanded exit velocity u_j. A single fundamental screech peak is evident across most of the NPR range as narrow-band high dB scars with additional harmonics. The discontinuities in screech tone and general spectra at NPR = 3.4 and 4.4 suggest mode switches.

Where Knast *et al.* (2018) considered only the phase at the peak-amplitude frequency, instead the authors here consider phase and coherence for all frequencies. CPSD is used to provide this estimate of sample-averaged coherence and phase. To reduce random error, the records are broken into 2^{13} sample sub-records and ensemble averaged

$$\hat{G}_{xy}(f) = \frac{2}{n_d T} \sum_{i=1}^{n_d} {X_i}^*(f) Y_i(f) \tag{3.1}$$

where f is the independent variable representing frequency, n_d is the number of sub-records of length T, ${X_i}^*(f)$ is the complex conjugate of the finite Fourier transform of the first signal, and $Y_i(f)$ is the finite Fourier transform of the second signal. $\hat{G}_{xy}$ is the complex CPSD estimate. The measure of coherence between the signals is defined by equation 3.2.

$$\hat{C}_{xy}(f) = \frac{\mid G_{xy}(f) \mid^2}{G_{xx}(f) G_{yy}(f)} \tag{3.2}$$

Phase is calculated from the CPSD as the angle of the two-component complex-valued function, equation 3.3, as a function of frequency.

$$\hat{\theta}_{xy}(f) = \tan^{-1} \frac{Im(G_{xy}(f))}{Re(G_{xy}(f))} \tag{3.3}$$

Contours of coherence and phase from the CSPD are presented in figures 4(a) and 4(b)) respectively. Figure 4(a) demonstrated the presence of additional highly-coherent

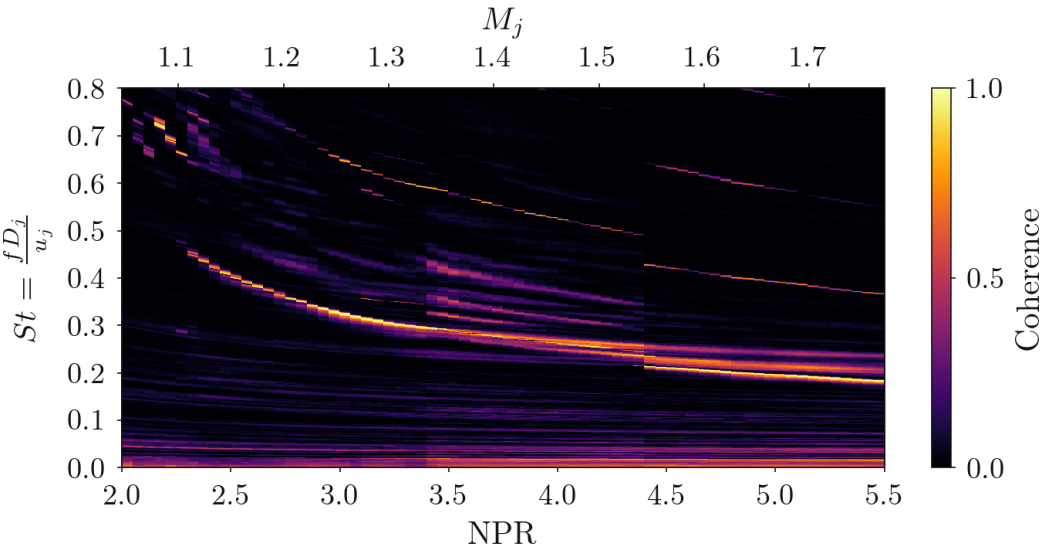

(a) Waterfall combination plot of Cross Spectral Density Coherence.

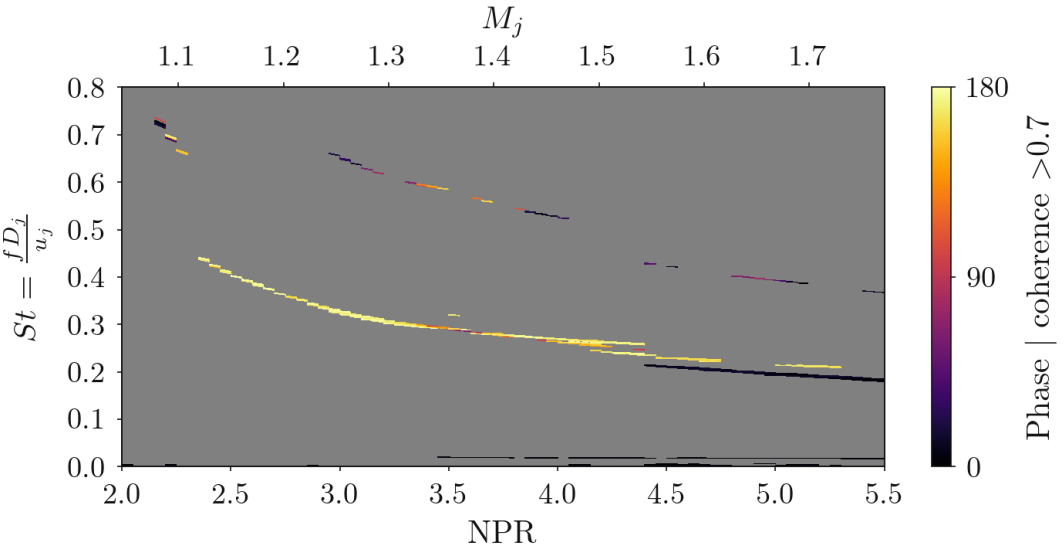

(b) Waterfall combination plot of Cross Spectral Density phase given that coherence $\geqslant 0.7$.

FIGURE 4. Cross spectral density results between opposing microphones from the experiments performed in Knast *et al.* (2018).

tones, which have relatively low acoustic amplitude. Regions exhibiting high coherence and low amplitude are particularly concentrated in the phase anomaly region.

The magnitude of the phase wrapped between 0 and 180 degrees is presented in Figure 4(b), excluding all frequencies where coherence is less than 0.7.

Three (excluding harmonics) processes that are continuous across the NPR range are labelled in Figure 5. Continuous variation of tonal frequency with changes in pressure ratio are typical of aeroacoustic resonance, thus each of these continuous processes are likely linked to a particular aeroacoustic feedback process. Process 1 is evident across most of the NPR range, and at low pressures is associated with a 180 degree phase offset. Process 2 begins at approximately NPR = 3.5 and continues until the end of the range,

and is not associated with a particular phase. Process 3 begins at NPR = 4.4 with a zero degree phase offset and extends until the end of the measured NPR range.

Examining the phase value along Processes 1 and 2, it is why the region in which these processes are both active has previously resisted classification on the basis of phase; within the phase anomaly region ($3.4 \leqslant \mathrm{NPR} \leqslant 4.4$) two processes with highly varying phase are evident.

Small changes in NPR are associated with large (and seemingly random) changes in the phase associated with the peak tone, and at some conditions multiple high-coherence frequency bands are evident. Therefore, the reporting of CPSD-phase originating from a single frequency in this region is likely to return spurious values despite the high coherence.

The analysis in Knast *et al.* (2018), and that presented here so far, considers phase and amplitude only in a ensemble-averaged sense. The analysis is now extended to include temporal variation in the signal to identify whether the phase anomaly is a transient phenomenon.

4. Time-resolved analysis of the acoustic field

A range of techniques exist to extract time-resolved quantities from acoustic data. Here, a combination of bandpass filtering with the Hilbert transform is used to gain access to the instantaneous signal amplitude and phase as a function of time; a short-windowed Fourier transform (SWFT) provides insufficient temporal resolution.

The Hilbert Transform of a single process is found from the convolution integral in equation 4.1.

$$\tilde{x}(t) = x(t) * (1/\pi t) \tag{4.1}$$

where $\tilde{x}(t)$ is the Hilbert transform, $x(t)$ is the original signal, $*$ is the convolution integral, and t is time. The Hilbert transformed variable, $\tilde{x}$, can be used to represent a new analytic signal of the original process, as in equation 4.2.

$$z(t) = x(t) + j\tilde{x}(t) \tag{4.2}$$

where $z(t)$ is the new analytic function, $x(t)$ remains the original function represented in the real domain, and the Hilbert transform is represented in the complex domain via the complex number j. $z(t)$ can also be represented in polar notation

$$z(t) = A(t)e^{j\theta(t)} \tag{4.3}$$

where $A(t)$ is the amplitude of the complex value,

$$A(t) = [x^2(t) + \tilde{x}^2(t)]^{1/2} \tag{4.4}$$

and $\theta(t)$ is the phase of the complex value,

$$\theta(t) = \tan^{-1}\left[\frac{\tilde{x}(t)}{x(t)}\right]. \tag{4.5}$$

$A(t)$ and $\theta(t)$ represent the process amplitude envelope and phase angle as a function of time, and hence provide access to the temporal information of the input process.

The difference between the two phase signals is evaluated to calculate phase between the two microphones

$$\Delta\theta(t) = \theta_1(t) - \theta_2(t). \tag{4.6}$$

The Hilbert transform has the advantage that it can operate on non-linear and non-stationary signals provided that it operates on a single process. In this context, a process

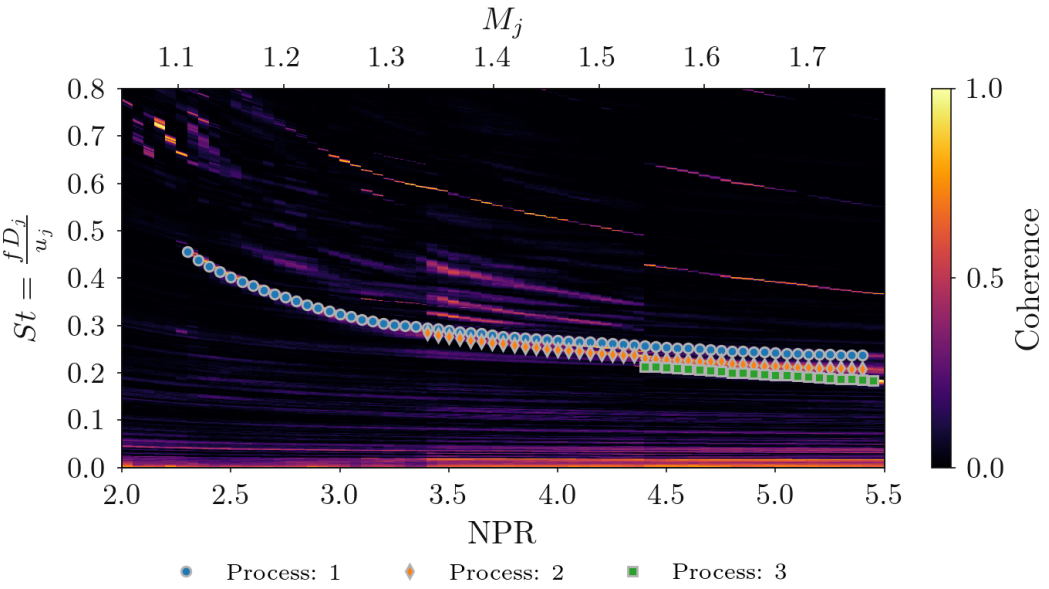

FIGURE 5. Coherence vs. NPR marked with processes where acoustic temporal information is examined with the bandpass-Hilbert technique.

is a stochastic 1D record corresponding to a repeatable input-output system. This makes the application to jet noise challenging, as within a jet-noise acoustic-spectra there are multitudes of different processes contributing to the farfield measured sound. A mechanism that extracts the relevant processes from the raw signal is required to enable the application of the Hilbert transform individually to these processes. A bandpass filter was used to filter the acoustic signals surrounding the process frequencies. A width of 200 Hz was found sufficient to ensure that the tones do not overlap and the peak frequency is captured.

Within Figure 4(a) some regions where multiple coherent peak frequencies are observed to exist. To determine the time-based physical processes along each of the contiguous screech tones; the bandpass-Hilbert analysis is applied to each of the frequencies separately. From each application at a particular frequency, a time-trace of phase and signal envelope is extracted. These quantities are examined first.

4.1. *Examining transient phase and amplitude*

The timescales on which the flow operates resulted in the raw Hilbert-bandpass signals being too laborious to examine. Instead, ensemble statistics and histogram representation provided a clearer view into the signal characteristics. Histograms of instantaneous phase and amplitude are shown in Figure 6 for the separate processes. Process 1 persists across most of the NPR range as shown in figures 6(a) and 6(b). Between $2.3 \leqslant \text{NPR} \leqslant 3.0$ the phase distribution is wide and centred on 180 degrees. Here a "wide" distribution is defined as where the distribution standard deviation is greater than 20 degrees for phase, and 3 dB for amplitude; plots of standard deviation of the distributions are included in appendix C . Around NPR = 3.0, process 1 exhibits a phase centred on 180 degrees, and the distribution of both the phase and amplitude is narrow. The amplitude within this region corresponds to the highest acoustic intensity within the NPR range. Beyond NPR = 3.5 the process transitions to lower amplitude and a wider phase without a clear distribution centre. It shall be investigated in the following sections whether the process continues to exist at these higher NPR values. However, at this stage there is a faint Process 1 signal in the coherence waterfall (figures 3 and 5), so the authors presume

	Process					
	1		2		3	
NPR Range	Amp.	Phase	Amp.	Phase	Amp.	Phase
$2.3 < \text{NPR} < 3.0$	W	W-180	-	-	-	-
$3.0 < \text{NPR} < 3.5$	N	N-180	-	-	-	-
$3.5 < \text{NPR} < 3.9$	W	W-UC	W	W-180	-	-
$3.9 < \text{NPR} < 4.4$	W	W-180	W	W-180	-	-
$4.4 < \text{NPR} < 5.4$	W	W-180	N	W-180	N	N-0

TABLE 1. N/W corresponds to narrowly/widely statistically-distributed respectively. 0 and 180 correspond to observed centre of the phase distribution. UC corresponds to an uncentred distribution.

that it does exist at the higher NPRs in a reduced capacity. Process 2 (Figures 6(c) and 6(d)) begins around NPR = 3.5, (the point where Process 1 rapidly reduces in amplitude and increases in phase variance). Process 2 exhibits a wider distributed phase centred on 180 degrees. The amplitude is more widely distributed than the other processes, which spreads histogram bin counts over a wider range. Hence the normalised histogram results in lower probability density estimates for Process 2 compared to Process 1 or 3. Around NPR = 3.9, the phase and amplitude distributions of both Process 1 and 2 change without a significant change in observed frequency. Process 1 is observed to become very wide in its phase distribution with lower amplitude. For $\text{NPR} \geqslant 4.1$, the phase distribution of Process 2 somewhat narrows around a peak of 180 degrees, with a corresponding increase in acoustic amplitude. Beyond NPR = 4.4, Process 3 becomes evident (Figures 6(e) and 6(f)), exhibiting a narrow phase distribution centred on zero degrees phase, with a narrow distribution of high amplitude. The observations are summarised in Table 1.

Narrow distributions of phase and amplitude are generally observed together. Additionally, when the amplitude is narrow, the corresponding process generally shows constant amplitude. Knast *et al.* (2018) identified that coupling oscillation was strongest where the phase is well defined ($3.0 \leqslant \text{NPR} \leqslant 3.4$). Over this NPR range, the most intense screech tones are observed in the present data. This is consistent with the findings of Seiner *et al.* (1986), where the coupling was found to increase the acoustic amplitude beyond the summation of two single screeching jets when the coupling motion was strong.

Some of the wide amplitude distributions exhibit a long tail towards lower values. Do the lower values indicate that the tone becomes interrupted? This is considered in the following section.

4.2. *Examining screech interruptions and intermittency on an individual jet*

In regions where the amplitude is widely distributed, the distribution is strongly skewed, with a long tail of lower amplitudes. This long tail indicates that there are events where the screech tone is either damped or entirely interrupted. To quantify the frequency of these "quiet" events, a dB threshold was defined as when the amplitude drops below 5 dB of its mean value. The technique is discussed in appendix A. Figure 7 shows the total interruption duration as a percentage of total signal length. The regions of wide phase and amplitude distribution generally overlap with regions of higher interruption rate (high interruption rate is considered 20 % here). An exception is found for $3.5 < \text{NPR} < 3.9$, where there is widely distributed phase on Process 1 but it is accompanied by a relatively

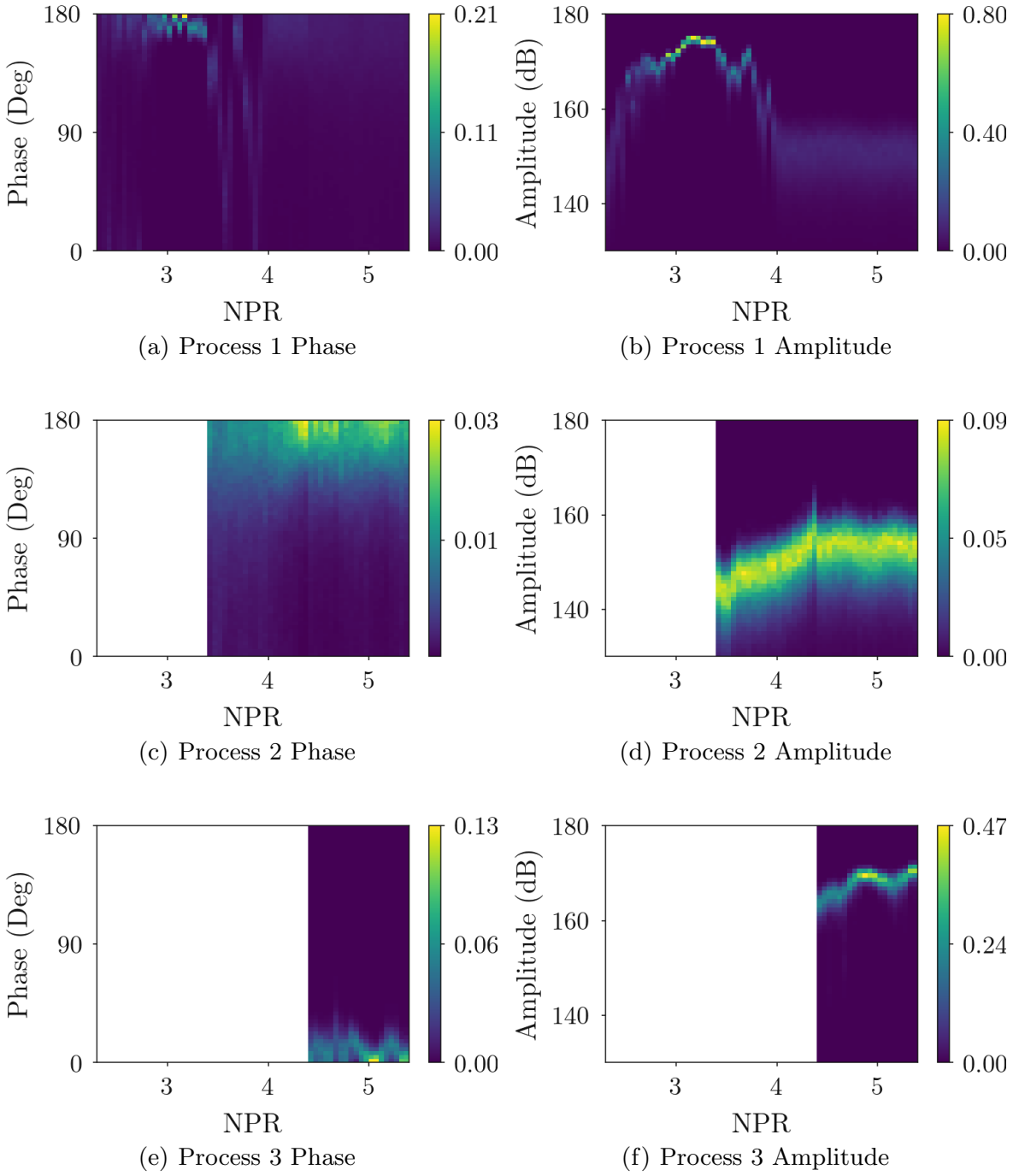

(a) Process 1 Phase (b) Process 1 Amplitude

(c) Process 2 Phase (d) Process 2 Amplitude

(e) Process 3 Phase (f) Process 3 Amplitude

FIGURE 6. Phase and amplitude response from Processes 1,2,3. Colour-bars represent histogram probability density.

low interruption rate (approximately 2 %). This interruption rate then increases when NPR > 3.9.

Figure 8 shows the distribution of interruption duration along Processes 1 and 2. The duration values are non-dimensionalised by the respective screech period of the tone. For brevity, Process 3 has been omitted as similar behaviour is observed. The higher NPR values (NPR $\geqslant 3.5$) where the interruptions are observed have an interruption duration lasting on the order of 5-15 acoustic screech periods. The screech tone is approximately 10 kHz, which is well resolved by the acquisition rate and microphone frequency limit of 250 kHz and 100 kHz respectively. The coupling feedback-loop and the interruption

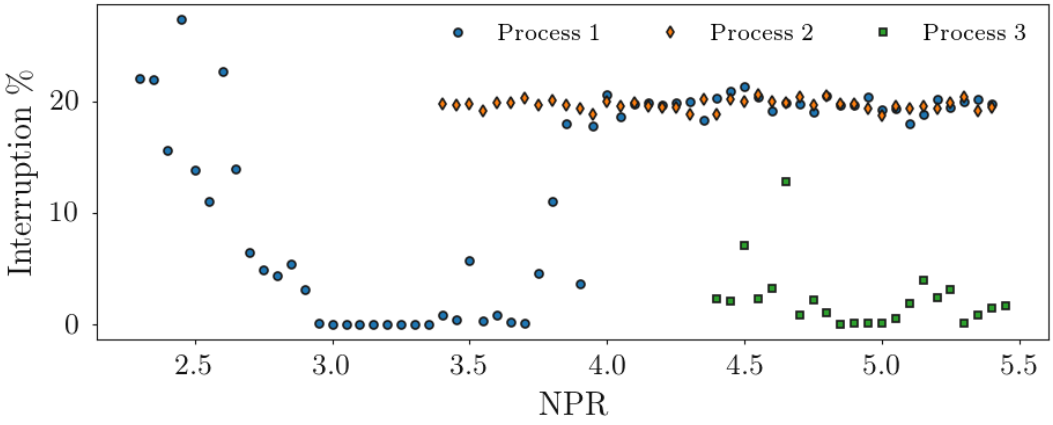

FIGURE 7. Percentage of acoustic interruptions detected within the Hilbert amplitude acoustic signals across NPR for each process.

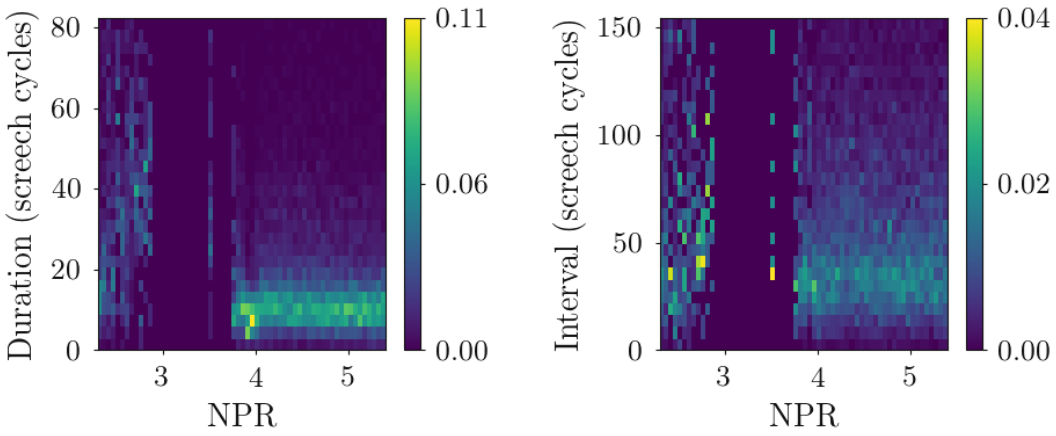

(a) Process 1 (b) Process 1

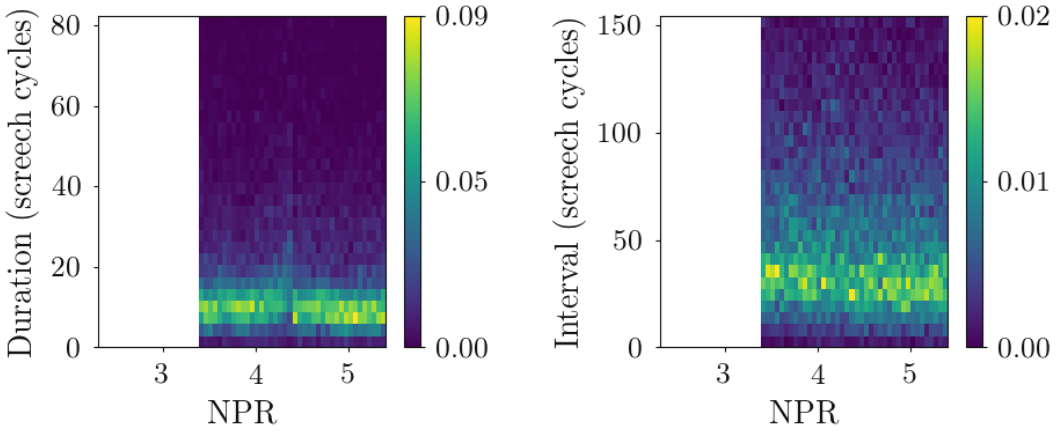

(c) Process 2 (d) Process 2

FIGURE 8. Distribution of interruption duration and interval histograms across Process 1 and 2. Colour-bars represent histogram probability density.

duration therefore operate within an order of magnitude. In contrast, the interruptions in the region $2.5 \leqslant \mathrm{NPR} \leqslant 3.0$ show timescales with a significantly wider distribution.

The duration between interruption events along Process 1 and 2 are shown in Figures 8(b) and 8(d) respectively. An interval is defined here from the end of one interruption

to the beginning of the next. For the higher NPR values, clustering of the timescales is observed around 20-30 screech cycles with a skewed distribution towards longer duration intervals of up to 150 cycles. For lower NPR values the shortest timescales appear randomly distributed above approximately 20 screech cycles.

4.3. *On whether interruptions occur in both jets simultaneously*

While there is evidence that at some conditions there are interruptions in the tones associated with aeroacoustic feedback, is it not yet clear whether these interruptions are restricted to a single jet, or experienced by both jets simultaneously. To address this question, joint-histograms of bandpass-Hilbert process amplitude from the two microphones are shown for selected NPRs in Figure 9. Figure 9(a) shows NPR = 2.75, for which both microphones demonstrate a narrow distribution in amplitude. Similar behaviour is observed for NPR = 3.20 in Figure 9(d). This same narrow amplitude is observed for Process 3 at NPR = 4.60. Figures 9(g), 9(h), 9(j), 9(k) 9(m), and 9(n) - which correspond to NPR = 3.85, 4.30, and 4.60 respectively, correspond to regions where a high degree of tonal interruption is observed. Process 1 at NPR = 3.85 is shown in Figure 9(g). An upper-right corner distribution is observed, which suggests that reductions in the tonal amplitude of one jet do not correlate with reductions in acoustic emission from the opposing jet. The distribution shows the highest probability state is that of both jets producing high-amplitude tones. The horizontal and vertical distribution tails indicate that when interruptions do occur in one jet, they do not occur in the other jet at the same time; the interruptions are essentially anti-correlated. Conversely, correlated interruption behaviour is observed in Figures 9(h), 9(j), 9(k) 9(m), and 9(n), which is represented by a fan shaped distribution. This indicates that there are moments in time where both jets simultaneously experience tonal interruption emission, and few events where only one jet is interrupted. Having considered the relationship between the jets, consideration is now given as to the relationship between interruptions of the three feedback processes in a given jet.

4.4. *On the correlation between an individual jet's screech tones*

Joint-histograms of the same microphone examining bandpass-Hilbert amplitude signals are presented in Figure 10. For the three cases considered, it is clear that the processes produce tones simultaneously. For Processes 1 and 2 at NPR = 4.0, the interruption phenomena are associated with a distributed skewness with a tail towards lower values, evident in the fan shape (Figure 10(a)). At this operating condition, there is no clear relationship between the processes; at times both are active, at other times only one is active, and at times both are interrupted.

At NPR = 5.0, Process 3 is very steady, and does not exhibit any interruptions in tone, as per Figure 7. At this condition, both Processes 1 and 2 are unsteady, and have a wide amplitude distribution. The steadiness of Process 3 makes clear that the tones produced by all the processes are not mutually exclusive; the tone associated with Process 3 is always present at this pressure ratio, with the (much weaker) tones associated with Processes 1 and 2 appearing intermittently. This is in contrast with some observations for isolated screeching jets, such as the analysis of Mancinelli *et al.* (2019) using the wavelet transform. In that work, the A1 and A2 (toroidal) modes were shown to be mutually exclusive, with switching between them occurring on timescales of seconds. An interim summary of the results of the acoustic study is provided in the following section, prior to a consideration of the hydrodynamic field.

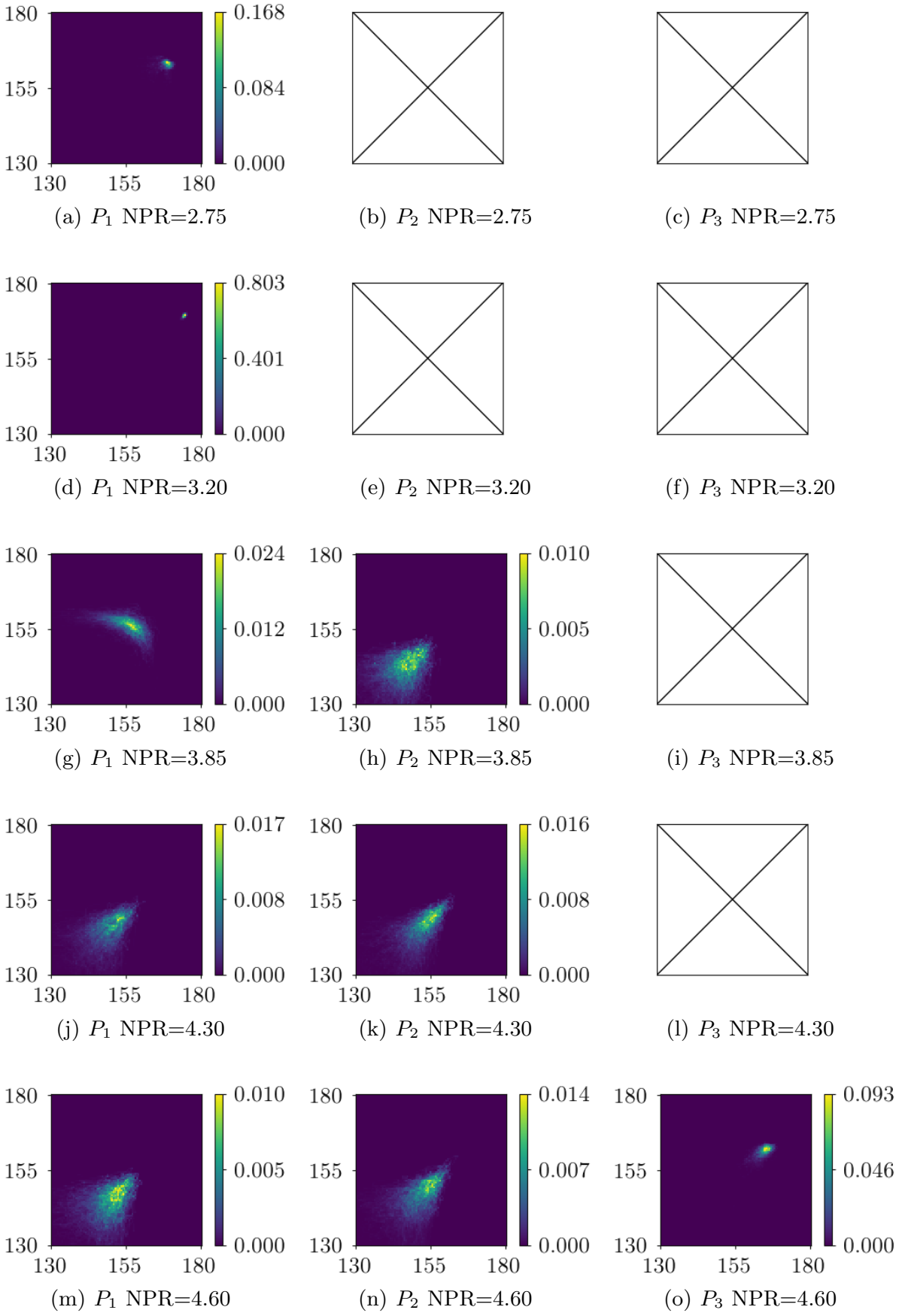

FIGURE 9. Bandpass-Hilbert amplitude joint histograms for various NPRs. horizontal axis represents microphone 1 in dB, vertical axis represents microphone 2 in dB. P_1, P_2, P_3 represents Process 1, 2, and 3 respectively.

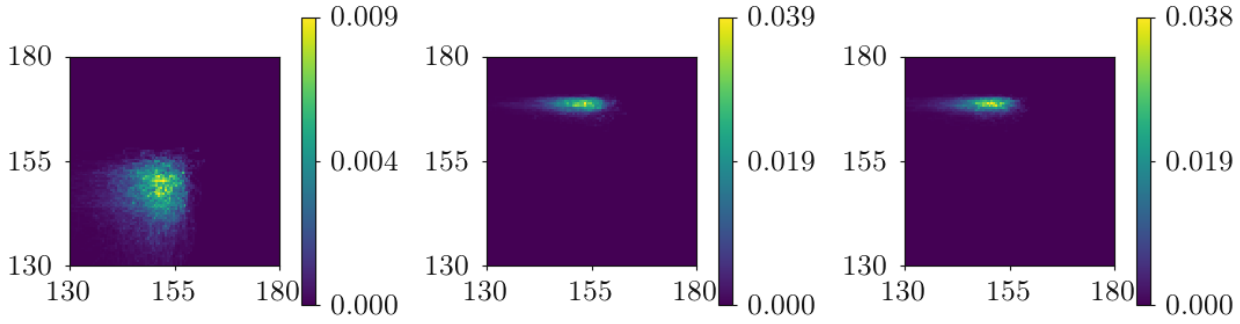

(a) P_1 vs. P_2, NPR=4.0 (b) P_2 vs. P_3, NPR=5.0 (c) P_1 vs. P_3, NPR=5.0

FIGURE 10. Joint histograms of bandpass-Hilbert amplitude (dB) response between two processes. Axes are for a single microphone in dB. P_1, P_2, P_3 correspond to Process 1, 2, and 3 respectively. P_1 vs. P_2 corresponds to P_1 on the vertical and P_2 on the horizontal axes. Colour-bars represent histogram probability density.

4.5. *Interim summary - Acoustic field*

Across the range of operating parameters considered here, the twin-jet system exhibits between one and three aeroacoustic resonance processes. Analysis of the acoustic field has demonstrated that some of these processes are acoustically unsteady, showing periods of interruption. These interruptions can affect either one or both jets. The tones associated with the three resonance processes are not mutually exclusive and in fact are generally uncorrelated. The farfield acoustic tones are signatures of events occurring in the hydrodynamic field of the jet. A direct examination of the hydrodynamic field, via the construction of reduced-order models, is thus the focus of the remainder of the paper.

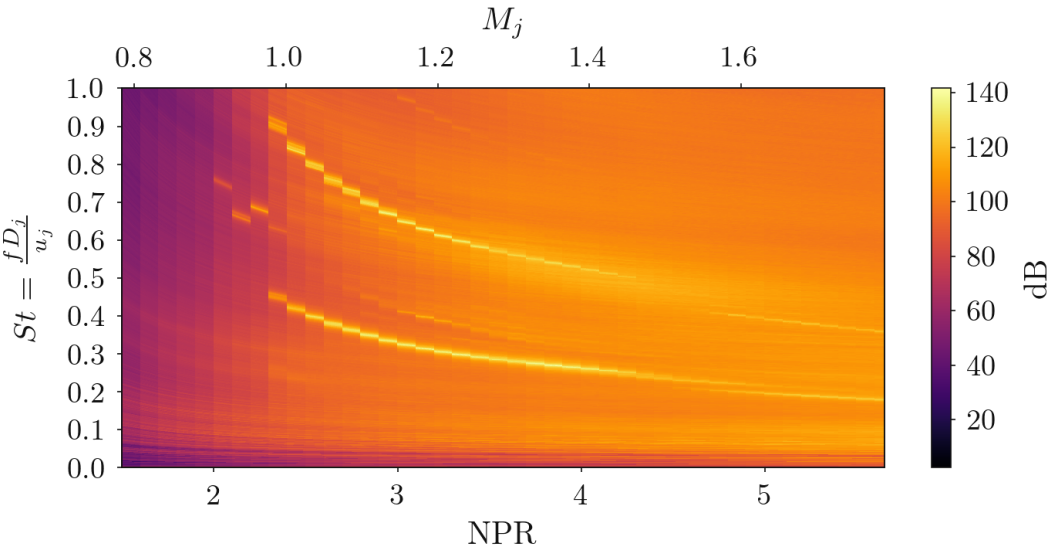

FIGURE 11. Power spectral density vs. NPR of cases for which the PIV measurements of Bell *et al.* (2018) were obtained.

5. The hydrodynamic field of coupled underexpanded jets

This section presents an examination of the PIV dataset described in section 2.2.1. As well as providing quantification of the hydrodynamic field, PIV has the additional advantage that each snapshot is essentially instantaneous with respect to the timescales of the flow. Therefore there is no concern of temporal resolution as with the acoustic analysis. Conversely, the repetition rate of the PIV in Bell *et al.* (2018) was approximately 0.5 Hz and thus each snapshot is essentially statistically independent with respect to other snapshots. Resonant processes in jets are generally amenable to decomposition via Proper Orthogonal Decomposition (POD) (Lumley 1967; Sirovich 1987*a*,*b*). The fluctuations associated with resonance are typically well described using a relatively small number of modes (Edgington-Mitchell *et al.* 2014*a*, 2015; Weightman *et al.* 2016, 2017; Berry *et al.* 2017; Tan *et al.* 2017; Mancinelli *et al.* 2018; Crawley *et al.* 2018). In the following analysis, POD is used to educe the coherent structures that form the downstream-convecting component of the aeroacoustic resonance process, and to analyse the relationship between simultaneous processes.

The PIV statistics of the $s/D = 3$ twin-jet setup were described in previous work of Bell *et al.* (2018) and were recorded on Facility Two (section 2.2.1). Figure 11 presents a contour of the PSD of acoustic amplitude as a function of NPR. Many of the same phenomena are observed in both facilities, with the appearance of a lower frequency tone (Process 3) at higher pressures. However, the exact NPR where this tone is first observed is different to that observed in the data of Knast *et al.* (2018). This result is unsurprising, given the now well-known sensitivity of aeroacoustic resonance to acoustic boundary conditions (Weightman *et al.* 2019). The higher-frequency tone appears to correspond to Process 1, and the lower frequency tone to Process 3. Without the ability to measure coherence (only one microphone could be placed in the PIV enclosure), the presence of Process 2 could not be ascertained. Given the sensitivity of these processes to the facility, a third dataset was acquired in the Gas Dynamics and Turbulence Laboratory within the Aerospace Research Center at The Ohio State University (OSU), as detailed in appendix B. These measurements were performed for the same nozzle spacing, and at the same pressure ratios, but in an anechoic facility, and with nozzles of different internal contour and lip thickness. The OSU data reinforces that mode staging is highly

facility-specific, but critically many of the same qualitative phenomena are observed: an anti-symmetric coupling at lower pressures, an intermediate region of indeterminate phase, and symmetric coupling at higher pressures. While Process 2 could only be clearly observed in the data presented in the first half of this paper, Processes 1 and 3 were observed in all facilities. These two processes are thus the focus of the remainder of the study. Two conditions are chosen for further analysis via PIV at NPR = 4.6 and 5.0. At the lower pressure, Process 1 is the stronger tone (and in a regime where it exhibits significant unsteadiness), while at the higher pressure, Process 3 is expected to be steady and high amplitude.

5.1. *Modal Decomposition Methodology*

POD constructs a set of basis modes that optimally represent the ensemble of energetic fluctuating velocities. The decomposed modes are orthogonal and ranked by eigenvalue. The eigenvalues are correlated to the specific kinetic energy of each mode. Here the authors use the snapshot POD variation first described by (Lumley 1967; Sirovich 1987*a*,*b*) and recently reviewed in Taira *et al.* (2017).

The velocity fields $\boldsymbol{x}(t)$ are stacked as vectors into the matrix X.

$$X = [\boldsymbol{x}(t_1), \boldsymbol{x}(t_2), \ldots, \boldsymbol{x}(t_i), \ldots, \boldsymbol{x}(t_n)] \in \mathbb{R}^{n \times m}. \tag{5.1}$$

where t_i is used to indicate snapshot time number of total snapshots of length n. The autocorrelation matrix, R, takes the form

$$R = X^T X. \tag{5.2}$$

The eigenproblem is then formed by

$$R\boldsymbol{\Psi}_j = \lambda_j \boldsymbol{\Psi}_j \tag{5.3}$$

where the eigensolution is made up from eigenvectors, $\boldsymbol{\Psi}_j$ and eigenvalues, λ_j. Both are a function of mode number denoted by subscript j. The eigensolution is reordered by eigenvalue such that $\lambda_1 > \lambda_2 > \ldots \lambda_m = 0$.

The POD mode shapes are found by calculating ϕ_j from $\boldsymbol{\Psi}_j$:

$$\boldsymbol{\phi_j} = X\boldsymbol{\Psi}_j \frac{1}{\sqrt{\lambda_j}},\ j = 1, 2, \ldots, m. \tag{5.4}$$

Finally, the mode coefficient for a given mode at a given snapshot is represented as

$$a_j(t) = X \cdot \boldsymbol{\phi_j} \tag{5.5}$$

The aforementioned method results in an energy-based decomposition, though with the use of planar PIV data the modes are ranked by their two-component specific turbulent kinetic energy. The authors have performed the decomposition using the velocity matrix as stated in Equation 5.1, using only the transverse velocity u_y as per equation 5.6. A decomposition based only on the transverse velocity component removes the shear-thickness mode from the high-energy modes, simplifying the identification of relevant structures in the flow (Weightman *et al.* 2018).

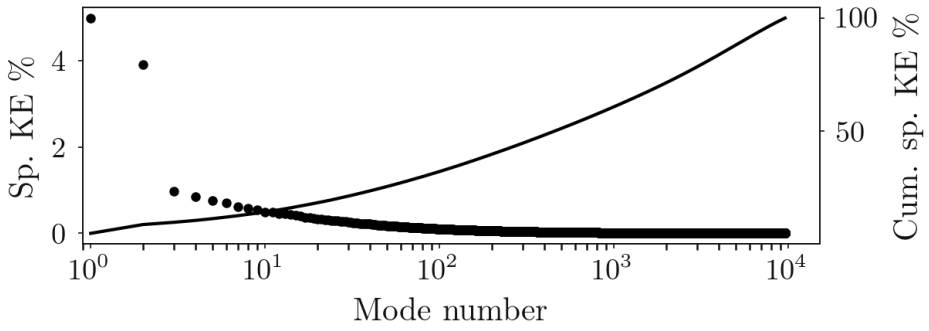

(a) POD ranked mode kinetic energy (KE) for NPR = 5.0. Dots indicate individual mode specific (sp.) energy contribution. Line shows cumulative specific energy contribution.

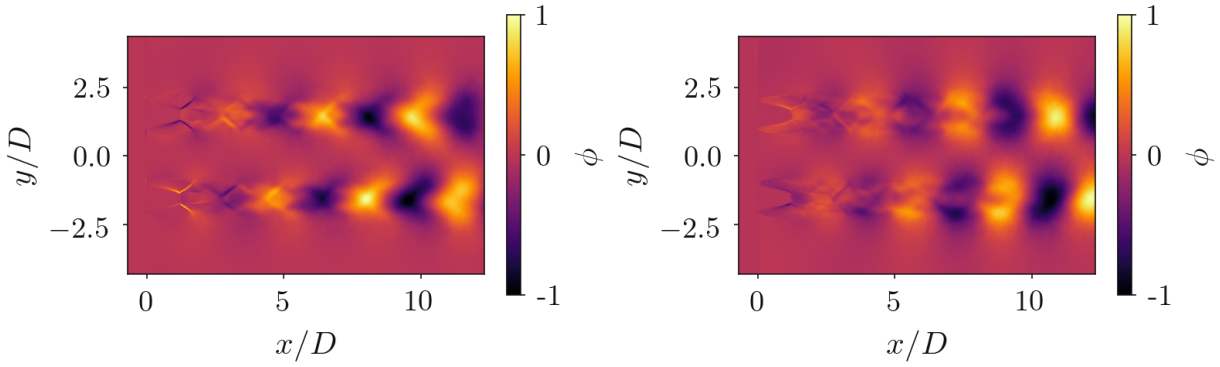

(b) ϕ_1 (c) ϕ_2

FIGURE 12. POD modes for NPR = 5.0.

$$X = [\boldsymbol{x}(t_1), \boldsymbol{x}(t_2), \ldots, \boldsymbol{x}(t_i), \ldots, \boldsymbol{x}(t_n)] = \begin{bmatrix} {u_y}^{1,1} & {u_y}^{1,2} & \cdots & {u_y}^{1,n} \\ {u_y}^{2,1} & {u_y}^{2,2} & \cdots & {u_y}^{2,n} \\ \vdots & \vdots & \ddots & \vdots \\ {u_y}^{m,1} & {u_y}^{m,2} & \cdots & {u_y}^{m,n} \end{bmatrix}. \tag{5.6}$$

5.2. *Modal decomposition when coupling is steady:* NPR = 5.0

At NPR = 5.0 the flow is expected to be dominated by a steady, high-amplitude tone associated with Process 3. The mode energy distribution for this case is shown in Figure 12(a). Two leading modes are evident (modes 1 and 2) followed by a trail-off of lower energy modes.

The mode shapes for the two leading modes (1 and 2) are presented in Figures 12(b) and 12(c). Dark and light bands indicate negative and positive u_y velocity respectively. The leading mode pair have a similar spatial structure with a 90 degree phase offset, indicative of a travelling wave, in this case associated with the Kelvin-Helmholtz wavepacket (Taira *et al.* 2017). The transverse velocity fluctuations are mirrored about the symmetry plane between the two jets, representing a symmetric coupling. This symmetry is consistent with the zero degree acoustic phase associated with Process 3 demonstrated in figure 3. At this operating condition, both the acoustic and hydrodynamic fields are relatively straightforward to interpret; the twin-jet system is characterised by steady symmetric coupling about the symmetry plane, producing a high-amplitude tone with no phase delay between opposite sides of the system.

5.3. *Modal decomposition when coupling is unsteady:* NPR = 4.6

At NPR = 4.6 11 suggests the presence of tones associated with both Process 1 and Process 2. The acoustic analysis in Section 4.1 suggests that tones in this region are characterised by unsteadiness and tonal interruption. The POD mode energy spectrum presented in Figure 13(a) exhibits four leading modes as opposed to two, followed by trailing lower-energy modes. The four leading modes combined contain less energy ($\approx 6\,\%$ of total specific energy) than the two leading modes of the NPR = 5.0 case ($\approx 9\,\%$ of total specific energy).

The mode shapes associated with the four highest-energy modes are presented in figures 13(b), 13(c), 13(d), and 13(e). The spatial structure of the modes is somewhat reminiscent of the leading modes for NPR = 5.0, but there are uneven fluctuation levels in the two jets, and there is no clear modal pairing between the four modes. Where the modal decomposition educed a symmetric coupling behaviour for the higher pressure ratio, no such simple interpretation is possible here. All four POD modes present evidence that the individual jets are characterized by a flapping or helical instability, but the coupling across the symmetry plane is unclear. In an attempt to provide greater clarity, POD is applied to each jet individually by truncating the domain at $y/D = 0$.

The mode-energy distributions for the decompositions performed on the lower and upper jet sub-domains are presented in figures 14(a) and 14(b) respectively. These sub-domain decompositions result in two leading modes, as opposed to four observed for the full-field decomposition. The leading modes of the subsets are also higher in energy, each with approximately $\approx 2.5\,\%$ of total specific energy compared to $\approx 1.2\,\%$ as observed for the full-field.

The lower-jet mode shapes for modes 1 and 2 are presented in figures 15(b) and 15(d). The upper-jet mode shapes for modes 1 and 2 are presented in Figures 15(a) and 15(c). In both cases these modes clearly form a pair, representing a periodic oscillation typical of aeroacoustic resonance processes. Thus when considered individually, the jets are observed to oscillate in the manner of an isolated screeching jet. This is also the case for this higher pressure ratio and has been omitted for brevity. The lack of clarity in the modes resulting from the full-field decomposition of the lower pressure ratio thus must be linked to the manner in which these oscillations couple together. The resemblance of lower-jet modes 1 & 2 to the full-field modes 1 & 2 is similar. A spatial correlation analysis identified that the highest matches for full-field modes 1-4 corresponded to lower-jet modes 1 & 2 and upper-jet modes 3 & 4 respectively. Therefore, the full-field mode pairs are now examined in further detail to extract the relationship between the overall coupling mode shape to that of the individual jets.

As mentioned, one advantage of the PIV with respect to the acoustic measurements is that each snapshot is effectively an instantaneous record of the flow. This makes the technique ideal for examining the interaction between multiple feedback modes or between oscillations of individual jets. The two leading modes $\phi_{1,2}$ for the subdomain represent the oscillatory behaviour of an individual jet, while the snapshot mode coefficient $a_j(t)$ indicates the contribution of this oscillatory behaviour to a given snapshot t_i. Thus the quantity $|a_{1,2}| = \sqrt{a_1^2(t) + a_2^2(t)}$ indicates how strongly the oscillation is present for a particular snapshot for this leading mode pair ($j = 1$ & 2), providing a lens through which to examine the coupling between the two jets. Figure 16 presents a joint-histogram of $|a_{1,2}|$ for the lower and upper jet subdomains (colour contours), overlaid with the individual snapshots (dots). This map can be divided into four quadrants as shown in figure 16(b). On the lower left are snapshots where neither jet is oscillating strongly, while in the upper right quadrant are snapshots where both jets are oscillating strongly. The

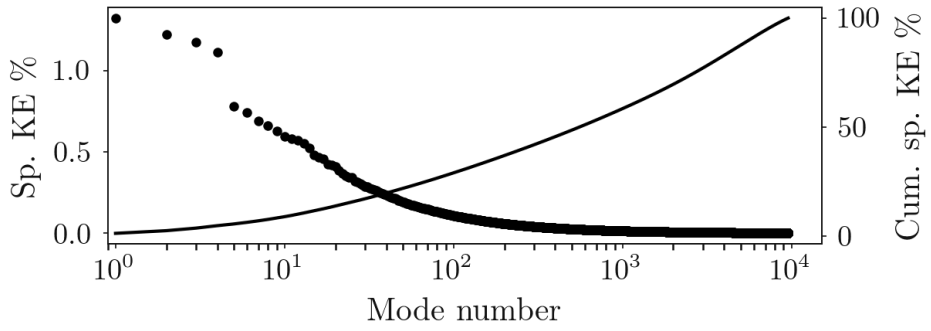

(a) POD ranked mode energy for NPR = 4.6. Dots indicate individual mode specific energy contribution. Line shows cumulative specific energy contribution.

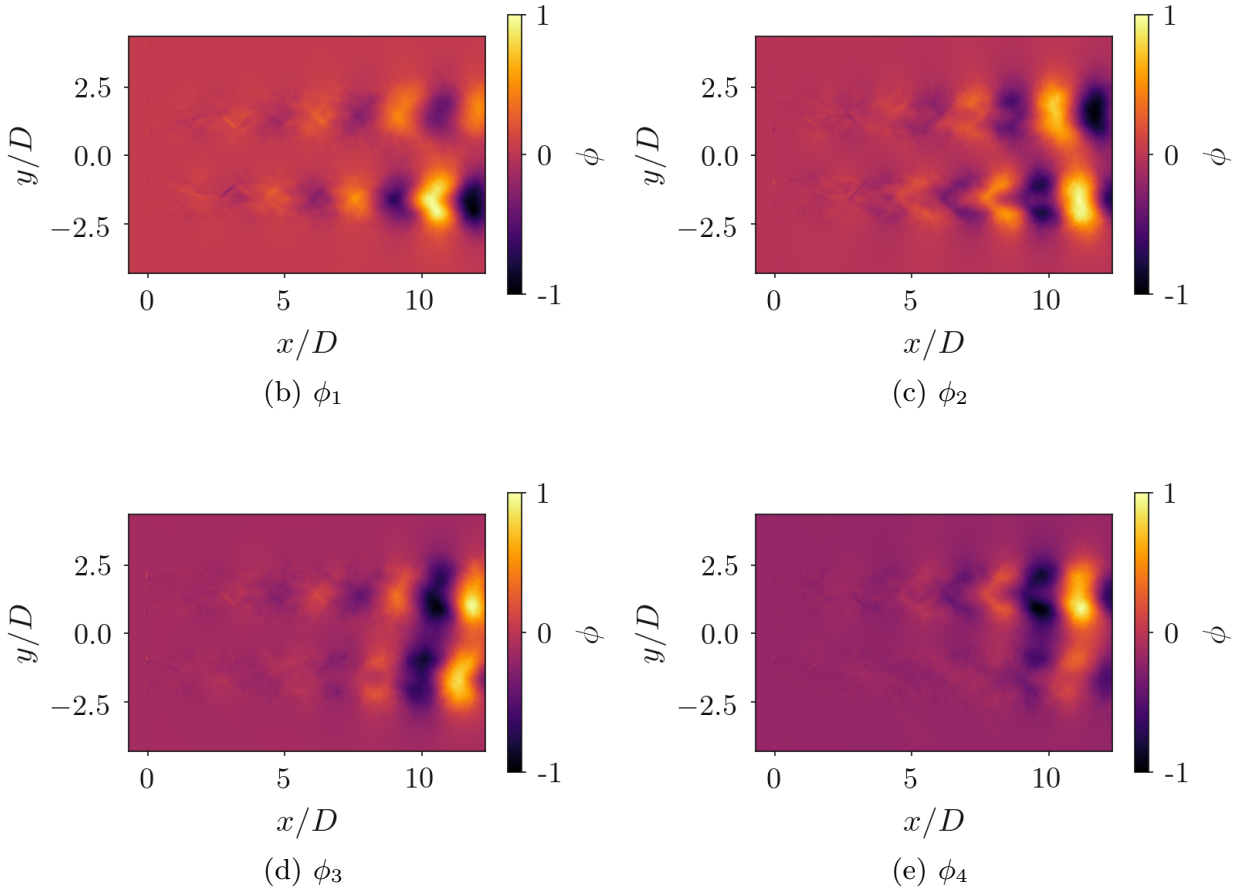

(b) ϕ_1 (c) ϕ_2

(d) ϕ_3 (e) ϕ_4

FIGURE 13. POD modes for NPR = 4.6.

remaining two quadrants represent snapshots where one jet is oscillating strongly, and the other is not. Overall, the correlation between the mode coefficients is weak; a large fraction of the snapshots indicate one jet oscillating strongly, while the other oscillates weakly or not at all.

Classifying the data by the POD eigenvectors enables a form of conditional sampling: A reduced dataset is defined based on the eigenvector magnitude, keeping only the snapshots whose value of $|a_{1,2}|$ fall in the upper quartile. These snapshots are indicated by the white scatter-points (using the lower jet as an example) in Figure 16. Once this reduced dataset is defined, a new proper orthogonal decomposition is performed on it, with the resultant mode energy distribution presented in Figure 16(c). When

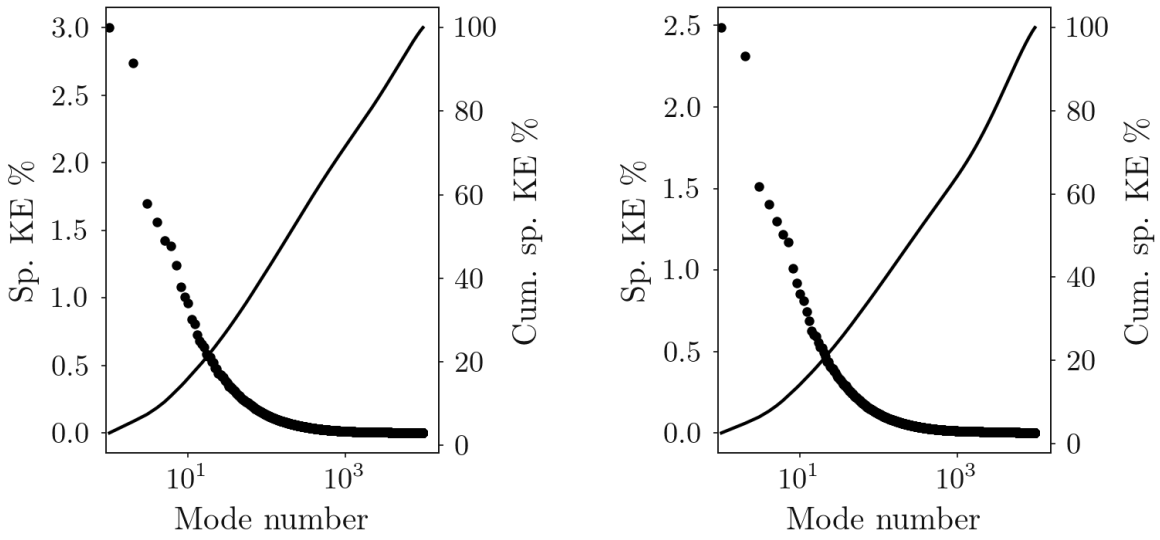

(a) Lower-jet (b) Upper-jet

FIGURE 14. Upper and lower jet subset POD energy for NPR = 4.6. Dots indicate individual mode specific energy contribution. Line shows cumulative specific energy contribution.

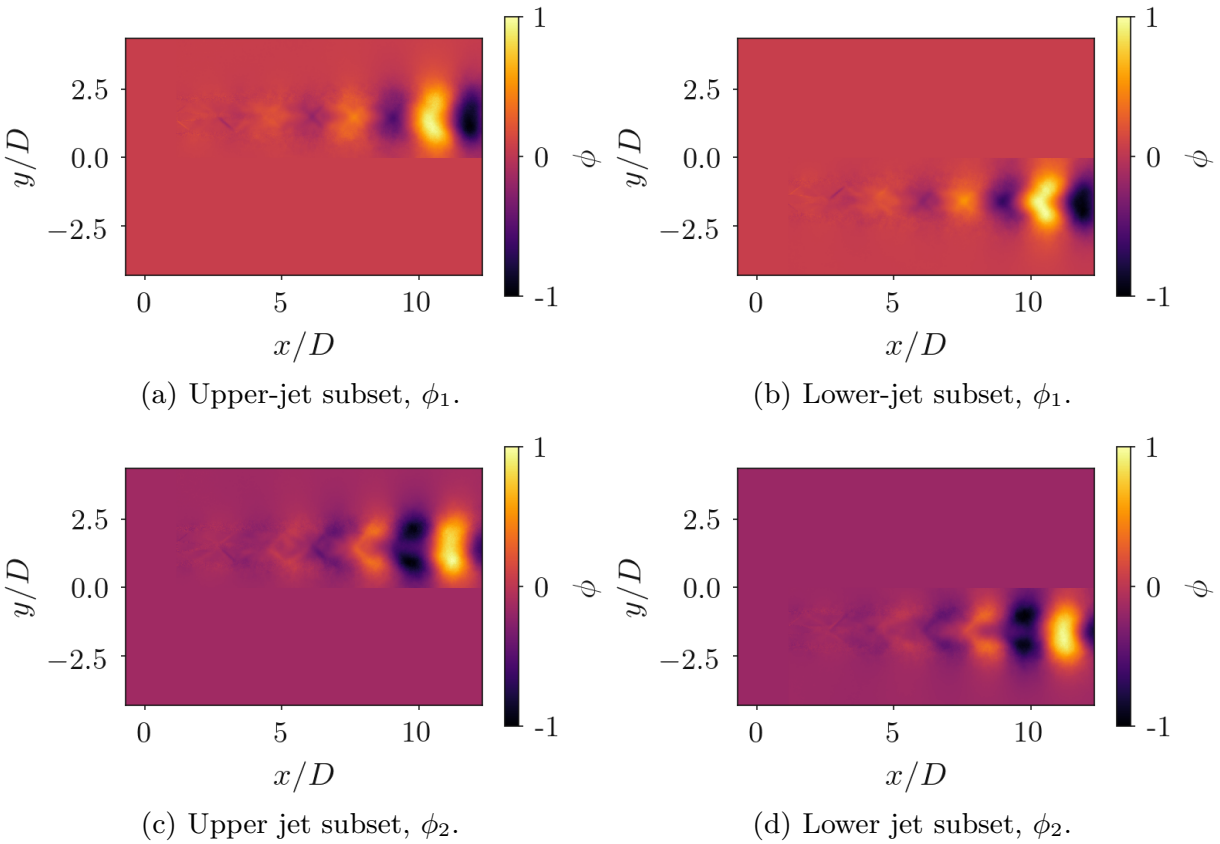

(a) Upper-jet subset, ϕ_1. (b) Lower-jet subset, ϕ_1.

(c) Upper jet subset, ϕ_2. (d) Lower jet subset, ϕ_2.

FIGURE 15. Subset POD modes of the lower and upper jets for NPR = 4.6.

conditionally sampled in this way, the oscillation of each individual jet is captured with separate modal pairs, as per Figures 17(a), 17(b), 17(c), 17(d). The strong oscillatory motion captured by each modal pair is associated with weak fluctuations in the other jet, indicating that the jets influence each other, but that their overall motion is not necessarily coupled. The same result is observed when the conditional sampling is

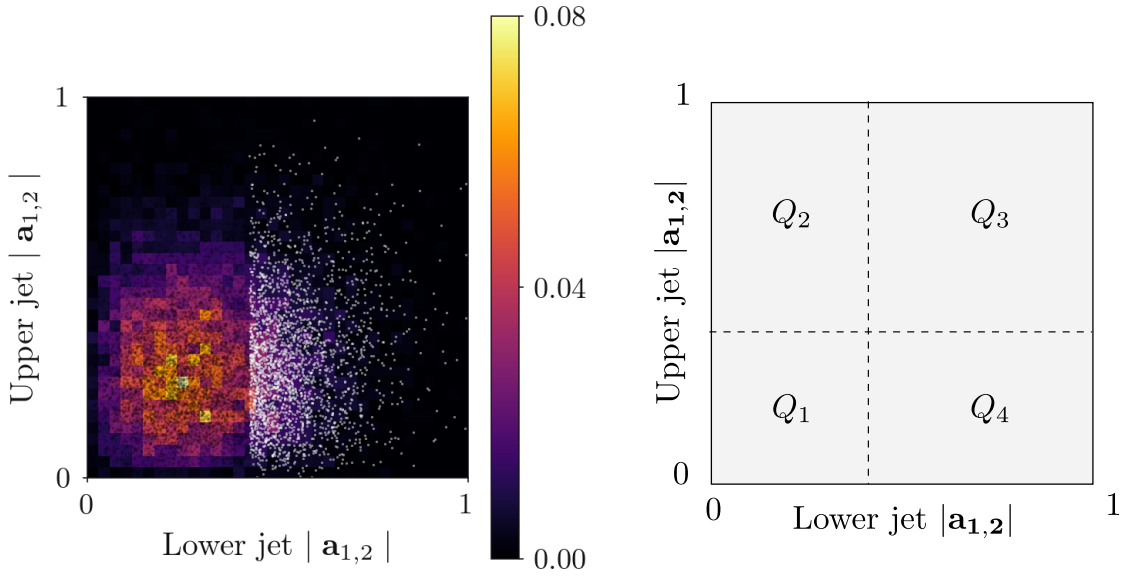

(a) POD mode energy coefficient distribution, combined with snapshot selection filter for the high mode amplitudes of the lower-jet only. The selective filtering (greater than the 75^{th} percentile of lower-jet mode energy) is shown by white coloured scatter points. Colour-bar represents the probability density of the histogram.

(b) Schematic of the four quadrants divided by the dominant mode coefficient levels. Snapshots falling within Q_1 have simultaneously low upper and lower-jet energy. Those falling within $Q_2/4$ have high upper-jet but low lower-jet energy or vice-versa. And snapshots falling within Q_4 have high energy in both jets.

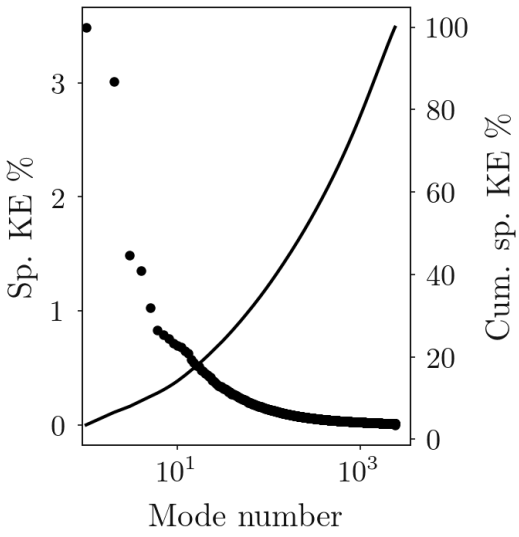

(c) POD mode energy distribution for POD performed on the full field with the 75^{th} snapshot filter extracting high energy snapshots, applied to the lower-jet only. Dots indicate individual mode specific energy contribution. Line shows cumulative specific energy contribution.

FIGURE 16. Snapshots and mode distribution for the NPR = 4.6 full-field dataset filtered for when the lower-jet is strong.

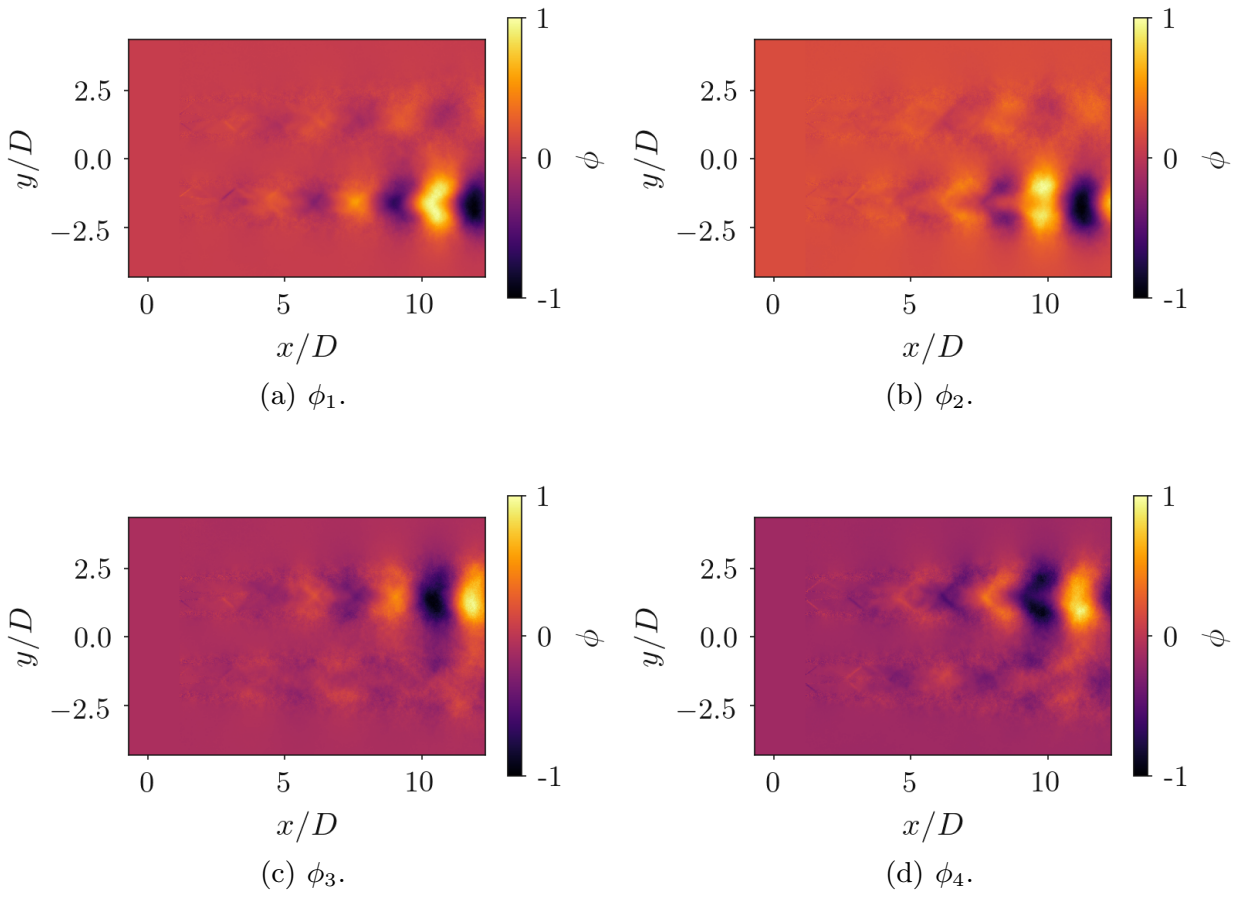

(a) ϕ_1. (b) ϕ_2.

(c) ϕ_3. (d) ϕ_4.

FIGURE 17. Leading mode shapes for POD performed on the snapshots above the 75$^{\text{th}}$ percentile lower-jet snapshot energy filter (figure 16(a)). NPR = 4.6.

performed based on the eigenvector magnitudes of the upper jet, but with the mode order reversed.

A final conditional sampling is performed including only snapshots in the upper quartile for both the upper and lower jet; these snapshots should represent moments when both jets are oscillating strongly. The chosen snapshots are shown in Figure 18(a) again as white scatter-markers above the 75$^{\text{th}}$ percentile of mode energy.

The mode energy distribution for the filtered subset is shown in Figure 18(b). The authors observe that there are 5 leading modes, the first four are examined in Figures 19(a) - 19(d), the fifth mode contained a mode-shape indicative of shear-layer variance and was determined to be unrelated to the physics relevant for mode classification as examined here (Weightman *et al.* 2019).

Mode shapes ϕ_1 and ϕ_2 (Figures 19(a) and 19(b)) show a coupled symmetric oscillation between the two jets, and mode shapes ϕ_3 and ϕ_4 (Figures 19(c) and 19(d)) show a coupled anti-symmetric oscillation. Unlike the previous decompositions, the modes from this subset of data capture fluctuations equal in strength in both jets. Though this subset contains only a small fraction of the total snapshots, at least some of the time there is evidence of both symmetric and anti-symmetric coupling about the symmetry plane. Further, this demonstrates that when both jets are oscillating most strongly, this is associated with a coupling between the plumes. The two tones evident in Figure 11 at this condition, are suggested to be linked to the two modes of coupling observed in this subset of data. The first POD mode pair is linked to the lower-frequency tone associated

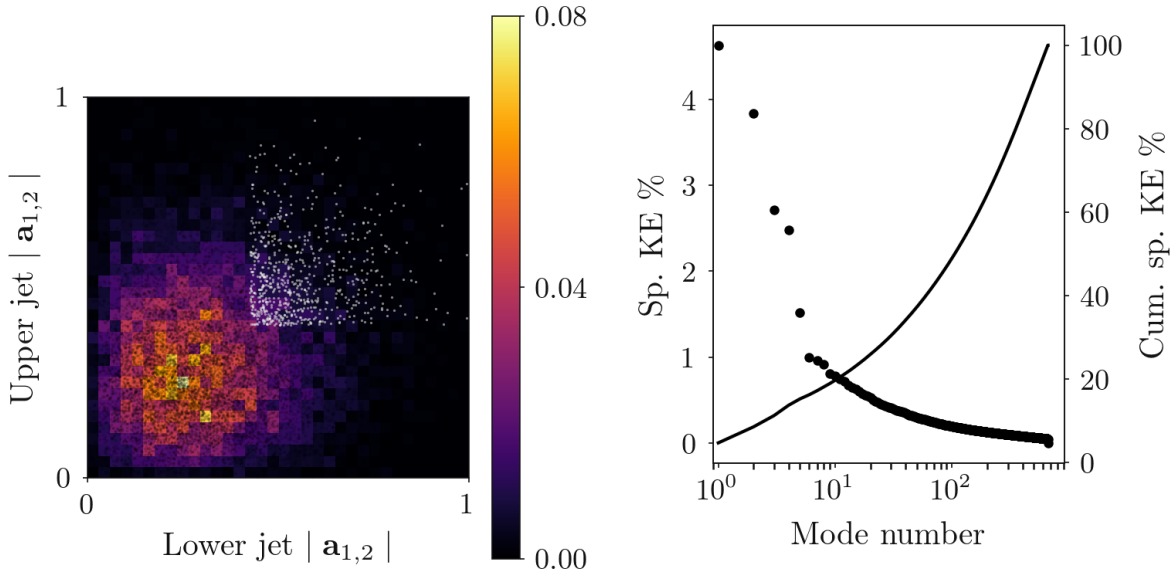

(a) POD mode energy coefficient distribution, combined with snapshot selection filter for the high mode amplitudes of both the lower and upper jets. Colour-bar represents the probability density of the histogram.

(b) POD mode energy distribution for POD performed on the full field with the 75$^{\text{th}}$ snapshot filter applied to both the lower and upper jets. Dots indicate individual mode specific energy contribution. Line shows cumulative specific energy contribution.

FIGURE 18. Snapshots and mode distribution for the NPR = 4.6 full-field dataset filtered for when both the lower and upper jets are strong.

with Process 3, while the second POD mode pair is associated with the higher-frequency tone associated with Process 1.

Therefore, when considering both the acoustic and hydrodynamic data, the complex behaviour in the phase anomaly region starts to become clearer. At NPR = 4.6, there are moments when neither jet is oscillating, when one is oscillating, and when both are oscillating. When both jets oscillate strongly, they may couple together either symmetrically or anti-symmetrically. Despite the presence of two different tones, when considered in isolation the individual jets only exhibit structures with one wavelength, which further suggests that the two tones are associated with two distinct modes of coupling. It is likely that when either jet is not oscillating, this is the condition that generates the interruption as observed in the time-resolved acoustic section. When either jet is oscillating, then it generates a screech tone that is generally independent from the other jet. Within the time-resolved acoustics, the tones from individual jets were generally uncorrelated.

As a sanity check, the various POD subdomain flow-fields have been reconstructed using the filtered snapshot information and are included as supplementary video 1 for the reader. The reconstructed velocity animation comprises of the snapshot reconstruction based on their energy contained in the first twenty POD modes. Each snapshot is assigned a phase based on its position in the mode coefficient phase-space of a particular high-energy mode pair. Reconstructed snapshots are assigned a 10 degree bin and ensemble averaged to produce a phase animation. The following reconstructions are included:

- NPR = 5.0: Leading mode pair 1 & 2 showing a very clear symmetric oscillation
- NPR = 4.6: Representations of the flow field where the lower-jet is comprised of high-energy snapshots: Mode pair 1 & 2
- NPR = 4.6: Representations of the flow field where the upper-jet is comprised of high-energy snapshots: Mode pair 1 & 2

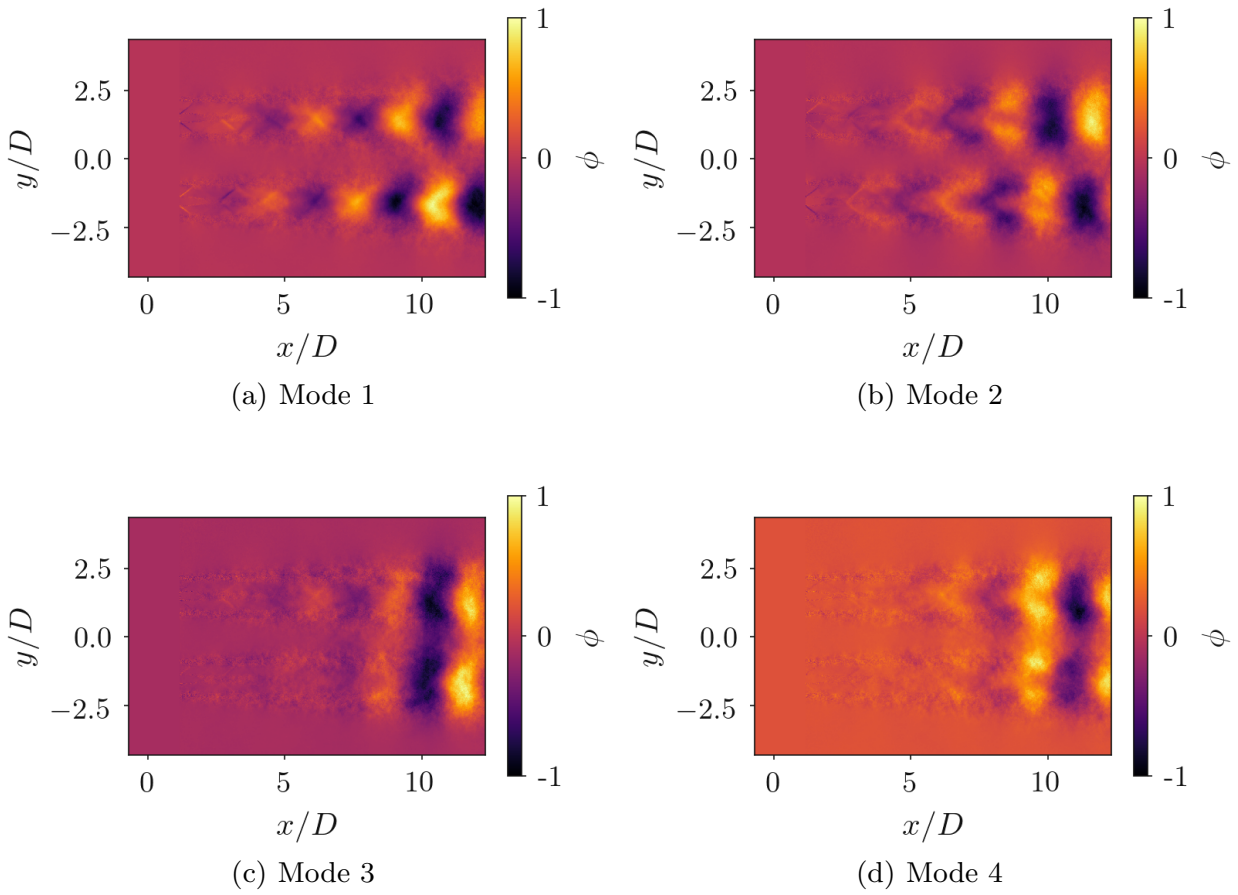

(a) Mode 1 (b) Mode 2

(c) Mode 3 (d) Mode 4

FIGURE 19. Leading mode shapes for POD performed on the snapshots above the 75$^{\text{th}}$ percentile lower-jet and upper-jet snapshot energy filter (figure 18(a)). NPR = 4.6.

- NPR = 4.6: Representations of the flow field where the upper-jet and lower-jet are both comprised of high-energy snapshots: Mode pair 1 & 2
- NPR = 4.6: Representations of the flow field where the upper-jet and lower-jet are both comprised of high-energy snapshots: Mode pair 3 & 4

If the aforementioned description is correct, this range of coupling behaviours should be visible in the ultra-high-speed schlieren visualisations of Knast *et al.* (2018). Due to their short time-record length, the schlieren visualisations are qualitative in nature, but should nonetheless suffice to demonstrate the nature of coupling. The authors revisited this dataset, and indeed, the various coupling behaviours are clearly observed in the phase anomaly region (which occurs at a moderately lower pressure in the schlieren/acoustics facility, $3.4 \leqslant \text{NPR} \leqslant 4.4$). A video covering a range of pressure ratios is included as supplementary video 2 and stills for reference are included in appendix D. At low and high pressures, clear anti-symmetric and symmetric coupling behaviour are observed. In the range $3.9 \leqslant \text{NPR} \leqslant 4.4$, the video clips show cases where the left jet oscillates while the right does not, the right jet oscillates while the left does not, both jets oscillate, and neither jet oscillates.

6. Conclusion

At many operating conditions, adjacent supersonic jets couple together, significantly amplifying the aeroacoustic resonance process of jet screech. This coupling can take a number of forms that are well predicted by stability theory. However, regions also exist where the coupling is unsteady. Previous authors have identified these regions of unsteady coupling, classifying them as weakly coupled or erratic (Raman 1998; Knast *et al.* 2018). In this work we have considered this unsteady coupling in more detail, using a range of experimental techniques and analyses.

Data from three facilities were considered at a fixed nozzle spacing of $s/D = 3.0$. All three facilities exhibited at least two continuously varying frequencies assumed to be associated with a particular aeroacoustic feedback process; an additional distinct process was observed in one dataset. At lower pressure ratios, only one process is evident in the data, associated with a steady, high-amplitude, anti-symmetric oscillation about the symmetry plane. As pressure increases, the amplitude of the tone associated with this process and coupling of the jets becomes intermittent. As pressure increases further, an aeroacoustic process linked to a symmetric oscillation about the symmetry plane gains strength, eventually producing a steady, high-amplitude tone at the highest pressures considered. Therefore, there are multiple mechanisms of coupling in twin jet systems, associated with different acoustic tones. In some regions one of these coupling mechanisms dominates and produces a single tone. In other regions there appears to be competition between multiple coupling mechanisms, which results in multiple peaks in the acoustic spectra, all of which are characterized by interruption and unsteadiness. Though at some operating conditions multiple tones exist, analysis of the individual jets suggests structures with only a single wavelength, therefore the tones must arise from different manners of coupling between the jets.

Declaration of Interests

Declaration of Interests. None.

The authors would like to acknowledge Thomas Knast for providing access and reproduction of the high-speed schlieren visualisations. This research benefited from computational resources provided through the National Computational Merit Allocation Scheme, supported by the Australian Government. The computational facilities supporting this project included the Australian National Computational Infrastructure (NCI) Facility, the partner share of the NCI facility provided by Monash University through a ARC LIEF grant and the Multi-modal Australian ScienceS Imaging and Visualisation Environment (MASSIVE). Components of this research were supported through ARC DP190102220.

Appendices

A. Interruption Detection Method

Figure 20(b) shows the time trace of amplitude for a process exhibiting what is deemed interruption free behaviour. Figures 20(a) and 20(c) show the amplitude for processes at NPRs exhibiting acoustic interruptions. The downward spikes in the signals correspond to the interruption events. The black horizontal line in the Figures indicates the ensemble mean value (μ). It is clear that the interruption events make up a small fraction of the total signal. Based on the normal variation in amplitude of a steady signal (approx 5 dB), the authors defined a threshold filter of $\mu - 5\,\mathrm{dB}$ to detect the interruption events. This threshold is shown as a red horizontal line.

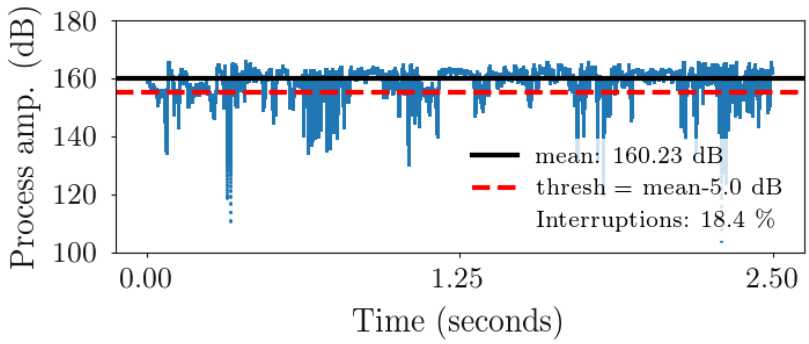

(a) Process 1: Hilbert amplitude signal for NPR = 2.60; characterised by unsteady coupling, interruptions detected.

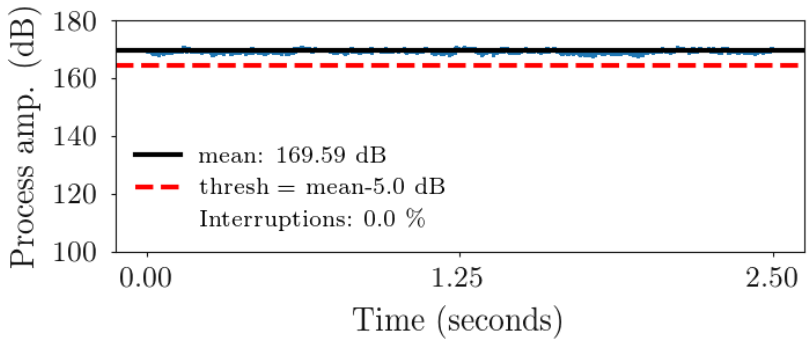

(b) Process 1: Hilbert amplitude signal for NPR = 3.20; characterised by steady coupling, no interruptions detected.

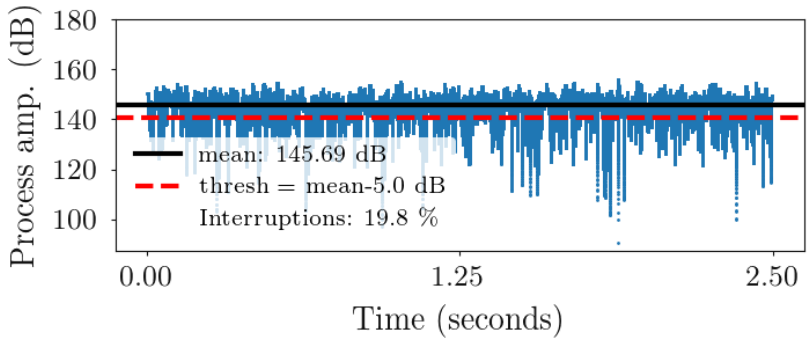

(c) Process 1: Hilbert amplitude signal for NPR = 4.30; characterised by unsteady coupling and acoustic interruption events, many interruption instances detected.

FIGURE 20. Illustration of the interruption detection process, which was used to characterise the duration and frequency of the acoustic interruptions experienced at some NPRs. Figures show process amplitude vs. time. Process amplitude is derived from the bandpass-Hilbert technique used to isolate the transient behaviour of the individual processes present in the acoustic spectra. The black horizontal line indicates the signal mean. The red horizontal line indicates the signal mean - 5 dB. Interruptions are detected where the acoustic signal dips below the red line threshold.

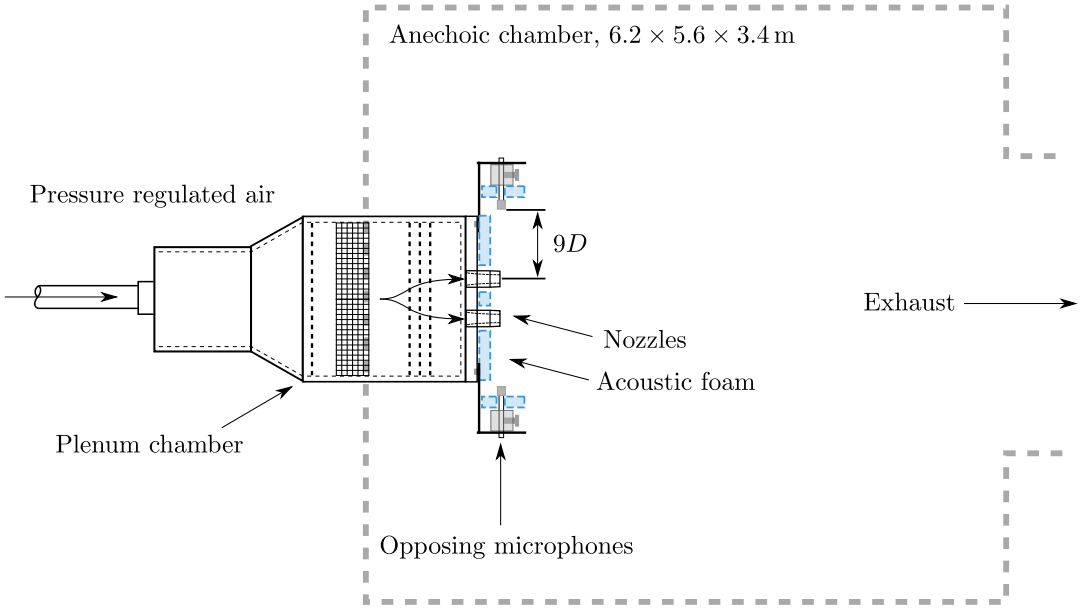

FIGURE 21. Anechoic opposing microphone measurements performed within the anechoic jet facility at The Ohio State University.

B. Facility Three; Additional Opposing Microphone Study for Facility Independence

The final experiment examined the acoustic response between opposing microphones at a different facility to confirm that the observed results are generally impartial to the facility used. The experiments were conducted at the Gas Dynamics and Turbulence Laboratory (GDTL) within the Aerospace Research Center at The Ohio State University (OSU). The jet anechoic chamber facility consists of a $6.2 \times 5.6 \times 3.4$ m room covered with fiberglass wedges with a cutoff frequency of 160 Hz. The jets are fed with compressed air, which originates from large cylindrical tanks at 16 MPa that is regulated down to the desired pressure. The nozzles are mounted on the end of the plenum chamber with a non-dimensional separation distance (s/D) of 3. The nozzle profile is purely converging, with a nozzle exit diameter (D) of 19.05 mm (3/4").

B.1. *Setup and Microphone Array*

This acoustic based phase study was performed using a microphone array shown schematically in figure 21. The microphones were arranged in opposing pairs so that the acoustic phase between the received signals can be evaluated and the underlying mode shape evaluated. These measurements were performed at a higher Reynolds number, with different nozzles, but at the same non-dimensionalised spacing. The diameter of the jets at OSU was 19.1 mm (3/4"), as opposed to 10.0 mm for the Monash University measurements. The opposing microphones are placed nine nozzle diameters from the respective nozzle centrelines and were carefully positioned so that the tip of each microphone was displaced by the same distance as its opposing counterpart.

B&K 4939 1/4" microphones are used and conditioned by a B&K Nexus 2690 conditioning amplifier with a built-in bandpass filter from 20 Hz to 100 kHz. The signals are sampled by National Instruments PXI-6133 DAQs and are archived using LabVIEW software. Microphone calibration is performed with a B&K acoustic calibrator (model 4231), and the microphone calibration constants are recorded to provide the conversion from measured voltage to the equivalent pressure. The sample rate is 200 kHz, and 819,200

data points are collected. The collected data points are split into 8192 data points per segment. The resultant frequency bandwidth is 24.4 Hz.

B.2. *Comparison*

The PSD as a function of nozzle pressure ratio for the OSU data is presented in Figure 22(a), the coherence in Figure 22(b), the phase in Figure 22(c), and the extracted coherent process in Figure 22(d).

The mode staging behaviour of the jets in the OSU facility is noticeably different, particularly in the range $3.0 \leqslant NPR \leqslant 4.0$, which is typical of the well-established sensitivity of resonance to boundary conditions, shear-layer thickness, etc. The purpose of this dataset is to verify whether the core observation of this paper holds across multiple facilities. At least two processes associated with either anti-symmetric or symmetric oscillations about the mid-plane are observed. There are an intermediate range of pressures where there is no clear phase relation between the jets, consistent with observations in the two facilities at Monash University.

As performed in the paper, coherent processes are extracted from frequencies showing high coherence (Figure 22(d)) and processed using the bandpass-Hilbert transform technique to produce the phase and amplitude histograms in Figure 23. Again, similar behaviour is observed in these results as within the paper. Process 1 and 2 (Figures 23(a) and 23(c)) show widely distributed phase before transitioning into an NPR region with narrow phase. The middle range of NPR values (Process 3) shows very widely distributed phase and amplitude. Lastly, Process 4 (Figures 23(g) and 23(h)) shows the transition from widely distributed phase and amplitude to steady coupling beyond NPR $\geqslant 5.0$.

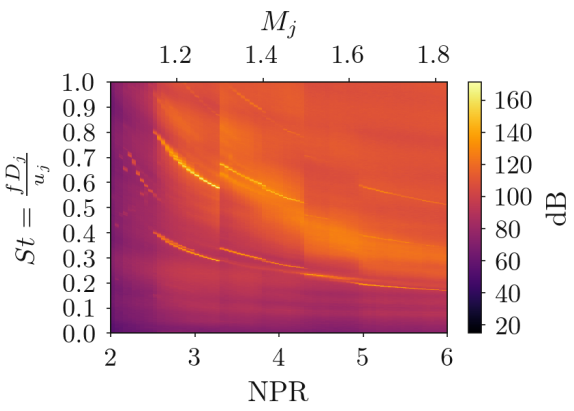

(a) PSD estimate.

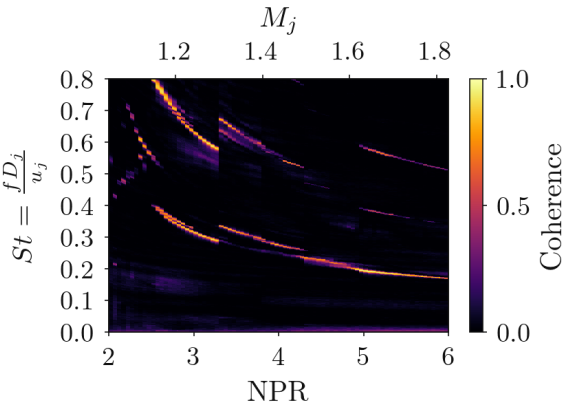

(b) CPSD coherence. estimate

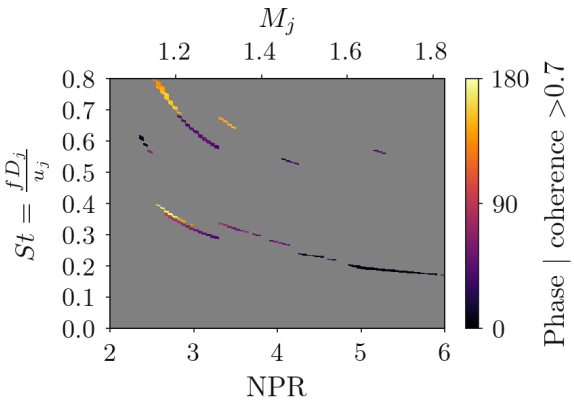

(c) CPSD phase. estimate

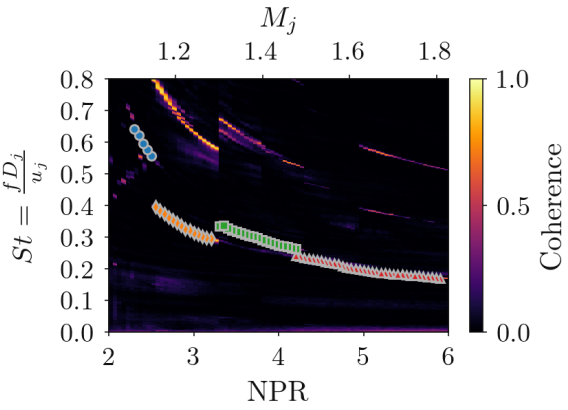

(d) Labelled processes from CPSD coherence. Process 1: blue ○, Process 2: orange ◇, Process 3: green □, Process 4: red △.

FIGURE 22. Acoustic spectra results from an analogous twin-jet experiment performed at the Gas Dynamics and Turbulence Laboratory within the Aerospace Research Center at The Ohio State University. Converging twin-jet nozzles at $s/D = 3$ spacing exhaust into an anechoic chamber with an opposing microphone array similar to that used in the Monash University experiments.

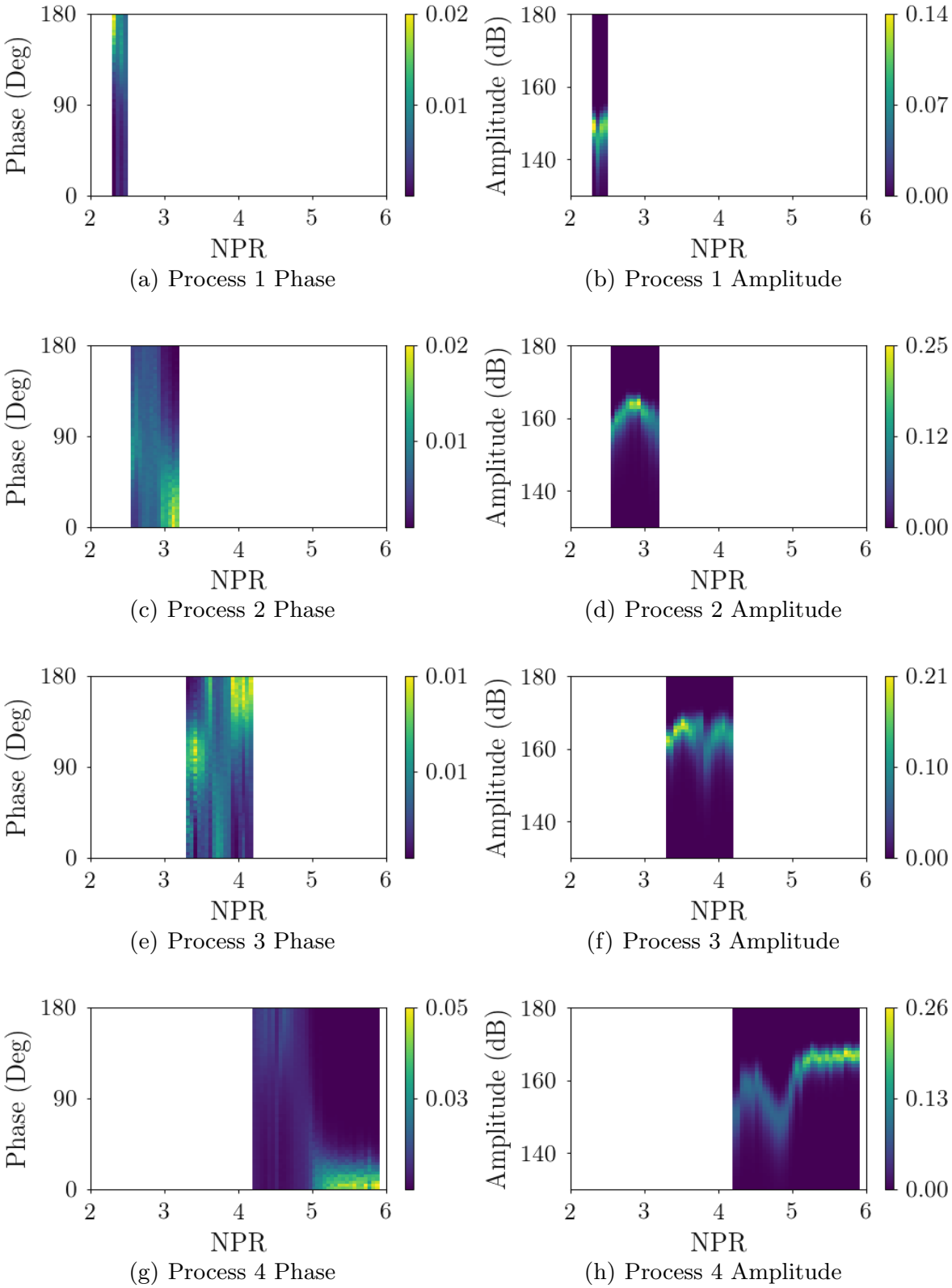

(a) Process 1 Phase (b) Process 1 Amplitude

(c) Process 2 Phase (d) Process 2 Amplitude

(e) Process 3 Phase (f) Process 3 Amplitude

(g) Process 4 Phase (h) Process 4 Amplitude

FIGURE 23. Acoustic process phase and amplitude from the extracted processes from Figure 22(d) using the bandpass-Hilbert technique on measurements taken at The Ohio State University. Colour-bars represent histogram probability density.

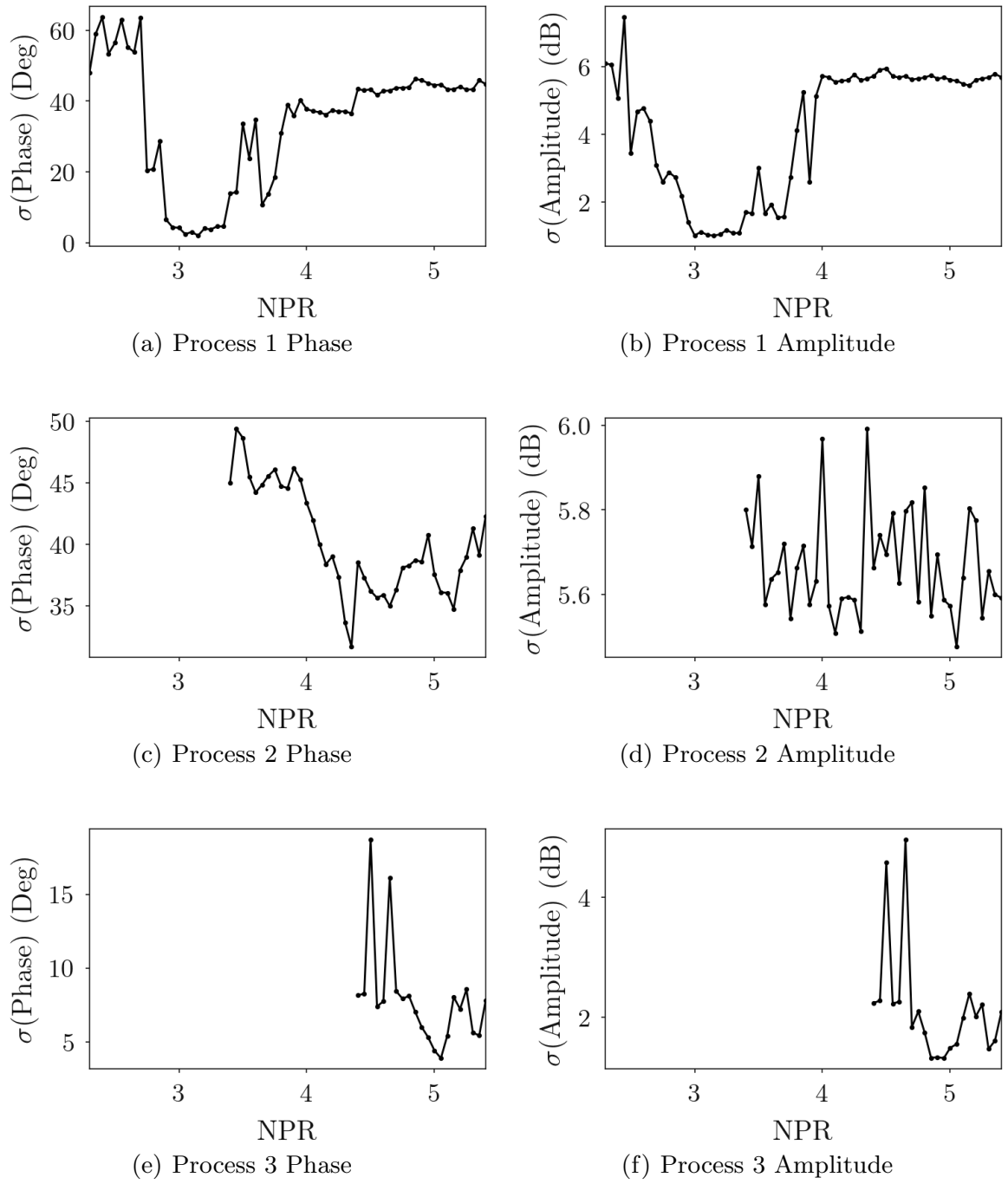

FIGURE 24. Standard deviation of phase and amplitude response from Processes 1,2,3 with distributions presented in Figure 6.

C. Standard deviation of time-dependent acoustic distributions for distribution classification

Standard deviation corresponding to the time-resolved acoustic distributions presented in section 4.1 is calculated. Figures are shown in the collective Figure 24 to allow individual distributions to be classified as narrow or wide.

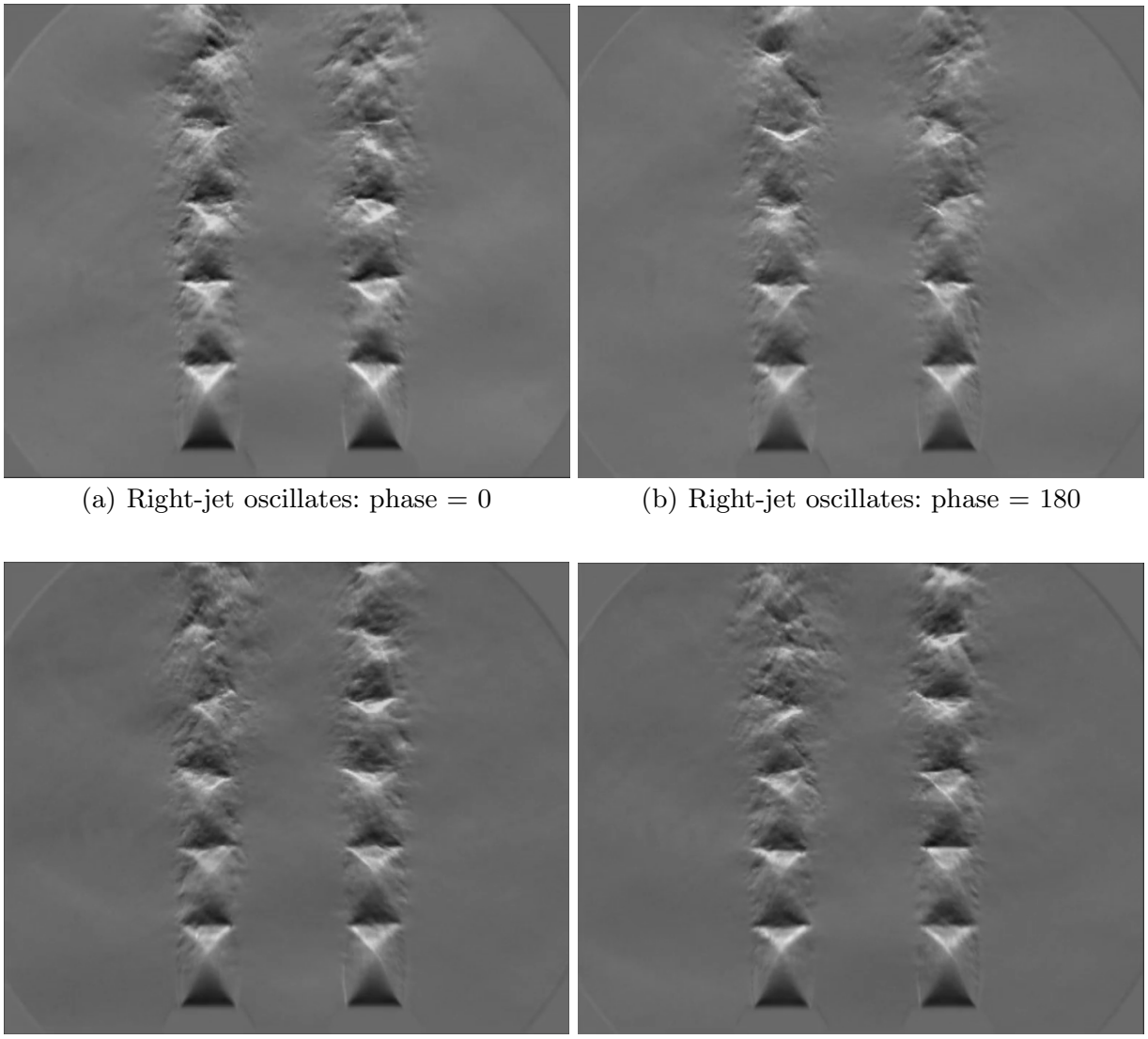

(a) Right-jet oscillates: phase = 0

(b) Right-jet oscillates: phase = 180

(c) Left-jet oscillates: phase = 0

(d) Left-jet oscillates: phase = 180

FIGURE 25. Schlieren stills from Knast *et al.* (2018) showing independent left and right jet oscillations. These figures are supplementary to supplementary video 2, which depicts time-resolved footage. The snapshots show the two phase extremes of the oscillation cycles. Figures 25(a) and 25(b) show the right jet oscillating while the left does not. The phase cycle is mostly clearly observed by following the spanwise motion of the shock-cells.

D. Schlieren Snapshots

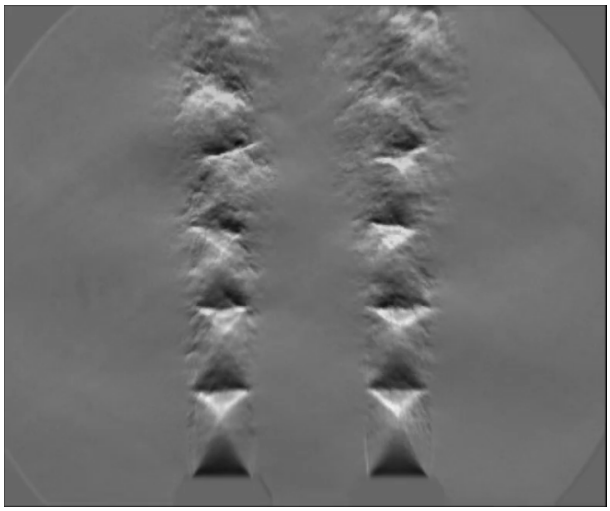

(a) Both jets oscillating: phase = 0

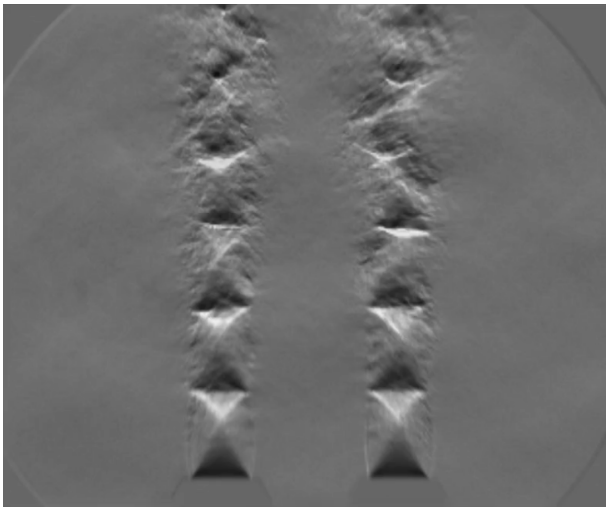

(b) Both jets oscillating: phase = 180

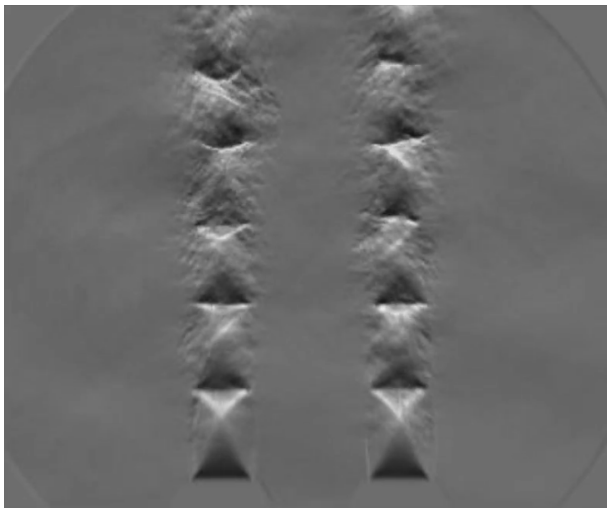

(c) Neither jet oscillates

FIGURE 26. Schlieren stills from Knast *et al.* (2018) showing both jets oscillating and neither jet oscillating. See the supplementary video for the time-resolved footage.

REFERENCES

Alkislar, Mehmet B., Krothapalli, A, Choutapalli, I & Lourenco, L 2005 Structure of Supersonic Twin Jets. *AIAA journal* **43** (11), 2309–2318.

Alkislar, Mehmet B., Krothapalli, Anjaneyulu & Lourenco, Luiz M. 2003 Structure of a screeching rectangular jet: A stereoscopic particle image velocimetry study. *Journal of Fluid Mechanics* **489** (489), 121–154.

Bell, Graham, Soria, Julio, Honnery, Damon & Edgington-Mitchell, Daniel 2017 Particle Image Velocimetry Analysis of the Twin Supersonic Jet Structure and Standing-Wave. *23rd AIAA/CEAS Aeroacoustics Conference* (June), 1–17.

Bell, Graham, Soria, Julio, Honnery, Damon & Edgington-Mitchell, Daniel 2018 An experimental investigation of coupled underexpanded supersonic twin-jets. *Experiments in Fluids* **59** (9), 139.

Berndt, D. E. 1984 Dynamic Pressure Fluctuations in the Internozzle Region of a Twin-Jet Nacelle. In *SAE Technical Paper*, p. 10. Society of Automotive Engineers.

Berry, M. G., Magstadt, A. S. & Glauser, M. N. 2017 Application of POD on time-resolved schlieren in supersonic multi-stream rectangular jets. *Physics of Fluids* **29** (2), 020706.

Brès, Guillaume A., Ham, Frank E. & Lele, Sanjiva K. 2013 Unstructured large eddy simulations of heated supersonic twin jets. *The Journal of the Acoustical Society of America* **134** (5), 4128–4128.

Cluts, Jordan, Kuo, Ching-Wen & Samimy, Mo 2015 Exploring Physics and Control of Twin Supersonic Circular Jets. In *53rd AIAA Aerospace Sciences Meeting*. Reston, Virginia: American Institute of Aeronautics and Astronautics.

Cluts, Jordan, Kuo, Ching-Wen & Samimy, Mo 2017 An Investigation of Effects of Jet Temperature on Twin-Jet Flow and Acoustic Fields. In *55th AIAA Aerospace Sciences Meeting*, pp. 1–15. Reston, Virginia: American Institute of Aeronautics and Astronautics.

Crawley, Michael, Gefen, Lior, Kuo, Ching-Wen, Samimy, Mo & Camussi, Roberto 2018 Vortex dynamics and sound emission in excited high-speed jets. *Journal of Fluid Mechanics* **839**, 313–347.

Du, Joshua Z 2002 Kelvin-Helmholtz Instability Waves of Supersonic Multiple Jets. In *Proceedings of the forth international conference on dynamical systems and differential equations*.

Du, Zihua 1993 Acoustic and Kelvin-Helmholtz instability waves of twin supersonic jets. PhD thesis, Florida State University.

Edgington-Mitchell, Daniel 2019 Aeroacoustic resonance and self-excitation in screeching and impinging supersonic jets - a review. *International Journal of Aeroacoustics* .

Edgington-Mitchell, Daniel, Honnery, Damon R. & Soria, Julio 2014*a* The underexpanded jet Mach disk and its associated shear layer. *Physics of Fluids* **26** (9), 096101.

Edgington-Mitchell, Daniel, Honnery, Damon R. & Soria, Julio 2015 Multimodal Instability in the Weakly Underexpanded Elliptic Jet. *AIAA Journal* **53** (9), 2739–2749.

Edgington-Mitchell, Daniel, Jaunet, Vincent, Jordan, Peter, Towne, Aaron, Soria, Julio & Honnery, Damon 2018 Upstream-travelling acoustic jet modes as a closure mechanism for screech. *Journal of Fluid Mechanics* **855**, R1.

Edgington-Mitchell, Daniel, Oberleithner, Kilian, Honnery, Damon R. & Soria, Julio 2014*b* Coherent structure and sound production in the helical mode of a screeching axisymmetric jet. *Journal of Fluid Mechanics* **748**, 822–847.

Gojon, Romain, Baier, Florian, Gutmark, Ephraim & Mihaescu, Mihai 2017 Temperature effects on the aerodynamic and acoustic fields of a rectangular supersonic jet. In *AIAA SciTech Forum - 55th AIAA Aerospace Sciences Meeting*. Reston, Virginia: American Institute of Aeronautics and Astronautics.

Gojon, Romain, Bogey, Christophe & Mihaescu, Mihai 2018 Oscillation Modes in Screeching Jets. *AIAA Journal* **56** (7), 2918–2924.

Gojon, Romain, Gutmark, Ephraim & Mihaescu, Mihai 2019 Antisymmetric Oscillation Modes in Rectangular Screeching Jets. *AIAA Journal* **57** (8), 3422–3441.

Goparaju, Kalyan & Gaitonde, Datta V 2017 Dynamics of Closely Spaced Supersonic Jets. *Journal of Propulsion and Power* pp. 1–13.

Knast, Thomas, Bell, Graham, Wong, Marcus, Leb, Corey M., Soria, Julio, Honnery, Damon R. & Edgington-Mitchell, Daniel 2018 Coupling modes of an underexpanded twin axisymmetric jet. *AIAA Journal* **56** (9), 3524–3535.

Kuo, Ching-Wen, Cluts, Jordan & Samimy, Mo 2016*a* Active Flow Control of Supersonic Twin-Jet Plumes. *Journal of Aeronautics, Astronautics and Aviation* **48** (4), 243–251.

Kuo, Ching-Wen, Cluts, Jordan & Samimy, Mo 2016*b* An Investigation of Twin Supersonic Jet Coupling. In *54th AIAA Aerospace Sciences Meeting*, pp. 1–20.

Kuo, Ching Wen, Cluts, Jordan & Samimy, Mo 2017*a* Effects of excitation around jet preferred mode Strouhal number in high-speed jets. *Experiments in Fluids* **58** (4), 35.

Kuo, Ching Wen, Cluts, Jordan & Samimy, Mo 2017*b* Exploring physics and control of twin supersonic circular jets. In *AIAA Journal*, , vol. 55, pp. 68–85. American Institute of Aeronautics and Astronautics.

Lumley, J 1967 The structure of inhomogeneous turbulence. Atmospheric Turbulence and Wave Propagation. *AM Yaglom, VI Tatarski* pp. 166–178.

Mancinelli, Matteo, Jaunet, Vincent, Jordan, Peter & Towne, Aaron 2019 Screech-tone prediction using upstream-travelling jet modes. *Experiments in Fluids* **60** (1), 22.

Mancinelli, Matteo, Pagliaroli, Tiziano, Camussi, Roberto & Castelain, Thomas 2018 On the hydrodynamic and acoustic nature of pressure proper orthogonal decomposition modes in the near field of a compressible jet. *Journal of Fluid Mechanics* **836**, 998–1008.

Morris, Philip J. 1990 Instability waves in twin supersonic jets. *Journal of Fluid Mechanics* **220** (1), 293–307.

Panda, Jayanta 1999 An experimental investigation of screech noise generation. *Journal of Fluid Mechanics* **378**, 71–96.

Panickar, Praveen, Srinivasan, K. & Raman, Ganesh 2004 Aeroacoustic features of coupled twin jets with spanwise oblique shock-cells. *Journal of Sound and Vibration* **278** (1-2), 155–179.

Panickar, Praveen, Srinivasan, K. & Raman, Ganesh 2005 Nonlinear interactions as precursors to mode jumps in resonant acoustics. *Physics of Fluids* **17** (9), 1–18.

Powell, Alan 1953 On the mechanism of choked jet noise. *Proceedings of the Physical Society. Section B* **66** (12), 1039–1056.

Powell, Alan 1954 The reduction of choked jet noise. *Proceedings of the Physical Society. Section B* **67** (4), 313–327.

Raman, Ganesh 1998 Coupling of Twin Rectangular Supersonic Jets. *Journal of Fluid Mechanics* **354** (5), 123–146.

Raman, Ganesh, Panickar, Praveen & Chelliah, Kanthasamy 2012 Aeroacoustics of twin supersonic jets: a review. *International Journal of Aeroacoustics* **11** (7), 957–984.

Seiner, J, Manning, James C & Ponton, Michael K 1986 Dynamic pressure loads associated with twin supersonic plume resonance. *AIAA Journal* **26** (8), 954–960.

Shaw, Leonard 1990 Twin-jet screech suppression. *Journal of Aircraft* **27** (8), 708–715.

Shen, H & Tam, Christopher K W 2000 Effects of Jet Temperature and Nozzle-Lip Thickness on Screech Tones. *AIAA Journal* **38** (5).

Shen, H & Tam, C. K. W. 2002 Three-dimensional numerical simulation of the jet screech phenomenon. *AIAA Journal* **40** (1), 33–41.

Sirovich, Lawrence 1987*a* Turbulence and the dynamics of coherent structures - part 1: coherent structures. *Q. Appl. Math.* **XLV** (3), 561–571.

Sirovich, Lawrence 1987*b* Turbulence and the dynamics of coherent structures. II. Symmetries and transformations. *Quarterly of Applied Mathematics* **45** (3), 573–582.

Srinivasan, K., Panickar, Praveen, Raman, Ganesh, Kim, Byung Hun & Williams, David R. 2009 Study of coupled supersonic twin jets of complex geometry using higher-order spectral analysis. *Journal of Sound and Vibration* **323** (3-5), 910–931.

Taira, Kunihiko, Brunton, Steven L., Dawson, Scott T. M., Rowley, Clarence W., Colonius, Tim, McKeon, Beverley J., Schmidt, Oliver, Gordeyev, Stanislav, Theofilis, Vassilios & Ukeiley, Lawrence S. 2017 Modal Analysis of Fluid Flows: An Overview. *AIAA Journal* **55** (12), 4013–4041, arXiv: 1702.01453.

Tam, Christopher K W 1995 Supersonic Jet Noise. *Annu. Rev. Fluid Mech* **27**, 17–43.

Tan, D. J., Soria, J., Honnery, D. & Edgington-Mitchell, Daniel 2017 Novel Method for

Investigating Broadband Velocity Fluctuations in Axisymmetric Screeching Jets. *AIAA Journal* **55** (7), 2321–2334.

Umeda, Yoshikuni & Ishii, Ryuji 2001 Oscillation modes of supersonic multijets exhausting from very adjacent multiple nozzles. *The Journal of the Acoustical Society of America* **110** (4), 1873–1877.

Weightman, Joel L, Amili, Omid, Honnery, Damon, Edgington-Mitchell, Daniel & Soria, Julio 2016 Supersonic Jet Impingement on a Cylindrical Surface. In *22nd AIAA/CEAS Aeroacoustics Conference*, pp. 2016–2800.

Weightman, Joel L, Amili, Omid, Honnery, Damon, Edgington-Mitchell, Daniel & Soria, Julio 2019 Nozzle external geometry as a boundary condition for the azimuthal mode selection in an impinging underexpanded jet. *J. Fluid Mech* **862**, 421–448.

Weightman, Joel L, Amili, Omid, Honnery, Damon, Soria, Julio & Edgington-Mitchell, Daniel 2017 An explanation for the phase lag in supersonic jet impingement. *Journal of Fluid Mechanics* **815**, 815R11–815R111.

Weightman, Joel L, Amili, Omid, Honnery, Damon, Soria, Julio & Edgington-Mitchell, Daniel 2018 Signatures of shear-layer unsteadiness in proper orthogonal decomposition. *Experiments in Fluids* **59** (12), 180.

Wlezien, Richard 1989 Nozzle geometry effects on supersonic jet interaction. *AIAA Journal* **27** (10), 1361–1367.

Zilz, David & Wlezien, Richard 1990 The sensitivity of near-field acoustics to the orientation of twin two-dimensional supersonic nozzles. In *26th Joint Propulsion Conference*. Reston, Virigina: American Institute of Aeronautics and Astronautics.

6.2 Concluding Statement

The analysis provided an explanation for the nature of the coupling in regions that have previously been described as complex coupling (Raman, 1998; Knast *et al.*, 2018; Bell *et al.*, 2018).

The three facilities described in this study were used in conjunction. The coupling modes of the $s/D = 3$ twin-jet were generally found to be independent of facility. Two intense and continuously varying frequencies were observed across the pressure range. These were associated with different aeroacoustic feedback processes. At low pressure, a tone emerges that was associated with a steady anti-symmetric coupling mode. At higher pressures, the introduction of a steady symmetric coupling mode and an associated tone was encountered. This work provided evidence to suggest that region II is formed from the competition between these two feedback processes. The competition was not purely mutually exclusive. The analysis revealed that the jets often become uncoupled and screech independently. In the uncoupled state, the individual jets experience frequent interruptions to their screeching process and significant reductions in acoustic amplitude. As predicted by the analysis, direct observation of the interrupted process was observed via ultra high speed schlieren photography.

The jets were coupled for only a small fraction of time. When they were coupled the jets do so in either one of the competing modes. Analysis of the individual jets during coupling in either mode provided a single instability mode and hydrodynamic wavelength. The individual jets contained the same structure in either coupling mode. Thus, the tone frequency difference between the competing modes must be produced by the way the jets couple together. Potentially this could be a change in returning acoustic path-length or upstream closure mechanism.

The coupling behaviour inside the complex coupling regions has been shown to exhibit features of a competition between existing coupling modes. The competition exists due to the Powell's amplitude criteria being approximately equal for both modes. Thus the unsteady competition between the modes demonstrates essentially no preference.

Chapter 7 includes a final study that examines the response to perturbation and amplification of the mode feedback loop. Additionally, the out-of-plane azimuthal structure was examined and classified. These were used to link the modes to those observed to be hydrodynamically unstable from stability analysis.

Chapter 7

Response to Forcing

7.1 Introduction

This chapter examines an experimental campaign focused on examining the facility dependence to mode staging, out-of-plane components of coupling modes, and mode response to jet forcing for a supersonic twin-jet. The campaign was conducted in collaboration with the The Ohio State University (OSU) at the Gas Dynamics Laboratory's large jet anechoic chamber in Ohio, USA. Facility three was used to provide all results in this chapter. It was described in section 3.3.1.

Determining the three-dimensional azimuthal mode shape in a twin-jet has proven to be an experimental challenge (Seiner *et al.*, 1986; Wlezien, 1989; Knast *et al.*, 2018). Interpretation via schlieren photography is ambiguous in the out-of-plane direction as the technique is path-integrated. Opposing microphone phase measurements have so far only been performed between two microphones. In this chapter an orthogonal microphone array was used to determine the in- and out-of-plane components to deduce the azimuthal mode shape of the coupling modes. Determination of the azimuthal mode shape allows the experimental comparison with stability analysis, which differentiate modes based on the in- and out-of-plane mode shape. Additionally it provides a reference for determining the parameters of the feedback loop.

The mode staging behaviour and the concept of mode competition reaffirm Powell's amplitude criteria for mode selection. Jet forcing is applied to assess the response and amplification of these dormant modes outside of their natural mode staging appearance. The demonstration of these modes can be used along side future aeroacoustic twin-jet stability models.

7.2 Results and Discussion

7.2.1 Natural Mode Classification

The natural modes of the twin-jet are examined first. The intention is to provide a baseline and comparison of facility dependence to previous experiments at LTRAC. The NPR was traversed over

the range $2.2 \leq \text{NPR} \leq 6.0$ for a fixed jet spacing of $s/D = 3$. The corresponding stacked waterfall plots of individual PSD and CPSD spectra are shown in the collective figure 7.1 for microphones 0 and 1. Figure 7.1e indicates the microphone configuration. The PSD plot (figure 7.1a) shows several high-amplitude narrow-band frequencies that show mode staging behaviour. CPSD-coherence between the microphone pair is shown in figure 7.1b. The CPSD-phase is shown in figure 7.1c. Examining the phase and coherence in conjunction indicates similar mode staging behaviour to facilities one and two. Two modes appear at low pressure ratios. These have been labelled as processes 1 and 2 in figure 7.1d and are later shown to be the A1 and A2 toroidal modes. The next mode begins at $\text{NPR} \approx 3.0$ and requires the coupling descriptions from chapter 6 for interpretation. It continues until approximately $\text{NPR} \approx 4.8$. Another mode that overlaps with the previous is observed to begin at $\text{NPR} \approx 3.6$ and continues until the end of the measurement domain.

The overlap between these latter two modes extends over $3.6 \leq \text{NPR} \leq 5.1$. The overlapping region is indicative of region II where the two modes were shown to be in competition. The lower mode is labelled as process 3 where it appears alone and process 4 where it overlaps. The separate labelling allows CPSD analysis to derive the phase of the mode where it is statistically stationary and to avoid the application of CPSD where it is not. The high pressure mode is labelled as process 5 where it overlaps and process 6 where it appears alone.

Facility one and two identified that the higher pressure mode was symmetric about the centreline. A symmetric mode with zero degrees phase difference is found for process 6 where the acoustic signal is steady. The anti-symmetric mode appears under process three for a much shorter NPR range than observed on facility one or two. Despite the anti-symmetric mode indicating high coherence in the process 4 region, it is dominated by the phase of process 5 as a zero degree phase difference is observed. The competing modes in this region appear to cause spurious CPSD results through a non-stationary input signal.

The mode-staging of the $s/D = 3$ twin-jet is therefore shown to be facility independent. A similar structure of modes has been observed across three facilities: Two low pressure modes with high frequency and zero phase, followed by an anti-symmetric mode that eventually competes with a symmetric mode at higher pressures.

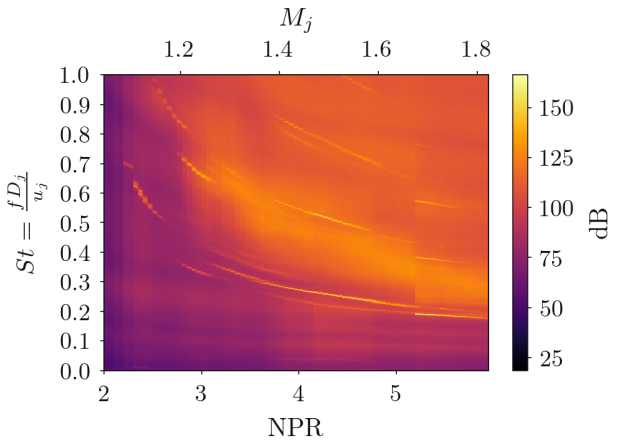

(a) Power Spectral Density

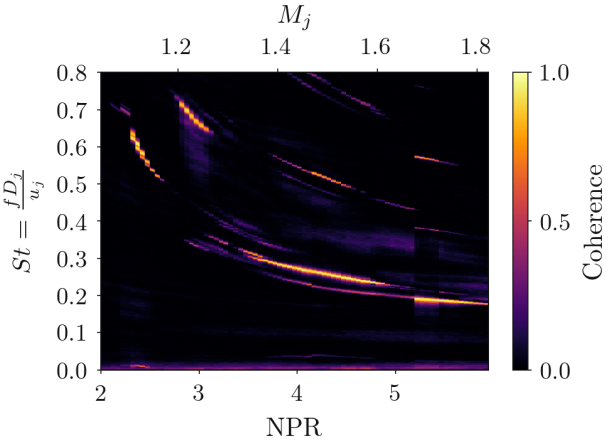

(b) Cross power spectral density - coherence

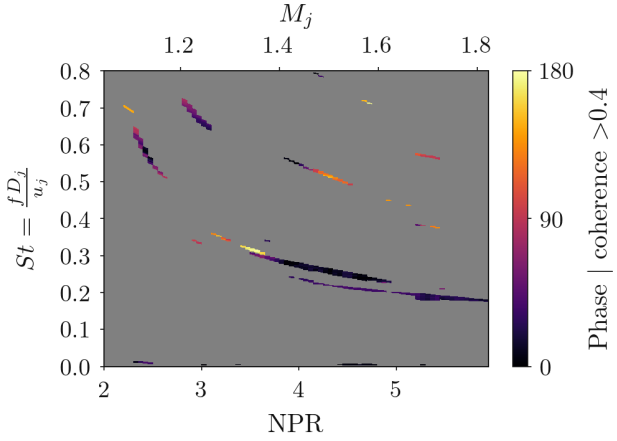

(c) Cross power spectral density - phase

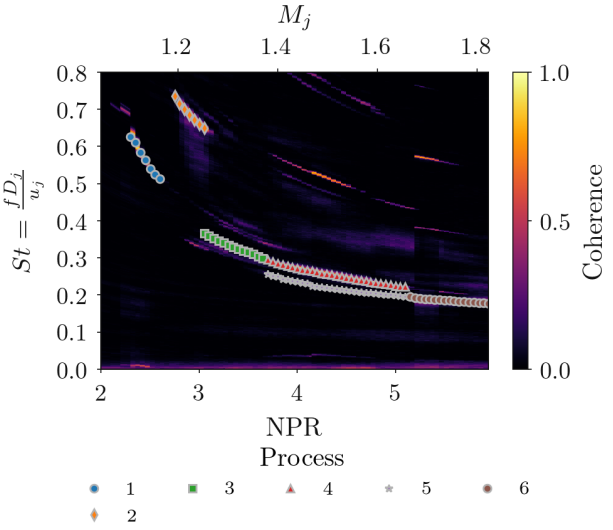

(d) Coherence with tracked ridges labelled

(e) Microphone 0 and 1 configuration.

Figure 7.1: Natural spectra and screech tones occurring for the twin-jet system at Ohio State University. Cases shown correspond to polished steel C-D nozzles.

7.2.2 Out-of-Plane Mode-Shape Assessment

The orthogonal array of microphones around the nozzles is used to assess the out-of-plane mode shape. PSD responses of out-of-plane microphones 4 and 6 (schematic shown in figure 7.2c) are included in figures 7.2a and 7.2b.

The phenomenon of frequency doubling occurs for flapping jets when recorded in the direction normal to the flapping plane (Humphrey & Edgington-Mitchell, 2016). As the flapping mode moves through its phase cycle, it emits an acoustic wave as it oscillates to either side. This emission is observed at the screech frequency for a microphone placed in the flapping plane. The emission is observed twice as often for a microphone placed normal to the flapping plane. In these measurements, the jets have been observed to oscillate strongly in the in-plane direction. Therefore the frequency doubling is encountered for microphones placed orthogonal to the direction of a major flapping plane. Some frequency doubling is observed for microphones placed orthogonal to the in-plane direction for the twin-jet. This is shown in figures 7.2a and 7.2b. Essentially, all parts of the narrowband/high-dB screech tone show a strong harmonic at double their respective frequencies. The fundamental frequency remains sufficiently clear and high-amplitude that it permits analysis. CPSD spectra of the out-of-plane directions are provided in appendix B.

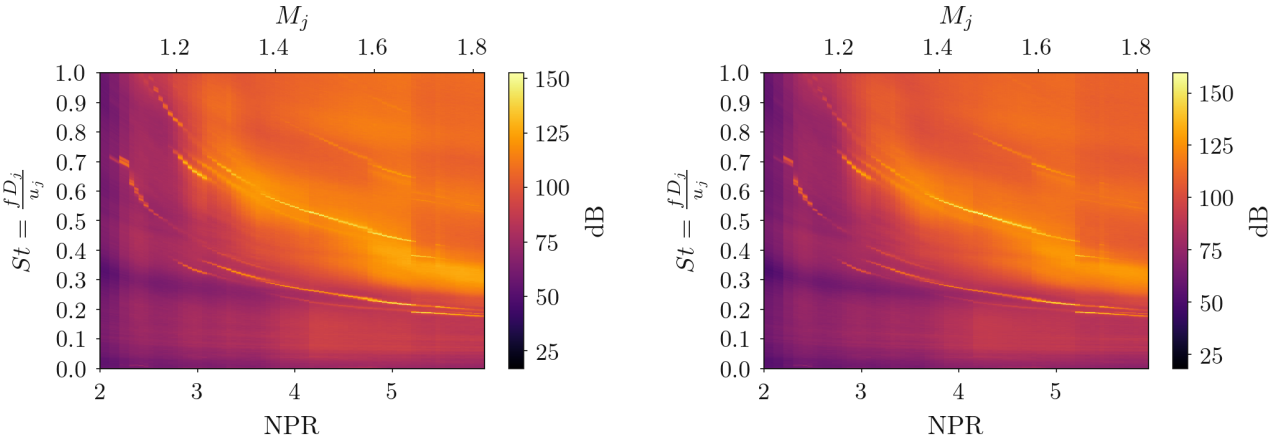

(a) Microphone 4

(b) Microphone 6

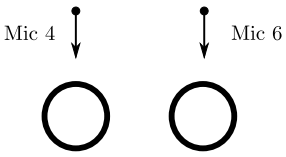

(c) Microphone 4 and 6 configuration.

Figure 7.2: Power spectral density response for out-of-plane microphones 4 and 6 for the unforced OSU experiments under case 2: unforced steel nozzles. Due to the microphones being at 90 degrees (out-of-plane) to the preferred flapping direction of the jets frequency doubling is observed.

The frequencies of the identified processes are aligned regardless of the microphone pair but their individual CPSD response differs markedly. The differing CPSD response is used to compare the dominant coherent oscillations of the jet in and out-of-plane as the direct phase evaluation method used previously cannot be extended in this circumstance due to the lack of a reference phase value.

The average CPSD properties for a given process are used to examine the coherence and phase results across different microphone pairs. Figure 7.3a shows the mean coherence value for a given microphone pair for the most clearly defined processes. The bar height indicates the mean coherence value of the process, with the dots overlaid indicating the individual coherence values that make up the process. The plotting of mean and individual values allows the trends and outliers to be observed in the same figure for a given process, which provides an indication of the process's stability. Refer to figure 7.1d for process numbering and to figure 7.3c for microphone numbering.

The phase of those corresponding processes (and scatter markers within the process) are shown within figure 7.3b. As the phase wraps between -180 and 180 degrees, a mean phase cannot be meaningfully calculated. An averaging of process three between Mic 0-1, for example, would incorrectly result in 0 degrees. Thus only the scatter markers are shown to classify the different processes and microphones. The precision of the phase measurements appears to be high as many of the scatter markers are often overlaid. The accuracy is more challenging to estimate. It is unknown whether clusters of scatter points away from 0, 90, and 180 degrees are physical or a function of microphone positioning error. The microphones were positioned via careful measurement from a central reference point in these experiments. It is proposed in future a piezo clicker or similar be placed in each nozzle centre to calibrate the time offset between the acoustic signals precisely.

Process 1 and 2 were expected to correspond to the A1 and A2 toroidal modes. Toroidal modes were clearly observed within the ultra high speed footage during the Knast *et al.* (2018) study. There is evidence for process 1 existing as a toroidal mode. High coherence is observed between all microphone pairs and the phase difference is approximately zero across all microphone pairs. Process 2 presents exceptionally low coherence for the right angle microphone combination 0-4. This is also observed for the other right angle combinations. The other microphone combinations show high coherence. For the in-plane microphone pair (0-1), process 3 shows a 180 degree phase difference and process 4 shows a zero degree phase difference. This corresponds to the anti-symmetric and a symmetric mode that has been consistently observed. Both symmetric and anti-symmetric modes show high coherence for the out-of-plane microphone pairs (0-4 and 4-5). Process 3 shows a 90 degree phase offset for the right angle measurement (microphones 0-4) and a 180 degree difference for the out-of-plane pair 4-5. Therefore it appears that process 3 shows a helical mode that is anti-symmetric between jet plumes. Process 4 shows a 180 degree phase difference for the right-angle measurement (microphones 0-4) and a 0 or 90 degree difference for the out-of-plane pair 4-5. It is not straightforward to observe how this mode fits within the azimuthal mode framework. The characterisation study yielded an uncertain out-of-plane identification of this mode (Knast *et al.*, 2018). The stability analysis of Rodríguez *et al.* (2018) identified twin-jet hydrodynamic mode shapes that fit this description. These were shown in figure 2.14b. It appears that process four fits the 2SS mode shape. 2SS is also presented one of the most unstable growth-rates as shown in figure 2.14a. However, direct comparison cannot be made for two reasons. Firstly, further evidence cannot be provided to infer the azimuthal mode number, this higher mode will be referred to as the XSS mode. The XSS mode is symmetric in the out-of-plane, symmetric in the in-plane, with a 90 degree phase difference between the two plane oscillations. Secondly, stability analysis results are highly dependent on Mach number. The unstable mode ranking may drastically change between $M = 0.4$ and $1.1 \leq M \leq 1.7$, which is currently examined.

The natural modes of the jet system have been characterised in both the in-plane and out-of-plane directions. Two toroidal modes are low pressure that appear to be the A1/2. A helical anti-symmetric mode appears that is selected at low pressures and competes with a symmetric mode at higher pressures. The symmetric mode appears to have an additional out-of-plane flapping component consistent with the XSS mode defined by Rodríguez *et al.* (2018).

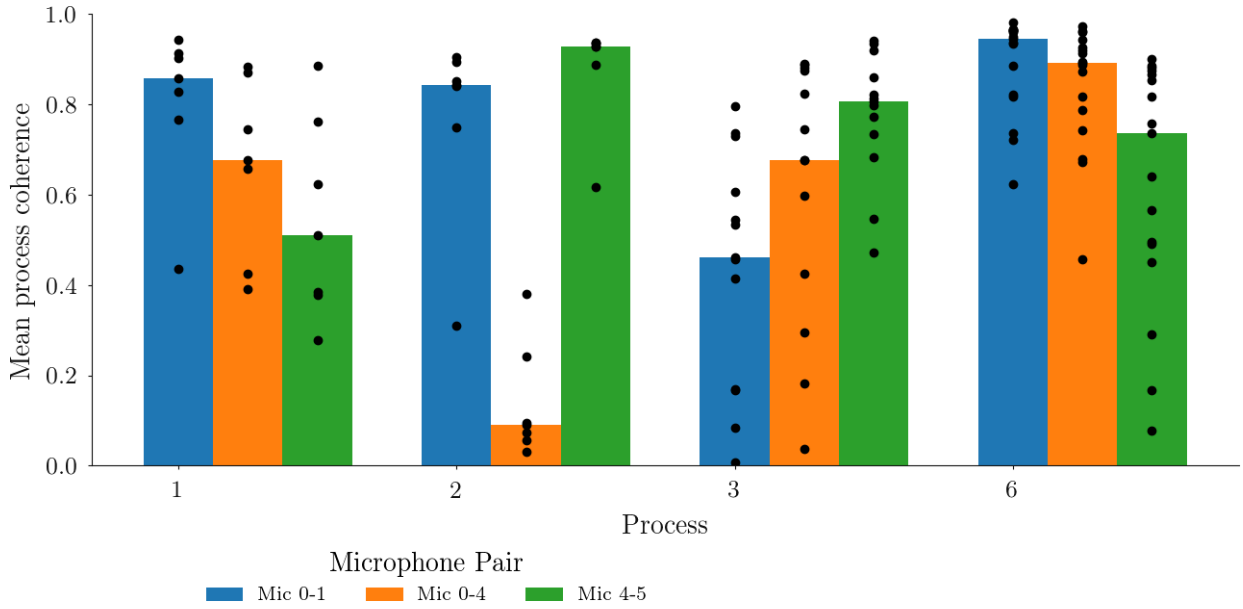

(a) CPSD-coherence comparison.

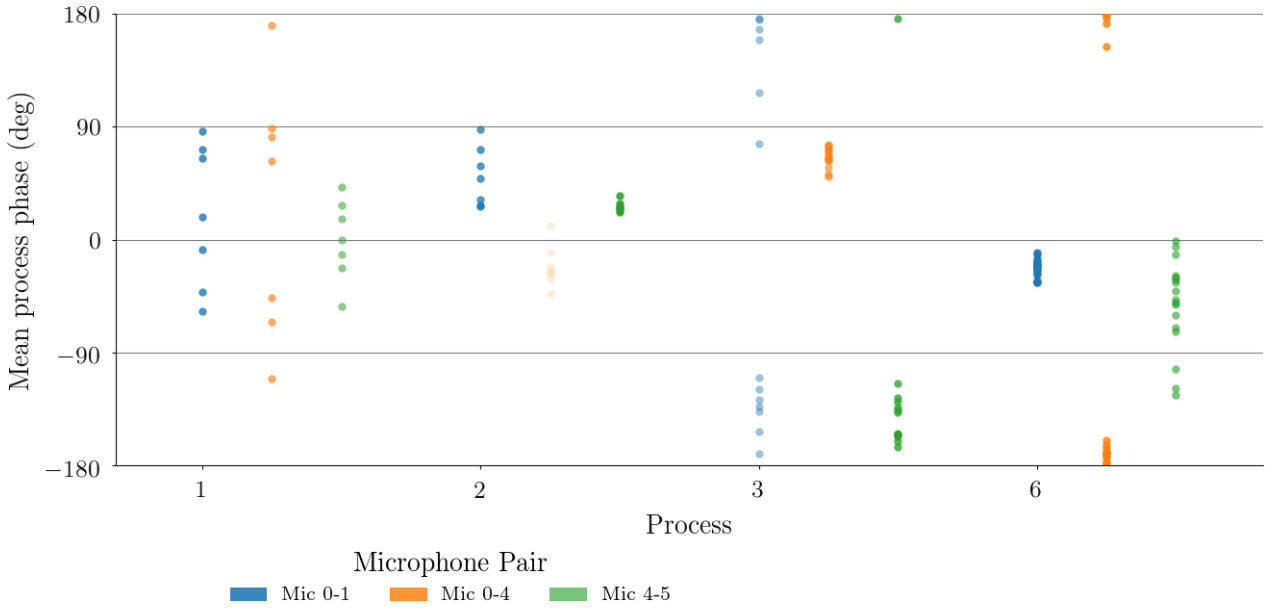

(b) CPSD-phase comparison. The transparency of the scatter points is proportional to the value of its coherence above. Phase of low coherence signals is physically meaningless.

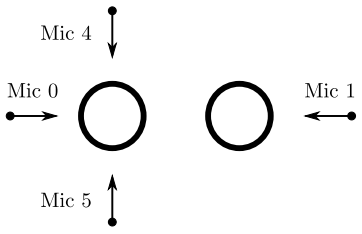

(c) Microphone configuration for reference.

Figure 7.3: CPSD results comparison for individual microphone pairs against the selected processes for case 2: unforced steel nozzles. Bar height indicates mean coherence and scatter points indicate the individual measurements. This chart provides the identification of when in and out-of-plane acoustics are prominent and aides in the mode identification process.

7.2.3 Jet Actuation

The forcing of the flow is performed using ceramic nozzles. These have an associated material surface roughness and electrode installations in the nozzles protrude slightly. The protrusions therefore have the potential to act as streamwise vortical generators. Comparison between the polished steel nozzles and the ceramic nozzles is briefly discussed to identify changes to the mode staging using the ceramic actuator nozzles.

A spectral comparison between the steel and ceramic nozzles is shown in figure 7.4. The selected process patterns are shown in figures 7.4e and 7.4f. Processes 1-6 are identifiable between the two spectra but some minor differences exist. Process 1 for the ceramic nozzles overlaps process 2. Mancinelli *et al.* (2019) identified that the A1 and A2 modes (and any overlap) were mutually exclusive for a single jet. This analysis is outside of the scope of the current work. Process 3 appears to become clear much later in the ceramic than in the steel nozzles. The behaviour of the competition between the anti-symmetric and symmetric mode appears to be similar between the nozzles. Process 7 is introduced in the ceramic nozzles. This has an anti-symmetric phase similar to process 3 and runs parallel to it. The faint outline of process 7 appears in the polished steel nozzles but it was not considered for analysis.

A comparison between OASPL for the different nozzles is shown in the collective figure 7.5. Both cases generally follow the same OASPL profile with a maximum peak at approximately 120 dB. Bumps in the loudness are observed at NPR $\approx$ 2.3 and 3.0, which correspond to particularly coherent coupling of the toroidal modes. Beyond NPR $\geq$ 4.0 the modes transition to symmetric coupling, which increases the acoustic pressure level. A larger difference is observed for microphone 0 (and 1, which is not shown) within figure 7.5b. No explanation can be provided for this.

7.2.4 Process Response to Short Duration Actuation

The effect of disruptive actuation on the natural modes occurring within the jet is examined first. The actuators are pulsed from an off-on-off state under an A forcing mode at St = 0.3. The forcing was activated and deactivated over two short periods of approximately one second duration. The response on the processes under was investigated: NPR = 2.52, 2.75, 3.00, 3.25, 3.75, 4.00, 4.50, 5.00. NPR = 3.50 was unable to be collected for technical reasons.

The Hilbert-bandpass technique presented in chapter 6 is use to assess the temporal components of the individual processes and the time traces are shown in figure 7.6. The actuation period is shown by the dark shadowing. The traces are produced by taking the ensemble average of the amplitude envelope of microphones 0-7. A low pass filter with a 10 Hz cut-off was applied to the traces for clarity. 200 ms at the beginning and end of the signal is clipped due to end-effects from the low-pass filtering.

Not all processes show response to actuation. The transient responses of those that do are shown in figures 7.6a and 7.6b. The remaining figures are included in appendix C. Process 3 and 5 do not show a response to actuation at this particular mode and frequency. The suppression of process 2 and 7 is clear in figures 7.6a and 7.6b. Low-frequency unsteadiness is observed for process 7 in figure 7.6b. The results of chapter 6 suggest that it experiences frequent interruptions to its acoustic production. When the forcing is activated the sound pressure level reaches a steady minimum that

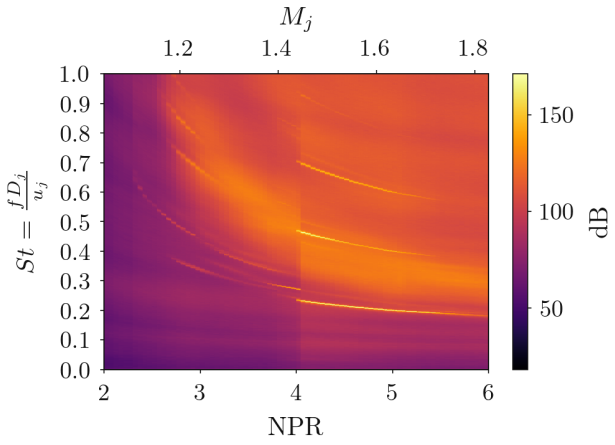

(a) Unforced ceramic nozzles.

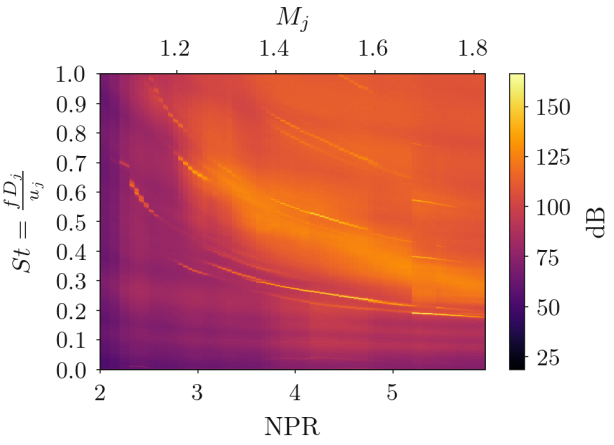

(b) Unforced steel nozzles.

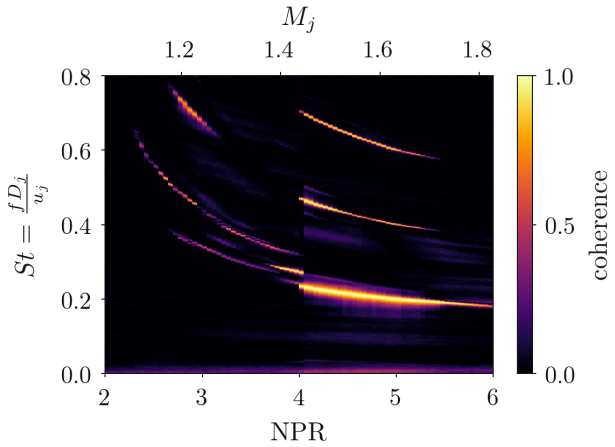

(c) Unforced ceramic nozzles.

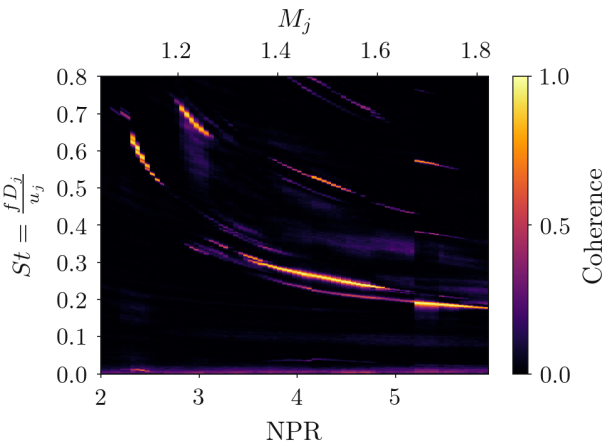

(d) Unforced steel nozzles.

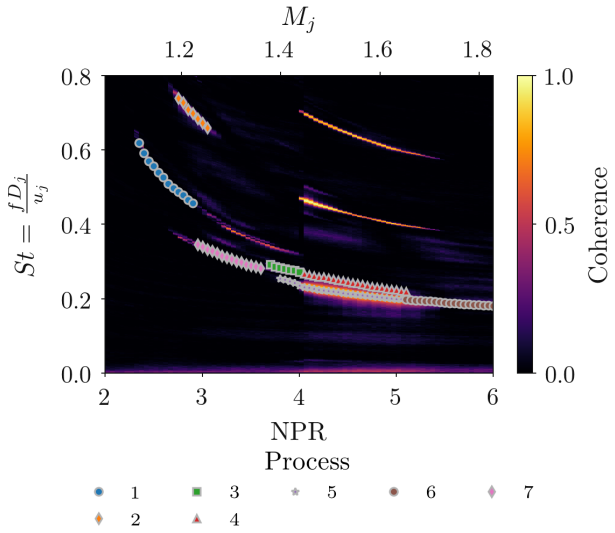

(e) Unforced ceramic nozzles, CSD-coherence with accompanying process classification.

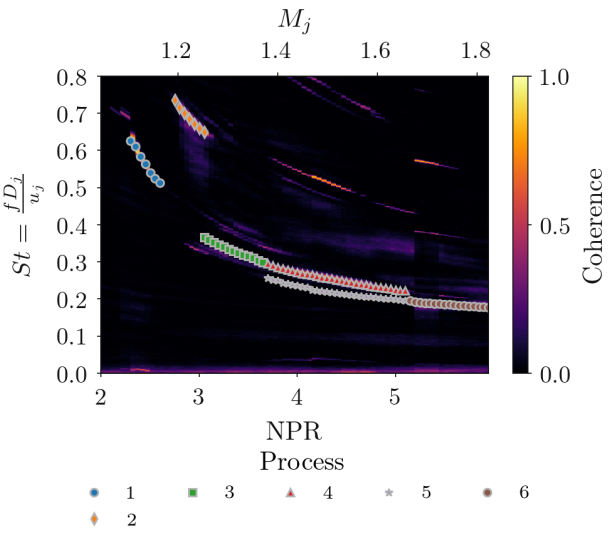

(f) Unforced steel nozzles, CSD-coherence with accompanying process classification.

Figure 7.4: OSU acoustic results depicting a comparison of ceramic nozzles (case 0) with plasma actuators compared to steel nozzles (case 2). Power and cross spectral density plots of the two cases for comparison are shown. Despite the ridges beginning and ending in different locations, the occurrence of the same processes is generally observed. Therefore the ceramic nozzles with plasma actuators do not significantly alter the aeroacoustic behaviour of the flow.

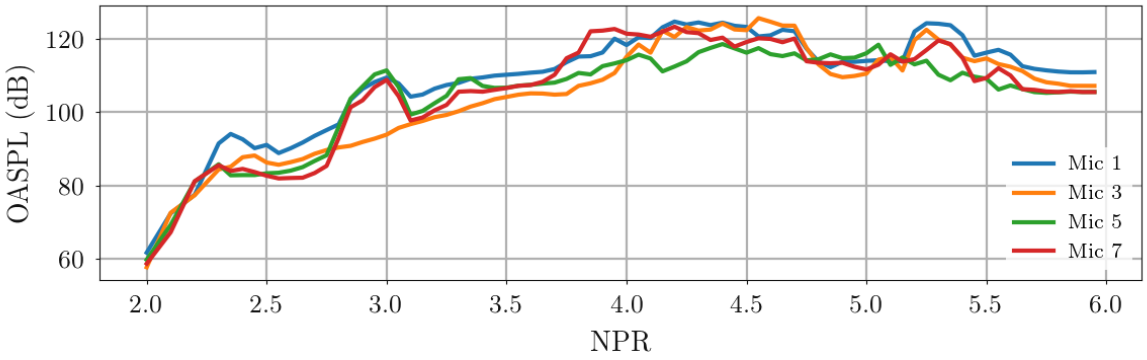

(a) Polished steel nozzles for canonical flow (case 2).

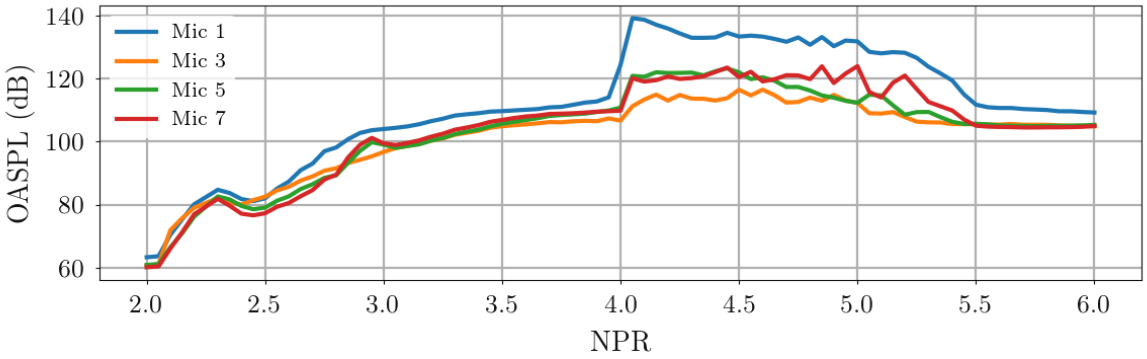

(b) Ceramic nozzles used for forcing (case 0).

Figure 7.5: Overall sound pressure level comparison between the polished steel nozzles (case 2) and the ceramic (case 0) ones used for forcing.

is equal with the troughs of its unactuated behaviour. Therefore the actuation shows the ability to completely remove the tone. The interruptions indicate that the gain of this particular tone is low or potentially in competition with process two.

For process 2 the response and relief of the forcing occurs on a time scale shorter than the low-bypass filter (10 Hz). Process 7 within figure 7.6b shows some lag to return to natural unsteadiness when the actuation is removed. The lag in unsteadiness indicates that the feedback loop gain of this particular process is low compared to others.

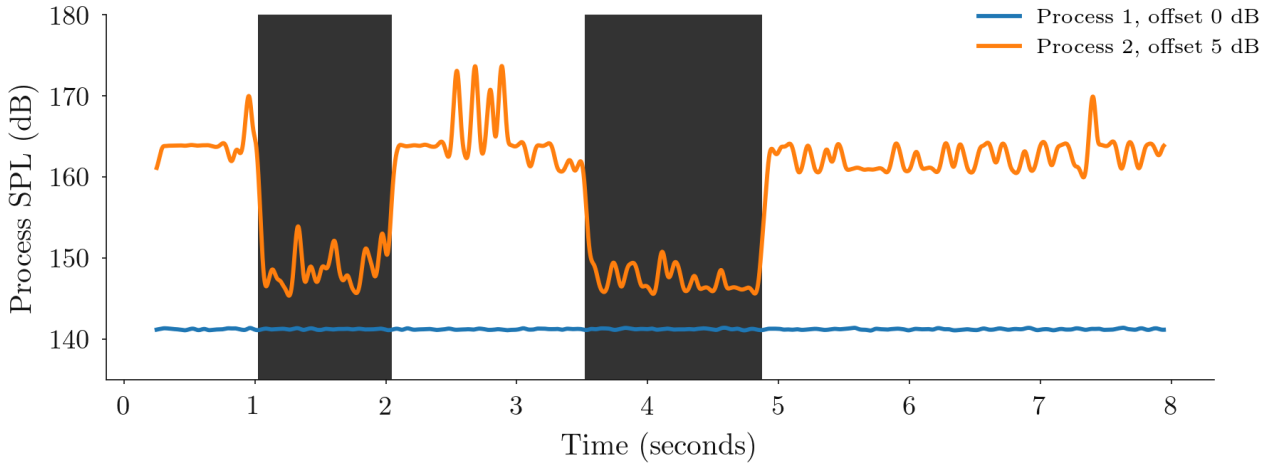

(a) NPR = 2.75

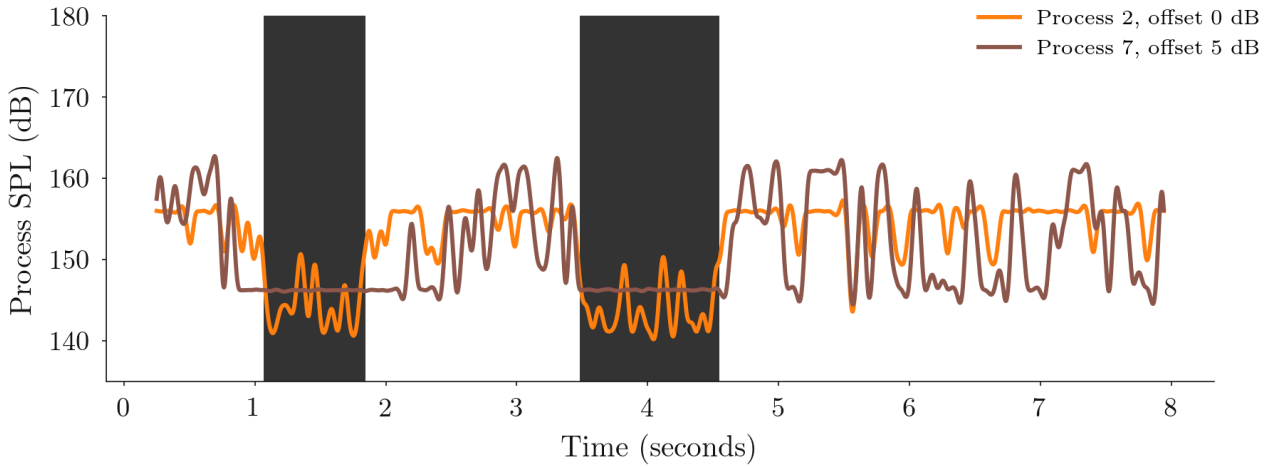

(b) NPR = 3.00

Figure 7.6: Acoustic amplitude of various processes during transient forced response. Actuators are switched on within the shaded regions. Amplitudes are the ensemble average of microphones 0-7. A 10 Hz low-pass filter has been applied for visualisation purposes as the raw data contains high-frequency fluctuations.

7.2.5 Sound Pressure Level Response to Constant Actuation

Overall Sound Pressure Level (OASPL) has been used to assess jet acoustic amplification or suppression response to actuation (Kuo *et al.*, 2017*b*). The overall change in acoustic pressure level serves to quantify the acoustic change in modes regardless of whether they occur at the actuation frequency.

OASPL is estimated via equation 7.1.

$$\text{OASPL} = 10\log\left(\sum_{i=1}^{n} 10^{\frac{\text{SPL}_i}{10}}\right) \tag{7.1}$$

where SPL_i is the sound pressure level at the i^{th} frequency within the PSD spectrum and n is the total number of frequency bins.

The effect of actuated modes on sound pressure level has been investigated by the GDTL at OSU (Kuo *et al.*, 2017*b*; Cluts *et al.*, 2016). OASPL has been investigated by Cluts *et al.* (2015*b*) as a tool to quantify the change in broadband acoustic amplification of a twin-jet under different forcing arrangements at different azimuthal angles.

The response to five representative forced modes are examined: toroidal (A), in-plane anti-symmetric (E), in-plane symmetric (F), out-of-plane (C), and helical (I). The azimuthal formed mode shapes are shown in the sub-figures of figure 7.8. The change in OASPL is referenced against the unforced condition, which was recorded moments before the forcing was applied. Actuated mode shapes are included for convenience in figure 7.7. The figures show the mean response between the microphone pairs. Examples of the individual microphone responses are included in appendix G where it is shown that the mean of the microphone pairs is suitable as a general indicator for the increase or decrease of jet OASPL.

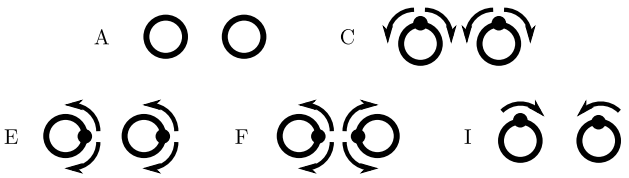

Figure 7.7: Actuated representations of modes A, C, E, F, and I. The complete set is shown in figure 3.13.

The highest amplifications are observed for mode C at pressure ratios where process 3 and 7 exist. Process 3 and 7 are naturally anti-symmetric modes. Mode C has a symmetric forced mode shape. It would be expected to produce a jet structure similar to XSS (processes 5 and 6). The natural XSS mode was encountered at approximately NPR = 3.75 and becomes dominant at NPR $\approx$ 5.0. Forced mode F has an in-plane flapping shape. When forced, it does not show greater amplification than forced mode C, which has a significant out-of-plane component. This is also true of forced mode I. Therefore further evidence is provided to suggest that the structure of the natural high pressure observed mode is similar to that of XSS.

Process 3 and 7 are in-plane anti-symmetric modes. These modes would be most amplified by

forced mode E, which is also has a dominant in-plane anti-symmetric component. Evidence for this amplification when mode E forcing is clear in NPR = 3.25 and 3.50 where process 7 can be used as a marker for where process 3's sensitivity might extend to.

The forced mode A with toroidal shape consistently shows low levels of amplification. The natural toroidal modes have consistently been experimentally observed at low NPR values. Therefore the instability modes that are provoked by forced toroidal actuation are particularly stable at higher pressure ratios. A peak in amplification is observed where process 1 and 2 is found. The forced toroidal mode is otherwise observed to reduce the OASPL for the majority of pressure ratios. The application of eight LAPFA actuators firing at once is likely to generate the most significant hydrodynamic perturbation compared to the other forced modes. Potentially this strong perturbation disrupts all other natural modes, increases the shear-layer thickness, and reduces the OASPL of the system.

Examining the contributing microphones to the OASPL reveals the direction of maximum acoustic amplification. Figure 7.9 shows the orthogonal microphone pairs 0-1 and 4-7 for select cases of high amplitude forced response provided by figure 7.8. The toroidal A mode is examined where it produces an amplification at [NPR = 2.52, St_{forced} = 0.48, figure 7.9a]. At the peak in the amplification for NPR = 2.52 where the toroidal A mode is expected to be the dominant mode, figure 7.9a shows the out-of-plane microphones (4-7) experience an amplification and the in-plane microphones (0-1) show a slight decrease in OASPL. The increase in OASPL of the out-of-plane compared to the in-plane of the toroidal mode is also observed in other twin-jet studies (Cluts *et al.*, 2015*a*). The predominantly in-plane E mode and predominantly out-of-plane C mode are shown for [NPR = 3.25, St_{forced} = 0.36, figure 7.9b] and [NPR = 3.50, St_{forced} = 0.28, figure 7.9c] respectively. Both modes clearly show a larger amplification in the dominant plane of oscillation. The increased acoustic emission in this direction is proposed to be due to the natural increased hydrodynamic instability of these modes at the respective operating conditions. The larger gain of the downstream process provides more energy for the conversion to the upstream process and thus an increased OASPL in this direction is observed.

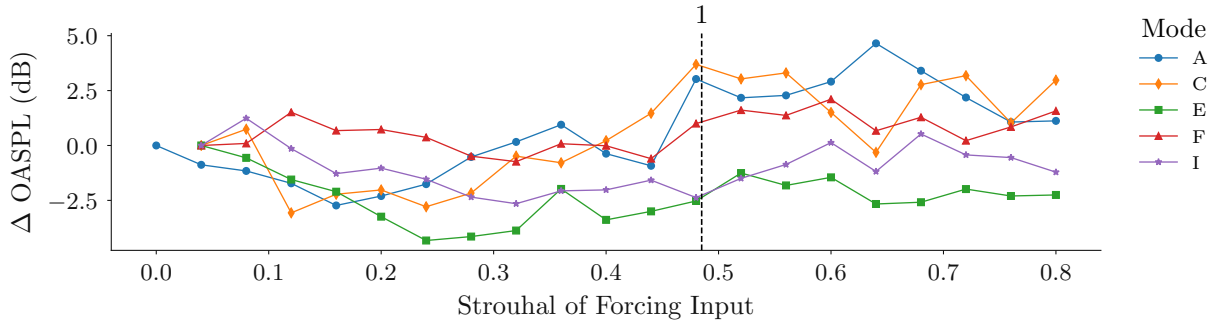

(a) Change in Overall Sound Pressure Level (OASPL), NPR = 2.52.

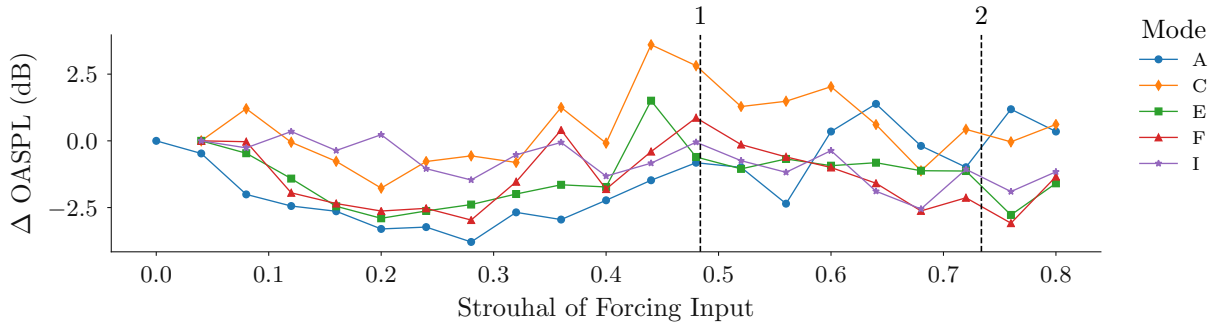

(b) Change in Overall Sound Pressure Level (OASPL), NPR = 2.75.

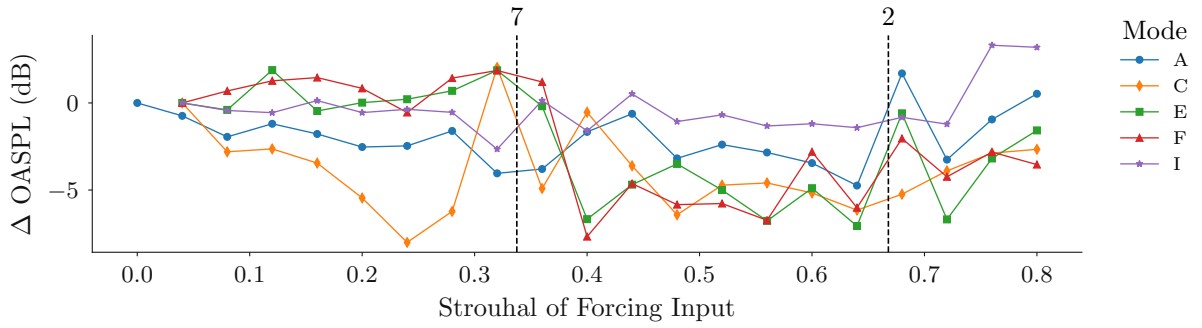

(c) PSD, NPR = 3.00.

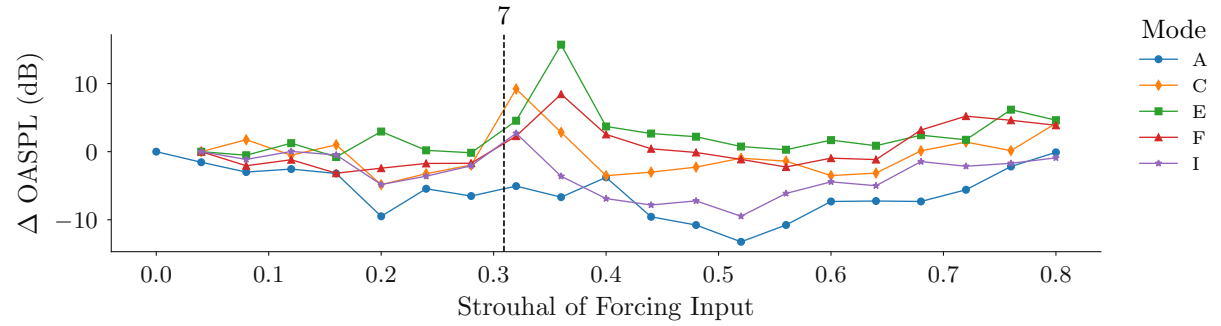

(d) PSD, NPR = 3.25.

Figure 7.8: Change in Overall Sound Pressure Level (OASPL) in response to different forcing modes. Black-dashed vertical lines indicate identified processes based on highly coherent frequencies in the unforced jet parameter space with an accompanying annotated process identification number.

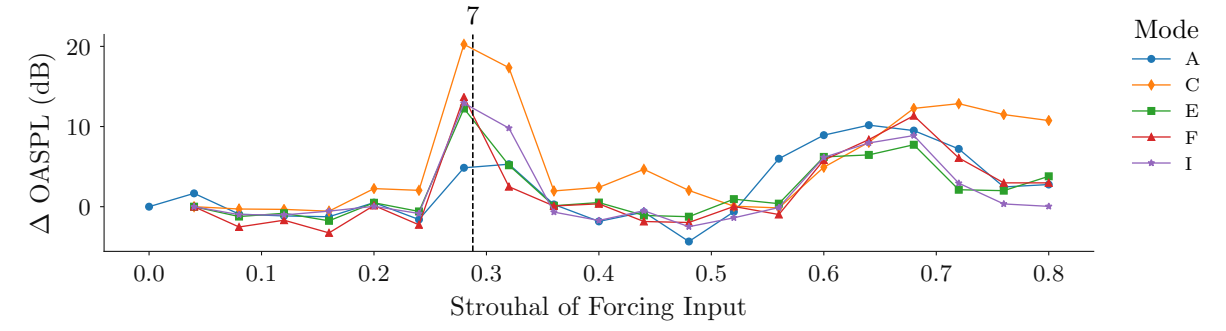

(e) PSD, NPR = 3.50.

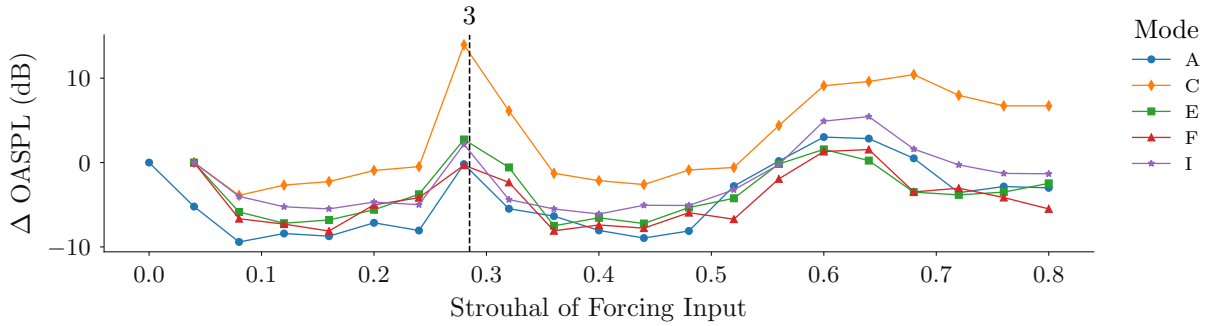

(f) PSD, NPR = 3.75.

Figure 7.8: Change in Overall Sound Pressure Level (OASPL) in response to different forcing modes. Black-dashed vertical lines indicate identified processes based on highly coherent frequencies in the unforced jet parameter space with an accompanying annotated process identification number.

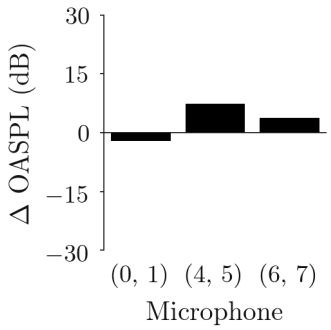

(a) Mode A, NPR = 2.52, St_{forced} = 0.48.

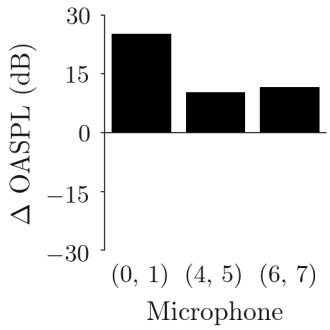

(b) Mode E, NPR = 3.25, St_{forced} = 0.36.

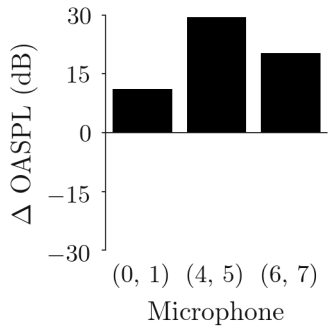

(c) Mode C, NPR = 3.50, St_{forced} = 0.28.

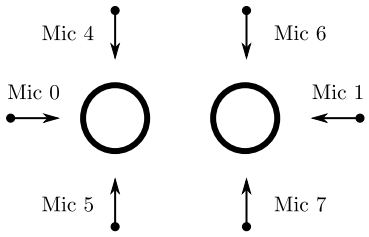

(d) Microphone configuration for reference.

Figure 7.9: OASPL of individual microphone pairs under steady forcing. Bracketed numbers on the horizontal axis indicate an averaging performed on that microphone pair.

7.2.6 Response of an Unactuated Jet To Adjacent Jet Forcing

A final case is considered that examines the natural response of a jet to the actuation of its neighbour. Case 6 is considered, which is comprised of a ceramic actuated nozzle and a polished steel (unactuated) nozzle.

The unforced natural response is shown in the sub-figures of figure 7.10. The competition between the two modes is clear. Under this configuration both the anti-symmetric (process 3) and symmetric (process 4, likely XSS) mode exist for majority of the pressure range. The toroidal modes 1 and 2 are also clear.

The response of the adjacent jet actuation setup is shown in the sub-figures of figure 7.11. Microphone 0 and microphone 1 correspond to the ceramic and steel nozzles respectively. The overlap between the forcing range and the natural toroidal modes includes only process 1. Therefore the forcing can only be applied to the natural toroidal modes for NPR = 2.52. A small amplification for process 1 is observed for NPR = 2.52 for microphone 1 and a slight suppression for microphone 0. The anti-symmetric mode corresponding to process 3 is enhanced by mode E. Its proximity to process 4 makes the detection of a change in response challenging to resolve. Figures 7.11b, 7.11c, 7.11d, 7.11e, and 7.11f all show amplification of both microphones for mode E. This is also the case considering modes C and G and their effect on the XSS mode shown in appendix D: figures D.1b, D.1c, D.1d, D.1e, and D.1f. Thus both jets (and feedback loops) were amplified from the actuation of a single jet. Therefore there exists a common and communicable feedback pathway between the jets. There must be a pathway for the acoustic waves generated by the actuated jet to reach the unforced jet in order to enhance its acoustic production. If a single jet actuated jet can achieve coupling then it suggests this acoustic coupling is done via the inter-nozzle region.

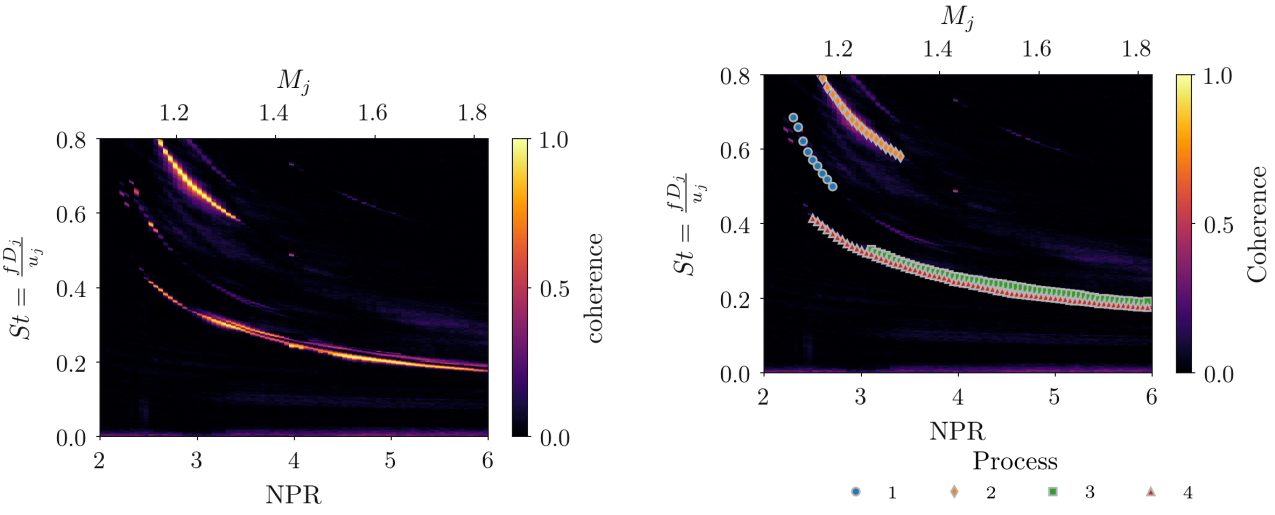

(a) Unforced ceramic nozzles.

(b) Unforced steel nozzles.

Figure 7.10: OASPL for individual microphones directions for select examples in from the single actuator forcing.

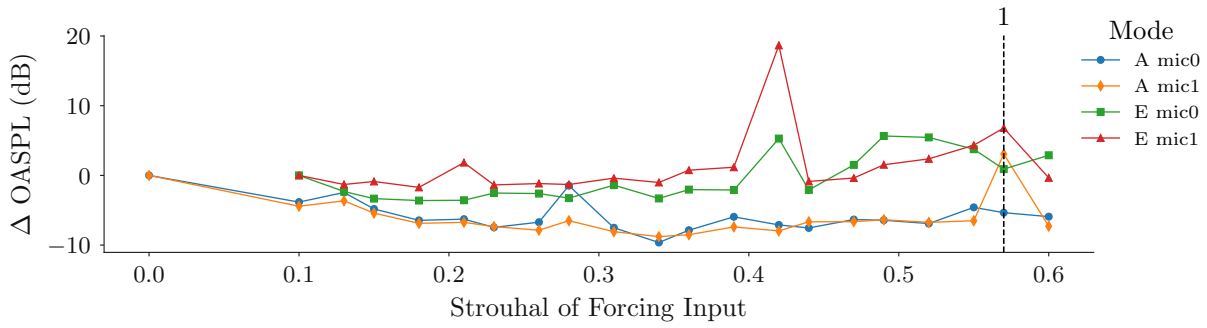

(a) Change in Overall Sound Pressure Level (OASPL), NPR = 2.52.

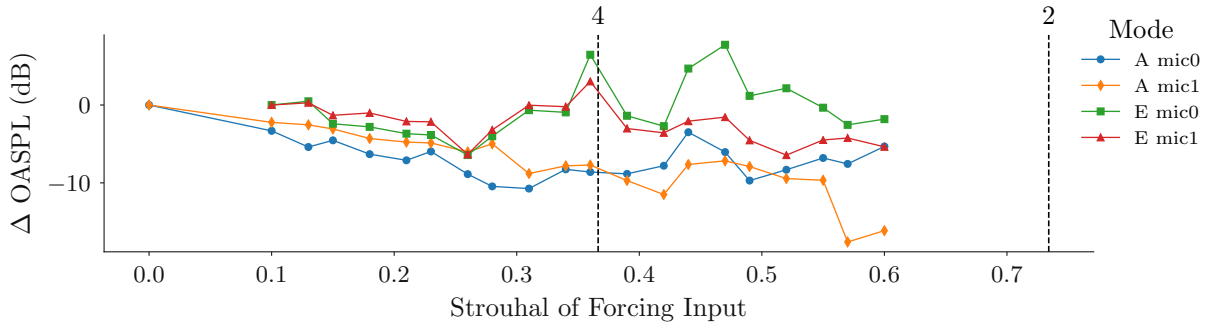

(b) Change in Overall Sound Pressure Level (OASPL), NPR = 2.75.

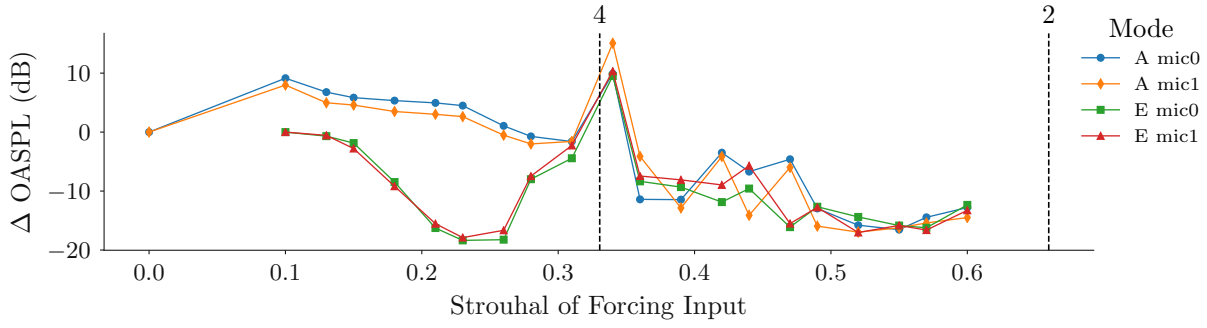

(c) PSD, NPR = 3.00.

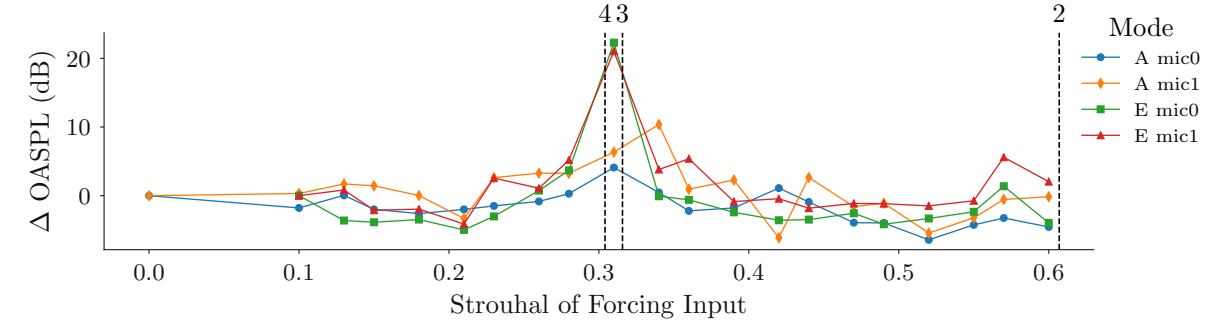

(d) PSD, NPR = 3.25.

Figure 7.11: Change in Overall Sound Pressure Level (OASPL) in response to different forcing modes. Black-dashed vertical lines indicate identified processes based on highly coherent frequencies in the unforced jet parameter space with an accompanying annotated process identification number.

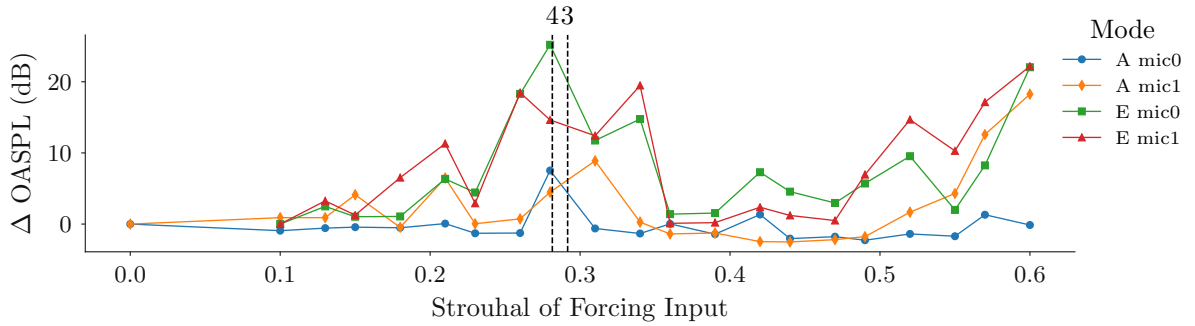

(e) PSD, NPR = 3.50.

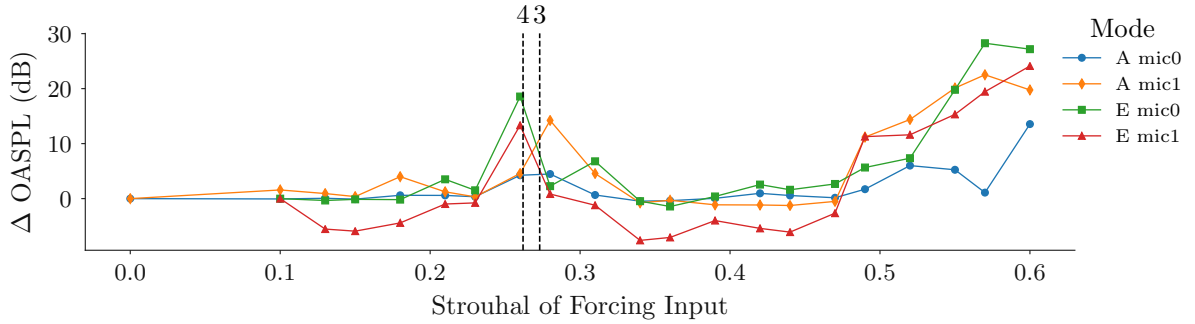

(f) PSD, NPR = 3.75.

Figure 7.11: Change in Overall Sound Pressure Level (OASPL) in response to different forcing modes. Black-dashed vertical lines indicate identified processes based on highly coherent frequencies in the unforced jet parameter space with an accompanying annotated process identification number.

7.3 Conclusion

This chapter provided an investigation of the out-of-plane coupling mode structure and examined the response of the natural modes to input perturbations of the $s/D = 3$ circular twin-jet. Additionally, steady forcing of the natural modes at pressures where they were not mode staged showed that they could be amplified to become the dominant mode. Lastly, a demonstration of the receptivity to coupling to an adjacent azimuthal mode was also included via the application of forcing to a single nozzle.

The natural modes of facility three were compared to those found on facility one and two. However, the mode staging of the individual modes was found to start and end at different mode switch locations. The out-of-plane components of the modes were assessed. Two low pressure modes were found that were shown to have a toroidal structure and correspond to the A1 and A2 modes respectively. The low pressure anti-symmetric mode was found to have helical or flapping structure. The higher pressure mode was found to have a structure similar to that of 2SS as defined by Rodríguez *et al.* (2018). The azimuthal mode number could not be confirmed so the mode was called the XSS mode. The XSS mode is comprised of an in-plane symmetric flapping mode with an out-of-plane anti-symmetric flapping mode offset by 90 degrees in phase.

Forcing was used to investigate the stability of the natural modes outside of the locations that they are dominant under natural mode staging. ΔOASPL was used to determine the acoustic enhancement of the natural modes. The effect of the actuators was explored first by applying them transiently. The acoustic response of the actuators showed that suppression of a natural mode was achieved by forcing a toroidal mode to disrupt the shear-layer. Forcing a mode with temporal unsteadiness showed the complete suppression of the tone. The temporally stable (non-competing) modes showed no hysteresis when the actuator was switched off. They returned to the natural modes on a very short time scale. Modes that have tone unsteadiness showed a lag to return to its natural behaviour when the actuator was turned off.

Steady state forcing showed that the natural modes could be significantly extended in NPR range by forcing similar shaped modes. Therefore the high (but not dominant) instability of the natural modes outside of their dominant regions was demonstrated. This is in agreement with existing stability studies. The high pressure symmetric mode, XSS, was found to have the greatest acoustic enhancement of approximately 20 dB. Toroidal modes were found to be the most resistant to amplification. At higher pressure ratios than where the toroidal modes were naturally staged, they were found to suppress the sound pressure level of the jet. It was proposed that this is due to the suppression of other modes and thickening of the shear-layer from all eight actuators firing simultaneously.

Forcing only one of the two nozzles was found to cause approximately the same amplitude rise in the unforced jet. An unforced jet was able to couple with the feedback loop of an adjacent jet. Therefore it was proposed that the twin-jet feedback pathway must travel acoustically be via the inter-nozzle region.

Chapter 8

Conclusions

An experimental investigation into the coupling modes of circular underexpanded supersonic twin-jet was undertaken. The behaviour of some twin-jet coupling modes had been described as clear symmetric, toroidal, or anti-symmetric. Other regions of the pressure ratio and spacing parameter space have been described as complex. In these complex regions, the coupling behaviour between the jets was not known. This work investigates and provides a physical description of the coupling occurring in both the clear and complex coupling parameter space regions. Additionally further physical questions surrounding multi-modality and non-linear interactions in the coupling process were explored.

A characterisation study was undertaken to extend the understanding of the twin-jet parameter space and identify complex interactions between the jets. It was found that complex coupling also occurs in circular twin-jets. Previously this type of coupling had only been observed in rectangular configurations. It was found that nozzle spacing was found to play a significant role in coupling mode selection. Discontinuous jumps in dominant screech frequency were found to be insufficient to identify all changes in the coupling modes. Mode staging could not be explained by the existing models for screech (Panda, 1999; Gao & Li, 2010). Potentially a change in source location, path-length, or upstream propagating closure mechanism occurs between different coupling modes. This could be used to provide a model for twin-jet coupled screech frequency prediction. Cross-bicoherence is found not to overlap with the complex coupling region. It was inferred that complex coupling is not solely the result of non-linear interactions between frequencies in the flow.

After the complex mode coupling regions were identified, a PIV dataset was taken to examine the flow in clear and complex coupling regions. The dataset was required to examine the coupling in subsequent chapters. The inter-nozzle mixing, merge point, and shear-layer thicknesses were quantified. Inter-nozzle mixing was shown to be suppressed until $x/D \geq 10$ due to the low of velocity shear with quiescent fluid after the merge point. Decomposition of the flow field yielded a clear symmetric coupling mode for the clear region, but an inconclusive result for the complex coupling region.

A study was completed that specifically examines the physical relationship between the jets in the complex region. The strengths of three experimental facilities were used and new techniques were

developed to analyse the time-varying acoustic processes produced by the flow. Two intense and continuously varying frequencies were observed across the pressure range. These were shown to be associated with different aeroacoustic feedback processes. At low pressure a tone emerges that was associated with a steady anti-symmetric coupling mode. At higher pressures the introduction of a steady symmetric coupling mode and an associated tone was encountered. It was found that the complex coupling region is formed from the competition between these two feedback processes. The analysis revealed that the jets often became uncoupled and screech independently. In the uncoupled state, the individual jets experienced frequent interruptions to their screeching process and significant reductions in acoustic amplitude. As predicted by the analysis, direct observation of the interrupted process was observed within ultra high speed schlieren photography. Analysis of the individual jets during coupling in either mode revealed a single instability mode and hydrodynamic wavelength. The individual jets have the same structure in either coupling mode. Thus, the tone frequency difference between the competing modes must be produced by the way the jets couple together.

A final study examined the out-of-plane coupling mode structure and response to forcing for the natural modes of the $s/D = 3$ circular twin-jet. Two low pressure modes were found to have a toroidal structure and correspond to the A1 and A2 modes respectively. The low pressure anti-symmetric mode was found to have a helical or flapping structure. The higher pressure mode was found to have a structure similar to that of 2SS as defined by Rodríguez *et al.* (2018). 2SS is comprised of an in-plane symmetric flapping mode with an out-of-plane anti-symmetric flapping mode. Forcing was used to investigate the stability of the natural modes outside of the locations they normally appear under normal mode staging. Acoustic amplification was used as a proxy to the stability margin. Steady state forcing showed that the natural modes could be significantly extended in NPR range by forcing similar shaped modes. It was shown that all modes could be enhanced outside of their natural staging. The high pressure symmetric mode, 2SS, was found to have the greatest acoustic enhancement. Toroidal modes were found to be the most resistant to amplification. Forcing only one of the two nozzles was found to cause approximately the same amplitude rise in the unforced jet. An unforced jet was able to couple with the feedback loop of an adjacent jet. Therefore it was proposed that the twin-jet feedback pathway must travel acoustically via the inter-nozzle region.

Bibliography

Alkislar, Mehmet B., Krothapalli, A, Choutapalli, I & Lourenco, L 2005 Structure of Supersonic Twin Jets. *AIAA journal* **43** (11), 2309–2318.

Bell, Graham, Soria, Julio, Honnery, Damon & Edgington-Mitchell, Daniel 2018 An experimental investigation of coupled underexpanded supersonic twin-jets. *Experiments in Fluids* **59** (9), 139.

Benedict, L. H. & Gould, R. D. 1996 Towards better uncertainty estimates for turbulence statistics. *Experiments in Fluids* **22** (2), 129–136.

Berndt, D. E. 1984 Dynamic Pressure Fluctuations in the Internozzle Region of a Twin-Jet Nacelle. In *SAE Technical Paper*, p. 10. Society of Automotive Engineers.

Bogey, Christophe & Gojon, Romain 2017 Feedback loop and upwind-propagating waves in ideally expanded supersonic impinging round jets. *Journal of Fluid Mechanics* **823**, 562–591.

Cluts, Jordan, Kuo, Ching-Wen & Samimy, Mo 2015*a* An Investigation of Twin Supersonic Jets' Near-field. In *21st AIAA/CEAS Aeroacoustics Conference*. Reston, Virginia: American Institute of Aeronautics and Astronautics.

Cluts, Jordan, Kuo, Ching-Wen & Samimy, Mo 2015*b* Exploring Physics and Control of Twin Supersonic Circular Jets. In *53rd AIAA Aerospace Sciences Meeting*. Reston, Virginia: American Institute of Aeronautics and Astronautics.

Cluts, Jordan, Kuo, Ching-Wen & Samimy, Mo 2016 Coupling Dynamics of Twin Supersonic Round Jets. In *22nd AIAA/CEAS Aeroacoustics Conference*, pp. 1–22.

Cluts, Jordan, Kuo, Ching-Wen & Samimy, Mo 2017 An Investigation of Effects of Jet Temperature on Twin-Jet Flow and Acoustic Fields. In *55th AIAA Aerospace Sciences Meeting*, pp. 1–15. Reston, Virginia: American Institute of Aeronautics and Astronautics.

Corke, Thomas C., Enloe, C. Lon & Wilkinson, Stephen P. 2010 Dielectric Barrier Discharge Plasma Actuators for Flow Control. *Annual Review of Fluid Mechanics* **42** (1), 505–529.

Davis, M G & Oldfield, D E S 1962 Tones from a choked axisymmetric jet. I. Cell structure, eddy velocity and source locations. *Acustica* **12** (4), 257–277.

Du, Zihua 1993 Acoustic and Kelvin-Helmholtz instability waves of twin supersonic jets. PhD thesis, Florida State University.

Du, Zihua 2002 Kelvin-Helmholtz Instability Waves of Supersonic Multiple Jets. In *Proceedings of the forth international conference on dynamical systems and differential equations*.

Edgington-Mitchell, Daniel 2019 Aeroacoustic resonance and self-excitation in screeching and impinging supersonic jets - a review. *International Journal of Aeroacoustics* .

Edgington-Mitchell, Daniel, Honnery, Damon & Soria, Julio 2015 Staging behaviour in screeching elliptical jets. *International Journal of Aeroacoustics* **14** (7), 1005–1024.

Edgington-Mitchell, Daniel, Jaunet, Vincent, Jordan, Peter, Towne, Aaron, Soria, Julio & Honnery, Damon 2018 Upstream-travelling acoustic jet modes as a closure mechanism for screech. *Journal of Fluid Mechanics* **855**.

Gao, J. H. & Li, X. D. 2010 A multi-mode screech frequency prediction formula for circular supersonic jets. *The Journal of the Acoustical Society of America* **127** (3), 1251–1257.

Herbert, Thorwald 1997 Parabolized Stability Equations. *Annual Review of Fluid Mechanics* **29** (1), 245–283.

Huang, Norden E., Shen, Zheng, Long, Steven R., Wu, Manli C., Snin, Hsing H., Zheng, Quanan, Yen, Nai Chyuan, Tung, Chi Chao & Liu, Henry H. 1998 The empirical mode decomposition and the Hubert spectrum for nonlinear and non-stationary time series analysis. *Proceedings of the Royal Society A: Mathematical, Physical and Engineering Sciences* **454** (1971), 903–995, arXiv: NIHMS150003.

Humphrey, Nathan J & Edgington-Mitchell, Daniel 2016 The effect of low lobe count chevron nozzles on supersonic jet screech. *International Journal of Aeroacoustics* **15** (3), 294–311.

Kim, J.-H., Kastner, J. & Samimy, Mo 2009 Active Control of a High Reynolds Number Mach 0.9 Axisymmetric Jet. *AIAA Journal* **47** (1), 116–128.

Knast, Thomas, Bell, Graham, Wong, Marcus, Leb, Corey M., Soria, Julio, Honnery, Damon R. & Edgington-Mitchell, Daniel 2018 Coupling modes of an underexpanded twin axisymmetric jet. *AIAA Journal* **56** (9), 3524–3535.

Kuo, Ching-Wen, Cluts, Jordan & Samimy, Mo 2016*a* Active Flow Control of Supersonic Twin-Jet Plumes. *Journal of Aeronautics, Astronautics and Aviation* **48** (4), 243–251.

Kuo, Ching-Wen, Cluts, Jordan & Samimy, Mo 2016*b* An Investigation of Twin Supersonic Jet Coupling. In *54th AIAA Aerospace Sciences Meeting*, pp. 1–20.

Kuo, Ching-Wen, Cluts, Jordan & Samimy, Mo 2017*a* Effects of excitation around jet preferred mode Strouhal number in high-speed jets. *Experiments in Fluids* **58** (4), 35.

Kuo, Ching-Wen, Cluts, Jordan & Samimy, Mo 2017*b* Exploring physics and control of twin supersonic circular jets. In *AIAA Journal*, , vol. 55, pp. 68–85. American Institute of Aeronautics and Astronautics.

Mancinelli, Matteo, Jaunet, Vincent, Jordan, Peter & Towne, Aaron 2019 Screech-tone prediction using upstream-travelling jet modes. *Experiments in Fluids* **60** (1), 22.

Mercier, Bertrand, Castelain, Thomas & Bailly, Christophe 2017 Experimental characterisation of the screech feedback loop in underexpanded round jets. *Journal of Fluid Mechanics* **824**, 202–229.

Michalke, Alfons 1984 Survey on jet instability theory. *Progress in Aerospace Sciences* **21** (C), 159–199.

Mitchell, Daniel M, Honnery, Damon R & Soria, Julio 2012 The visualization of the acoustic feedback loop in impinging underexpanded supersonic jet flows using ultra-high frame rate schlieren. *Journal of Visualization* **15** (4), 333–341.

Morris, Philip J. 1990 Instability waves in twin supersonic jets. *Journal of Fluid Mechanics* **220** (1), 293–307.

Morris, Philip J. 2010 The instability of high speed jets. *International Journal of Aeroacoustics* **9** (1), 1–50.

Moustafa, Gamal H. 1994 Experimental investigation of high-speed twin jets. *AIAA Journal* **32** (11), 2320–2322.

Norum, T. D. 1983 Screech suppression in supersonic jets. *AIAA Journal* **21** (2), 235–240.

Norum, T D & Seiner, J M 1982 Broadband shock noise from supersonic jets. *AIAA journal* **20** (1), 68–73.

Pack, D. C. 1950 A note on prandtl's formula for the wave-length of a supersonic gas jet. *Quarterly Journal of Mechanics and Applied Mathematics* **3** (2), 173–181.

Panda, Jayanta 1999 An experimental investigation of screech noise generation. *Journal of Fluid Mechanics* **378**, 71–96.

Panda, J & Seasholtz, R G 1999 Measurement of shock structure and shock–vortex interaction in underexpanded jets using Rayleigh scattering. *Physics of Fluids* **11** (12), 3761–3777.

Panickar, Praveen, Srinivasan, K. & Raman, Ganesh 2004 Aeroacoustic features of coupled twin jets with spanwise oblique shock-cells. *Journal of Sound and Vibration* **278** (1-2), 155–179.

Panickar, Praveen, Srinivasan, K. & Raman, Ganesh 2005 Nonlinear interactions as precursors to mode jumps in resonant acoustics. *Physics of Fluids* **17** (9), 1–18.

Poloskei, Peter Zsolt, Papp, Gergely, Por, Gabor, Horvath, Laszlo & Pokol, Gergo I 2018 Bicoherence analysis of nonstationary and nonlinear processes.

Ponton, Michael K & Seiner, J. M. 1992 The effects of nozzle exit lip thickness on plume resonance. *Journal of Sound and Vibration* **154** (3), 531–549.

Ponton, Michael K, Seiner, John M & Brown, Martha C 1997 Near Field Pressure Fluctuations in the Exit Plane of a Choked Axisymmetric Nozzle. *Tech. Rep.* November. NASA Technical Memorandum.

Powell, Alan 1953*a* On edge tones and associated phenomena. *Acta Acustica united with Acustica* **3** (4), 233–243.

Powell, Alan 1953*b* On the mechanism of choked jet noise. *Proceedings of the Physical Society. Section B* **66** (12), 1039–1056.

Powell, Alan 1953*c* The Noise of Choked Jets. *Journal of the Acoustical Society of America* **25** (3), 385–389.

Powell, Alan 1954 The reduction of choked jet noise. *Proceedings of the Physical Society. Section B* **67** (4), 313–327.

Powell, Alan 1961 On the Edgetone. *The Journal of the Acoustical Society of America* **33** (4), 395–409.

Powell, Alan, Umeda, Yoshikuni & Ishii, Ryuji 1992 Observations of the oscillation modes of choked circular jets. *The Journal of the Acoustical Society of America* **92** (5), 2823–2836.

Raffel, Markus, Willert, Christian E, Wereley, Steve T & Kompenhans, Jurgen 2007 *Particle Image Velocimetry, A Practical Guide*, 2nd edn., , vol. 6. Heidelberg, New York: Springer Berlin Heidelberg, arXiv: 1011.1669v3.

Raman, Ganesh 1998 Coupling of Twin Rectangular Supersonic Jets. *Journal of Fluid Mechanics* **354** (5), 123–146.

Raman, Ganesh, Panickar, Praveen & Chelliah, Kanthasamy 2012 Aeroacoustics of twin supersonic jets: a review. *International Journal of Aeroacoustics* **11** (7), 957–984.

Rodríguez, Daniel, Jotkar, Mamta R. & Gennaro, Elmer M. 2018 Wavepacket models for subsonic twin jets using 3D parabolized stability equations.

Samimy, Mo, Kearney-Fischer, M, Kim, J. H. & Sinha, A 2012 High-speed and high-reynolds-number jet control using localized arc filament plasma actuators. *Journal of Propulsion and Power* **28** (2), 269–280.

Seiner, J 1984 Advances in high speed jet aeroacoustics. In *9th Aeroacoustics Conference*. Reston, Virigina: American Institute of Aeronautics and Astronautics.

Seiner, J, Manning, James C & Ponton, Michael K 1986 Dynamic pressure loads associated with twin supersonic plume resonance. *AIAA Journal* **26** (8), 954–960.

Settles, Gary S 2012 *Schlieren and shadowgraph techniques: visualizing phenomena in transparent media*. Springer Science & Business Media.

Shaw, Leonard 1990 Twin-jet screech suppression. *Journal of Aircraft* **27** (8), 708–715.

Shen, H & Tam, Christopher K. W. 2000 Effects of Jet Temperature and Nozzle-Lip Thickness on Screech Tones. *AIAA Journal* **38** (5).

Sinha, Aniruddha, Rodríguez, Daniel, Brès, Guillaume A. & Colonius, Tim 2014 Wavepacket models for supersonic jet noise. *Journal of Fluid Mechanics* **742**, 71–95.

Soria, Julio 1996 An investigation of the near wake of a circular cylinder using a video-based digital cross-correlation particle image velocimetry technique. *Experimental Thermal and Fluid Science* **12** (2), 221–233.

Srinivasan, K., Panickar, Praveen, Raman, Ganesh, Kim, Byung Hun & Williams, David R. 2009 Study of coupled supersonic twin jets of complex geometry using higher-order spectral analysis. *Journal of Sound and Vibration* **323** (3-5), 910–931.

Tam, Christopher K. W. 1971 Directional acoustic radiation from a supersonic jet generated by shear layer instability. *Journal of Fluid Mechanics* **46** (4), 757–768.

Tam, Christopher K. W. 1991 Jet noise generated by large-scale coherent motion. In *Aeroacoust. of Flight Vehicles: Theory and Practice, Vol. 1: Noise Sources*, p. 311. Washington DC: NASA.

Tam, Christopher K. W. & Ahuja, Krishan K. 1990 Theoretical model of discrete tone generation by impinging jets. *Journal of Fluid Mechanics* **214** (-1), 67–87.

Tam, Christopher K. W. & Seiner, J 1987 Analysis of Twin Supersonic Plume Resonance. In *AIAA 11th Aeroacoustics Conference*.

Tam, Christopher K. W., Seiner, J & Yu, J. C. 1986 Proposed relationship between broadband shock associated noise and screech tones. *Journal of Sound and Vibration* **110** (2), 309–321.

Tanna, H. K. 1977 An experimental study of jet noise part II: Shock associated noise. *Journal of Sound and Vibration* **50** (3), 429–444.

Welch, Peter 1967 The use of fast Fourier transform for the estimation of power spectra: a method based on time averaging over short, modified periodograms. *IEEE Transactions on audio and electroacoustics* **15** (2), 70–73.

Westerweel, J., Geelhoed, P. F. & Lindken, R. 2004 Single-pixel resolution ensemble correlation for micro-PIV applications. *Experiments in Fluids* **37** (3), 375–384.

Westley, R. & Woolley, J. H. 1969 The near field sound pressures of a choked jet during a screech cycle. In *Agard Cp*, , vol. 42, pp. 23.1–23.13. Reston, Virigina: American Institute of Aeronautics and Astronautics.

Willert, Christian E, Mitchell, Daniel M & Soria, Julio 2012 An assessment of high-power light-emitting diodes for high frame rate schlieren imaging. *Experiments in Fluids* **53** (2), 413–421.

Willert, Christian E, Stockhausen, G, Voges, M, Klinner, M, Schodl, R, Hassa, C, Schürmans, B & Güthe, F 2008 *Particle Image Velocimetry: New Developments and Recent Applications*, 1st edn., , vol. 112. Springer Berlin Heidelberg.

Wlezien, Richard 1989 Nozzle geometry effects on supersonic jet interaction. *AIAA Journal* **27** (10), 1361–1367.

Wlezien, Richard & Kibens, V. 1988 Influence of nozzle asymmetry on supersonic jets. *AIAA Journal* **26** (1), 27–33.

Zilz, David & Wlezien, Richard 1990 The sensitivity of near-field acoustics to the orientation of twin two-dimensional supersonic nozzles. In *26th Joint Propulsion Conference*. Reston, Virigina: American Institute of Aeronautics and Astronautics.

Appendix A

Coupling Modes of an Underexpanded Twin Axisymmetric Jet, AIAA Journal, 2018

Coupling Modes of an Underexpanded Twin Axisymmetric Jet

Thomas Knast,* Graham Bell,* Marcus Wong,* Corey M. Leb,† Julio Soria,‡ Damon R. Honnery,§ and Daniel Edgington-Mitchell¶
Monash University, Melbourne, Victoria 3800, Australia

DOI: 10.2514/1.J056434

An experimental investigation into the coupling behavior of screeching axisymmetric twin supersonic jets is presented. Acoustic measurements and schlieren photography are used to identify four distinct coupling modes over a wide range of pressure ratios and nozzle spacings. Nozzle spacing is found to have a significant effect on the selection of these modes as well as the transition between them. A discrete jump in the peak screech frequency is seen to accompany most but not all mode switches. Statistical analysis of schlieren photography provides evidence that the modes consist of two flapping (symmetric and antisymmetric) and two different helical oscillations. These coupling modes are shown to have a limited effect on the convection velocity of the large-scale structures within the jet, and as such, the characteristic length scales are investigated as a source of mode switching.

Nomenclature

D	=	nozzle diameter
D_j	=	fully expanded jet diameter
f	=	frequency
I	=	pixel intensity
M_c	=	convective Mach number
M_j	=	fully expanded Mach number
m	=	number of combined hydrodynamic and acoustic wavelengths
N	=	number of images in the data set
NPR	=	nozzle pressure ratio; $P_{\text{plenum}}/P_{\text{atm}}$
n	=	number of shock cells in the acoustic reinforcement region
R	=	covariance
S	=	nozzle spacing (center to center)
SPL	=	sound pressure level, dB
St	=	Strouhal number; $f \cdot D_j/U_j$
s	=	shock cell spacing
t	=	time, s
U_c	=	convective velocity, m $\cdot$ s^{-1}
U_j	=	fully expanded jet velocity, m $\cdot$ s^{-1}
x	=	downstream direction with respect to the jet
y	=	common nozzle axis direction
x_o	=	reference location in the downstream direction
y_o	=	reference location in the common nozzle axis direction
Δx	=	offset distance in the downstream direction
Δy	=	offset distance in the common nozzle axis direction
λ_A	=	acoustic wavelength
λ_L	=	hydrodynamic wavelength
λ_{SW}	=	standing wave wavelength
σ	=	standard deviation of pixel intensity

Received 15 June 2017; revision received 9 March 2018; accepted for publication 10 March 2018; published online 25 June 2018.

*Ph.D. Student, Laboratory of Turbulence Research in Aerospace and Combustion, Department of Mechanical and Aerospace Engineering. Member AIAA.

†Graduate, Department of Mechanical and Aerospace Engineering.

‡Professor, Laboratory of Turbulence Research in Aerospace and Combustion, Department of Mechanical and Aerospace Engineering. Associate Fellow AIAA.

§Professor, Laboratory of Turbulence in Aerospace and Combustion, Department of Mechanical and Aerospace Engineering. Member AIAA.

¶Senior Lecturer, Laboratory of Turbulence in Aerospace and Combustion, Department of Mechanical and Aerospace Engineering. Member AIAA.

I. Introduction

AN UNDEREXPANDED supersonic jet has multiple sources of noise generation. One of these sources is a discrete high-amplitude tone known as screech. Powell [1] first determined that screech is the result of a resonant aeroacoustic feedback loop. In this feedback process, coherent shear-layer vortices convect downstream from the nozzle lip, growing in strength as they propagate. These large-scale coherent structures interact with the shock cell structure within the jet core and produce strong acoustic waves. The acoustic waves propagate back upstream, where they excite the shear layer at the nozzle, forming new coherent structures to close the feedback loop [2]. For information on the other sources of noise generation within a supersonic jet, the reader is referred to Tam's [3] review on the topic.

Screech in supersonic axisymmetric jets is characterized by multiple stages. Each of these stages is typified by a different oscillation structure of the jet plume. Five distinct stages have been identified in a single axisymmetric jet: the A1 and A2 toroidal modes, the *B* and *D* lateral flapping modes, and the *C* helical mode [4]. Which oscillation mode dominates is dependent on the nozzle pressure ratio (NPR), the nozzle geometry, and (for multijet configuration) the separation between jets. In the twin-jet configurations, toroidal, helical, and flapping oscillations have been observed [5]; however, the staging behavior and transition between these oscillation modes is not well understood.

Because of the screech feedback process, a change in jet oscillation is typically accompanied by an abrupt shift in the screech tone frequency. For some oscillation modes, the frequency and directionality of the screech tone can be accurately predicted by a model based on three equally spaced monopole sources of equal strength [1]. Using shock cell spacing as the characteristic length scale within this model and assuming maximum upstream directivity, Powell produced an analytical formula for predicting the frequency of the screech tone:

$$f = \frac{U_c}{s(1 + M_c)} \tag{1}$$

where U_c and M_c are the convective velocity and convective Mach number, respectively. This model has been shown to be accurate during some but not all screech modes of a single jet. The accuracy of this model in predicting the screech tone in certain modes but not others has led previous authors to suggest the existence of multiple closure mechanisms to the screech feedback loop. In the classical understanding, the acoustic waves propagate freely upstream outside the jet, then perturb the flow at the nozzle lip. The other mechanism, known as the wave guide model, is based on instability waves identified by Tam and Hu [6]. Shen and Tam [7] showed that, in a single circular jet, a model based on the first mechanism can predict the A1 and B modes, whereas a model based on the second mechanism is capable of successfully predicting the A2 and *C* modes.

Recently, the length of the standing wave has been proposed as a more appropriate characteristic length scale for predicting screech. Westley and Woolley [8] first identified this standing wave that characterizes the acoustic near field of a supersonic jet. Panda [9] then showed that the standing wavelength is the result of an interaction between the hydrodynamic waves within the jet shear layer and the acoustic waves propagating upstream. He proposed the screech frequency to be predicted by

$$f = \frac{U_c}{\lambda_{\mathrm{SW}}(1 + M_c)} \tag{2}$$

where λ_{SW} is the standing wavelength and is given by

$$\frac{1}{\lambda_{\mathrm{SW}}} = \frac{1}{\lambda_A} + \frac{1}{\lambda_L} \tag{3}$$

where λ_A is the acoustic wavelength, and λ_L is the wavelength of the hydrodynamic waves. For both axisymmetric and elliptical single screeching jets, evidence has been provided to suggest that the change in feedback mechanism is associated with a matching or mismatching of the standing wavelength and shock cell spacing length scales [10,11]. This connection has not been investigated for a multijet configuration.

The effects of screech are potentially more significant in a multijet configuration. Supersonic jet plumes in close proximity couple, enhancing the feedback process associated with the screech phenomenon [12]. In the twin axisymmetric supersonic jet, the staging behavior is dictated by these coupling modes that have historically been classified by their symmetry properties about the midplane [13]. An antisymmetric coupling mode displays a 0 deg phase difference between the two plumes, whereas a symmetric coupling mode has a 180 deg phase difference between plumes. These oscillation modes are shown in Fig. 1. The amplitude of the screech tone is significantly affected by the dominant coupling mode and can be either increased or reduced as a result [14]. Work by Shaw [15] found that some twin-jet coupling modes can result in screech tone amplitudes as much as 20 dB higher than that of a single jet. Experimental work by Kuo et al. [5,16] furthered this by mapping the pressure along the twin-jet plane in the near field for multiple coupling modes, then investigating the stability of these modes by actively forcing the shear layer near the nozzle lip. Although the effects of these coupling modes have been investigated, more needs to be done to understand the selection and progression of coupling modes in twin jets.

Prior twin-jet research has focused primarily on the coupling effects of twin supersonic jets at a single nozzle spacing. A notable exception is the investigation of Wlezien [17], who found that closer nozzle spacings enhanced the A1 and *B* modes while suppressing the *C* mode, relative to a single jet. This phenomenon inverts at larger nozzle spacings, and the *C* mode is more strongly supported within the jet. Raman and Taghavi [18] also investigated variable nozzle spacings in a rectangular twin jet, finding that an increase in the internozzle spacing delayed mode transition. However, the aspect ratio of a rectangular jet constrains the oscillation modes to the major axis of the jets, significantly limiting the possible interactions between twin-jet plumes.

Given the dependence of the screech tone on the coupling mode of a twin jet and the limited experimental data available at varying nozzle spacing, this paper investigates the staging behaviors of a twin underexpanded axisymmetric jet at two nozzle spacings. Acoustic measurements are first used to discern the staging progression for each nozzle spacing. An investigation of the phase between the plumes of the jet suggests that progression of the modes in each stage is significantly different for the two spacings. This suggests that increasing the spacing between an axisymmetric twin jet has a larger effect on mode selection than simply delaying transition. Schlieren photography obtained in two orthogonal planes is used to identify four distinct coupling modes. Characteristic length and velocity scales are then investigated as possible mode selection parameters.

II. Experimental Methodology

A. Facility

The experiments were conducted at the Laboratory for Turbulence Research in Aerospace and Combustion at Monash University. The supersonic jet facility used is shown in Fig. 2a. The system is supplied by a continuous high-pressure air supply. The flow passes through a regulator as well as the relevant piping before entering the plenum chamber, where the stagnation pressure is measured using an RS-461 pressure transducer. The pressure transducer has a range of 0–10 bar and an accuracy of $\pm 0.25\%$.

A modular twin-nozzle attachment, shown in Fig. 2b, was designed and purpose built for this study. The design consists of two axisymmetric converging nozzles of 10 mm exit diameter. Both nozzles emanate from a shared plenum to ensure matched pressure ratios. The design allows for a variable nozzle spacing S/D between the nozzles of diameter D. Each of the two nozzles are able to slide in a track while maintaining orientation with respect to each other and are held in place with interchangeable sealing plates of fixed separation. Each nozzle's cross section follows an elliptical profile, as shown in Fig. 2c.

A Toepler Z-Type schlieren system [19,20] was used to image the twin supersonic jet. Two mirrors, each of focal length 2032 mm, were used to create a collimated light path through the test section. Only the density gradient in the streamwise direction ($\partial\rho/\partial x$) is presented in this investigation. A Shimadzu HPV-1 camera was used to obtain high-speed images of the twin jet. The camera has a resolution of 320×260 pixels and can capture 102 images at an acquisition speed of up to 1 million frames per second at an exposure of 0.25 μs. Illumination was provided with a Metz Mecablitz flash. A PCO4000 camera was used to obtain high-resolution images of the twin jet. The camera has a resolution of 4008×2672 pixels and was run at an

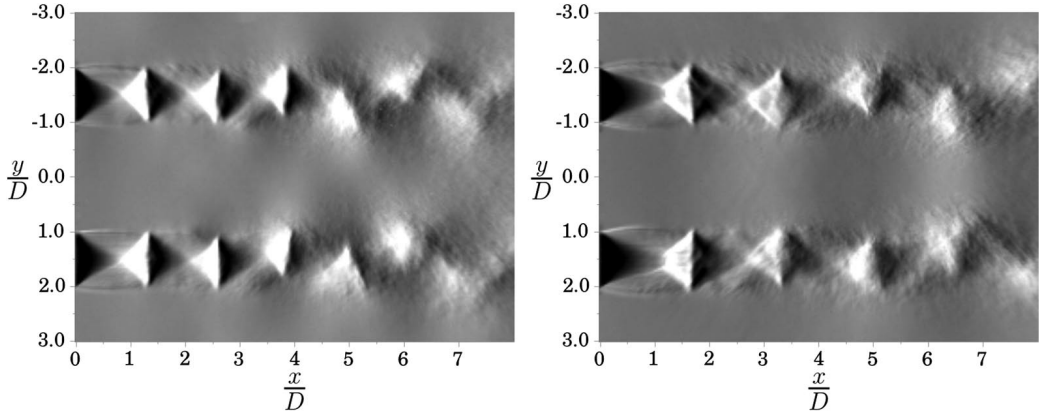

a) The antisymmetric oscillation, NPR = 3.2 **b) The symmetric oscillation, NPR = 4.4**

Fig. 1 Phase-mean schlieren images showing the two modes of the twin supersonic jet at a nozzle separation of $S/D = 3$.

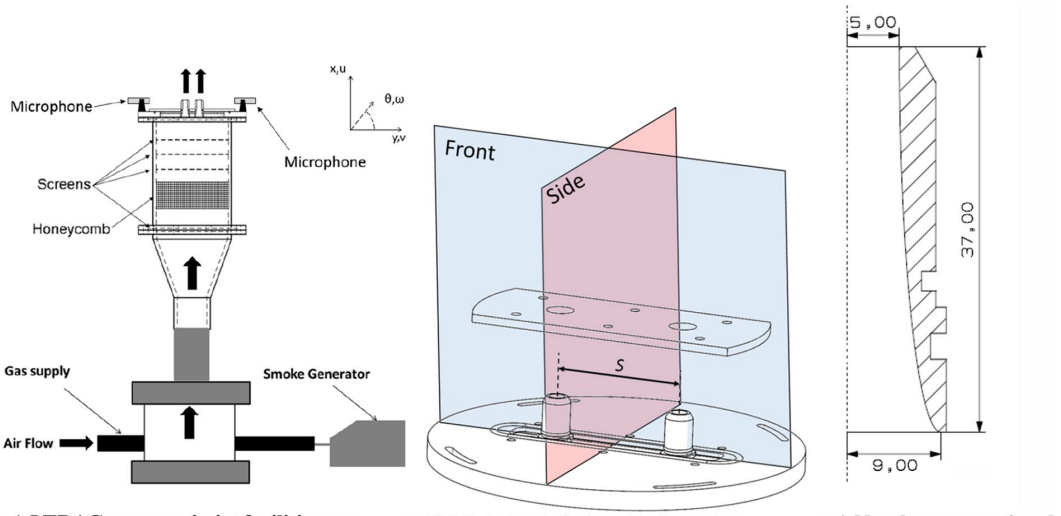

a) LTRAC supersonic jet facilitiy adapted from Edgington-Mitchell [11] **b) Modular twin jet attachment** **c) Nozzle cross sectional profile, (mm)**

Fig. 2 Supersonic jet facility.

acquisition speed of 1 Hz with an exposure of 1.6 μs. Illumination was provided with a pulsed light-emitting diode [21].

Acoustic measurements were obtained with a pair of G.R.A.S. Type 46BE 1/4-in.diam microphones with preamplification. The microphones have a bandwidth of 4 Hz to 80 kHz and a dynamic range of 35–160 dB. All acoustic measurements were obtained from two such microphones placed at a distance of 8D to either side of the nozzles along the shared nozzle plane, as measured from the center of the closest nozzle. The microphones were located at the height of the nozzle lip and orientated directly at the nozzle, as shown in Fig. 2a. Recordings consisted of 5×10^5 samples obtained at an acquisition frequency of 200 kHz. This facility does not, however, provide an anechoic environment, and as such only the fundamental screech peak measurements are considered here. The microphone signals are used solely to identify the peak frequency and phase relation; amplitude is not considered, and so no additional corrections are applied to the recorded signal.

B. Analysis Techniques

1. Acoustic Phase

Acoustic measurements from multiple microphones are used to investigate the relative phase of oscillation between the two jet plumes. Each plume of the twin jet undergoes the screech feedback cycle and hence produces individual acoustic waves at a certain point in that cycle. This results in both jets producing a tone at the screech frequency that may differ in phase. This difference in phase at the screech frequency is measured using the two microphones placed on opposite sides of the jet and can provide evidence as to the relative phase of the oscillation of each of the jet plumes. The difference in phase between the two microphone signals is taken as an ensemble average of five separate sets of recordings. Each of these sets consist of an acoustic recording from both microphones. These sets are processed using Welch's cross-spectral density method to obtain the coherence and phase spectra of the two recorded signals. Frequencies that exhibit a coherence of greater than 0.7 are identified. Locations that remain above this threshold over a range of at least 120 Hz are considered a coherent peak. These coherent peaks are then compared between the five sets. Peaks that overlap in multiple sets are grouped together, and the ensemble-averaged phase of these groupings is then taken.

2. Two-Point Spatial Correlation

Two-point correlation can provide insight into the oscillatory structure of the jet, allowing for the determination of jet instability modes [11,22]. In this paper, two-point correlation is used to compare the change in pixel intensity throughout a set of schlieren images. The two-point spatial correlation as defined by

$$R(x_0 + \Delta x, y_0 + \Delta y) = \frac{\sum_{i=1}^{N} I_i(x_0, y_0) \cdot I_i(x_0 + \Delta x, y_0 + \Delta y)}{\sigma(x_0, y_0) \cdot \sigma(x_0 + \Delta x, y_0 + \Delta y)} \tag{4}$$

where I is the pixel intensity, and R is the covariance of a given pixel with respect to a reference point, is a valuable tool in identifying coherent structures within a flow. The two-point correlation results presented in this paper are produced from processing no fewer than 900 images obtained with the PCO4000. As with any path-integrated data, caution should always be exercised when trying to identify all but the most dominant modes evident in the resulting correlations.

III. Results and Discussion

A. Screech Production

Discrete jumps in the peak screech frequency have traditionally been associated with a transition between jet instability modes. Acoustic data were obtained at nozzle spacings of $S/D = 3$ and $S/D = 6$ for a range in NPR of 2.5–5.5. To distinguish the effects of jet coupling, acoustic data were also acquired for a single jet emanating from the same nozzle, facility, and range of NPR. The peak screech frequency was then identified from the power spectral density of the data; Fig. 3 provides one such acoustic spectrum with the peak screech frequency indicated. For this purpose, a screech peak was defined as a point that is 7 dB above the local average. Nondimensionalized peak screech frequencies over the range of NPR and nozzle spacings are presented in Fig. 4.

The staging behavior of the single jet in this configuration is different from other nozzles used on this facility. This is likely a result of the sensitivity of staging behavior to nozzle geometry and facility boundary conditions. As a result, it is important to keep in mind when

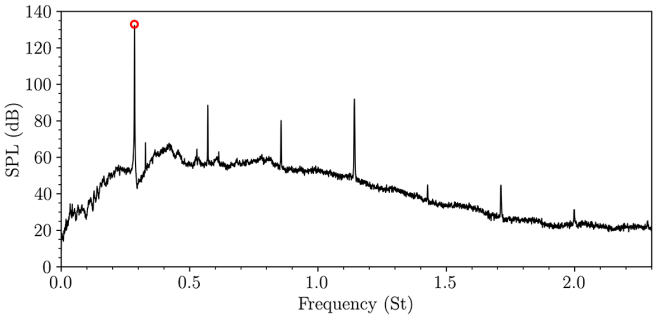

Fig. 3 Example acoustic spectrum with the peak screech frequency indicated.

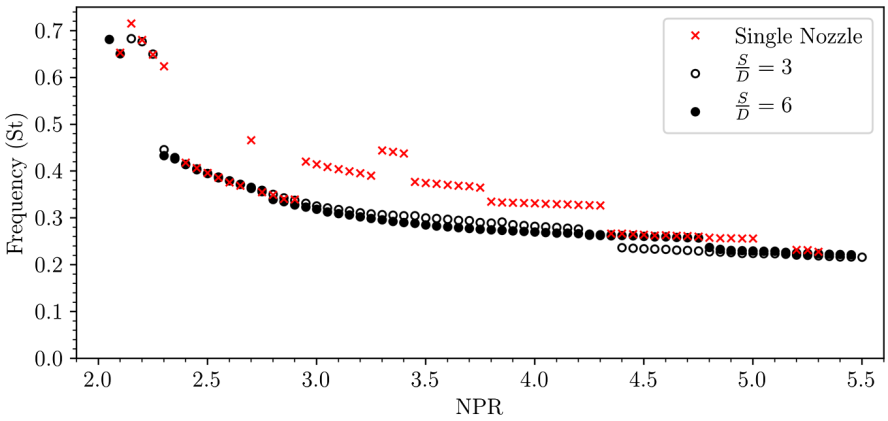

Fig. 4 Staging behavior of the twin supersonic jet. Strouhal number vs NPR.

interpreting the twin-jet results; this particular experiment has relatively short nozzles and a large reflective flange a short distance upstream of the nozzle exits. The exact nature of the coupling behavior will likely be specific to this facility, but this has been true for all studies on the staging of single jets.

The introduction of the second jet plume has a significant effect on the peak screech frequency produced by the jet. The twin jet displays a suppression of staging behavior in the NPR range of 2.9–4.35, which is in line with the observations of Wlezien [17]. The single jet also shows a delay in the final observed mode switch at NPR 5.0, after which the screech tone is significantly diminished and intermittent. Further investigation of the single jet is beyond the scope of this study; however, it is evident that, even at the larger nozzle spacing, jet plume coupling has a dominant effect.

The general trend observed at both twin-jet nozzle spacings is at first similar. At low nozzle pressure ratios, high-Strouhal-number screech tones are observed for $S/D = 3$. These tones appear to have a similar frequency in both the single- and twin-jet cases, suggesting that jet coupling may not be having a significant effect on screech tone in this low-NPR region. The distinct drop in screech frequency at NPR $= 2.3$ indicates a change in the oscillation of the jet plumes. A second transition in the jets' oscillation and coupling modes is suggested by the jump in Strouhal number at higher NPR. This jump occurs at differing NPR for the two nozzle spacings. For $S/D = 3$, the jump occurs between NPR 4.35 and 4.4, whereas the corresponding jump at $S/D = 6$ occurs between NPR 4.7 and 4.8. An additional jump can be seen in the $S/D = 6$ data at an NPR of 2.8.

Although the peak screech frequency cannot by itself identify the oscillation mode of the jet, there have been attempts by other authors to predict the oscillation mode of a single axisymmetric screeching jet based on the peak screech frequency. One such method is that of Gao and Li [23], who suggest that the oscillation mode of the jet can be categorized by the number of concurrent hydrodynamic and acoustic waves present in the jet. The model matches the length of the acoustic reinforcement region, taken to be five times the average shock cell spacing, with an integer number of the combined hydrodynamic and acoustic wavelengths at a specific screech frequency. It is suggested that the A1, B, and D modes have five concurrent hydrodynamic instabilities and acoustic waves and the A0, A2, and C oscillation modes have six. The screech frequency is then given by

$$\lambda_s = \frac{ns}{m}\frac{1 + M_c}{M_c} \tag{5}$$

where n is the number of shock cells making up the acoustic reinforcement region; s is the shock cell length; m is the number of combined wavelengths; and M_c is the convective Mach number. Implementing Eq. (5), the predicted screech frequency for $m = 4, 5$, and 6 is compared to the peak screech frequency found for each nozzle spacing. In these figures, the shock cell length and convective velocity models presented by Gao and Li [23] are used. The validity of these models for the present data set is verified in Sec. III.D. The results of this comparison are shown in Figs. 5 and 6. It can be

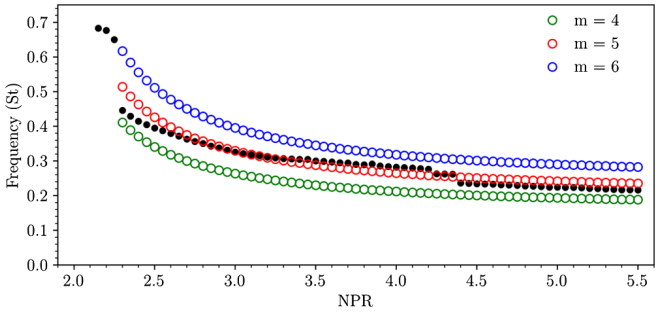

Fig. 5 Peak screech frequency (•) and predicted screech frequency at $S/D = 3$, against NPR.

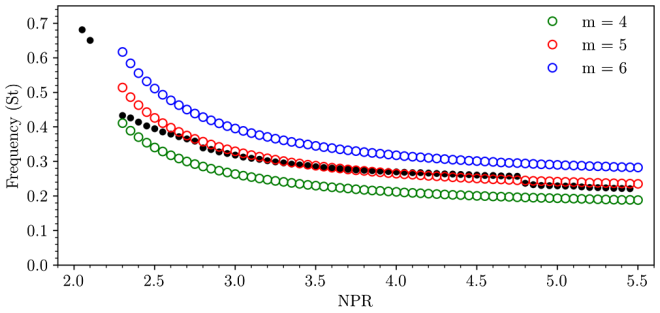

Fig. 6 Peak screech frequency (•) and predicted screech frequency at $S/D = 6$, against NPR.

seen that the high-frequency screech tones at low NPR align with an $m = 6$ prediction and are likely to be the result of an axisymmetric oscillation mode. Following the drop in Strouhal number, at NPR $= 2.3$, $m = 5$ provides the best agreement for both the $S/D = 3$ and 6 nozzle spacings, which corresponds to a B or D mode. However, this model does not capture the staging behavior of the twin-jet system, with the change in frequency for the twin-jet system being much smaller than that predicted through the model. This may suggest that the mechanism for mode selection in twin jets is somewhat different from that for single jets.

Additional information about the oscillation of the jet can be obtained from the difference in the phase of the screech tone generated by each of the jets plumes, which is shown in Figs. 7 and 8. This phase difference was obtained using the method discussed in Sec. II.B.1, with the additional condition that the coherence group considered had to contain the peak screech frequency. Since the microphones are positioned to either side of the jet, the phase difference measured in this way is 180 deg out of phase from the physical oscillation of the jet plumes. For the sake of clarity during later discussions, the measured phase is adjusted to match the reference frame of the jet.

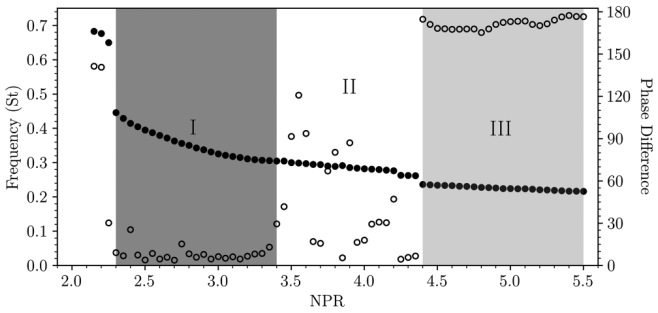

Fig. 7 Peak screech frequency (•) and phase difference (◦) at $S/D = 3$, against NPR.

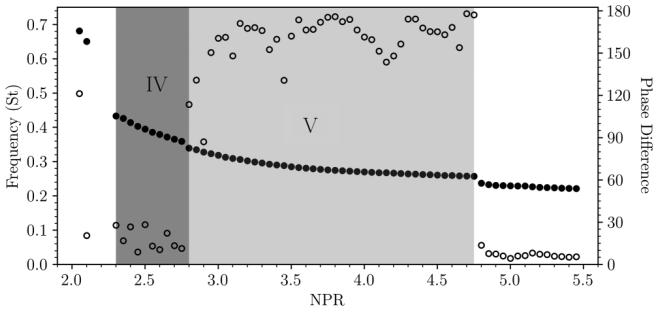

Fig. 8 Peak screech frequency (•) and phase difference (◦) at $S/D = 6$, against NPR.

Table 1 Summary of the twin-jet operating conditions considered at $S/D = 3$

NPR	U_j, m · s^{-1}	M_j	Screech frequency, Hz	Screech frequency (St)
3.0	422	1.36	12,570	0.33
3.3	443	1.43	12,050	0.31
3.6	562	1.49	11,750	0.30
4.0	584	1.56	11,200	0.28
4.6	513	1.65	9,250	0.23
5.0	531	1.70	8,800	0.22

For a nozzle spacing of $S/D = 3$, the phase difference data present additional discontinuities that are not present in the frequency data discussed previously. Initially, the acoustic signals appear to be 0 deg out of phase, suggesting an antisymmetric coupling mode of the jet similar to that seen in Fig. 1a. This persists until NPR = 3.4 and is denoted as region 1. The region after the frequency jump at NPR = 4.35 (region 3) has an approximately 180 deg phase difference, suggesting a symmetric coupling, as seen in Fig. 1b. The previously unidentified region between NPR 3.4 and 4.35 does not display a consistent difference in phase, instead varying between 0 and 120 deg. It is hypothesized that this may be the result of unsteadiness in the jets' coupling combined with the time average process by which the phase difference was obtained. The jets shifting between coupling modes or becoming entirely uncoupled for short periods may result in a varying phase difference, which, when averaged, could create the observed spread in the results

The $S/D = 6$ spacing exhibits a similar region of inconsistency in phase between the jet plumes, as shown in Fig. 8. This region differs from the $S/D = 3$ spacing in that it spans a much larger range of pressure ratios and is centered on a phase difference of 180 deg as opposed to a 0–120 deg difference in phase. Both regions above and below this range of pressures are characterized by a 0 deg phase difference between the jet plumes, which is again suggestive of an antisymmetric coupling mode. This is a significantly different staging progression from that seen at the $S/D = 3$ spacing, showing that an increase in nozzle spacing does not simply delay the transition of coupling modes but affects the mode selection process.

The remainder of this paper will focus on identifying these coupling modes and investigating potential mode selection criteria. For the sake of clarity and brevity, further discussion will focus primarily on the closer nozzle spacing, with evidence from the larger spacing only being introduced when it differs from the $S/D = 3$ case. Two nozzle pressure ratios in each phase region are chosen to represent the jet's various modes of coupling. The chosen NPR and respective jet operation and screeching conditions are summarized in Table 1.

B. Mean Structure

High-resolution schlieren photography was acquired both in line and perpendicular to the shared plane of the nozzles; these views will be referred to as the side and front viewing planes, respectively. A diagram of these imaging planes is shown in Fig. 2. Examples of the raw images can be seen in Fig. 9, with the front viewing plane on the left and the side view on the right.

The mean of these instantaneous data sets shows only a steady lengthening of the shock cells with an increasing NPR. This is in keeping with a single underexpanded jet and suggests that the different oscillation modes exhibited by the twin jet are not related to changes in the mean flow of the jet plumes. An example mean image is presented in Fig. 10.

C. Coupling Modes

The mean fields of the jet plumes provide little insight into the coupling modes of the jet. As such, two-point correlation is implemented to investigate the fluctuating component of the flow as discussed in Sec. II.B.2. For the data presented in this paper, the choice of initial correlation point was found to only affect the strength and not the pattern of the results. As such, an initial correlation point

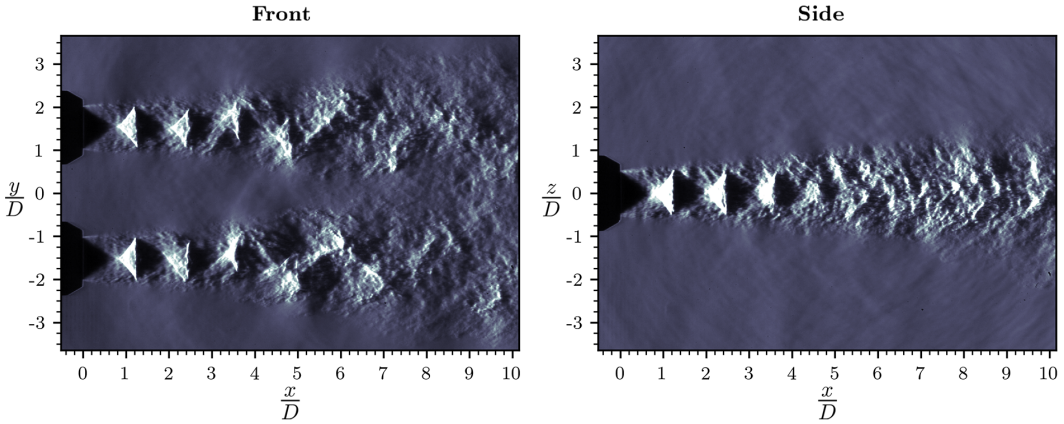

Fig. 9 Instantaneous high-resolution schlieren images NPR = 3.0, $S/D = 3$.

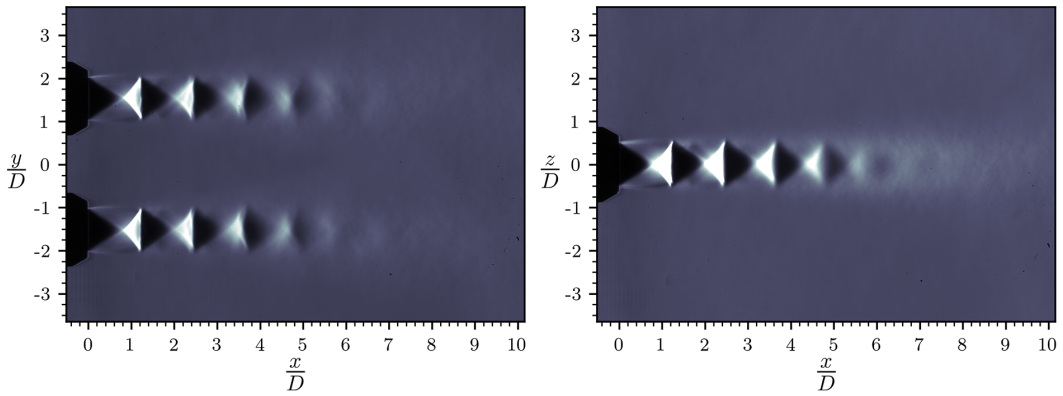

Fig. 10 Mean high-resolution schlieren images NPR = 3.0, $S/D = 3$.

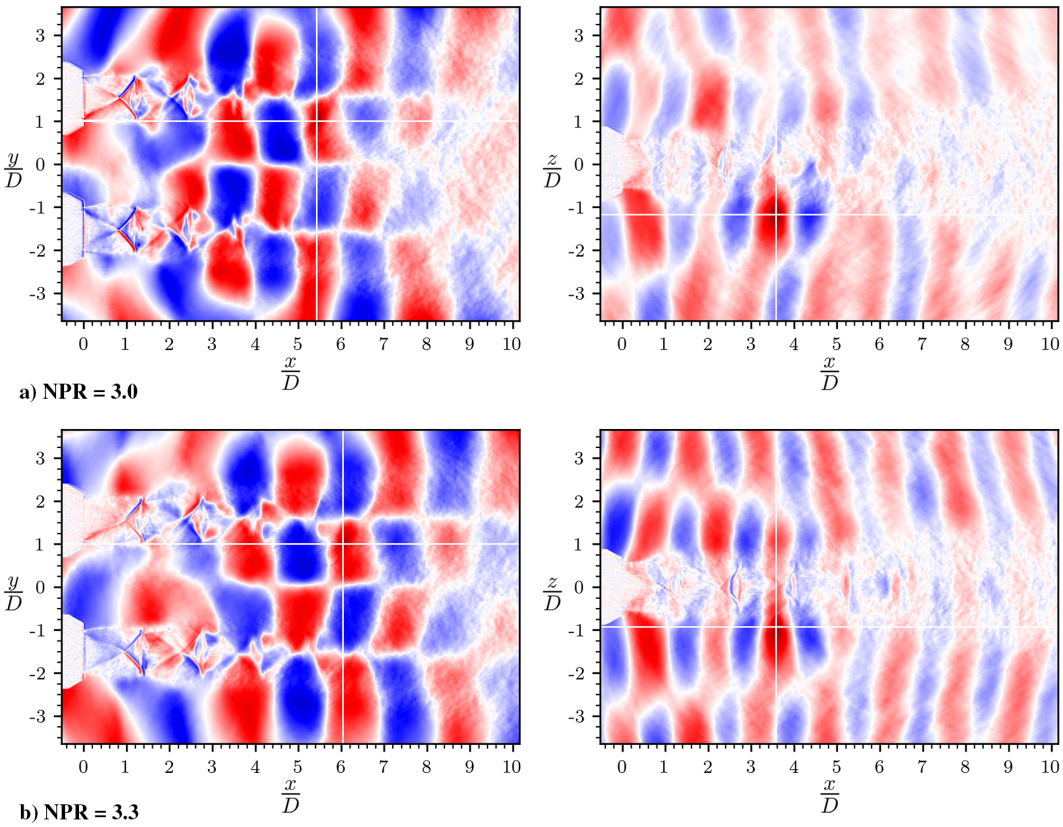

Fig. 11 Two-point spatial correlation of an antisymmetric flapping coupling mode, $S/D = 3$.

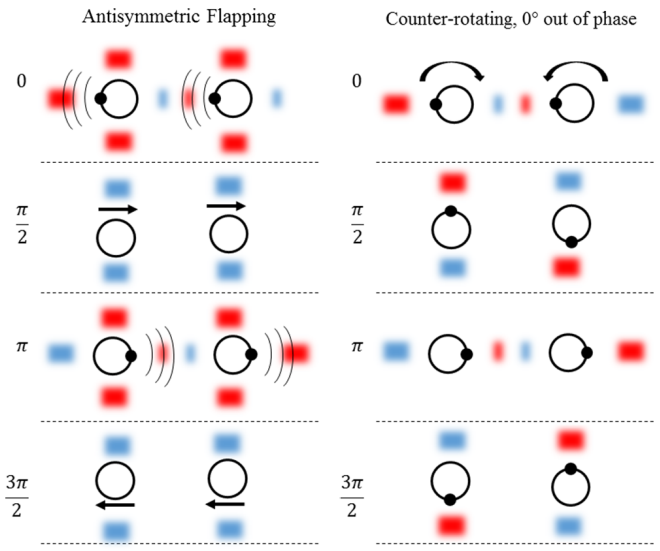

Fig. 12 Diagrammatic representation of expected correlation patterns.

was chosen to produce a strong global correlation and is indicated by the intersection of the white lines in Figs. 11–18. Contour levels for all images are scaled between a correlation of 1 and −1. Positive and negative correlation represent regions of similar and inverse fluctuation in image intensity. These bands can be indicative of the large-scale coherent structures and acoustic waves present in the twin supersonic jet. In addition to the difficulties presented by path-integrated data, two-point correlations favor the strongest correlation in the data set and may mask other relations. As a result, the presence of multiple modes or mode switching will not be resolved with this technique.

1. *Antisymmetric Flapping Coupling*

The two-point correlation results suggest that, at the lower pressure ratios (NPR = 3.0 and 3.3), the jet plumes are coupled in either an antisymmetric flapping mode or a pair of counter-rotating helical instabilities with a 0 deg difference in phase. These correlation results can be seen in Fig. 11. The front viewing plane (left) displays an alternating positive and negative correlation above and below each jet plume. This correlation pattern is antisymmetric about each jet plume as well as being antisymmetric about the jet's midline ($y/D = 0$).

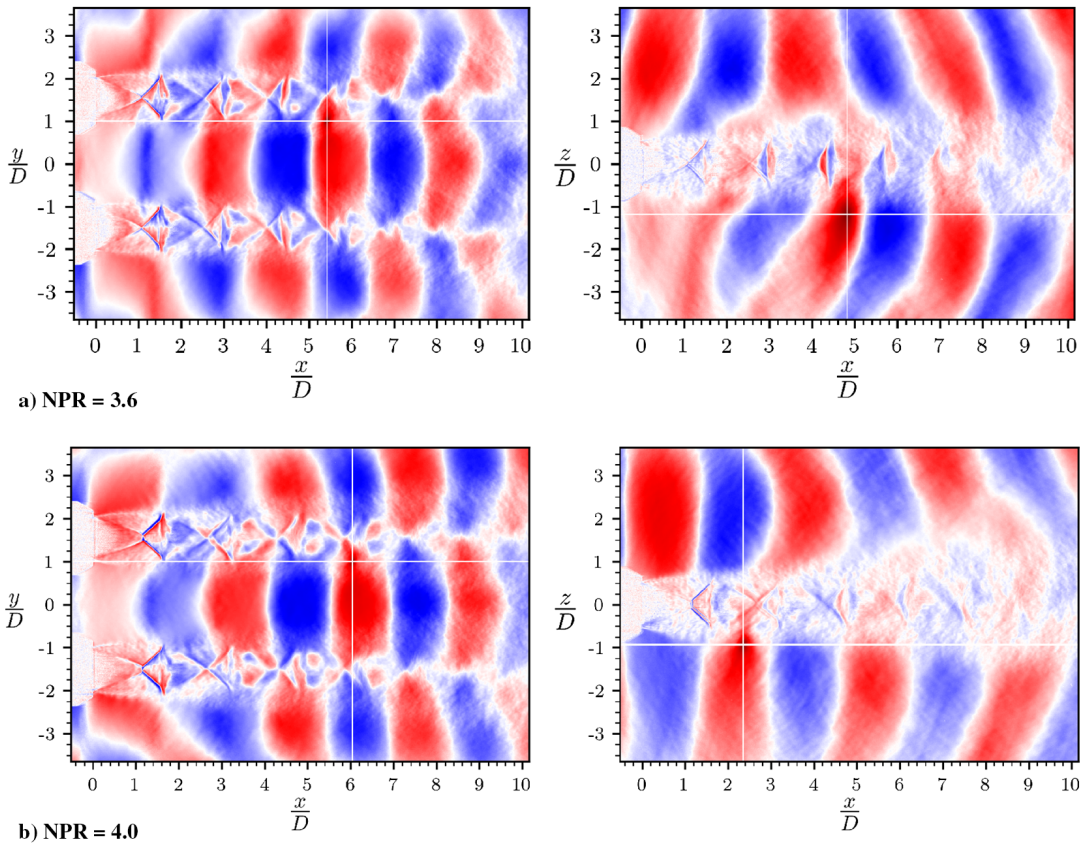

Fig. 13 Two-point spatial correlation of a counter-rotating helical coupling mode, $S/D = 3$.

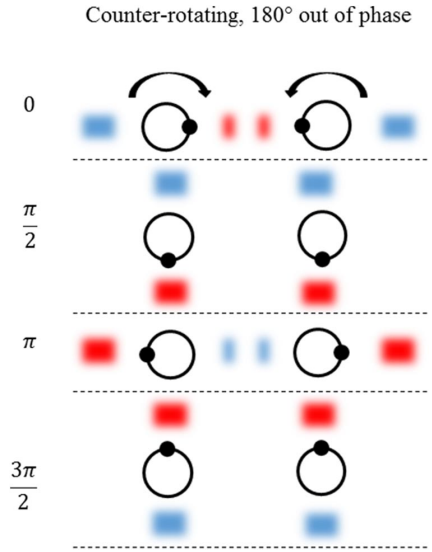

Fig. 14 Diagrammatic representation of expected correlation pattern for a counter-rotating helical coupling mode.

This would suggest that coherent structures in both jet plumes are located on either the left or right of each plume, respectively, at the same point in the oscillation cycle. This is consistent with an antisymmetric motion of the shock cells, as can be seen in the instantaneous high-speed image sets. This would be expected when either an antisymmetric flapping mode or a pair of counter-rotating helical instabilities are viewed in this plane.

Viewed from the side imaging plane, there is a symmetric correlation pattern about the centerline with a wavelength half that of the front view. It has been suggested [24] that the halving of this length is a result of the discrete production of acoustic waves at both extremes of the flapping motion. When these acoustic waves are viewed in the side plane with a path-integrated technique, they appear to be generated at twice the frequency, hence half the wavelength. However, uncertainty still exists because this correlation result would also be expected from a coupling mode consisting of a pair of counter-rotating helical instabilities. For clarity, diagrams of both oscillation modes and their associated correlation patterns are presented in Fig. 12. These diagrams identify the location of the vortical structures over one period of each different oscillation mode and the expected resulting correlation pattern. In this diagram, the jet nozzles are represented from above as the two hollow circles, the location of the vortical structures is represented as filled in dots, and the direction of motion of these structures is indicated with arrows. The front plane would view these diagrams from top to bottom, and the side plane would be orientated from left to right.

As a result of the uncertainty, instantaneous images were used to differentiate between the two potential modes. It would be expected that, during the helical instability, the magnitude of the deflection of the jet plume from its centerline would be similar in both imaged axis. Conversely, a flapping mode would exhibit considerably less deviation in the side view. Examination of these deviations in the instantaneous image sets, which have been omitted for brevity, supports the presence of an antisymmetric flapping mode in region 1.

2. *Counter-Rotating Helical Coupling with a 180 Degree Offset*

Figure 13 shows the two-point correlation results for both cases investigated within region 2, NPR = 3.6 and 4.0. These results differ significantly from the correlation patterns of the lower pressure ratios suggesting the presence of a different dominant coupling mode. In the front viewing plane, both NPR = 3.6 and 4.0 exhibit a symmetrical correlation pattern about the jet midline, with correlation lobes of similar sign spanning across the internozzle region. This suggests that coherent structures in both jet plumes are present in the internozzle region at the same point in the oscillation cycle. The side viewing plane reveals an antisymmetric correlation pattern about the jet with a correlation lobe length similar to that seen in the front view. This suggests that vortical structures in both jet plumes are present on the same side of the jet. These patterns are indicative of each jet plume containing a helical instability, which is counter-rotating with respect

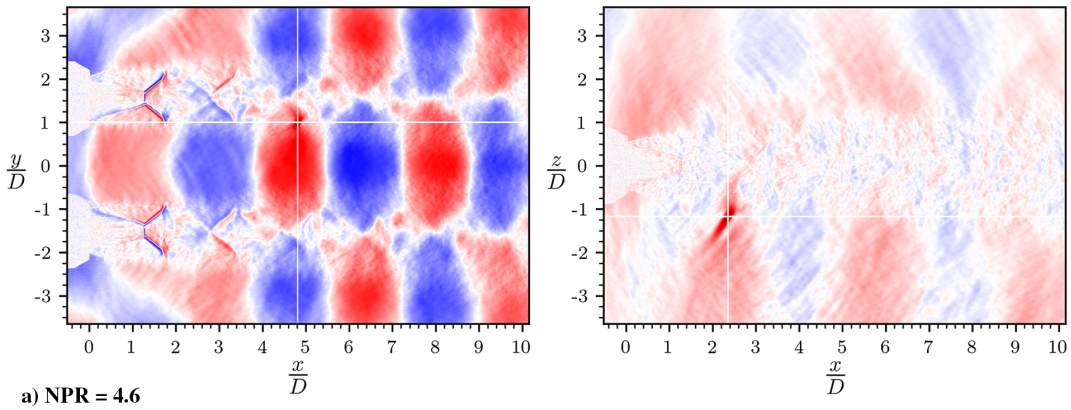

Fig. 15 Two-point spatial correlation of a symmetric flapping mode, $S/D = 3$.

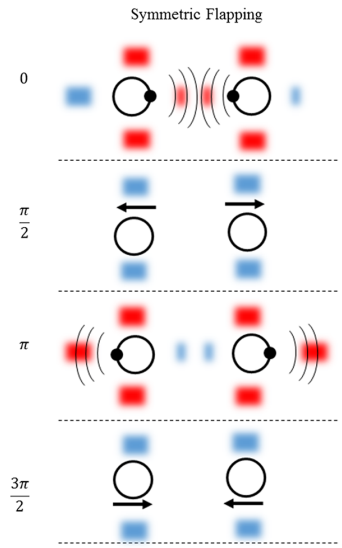

Fig. 16 Diagrammatic representation of expected correlation pattern for a symmetric flapping mode.

to the other, but coupled together approximately 180 deg out of phase. A diagram of this proposed coupling mode is given in Fig. 14.

The acoustic phase data, seen in Fig. 7, suggest that there is a wide range of phase differences between the two jet plumes in this region. Given that a pair of counter-rotating helical instabilities have been identified as the dominant coupling mode, the variable phase difference may be the result of either a dependence of the phase difference between helical instabilities on the pressure ratio or a temporal unsteadiness in the coupling. The side view of Fig. 13 goes some way to support a variability in phase difference. It can be seen that the lobes of positive correlation below the jet do not align precisely with lobes of negative correlation above the jet, as would be expected with a phase difference of 180 deg. This offset is more pronounced in the NPR $= 3.6$ case, whereas the NPR $= 4.0$ case is significantly closer to a 180 deg difference in phase. Although a changing phase difference between the helical instability in the two plumes is plausible, it would be expected to also create slight asymmetry about the $y/D = 0$ axis in the front view correlation pattern. Thus, it is believed that, because the acoustic phase and the two-point correlation are temporally averaged measurements, this variable phase difference is the result of the temporal unsteadiness in the jets' coupling, as previously discussed.

3. *Symmetric Flapping Coupling*

The highest range of pressure ratios investigated, NPR 4.6 and 5.0, display yet another different correlation pattern, as seen in Fig. 15. The front view correlation is similar to that seen in region 2 with lobes of alike correlation spanning the internozzle and connecting the two plumes. However, unlike region 2, the generally weak correlation in the side view suggests a lack of coherent motion in this plane. This weaker side view pattern is seen to be symmetric about the jet center, and it possesses a wavelength similar to that of the front view correlation pattern. This is believed to be the result of the high pressure generated between the jets when the coherent structures in both jets are closest to the centerline. As such, the correlation pattern is suggestive of an in-plane symmetric flapping coupling mode. A diagram of this coupling mode and the associated pattern is shown in Fig. 16.

Similar analysis is conducted for the $S/D = 6$ spacing with image sets being obtained at NPR $= 2.5$, 2.75, 3.2, 3.8, and 4.2. A correlation pattern indicative of a symmetric flapping mode is identified for NPR $= 3.2$, 3.8, and 4.2, all of which are within region 5 as defined by Fig. 8. An example of this pattern can be seen in Fig. 17. As such, both region 3 at $S/D = 3$ and region 5 at $S/D = 6$ are believed to be in-plane symmetrical flapping modes. However, from Figs. 7 and 8, there is a significant difference in the variation of the phase within each region, with the $S/D = 6$ case showing larger range of phase difference. It is hypothesized that this may be the effect of a less stable coupling for the larger nozzle spacing within this NPR range.

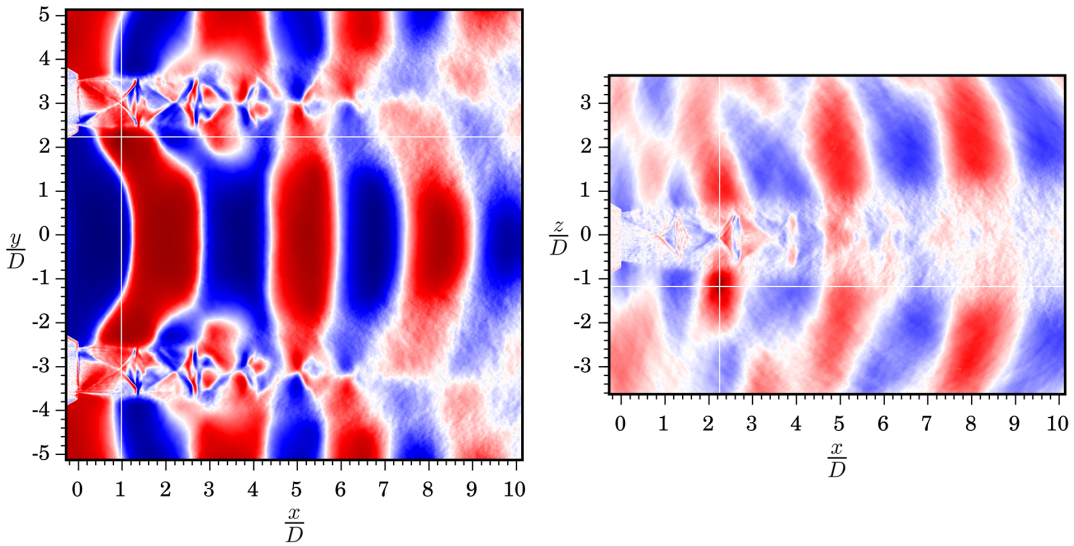

Fig. 17 Example two-point correlation results for $S/D = 6$ symmetric flap coupling mode, NPR shown = 3.2.

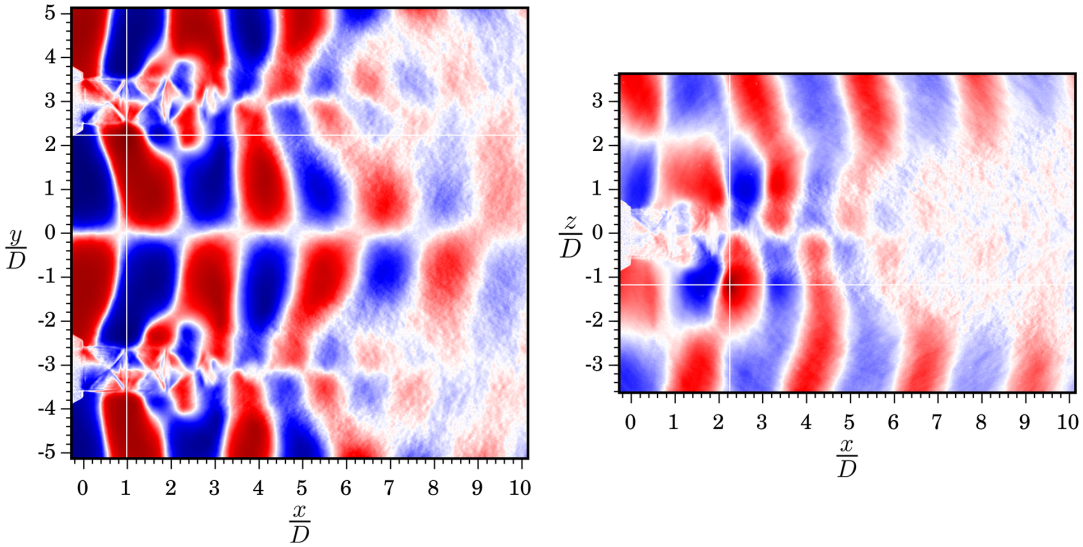

Fig. 18 Two-point correlation results for $S/D = 6$, NPR = 2.5.

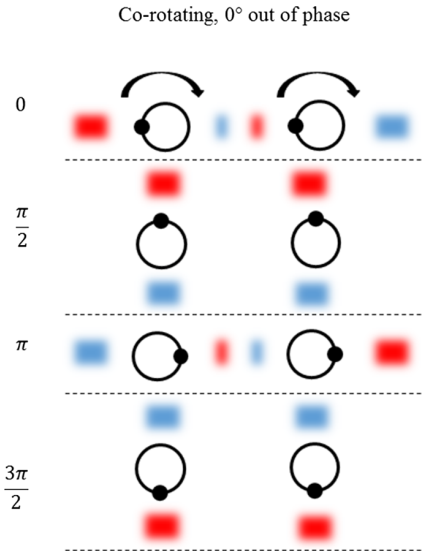

Fig. 19 Diagrammatic representation of expected correlation pattern for a corotating helical coupling mode.

4. Corotating Helical Coupling

Analysis of the $S/D = 6$ spacing reveals the presence an additional coupling mode. At the lowest measured NPR, 2.5, the two-point correlation results in a previously unobserved pattern, shown in Fig. 18. The antisymmetric correlation patterns in both orientations suggest that the dominant coupling mode in region 4 is a pair of corotating helical structures with a 0 deg phase difference between jet plumes. The diagrammatic representation of this coupling mode can be seen in Fig. 19. A summary of the coupling modes can be found in Table 2.

Table 2 Summary of twin-jet coupling modes

S/D	Region	NPR	Coupling mode
3	1	2.3–3.4	Antisymmetric flapping
3	2	3.45–4.35	Counter-rotating helical
3	3	4.4–5.5	Symmetric flapping
6	4	2.3–2.65	Corotating helical
6	5	2.8–4.45	Symmetric flapping

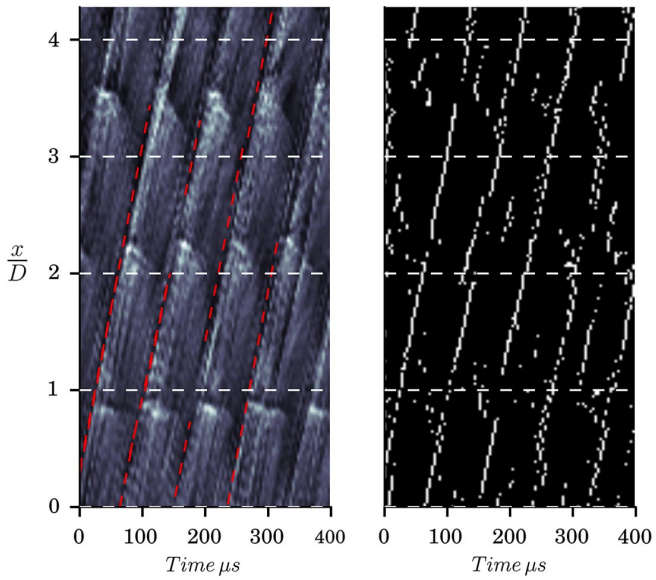

Fig. 20 Left: x/t plot of the twin jet at $S/D = 3$. Right: local maximum filtered x/t plot to identify the location of vortical structures.

Table 3 Convective velocity for varying pressure ratios, $S/D = 3$

NPR	3.0	3.3	3.6	4.0	4.6	5.0
Convective velocity, m · s^{-1}	253	265	270	277	307	320
95% confidence interval, m · s^{-1}	±1.8	±2.3	±2.6	±2.1	±4.7	±5.3
U_c/U_j	0.60	0.60	0.58	0.57	0.60	0.60

D. Staging Mechanisms

A possible cause of this mode switching behavior and the associated discontinuities in the peak screech frequency is a distinct change in the parameters that govern the screech feedback loop. One such parameter is the velocity with which the coherent structures in the jet plumes convect downstream. This velocity, known as the convective velocity, determines the time between the creation of a vortical structure, at the nozzle lip, and the generation of the next acoustic wave when that structure interacts with the shock cells farther downstream. As such, the screech frequency is highly dependent on the convective velocity, which is evidenced by its use in the formulation of both Powell's three-monopole model and the standing wave model for predicting the screech frequency, shown in Eqs. (1) and (2). Given this dependency, a discrete jump in convective velocity may have an effect on coupling mode selection.

To investigate this potential cause of the mode switching behavior, the average convective velocity U_c is obtained for each case by constructing it from the high-speed schlieren data. For this, 20 sets of 102 time-resolved images are acquired at each test case, similar in magnification and resolution to that shown in Fig. 1. Within each set, the row of pixels at a chosen y/D location is extracted. These rows are then arranged in consecutive time order to create the two-dimensional image seen on the left of Fig. 20, allowing for pixel intensity at a given downstream location x/D to be viewed against time. In schlieren photography, vortical structures typically result in abrupt changes from high to low pixel intensity. This abrupt change can be seen as a diagonal trace when viewed in the displacement-against-time (x/t) plot. The convective speed of coherent structures can then be found from the gradient of these traces. Five y/D locations within each of the four shear layers were selected to create 20 x/t plots from each data set. To isolate the signature of the turbulent structures, a local minimum filter is applied, producing the right image of Fig. 20. A Hough transform is then applied to find the gradient of the traces [25]. The results of the Hough transform have been shown as red dashed lines in Fig. 20. An ensemble average is then obtained for each case using at least 100 traces.

The results of this analysis, tabulated in Table 3, show no discrete changes in the normalized convective velocity U_c/U_j throughout the investigated range. Instead, the convective velocity is shown to be a strong function of fully expanded jet velocity, which in turn depends primarily on nozzle pressure ratio.

The other parameter of the screech feedback loop is the length scales associated with the jet. A change in the characteristic length scales within the flow may accompany a mode switch and would result in a change in screech frequency. For a single jet, the shock cell spacing and standing wave have been identified as the key characteristic lengths and as such will be investigated here. Additionally, once these lengths have been identified, the validity of the approximations of these lengths made in Gao and Li's [23] model can be assessed.

Prior work [11] has suggested that the standing wave phenomenon can be identified from schlieren photography by taking the standard deviation of image intensity. This standard deviation, an example of which is shown in Fig. 21, is represented by the rms of a set of over 900 high-resolution schlieren images. Bright regions within these images represent high fluctuations in image intensity, which have been shown to be the result of the standing wave phenomenon. By examining the image intensity along a vertical line in the internozzle region, the peak of each band can be identified and the standing wavelength found. The shock cell length was taken as the distance between shock reflection points. The lengths of both of these scales changed with downstream position. As such, an average of the first five shock cells was taken and the three standing wave nodes after the first from each jet plume. The first standing wave was excluded because it was typically substantially larger. This is to be expected because the shear-layer turbulent kinetic energy is at its lowest, and hence hydrodynamic waves are weakest close to the nozzle lip and have little effect on the standing wave [2]. It is likely that this first lobe is a standing wave consisting of the upstream propagating waves and reflected acoustic waves from the nozzle flange.

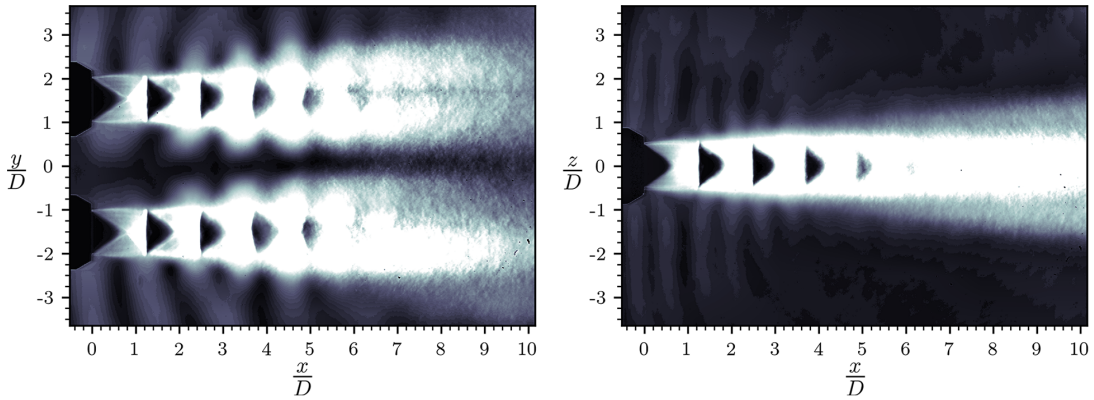

Fig. 21 Example standard deviation, $S/D = 3$, NPR = 3.0.

Table 4 Standing wavelength and shock spacing for different pressure ratios, $S/D = 3$

NPR	3.0	3.3	3.6	4.0	4.6	5.0
Shock spacing	1.15D	1.30D	1.39D	1.49D	1.65D	1.69D
Standing wavelength	1.17D	1.29D	1.33D	1.43D	1.71D	1.78D

Similarly, a secondary standing wave pattern can be seen in the front view farther outside the twin jet, approximately $> \pm 3(y/D)$. This is believed to be the result of acoustic wave reflection from the base plate of the twin jet, as seen in Fig. 2b, and will not be discussed further.

The average shock cell spacing and standing wavelength are presented in Table 4. A different relationship between these characteristic lengths is present for each of the three regions identified in Fig. 7, which have been shown to be dominated by different coupling modes. Within region 1, which is investigated at NPR 3.0 and 3.3, the shock cell and standing wave spacing are approximately equal. In contrast, at the other NPR investigated, the disparity between the two length scales is significantly larger. The standing wavelength is shorter than the shock cell spacing for NPR 3.6 and 4.0 where the twin jet is believed to be in a helical coupling mode. Conversely, during the symmetric coupling mode at NPR 4.6 and 5.0, the standing wavelength is found to be longer than the shock cell spacing.

Comparing the twin-jet shock cell spacing with the predictions of the modified Prandlt–Pack formula used in the model of Gao and Li [23] shows agreement to within 1%. The normalized convective velocities found in regions 1 and 3 also agree well with the $U_c/U_j = 0.615$ proposed for a single jet in either flapping and helical oscillation mode. There is a larger difference from the predicted convective velocity in region 2; however, when adjusted, this discrepancy does not significantly change the results presented in Figs. 5 and 6.

Consistent with prior observations for single jets [26], the staging behavior cannot be explained by changes in convective velocity. A consideration of the characteristic length scales of screech suggests that there may be a relationship between their ratio and the coupling mode of the jet, which is again consistent with prior work on single jets [11,26], but the exact mechanism remains unclear. The existence of discontinuities in phase, even in regions where tonal frequency varies continuously with nozzle pressure ratio, suggests that the staging behavior of twin jets is significantly more complicated than the behavior of single-jet systems.

IV. Conclusions

The coupling of an underexpanded twin axisymmetric supersonic jet has been studied. Nozzle spacing was found to play a significant role in coupling mode selection. Four dominant coupling modes were identified over two nozzle spacings. These modes are characterized by either helical or flapping oscillations of the jet plumes and by their symmetry, or antisymmetry, about the jet midplane. Discontinuous jumps in the peak screech frequency were found to be insufficient to identify all changes in twin-jet coupling modes; discontinuous changes in the phase between the jet plumes occurred at pressure ratios where no discontinuous jump in tonal frequency was observed. Convective velocity, when normalized by the ideally expanded jet velocity, was shown to be invariant with nozzle pressure ratio and thus cannot explain changes in tonal frequency associated with modal staging, consistent with the results for single jets. As in prior studies of single jets, jumps in tonal frequency were shown to be associated with changes in the ratio of the two characteristic length scales of screech: shock cell spacing and standing wave wavelength. Although the aforementioned similarities to single-jet staging were observed, it is clear that there are other mechanisms at work in the coupling of twin jets, as indicated by the inability of existing frequency prediction models for single jets to accurately capture the behavior of the twin-jet system.

Acknowledgments

The authors would like to acknowledge the support of the Australian Research Council through the Discovery (150101726) and Linkage Infrastructure, Equipment and Facility (LIEF) schemes.

References

[1] Powell, A., "On the Mechanism of Choked Jet Noise," *Proceedings of the Physical Society. Section B*, Vol. 66, No. 12, 1953, p. 1039. doi:10.1088/0370-1301/66/12/306

[2] Edgington-Mitchell, D., Oberleithner, K., Honnery, D. R., and Soria, J., "Coherent Structure and Sound Production in the Helical Mode of a Screeching Axisymmetric Jet," *Journal of Fluid Mechanics*, Vol. 748, Jan. 2014, pp. 822–847. doi:10.1017/jfm.2014.173

[3] Tam, C. K., "Supersonic Jet Noise," *Annual Review of Fluid Mechanics*, Vol. 27, 1995, pp. 17–43. doi:10.1146/annurev.fl.27.010195.000313

[4] Powell, A., Umeda, Y., and Ishii, R., "Observations of the Oscillation Modes of Choked Circular Jets," *Journal of the Acoustical Society of America*, Vol. 92, No. 5, 1992, pp. 2823–2836. doi:10.1121/1.404398

[5] Kuo, C.-W., Cluts, J., and Samimy, M., "Exploring Physics and Control of Twin Supersonic Circular Jets," *AIAA Journal*, Vol. 55, No. 1, 2016, pp. 68–85. doi:10.2514/1.J054977

[6] Tam, C. K., and Hu, F. Q., "On the Three Families of Instability Waves of High-Speed Jets," *Journal of Fluid Mechanics*, Vol. 201, April 1989, pp. 447–483. doi:10.1017/S002211208900100X

[7] Shen, H., and Tam, C. K. W., "Three-Dimensional Numerical Simulation of the Jet Screech Phenomenon," *AIAA Journal*, Vol. 40, No. 1, 2002, pp. 33–41. doi:10.2514/2.1638

[8] Westley, R., and Woolley, J., "The Near Field Sound Pressures of a Choked Jet When Oscillating in the Spinning Mode," *2nd Aeroacoustics Conference*, AIAA Paper 1975-0479, 1975.

[9] Panda, J., "An Experimental Investigation of Screech Noise Generation," *Journal of Fluid Mechanics*, Vol. 378, Jan. 1999, pp. 71–96. doi:10.1017/S0022112098003383

[10] Chatterjee, A., Ghodake, D., and Singh, A., "Screech Frequency Prediction in Underexpanded Axisymmetric Screeching Jets," *International Journal of Aeroacoustics*, Vol. 8, No. 5, 2009, pp. 499–510. doi:10.1260/147547209788549307

[11] Edgington-Mitchell, D., Honnery, D. R., and Soria, J., "Staging Behaviour in Screeching Elliptical Jets," *International Journal of Aeroacoustics*, Vol. 14, Nos. 7–8, 2015, pp. 1005–1024. doi:10.1260/1475-472X.14.7.1005

[12] Raman, G., Panickar, P., and Chelliah, K., "Aeroacoustics of Twin Supersonic Jets: A Review," *International Journal of Aeroacoustics*, Vol. 11, No. 7, 2012, pp. 957–984. doi:10.1260/1475-472X.11.7-8.957

[13] Morris, P. J., "Instability Waves in Twin Supersonic Jets," *Journal of Fluid Mechanics*, Vol. 220, Nov. 1990, pp. 293–307. doi:10.1017/S0022112090003263

[14] Seiner, J. M., Manning, J. C., and Ponton, M. K., "Dynamic Pressure Loads Associated with Twin Supersonic Plume Resonance," *AIAA Journal*, Vol. 26, No. 8, 1988, pp. 954–960. doi:10.2514/3.9996

[15] Shaw, L., "Twin-Jet Screech Suppression," *Journal of Aircraft*, Vol. 27, No. 8, 1990, pp. 708–715. doi:10.2514/3.25344

[16] Kuo, C.-W., Cluts, J., and Samimy, M., "Effects of Excitation Around Jet Preferred Mode Strouhal Number in High-Speed Jets," *Experiments in Fluids*, Vol. 58, No. 4, 2017, p. 35. doi:10.1007/s00348-017-2329-7

[17] Wlezien, R., "Nozzle Geometry Effects on Supersonic Jet Interaction," *AIAA Journal*, Vol. 27, No. 10, 1989, pp. 1361–1367. doi:10.2514/3.10272

[18] Raman, G., and Taghavi, R., "Coupling of Twin Rectangular Supersonic Jets," *Journal of Fluid Mechanics*, Vol. 354, Jan. 1998, pp. 123–146. doi:10.1017/S0022112097007441

[19] Settles, G., *Schlieren and Shadowgraph Techniques: Visualizing Phenomena in Transparent Media*, Springer, Berlin, 2001. doi:10.1007/978-3-642-56640-0

[20] Mitchell, D. M., Honnery, D. R., and Soria, J., "The Visualization of the Acoustic Feedback Loop in Impinging Underexpanded Supersonic Jet Flows Using Ultra-High Frame Rate Schlieren," *Journal of Visualization*,

Vol. 15, No. 4, 2012, pp. 333–341.
doi:10.1007/s12650-012-0139-9

[21] Willert, C. E., Mitchell, D. M., and Soria, J., "An Assessment of High-Power Light-Emitting Diodes for High Frame Rate Schlieren Imaging," *Experiments in fluids*, Vol. 53, No. 2, 2012, pp. 413–421.
doi:10.1007/s00348-012-1297-1

[22] Johnston, N. J., and Edgington-Mitchell, D. M., "Visualisation of Underexpanded Jet Flowfields in the Presence of an Intrusive Tab," *Journal of Visualization*, Vol. 19, No. 1, 2016, pp. 49–60.
doi:10.1007/s12650-015-0298-6

[23] Gao, J., and Li, X., "A Multi-Mode Screech Frequency Prediction Formula for Circular Supersonic Jets," *Journal of the Acoustical Society of America*, Vol. 127, No. 3, 2010, pp. 1251–1257.
doi:10.1121/1.3291001

[24] Humphrey, N. J., and Edgington-Mitchell, D., "The Effect of Low Lobe Count Chevron Nozzles on Supersonic Jet Screech," *International Journal of Aeroacoustics*, Vol. 15, No. 3, 2016, pp. 294–311.
doi:10.1177/1475472X16630872

[25] Duda, R. O., and Hart, P. E., "Use of the Hough Transformation to Detect Lines and Curves in Pictures," *Communications of the ACM*, Vol. 15, No. 1, 1972, pp. 11–15.

[26] Mercier, B., Castelain, T., and Bailly, C., "Experimental Characterisation of the Screech Feedback Loop in Underexpanded Round Jets," *Journal of Fluid Mechanics*, Vol. 824, Aug. 2017, pp. 202–229.
doi:10.1017/jfm.2017.336

D. Papamoschou
Associate Editor

Appendix B

Out-of-plane cross spectral density

The CPSD-coherence waterfall for microphones 4-6, figure B.1d, shows significant low frequency acoustic pollution. The pollution follows the general shape of background echoic features (when plotted as Strouhal number) within the CPSD plots. The author does not have a conclusive proposal of what is causing the low frequency coherent band. It seems to be a function of measuring acoustic response on the same side of the jets, as the feature is also observable on CPSD-coherence measures using the opposite microphones 5-7 (not shown).

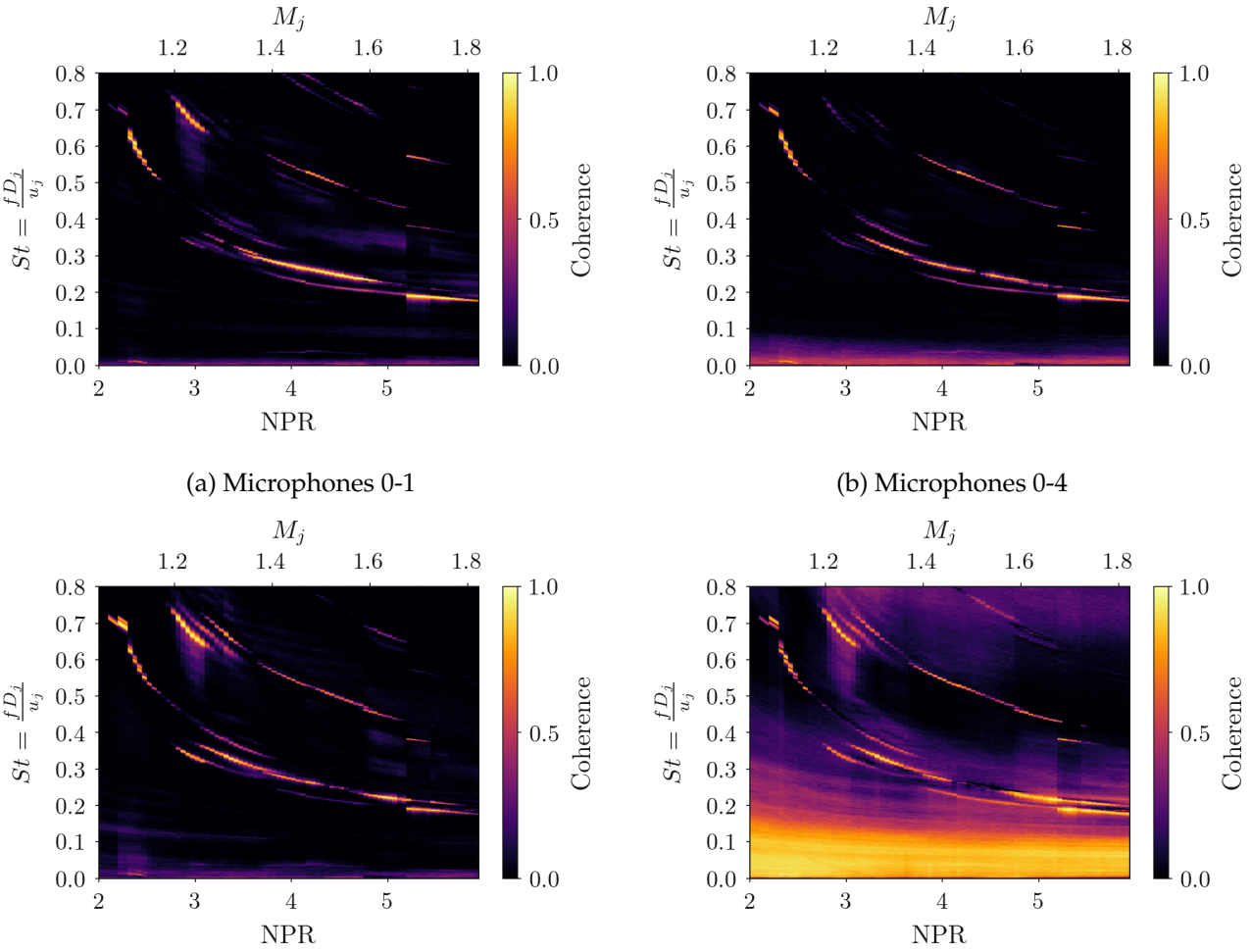

(a) Microphones 0-1

(b) Microphones 0-4

(c) Microphones 4-5

(d) Microphones 4-6

Figure B.1: Unforced Cross Spectral Power Density - coherence waterfall plots featuring different opposing microphone pairs; Case 2: Canonical C-D steel nozzles.

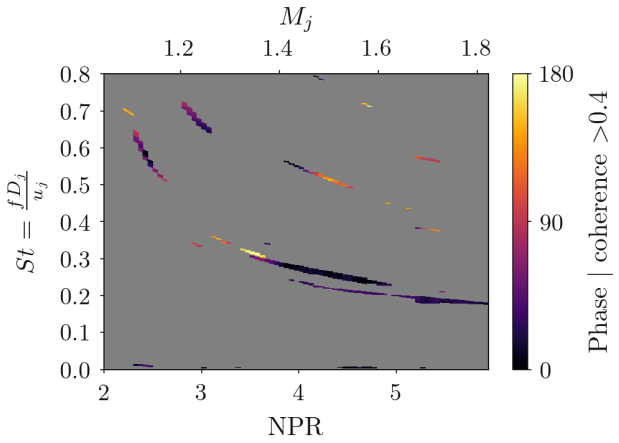

(a) Microphones 0-1

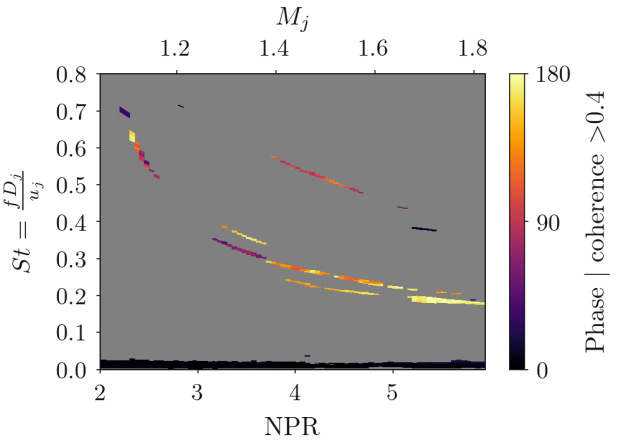

(b) Microphones 0-4

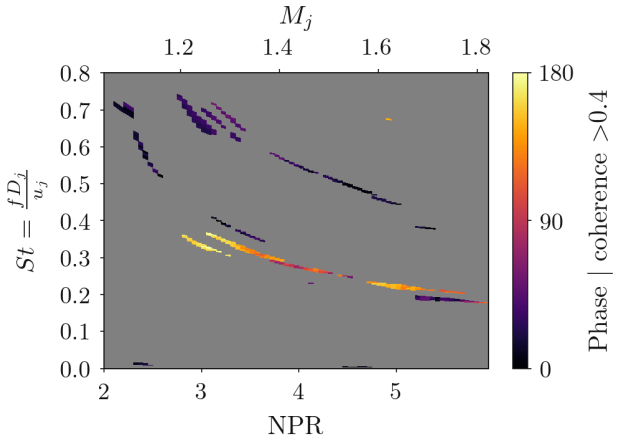

(c) Microphones 4-5

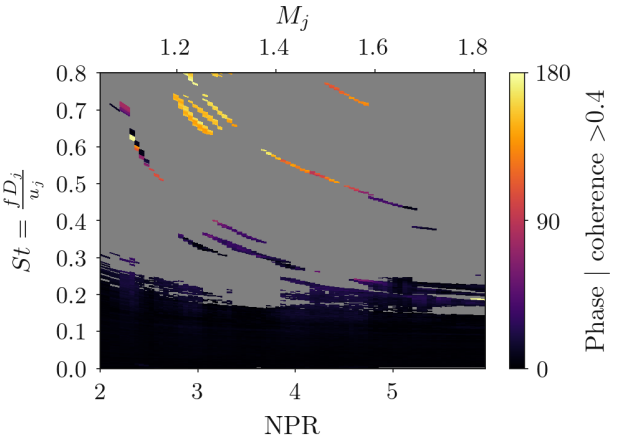

(d) Microphones 4-6

Figure B.2: Unforced Cross Spectral Power Density - coherence waterfall plots featuring different opposing microphone pairs; Case 2: Canonical C-D steel nozzles.

Appendix C

Transient Forcing Results

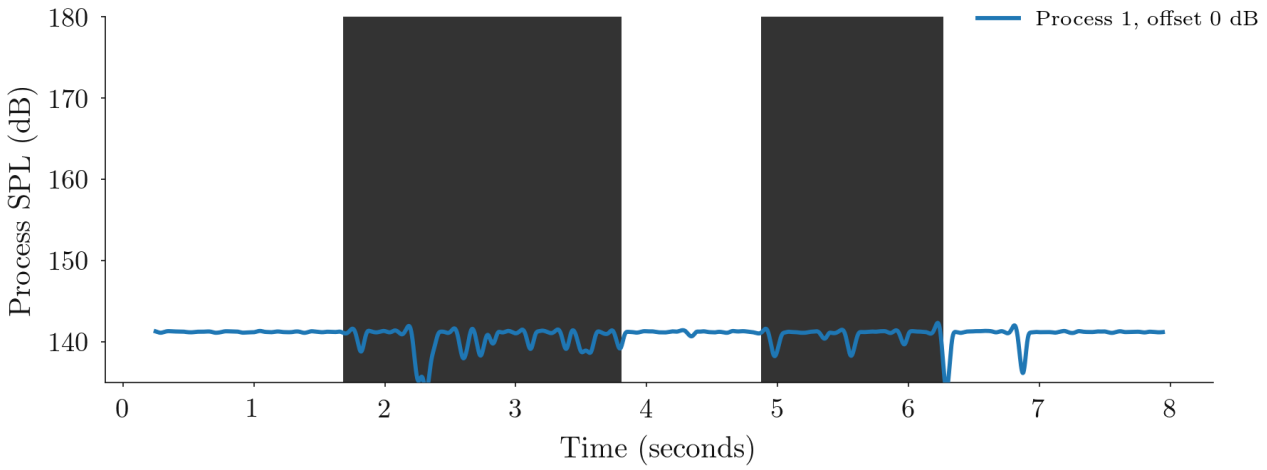

(a) NPR = 2.52

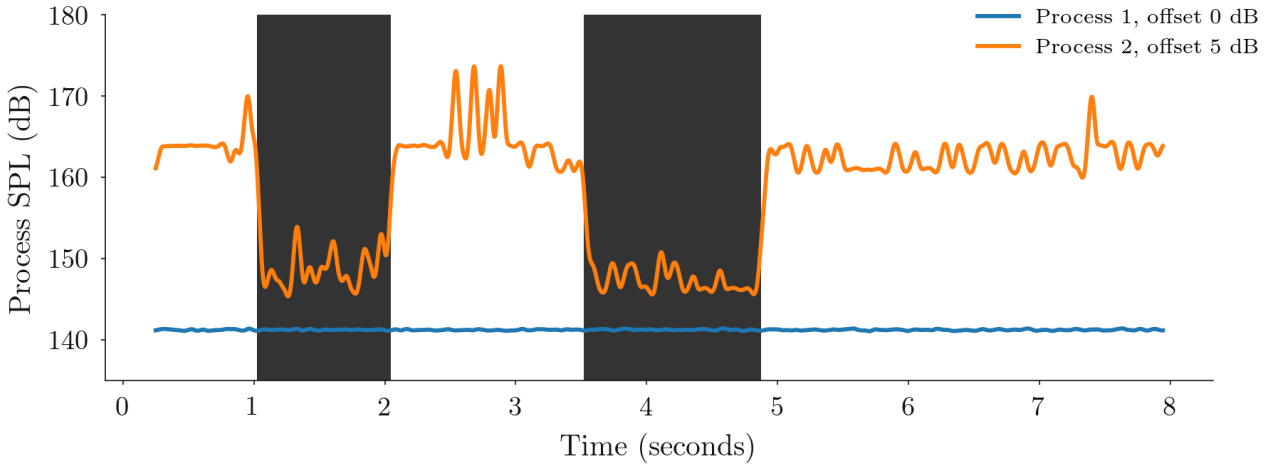

(b) NPR = 2.75

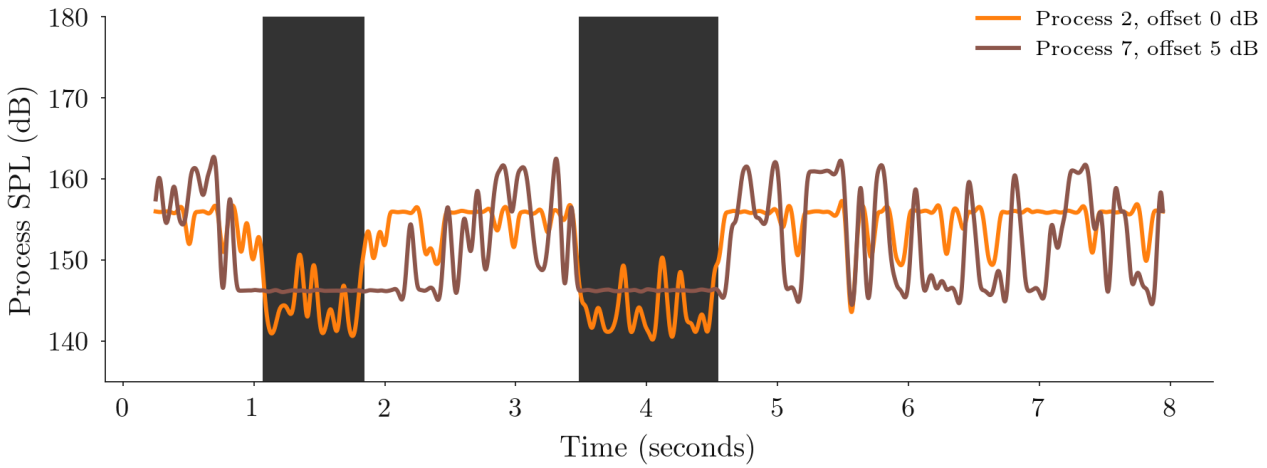

(c) NPR = 3.00

Figure C.1: Acoustic amplitude of various processes during transient forced response. Actuators are switched on within the shaded regions. Amplitudes are the ensemble average of microphones 0-7. A 10 Hz low-pass filter has been applied for visualisation purposes as the raw data contains high-frequency fluctuations.

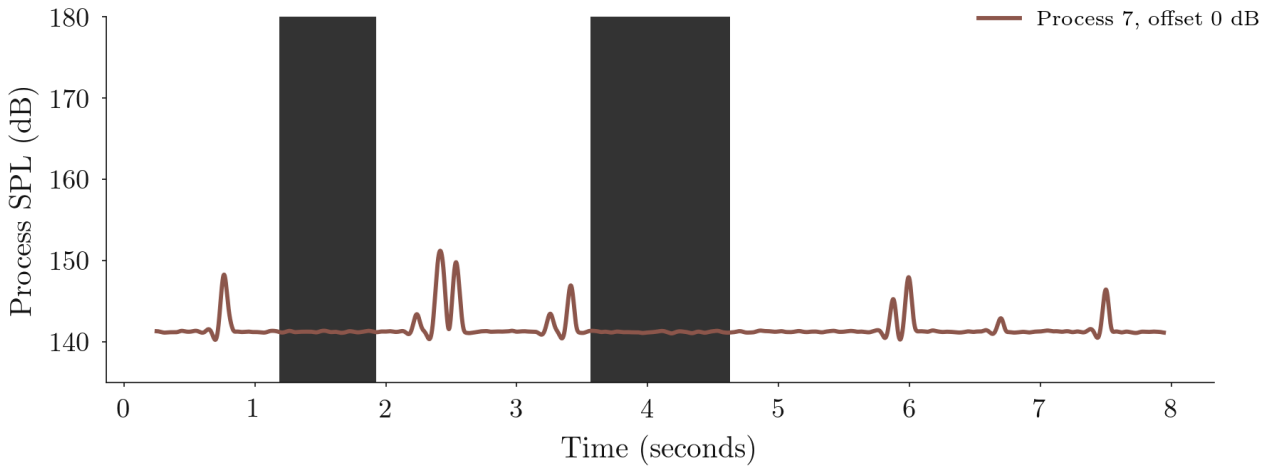

(d) NPR = 3.25

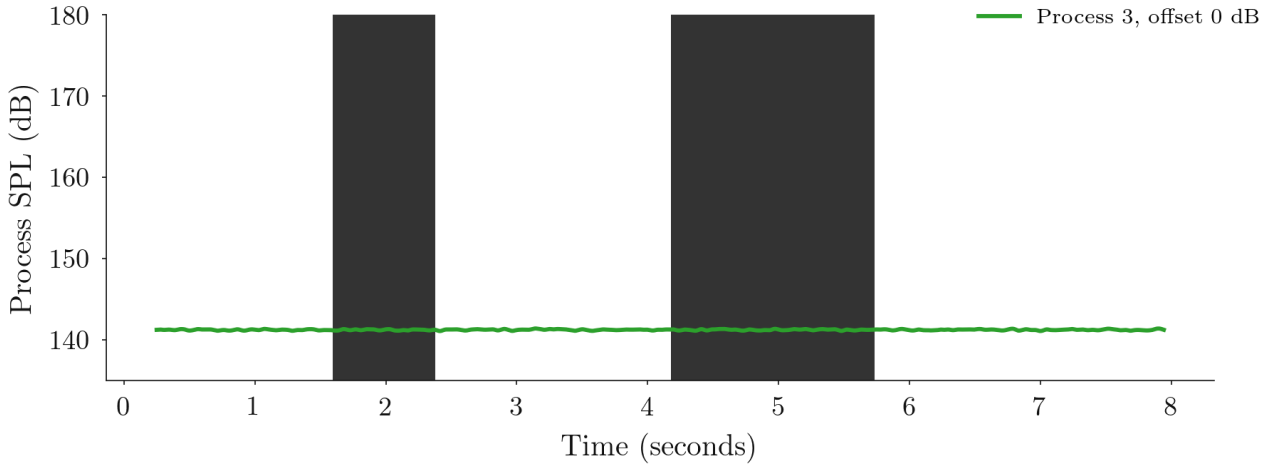

(e) NPR = 3.75

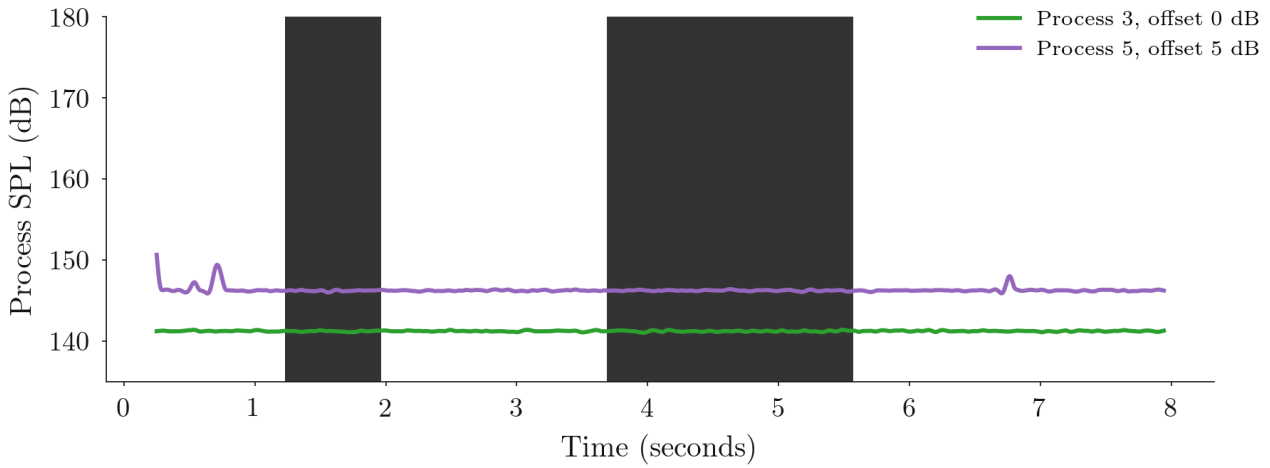

(f) NPR = 4.00

Figure C.1: Acoustic amplitude of various processes during transient forced response. Actuators are switched on within the shaded regions. Amplitudes are the ensemble average of microphones 0-7. A 10 Hz low-pass filter has been applied for visualisation purposes as the raw data contains high-frequency fluctuations.

Appendix D

Additional Adjacent Jet Forcing Results

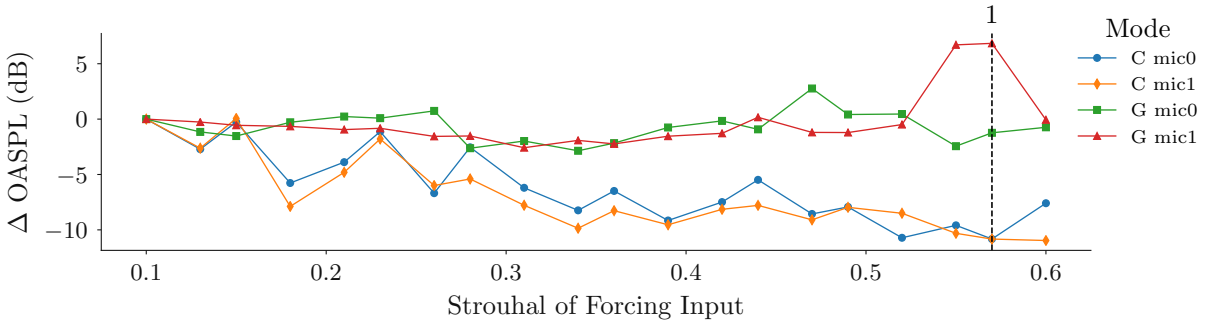

(a) Change in Overall Sound Pressure Level (OASPL), NPR = 2.52.

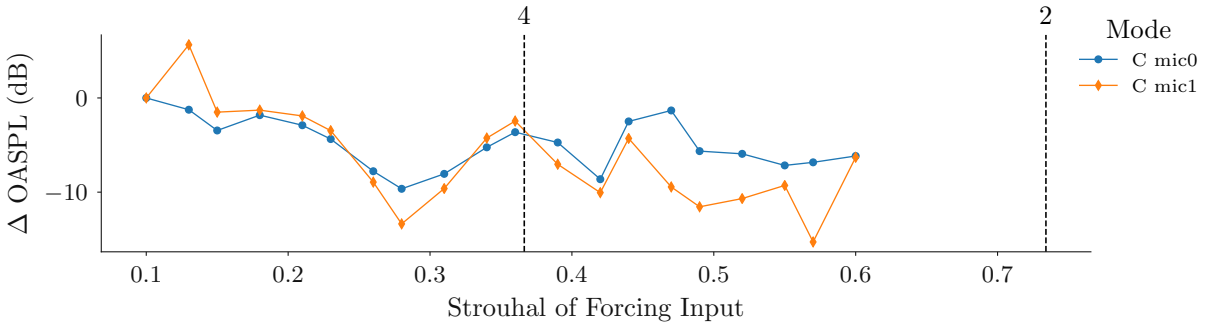

(b) Change in Overall Sound Pressure Level (OASPL), NPR = 2.75.

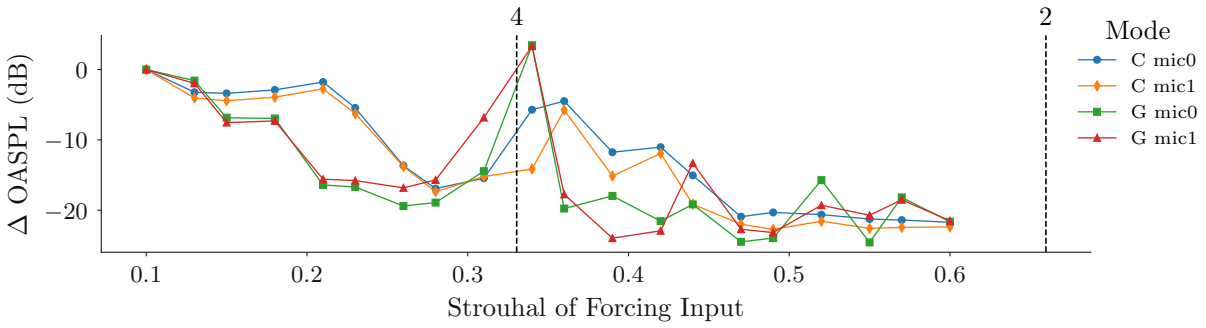

(c) PSD, NPR = 3.00.

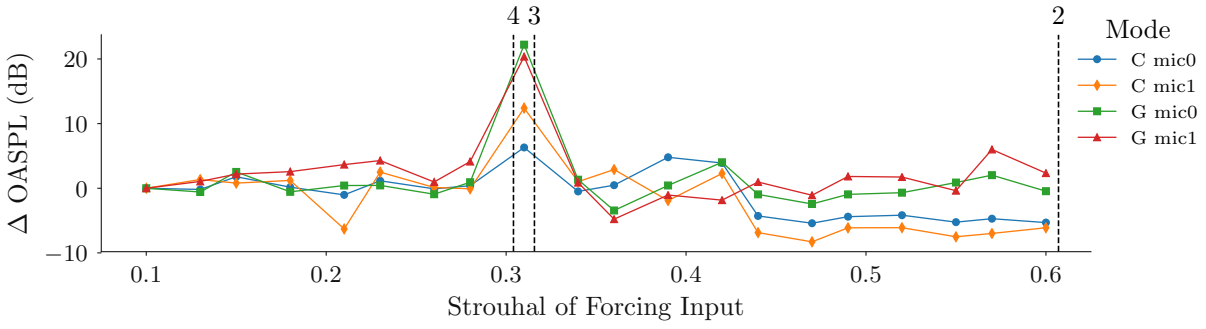

(d) PSD, NPR = 3.25.

Figure D.1: Change in Overall Sound Pressure Level (OASPL) in response to different forcing modes. Black-dashed vertical lines indicate identified processes based on highly coherent frequencies in the unforced jet parameter space with an accompanying annotated process identification number.

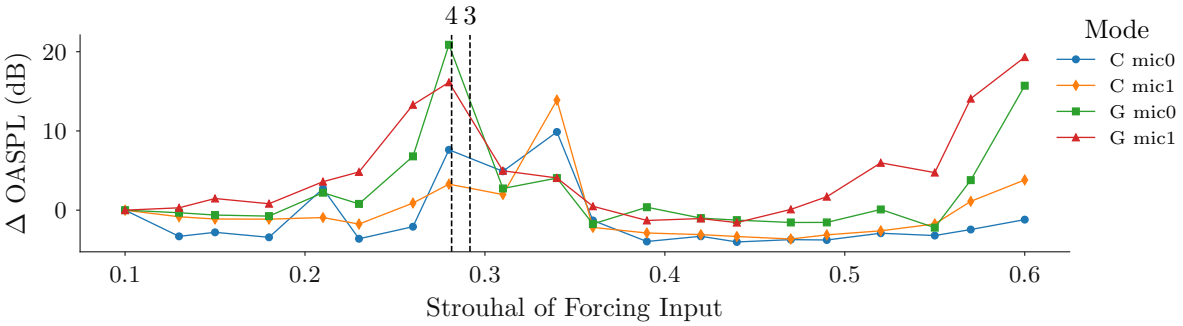

(e) PSD, NPR = 3.50.

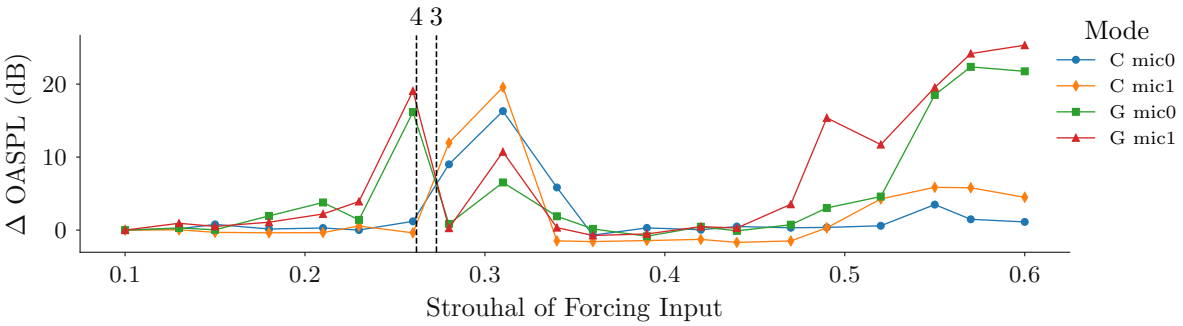

(f) PSD, NPR = 3.75.

Figure D.1: Change in Overall Sound Pressure Level (OASPL) in response to different forcing modes. Black-dashed vertical lines indicate identified processes based on highly coherent frequencies in the unforced jet parameter space with an accompanying annotated process identification number.

Appendix E

Twin-Jet Resonance in Industry

The first reports of empennage fatigue failure on twin-jet aircraft were made by Berndt (1984). Their study provided insight to the discovery and subsequent problem solving that the North American Aerospace and Rockwell International companies performed on the B-1A (prototype of the B-1B production aircraft). Rockwell produced four prototype aircraft for flight testing before production for the United States Air Force, designated the B-1A. In the particular case of the B-1A, problems were not encountered until flight testing progressed and the the testing envelope was expanded to include high-Mach numbers at low altitudes. Specifically, fatigue problems with the empennage and nozzle structure were encountered. It was reported that in certain flight conditions, small portions of the trailing edge of the external flaps of the engine exhaust nozzle were breaking off. A test and design team was created to identify the conditions where the damage was taking place and provide a new design that prevented the problem.

The B-1A was intended as a long-range precision nuclear strike bomber. Its primary mission was to fly undetected deep into enemy territory to drop bombs onto key targets and evade counter-attack. The aircraft would maintain tactical advantage by flying at transonic to low supersonic speeds at 500 ft altitude; The high speed results in very short loiter-time against ground-to-air defences and the low altitude results in poor radar signature for defence against fighter aircraft radar systems. In testing, it was found that the low altitude - high Mach number conditions were likely contributing to the conditions where nozzle fatigue was occurring.

Berndt performed tests on a 0.06 scale model of the twin-jet propulsion system exhausting jet flow into a transonic wind-tunnel simulating co-flow. They used 24 high-frequency pressure-transducers to measure root mean square (RMS) pressure around the circumference (in the azimuthal direction) of the nozzles. A parameter sweep of jet NPR, angle of attack to the tunnel co-flow, and Mach number of the tunnel flow was investigated. They found that significant pressure fluctuations (measured by ΔP_{rms}) was occurring in the inter-nozzle region between the jets (see figure E.1c) at a range of NPRs. The PSD of the pressure signal showed a strong peak, which they understood to be a signature of the resonance at fault. They performed PSD measurements at different co-flow Mach numbers ranging from 0.8 to 1.4 and found that the intensity of the peak decreased with increased co-flow Mach number.

Instrumented flight tests were also performed and a comparison between PSD spectra recorded in

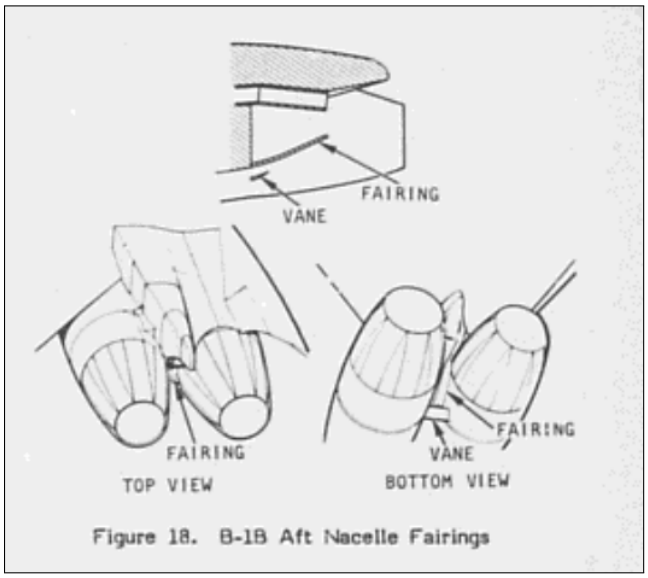

(a) B-1A engine configuration.

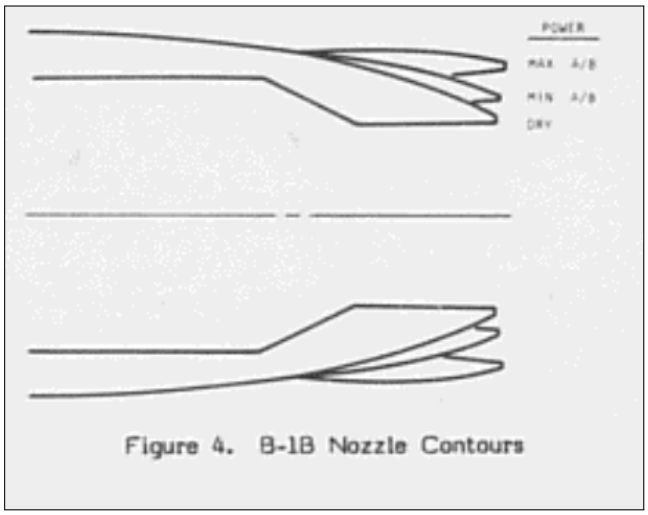

(b) Canonical engine nozzle contours used by the B-1A and scale models.

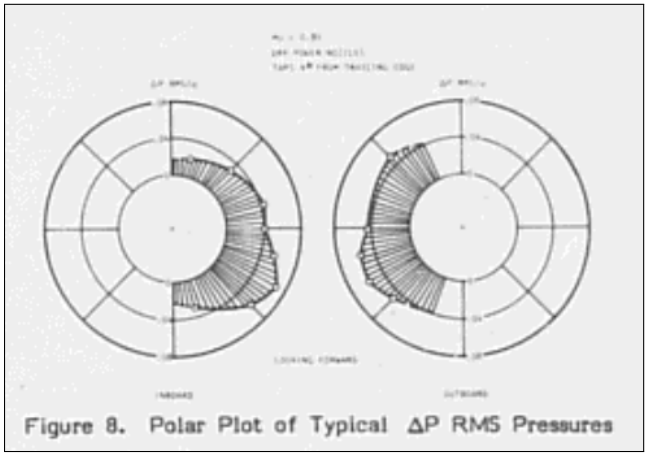

(c) Polar P_{rms} amplitude.

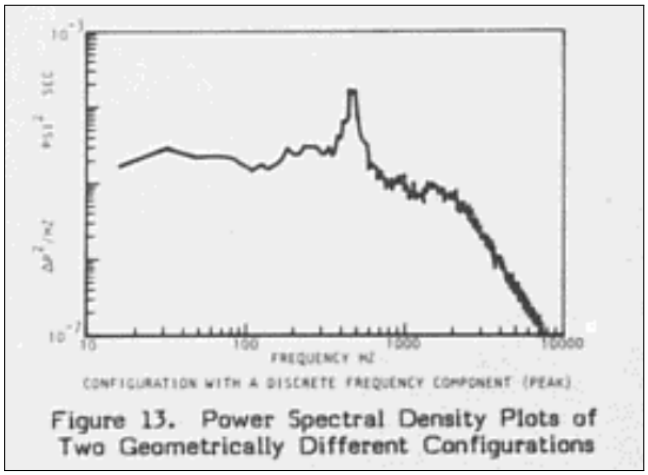

(d) Example PSD of pressure fluctuations showing an amplitude peak corresponding to the observed twin-jet resonance.

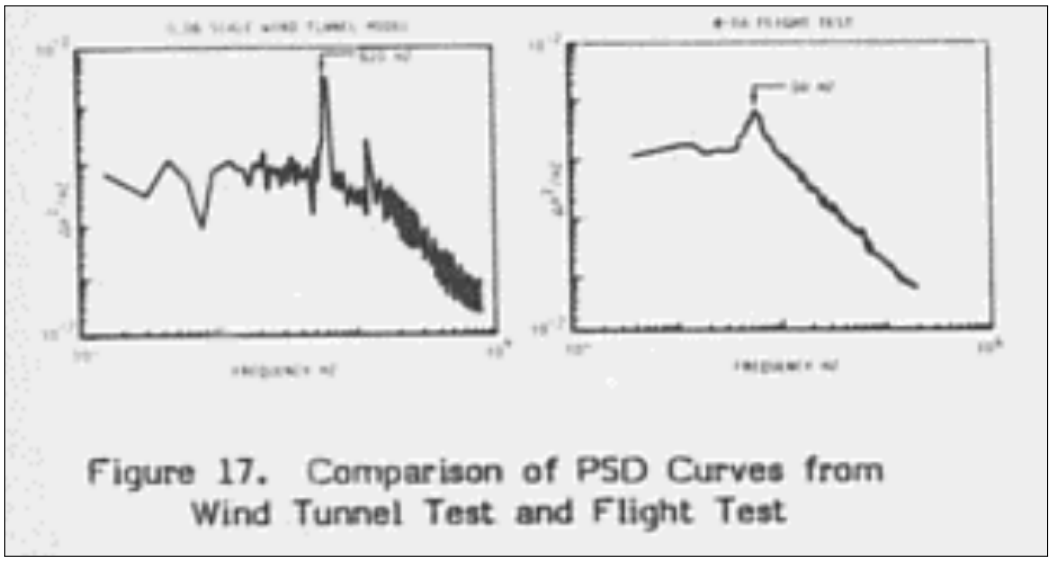

(e) Comparison between B-1A 0.06 scale model in wind-tunnel experiments and flight testing data of pressure transducers mounted in the engine internozzle region. x-axis is frequency, y-axis is $\Delta P/Hz$.

Figure E.1: Initial scale twin-jet testing by Berndt (1984) to determine the nature of the strong engine plume resonance observed in flight.

the scale conditions is shown in figure E.1e. Unfortunately, the plots are no longer legible but they show a similar frequency trend with a strong single peak in both cases. It was reported that vanes were installed (figure E.1a) to direct flow into the inter-nozzle region between the jets, which purportedly removed the resonance condition. This report, while limited in scope, highlights the impact that high-pressure ratio twin-engine exhaust resonance can have on aircraft durability.

Appendix F

Conference Paper, 23rd AIAA/CEAS aeroacoustics conference. 2017.

Particle Image Velocimetry Analysis of the Twin Supersonic Jet Structure and Standing-Wave

G. Bell *
Monash University, Melbourne, Victoria, 3800, Australia
J. Soria†
Monash University, Melbourne, Victoria, 3800, Australia
King Abdulaziz Univeristy, Jeddah, 23218, Kingdom of Saudi Arabia
D. Honnery ‡
Monash University, Melbourne, Victoria, 3800, Australia
D. Edgington-Mitchell §
Monash University, Melbourne, Victoria, 3800, Australia

High resolution particle image velocimetry measurements of under-expanded twin-jets are presented. Two nozzle pressure ratios are examined, which are selected due to a change in coupling family indicated by a discontinuous jump in screech frequency. Estimates of the turbulent flow statistics, shear-layer thickness, and shear-layer merge point are provided. The effect of the standing-wave on the velocity field is quantified for the first time. The higher nozzle pressure ratio case shows a strong standing-wave with a mismatch between the shock-cell spacing and standing-wavelength. A very weak standing-wave is observed in the lower pressure case, which more closely matches the shock-cell spacing. A snapshot based proper orthogonal decomposition of the instantaneous velocity fields reveal a symmetric coupling mode for the higher pressure case, which could either be flapping or helical in nature. The lower pressure case provided little evidence for plume coupling belonging to an in-plane oscillation.

I. Introduction

This work presents particle image velocimetry (PIV) measurements and analysis of under-expanded circular twin-jets. The circular twin-jet arrangement is common to many high speed air and spacecraft propulsion systems. The twin supersonic jet configuration can produce intense acoustic radiation. This acoustic radiation has led to fatigue damage to the nozzle structure and empennage in some high speed aircraft, including the F-15.[1] One major source of acoustic radiation is a self-reinforcing aeroacoustic feedback process called jet screech.[2,3] Screech occurs in shock containing supersonic jets as a result of the interaction between coherent vortical structures produced at the nozzle lip and downstream shock cells. This shock-vortex interaction produces intense acoustic waves that propagate primarily in the upstream direction. The arrival of these waves at the nozzle lip perturbs the shear layer, producing new coherent vortical structures and completing the feedback process.[4]

In a twin jet configuration, the screech cycle is modified by the presence of the adjacent jet and causes the jet plumes to become coupled.[5,6] The coupling behavior is a complex function of nozzle spacing and

*Ph.D. Candidate, Laboratory for Turbulence Research in Aerospace and Combustion, Melbourne, Australia, AIAA student member
†Professor, Laboratory for Turbulence Research in Aerospace and Combustion, Melbourne, Australia, AIAA member
‡Professor, Laboratory for Turbulence Research in Aerospace and Combustion, Melbourne, Australia, AIAA member
§Lecturer, Laboratory for Turbulence Research in Aerospace and Combustion, Melbourne, Australia, AIAA member

nozzle pressure ratio (NPR).[7] NPR is expressed as (NPR = p_0/p_∞), which represents the ratio of nozzle stagnation pressure upstream of the nozzle to ambient pressure in the exhaust region.

The problem of understanding the twin-jet coupling phenomena became significant during the development and early operation of the F-15. Early experimental work focused on parametric studies,[1,8,9] which observed a number of possible coupled modes within the jet plumes. The coupling modes could be classified by their symmetry about the center-line between the jets. Symmetric and anti-symmetric coupled flapping modes that are locked in the plane of the twin nozzles were found. To investigate the coupling and mode selection phenomenon, a simplified linear stability analysis of two canonical jet plumes was performed by Morris.[10] Morris proposed that the variety of coupling modes observed could be generated by combinations of azimuthal helical instabilities. Through the combination of $m = \pm 1$, in-phase and out-of-phase helical instabilities, the analysis was able to estimate the stability of each coupling mode within the parameter space. The most unstable mode was proposed to be the dominant selected mode by the physical system. The analysis results in mode predictions that include symmetric and anti-symmetric flapping, helical, and toroidal modes that occur both in-plane and out-of-plane. For the circular nozzle twin-jet configuration only in-plane modes have been observed experimentally. Kuo et al.[11] used instantaneous schlieren imaging phase-locked at the dominant screech frequency for qualitative mode classification. Symmetric toroidal, symmetric and anti-symmetric flapping, and helical modes were observed in-plane only. Due to the path integrated nature of the schlieren technique, out-of-plane observations are prevented from direct observation. Large aspect ratio rectangular jets predominantly flap in the plane orthogonal to the major dimension. Out-of-plane symmetric and anti-symmetric modes have been acoustically detected in rectangular twin-jet systems[12] and the modes have been predicted via a stability analysis.[13]

While the investigation of coupling modes within the twin-jet system has been a topic of recent twin-jet publications, the standing-wave present in the near-field of the twin supersonic jet has received little attention. The interaction between downstream convecting coherent structures and upstream propagating acoustic waves forms a standing-wave pattern in the near-field pressure. This standing-wave was identified and originally quantified through acoustic measurements.[14] The wavelength of the standing-wave has been proposed as a characteristic length-scale for screech.[15] Historically, the shock cell spacing has also been used as a characteristic length scale. Recent work has suggested that a match or mismatch between these length scales is linked to different acoustic feedback mechanisms.[16]

Few quantitative studies of the twin-jet velocity field exist in literature. A notable exception includes the twin-jet particle image velocimetry (PIV) study of Alkislar et al.[17] Alkislar et al. focused on obtaining turbulent flow properties of the twin-jet system and experimented with micro-jets surrounding the nozzle lip to disrupt the coupling process. There exists a need for quantitative velocity field measurements of coupled twin jets to investigate the coupling behavior and other twin-jet features, like the standing-wave, critical to understanding the deeper coupling mechanisms. The objective of this paper is thus to provide a quantitative experimental study of twin-jet coupling. High-resolution PIV measurements for two modal configurations of coupling are presented. The effect of the standing-wave on the velocity field is determined, and its link to coupling mode examined.

II. Experimental facility

The experiments were conducted in the Laboratory for Turbulence Research in Aerospace and Combustion (LTRAC) gas jet facility at Monash University. The experimental PIV setup is shown in figure 1. Compressed air at approximately 288 K is supplied directly to a mixing chamber where the jets are uniformly seeded with smoke particles from a Viscount 1300 smoke generator. The smoke particles have previously been estimated to be highly mono-disperse with a mean diameter of 0.6 μm.[18] Only one smoke source was needed for both jet core and ambient fluid measurements as after a short time the smoke particles completely filled the measurement facility. The mixing chamber is connected to the plenum chamber, which contains a honeycomb section and wire mesh screens to homogenize and condition the flow. The gas jet facility has been previously validated by experimental studies.[20,25] Both nozzles share the same plenum chamber. Compressed air exhausts from twin converging circular nozzles with an exit diameter of $D = 10$ mm and nozzle lip thickness of 1.5 mm. The converging nozzle section follows an elliptical profile (15 mm major and 5 mm minor axes) becoming tangent at the exit. The issued flow is sonic ($M_e = 1$) at the nozzle exit, with a jet exit velocity of $U_e \approx 310$ m/s. The Reynolds number based on isentropic flow through the nozzle is approximately 1.5×10^6.

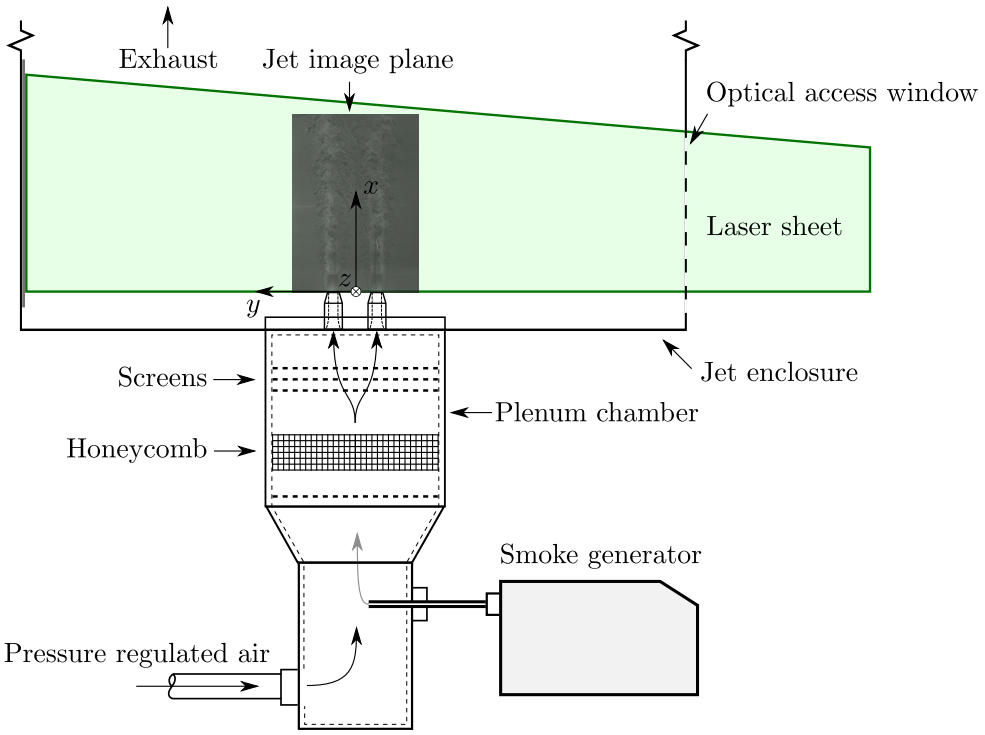

Figure 1. Experimental PIV setup.

From previous qualitative studies within the laboratory using the same twin-jet nozzles, it was found that an inter-nozzle spacing of 3 ($s/D = 3$) in the range NPR $\approx 2.0 \rightarrow 5.4$ produces strong coupling. Acoustic measurement and analysis were performed to characterize the fundamental screech tone peak frequency of the jet pair in the measurement facility as a function of NPR. A G.R.A.S. type 46BE 1/4" preamplified microphone with a frequency range of 20 Hz $\rightarrow$ 100 kHz was used. The microphone amplitude coefficient was referenced against a G.R.A.S. type 42AB sound level calibration unit. The signal output from the microphone was recorded on a National Instruments DAQ at a sample rate of 250 kHz to prevent aliasing. The single microphone was placed 23 D away at $x/D = 0$, $y/D = 0$, $z/D = 23$. The average acoustic spectra were calculated using a 2^{13} sample sliding-window via a Fourier transform. A 25 % window overlap and a Hann filter were used to minimize edge effects. Figure 2 shows the acoustic frequency spectra with vertical lines indicating the fundamental screech tone.

Figure 3 shows the identified fundamental screech tone as a function of NPR. The abrupt change in screech frequency at NPR = 4.85 was assumed to indicate a transition between jet oscillation modes. Two NPRs on either side of this switch point (NPR = 4.60 and 5.0) were selected for PIV analysis as the small change in NPR should result in minimal variation of the base flow.

Single exposure image pairs were acquired using a 12-bit Imperx B6640 camera with a CCD array of 6600 $\times$ 4400 px at a rate of 0.5 Hz. Approximately 9,000 velocity fields are used for the calculation of all statistics. A magnification of 19.9 µm/px is achieved using a 200 mm Nikon Micro-Nikkor lens, which results in a PIV image plane of 129.3 $\times$ 86.2 mm. The particle field is illuminated using a diverging light sheet of approximately 1 mm thickness produced from a dual cavity pulsed Nd:YAG laser at 532 nm with a maximum pulse energy of 200 mJ. A multi-grid cross-correlation digital particle image velocimetry algorithm[21] is used to analyze the image pairs. Table 1 describes the specific parameters of the PIV component of this work.

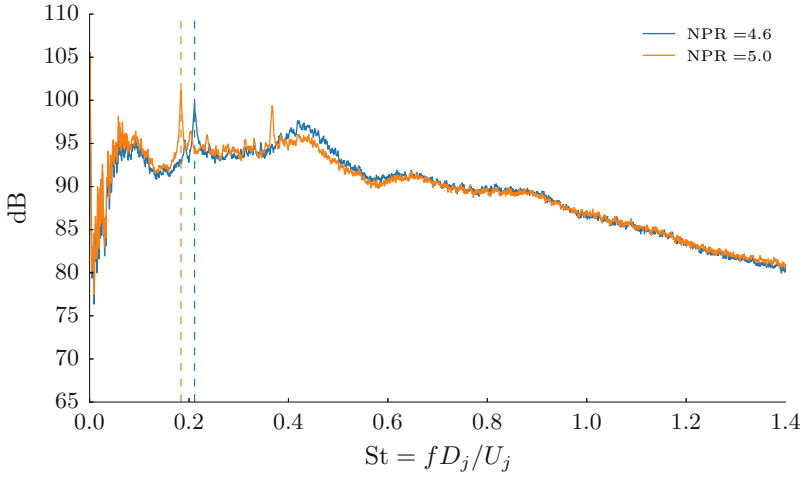

Figure 2. Acoustic spectra for two comparison cases: NPR = 4.6 **and** NPR = 5.0**.**

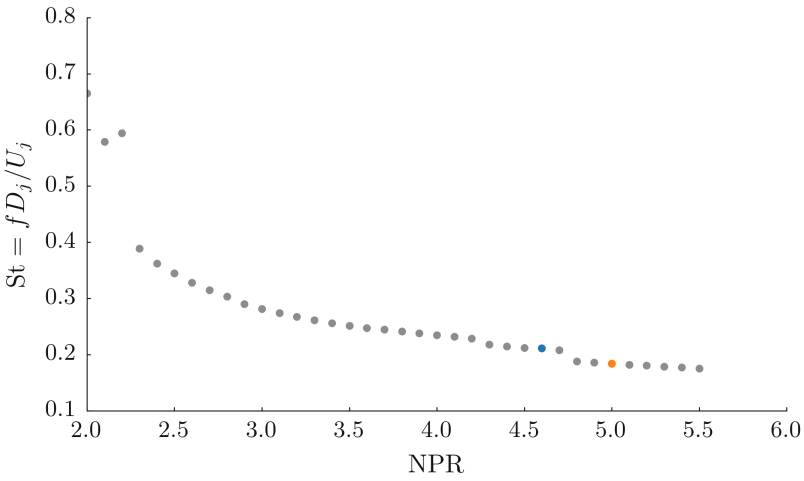

Figure 3. Fundamental screech tone for a variety of NPRs. The two cases examined using PIV are NPR = 4.6 **(blue marker) and** NPR = 5.0 **(orange marker).**

III. Results and Discussion

A. Mean Flow Fields

Mean axial velocity flow fields for NPR = 4.6 and 5.0 are provided in figures 4 and 5 respectively. Overlaid is the interior and exterior spatial extent of the shear-layer for qualitative illustration, which is described in section B. The white regions are masked in the analysis as they contained laser light reflections that could not be avoided.

The two cases are separated by a small change in NPR but correspond to a different coupling mode. A quantitative examination of the mean axial velocity fields (figures 4 and 5) reveals similar features between cases: Both flows are characterized by a large Mach disk at the first shock-cell, and include a cellular shock-expansion pattern typical of strongly under-expanded jets. Both cases are symmetrical about the inter-nozzle centerline. In neither case is the jet axial velocity or shock-cell pattern distorted towards each other as observed by Seiner.[1] The maximum axial component of velocity is $1.87\,U_e$ for NPR = 4.6 and

Table 1. PIV measurement parameters

Parameter	Value	Non-dimensional value
Field of view ($x \times y$)	129.3×86.2 mm	$12.9 \times 8.6D$
Laser inter-frame delay	0.9 µs	-
Initial PIV window size	128×128 px	$0.255 \times 0.255D$
Final PIV window size	16×16 px	$0.032 \times 0.032D$
Depth of field	0.66 mm	$0.066D$
Vector Spacing	8 px	$0.016D$
Vector overlap	50 %	-
Resulting vector field ($x \times y$)	1092×726	-

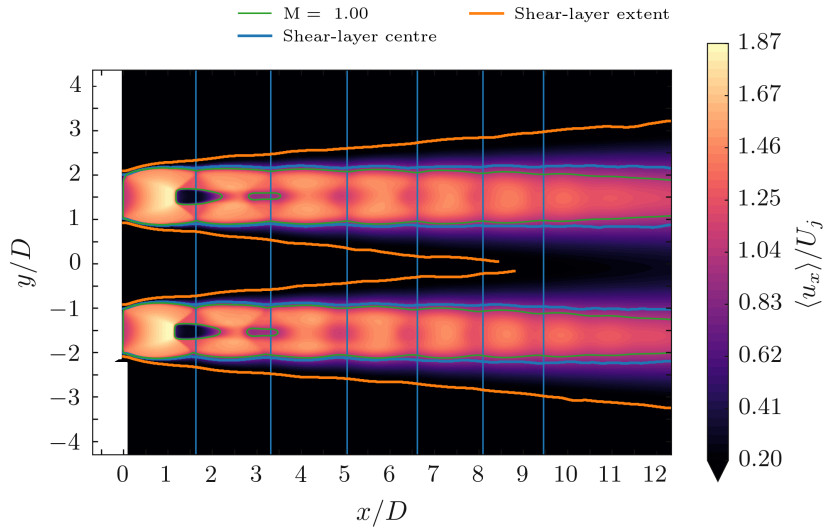

Figure 4. Mean axial velocity for case NPR = 4.6 **with shear layer and** M = 1.0 **(where the local Mach number is calculated assuming isentropic dependence on measured velocity) contour overlaid. Vertical lines indicate shock reflection locations.**

$1.92\,U_e$ for NPR = 5.0. The maximum velocities in both cases occur prior to the first shock-cell. Vertical lines indicate the shock reflection point locations, which were determined via changes in sign of the axial velocity gradient plotted at the jet boundary.

Due to the strong Mach disk and the indecent grazing angle of the laser sheet, the planar laser sheet is refracted after passing through the lower jet. A similar phenomenon was found by Yoo et al.[22] Consequently the upper jet receives less consistent illumination, which is clearly visible in higher order statistics. For this reason, and have demonstrated the symmetry of the flows in figures 4 and 5, 'half-half' contour plots are used for the remainder of this paper. The y-axis in figure 6 shows this accordingly with a negative axis extending both up and down, where both jets shown are the bottom jet.

The half-half contour of transverse (spanwise) velocity is shown in figure 6. The oscillating pattern of positive and negative velocity is the result of the turning angle produced by oblique shocks in the cascading shock structure. The turning angle and transverse velocity oscillation decrease with axial distance as the

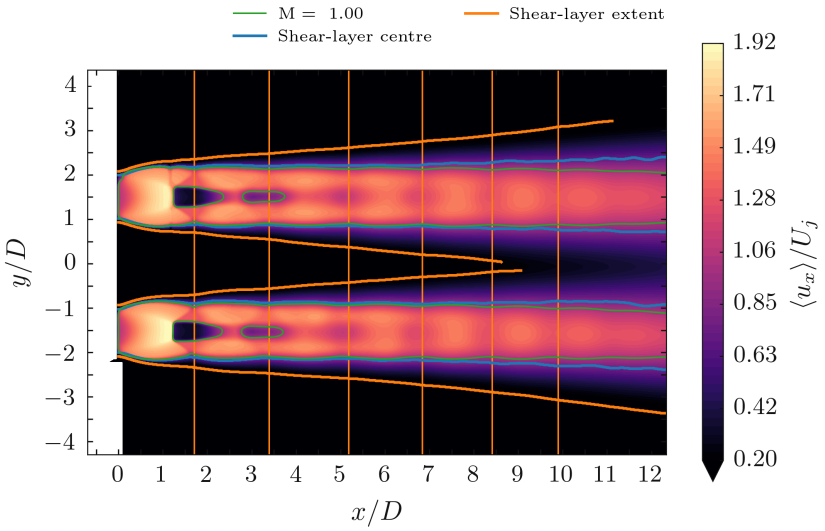

Figure 5. Mean axial velocity for case NPR = 5.0 **with shear layer and** M = 1.0**.**

under expanded jets reach ambient pressure, and the shock strength reduces.

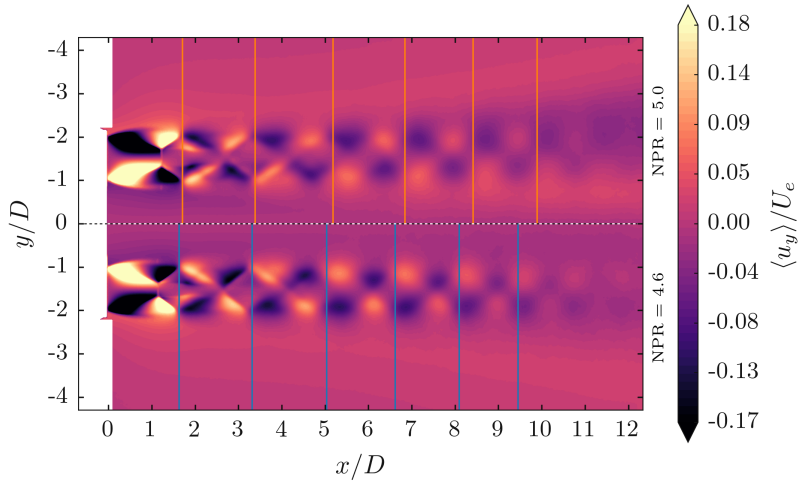

Figure 6. Mean transverse velocity for case NPR = 4.6 **(bottom half) and** NPR = 5.0 **(top half, reflected vertically). Vertical bars indicate shock reflection locations for each case respectively.**

Half-half contours of vorticity are shown in figure 7. The sliplines associated with the Mach disks can be observed emanating at the edges and translating downstream. The steep gradient of vorticity along the jet boundary provides a quantitative estimate of the shear layer extent. The shear layer associated with the Mach disk slip-lines is also particularly well highlighted. The Mach disk diameter is larger in the NPR = 5.0 case.

Profiles of axial velocity are provided in figure 8. For each case respectively, the top and bottom jet profiles are nearly identical. The jet-center line velocity oscillation due to the shock-cell structure has not ended within the measurement domain (greater than $x/D \approx 11$).

In both cases, evidence for Mach disks occurring in at least the first two shock-cells is provided by contours and profiles of local Mach number. Local flow Mach number was obtained assuming isentropic expansion as a function of velocity magnitude, a method similar to Andre et al.[23] This allows the calculation of spatial

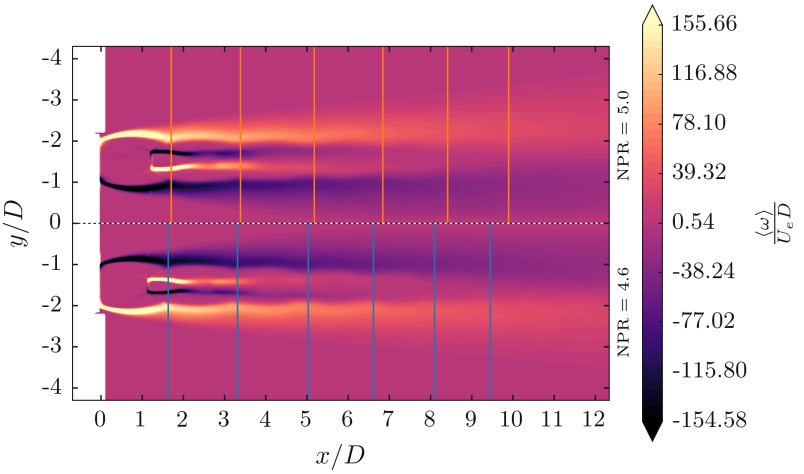

Figure 7. Mean vorticity for case NPR = 4.6 **(bottom half) and** NPR = 4.6 **(top half). Vertical bars indicate shock reflection locations for each case respectively.**

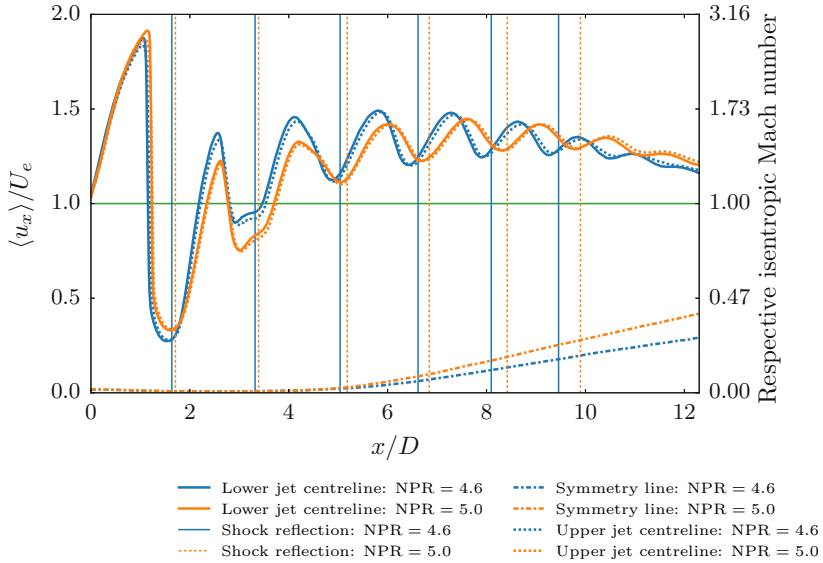

Figure 8. Mean axial velocity along symmetry and jet-center profiles.

temperature, which in turn provides the local speed of sound to be calculated. Contours and profiles of the local Mach number are provided in figures 4 and 5, and 8 respectively. The resulting relationship between non-dimensional velocity and isentropic local Mach number is strongly non-linear, as demonstrated by the parallel y-axis scales in figure 8. Figure 8 shows locally subsonic flow within the supersonic structure at both $x/D \approx 1.8$ and 3.2. The flat region of axial velocity at $x/D \approx 3.8$ corresponds to this subsonic flow pocket generated by the second Mach disk. The entropy generated by the normal Mach disk shock ensures that the isentropic assumption provides an over estimate of velocity in this region downstream of the shock.

Half-half contours for the standard deviation of axial and transverse velocity are provided in figures 9 and 10 respectively. The velocity artifact in the shear layer at $x/D \approx 1.0$, $y/D \approx -1.0$ is most visible in the standard deviation. It is the result of laser light refraction caused by the first Mach disk. The laser light refraction and produces a velocity artifact that is also propagated through to the top jet and into the top

exterior region at the top of the spatial measurement, partially visible in figures 4 and 5 (not visible in the half-half contour plots).

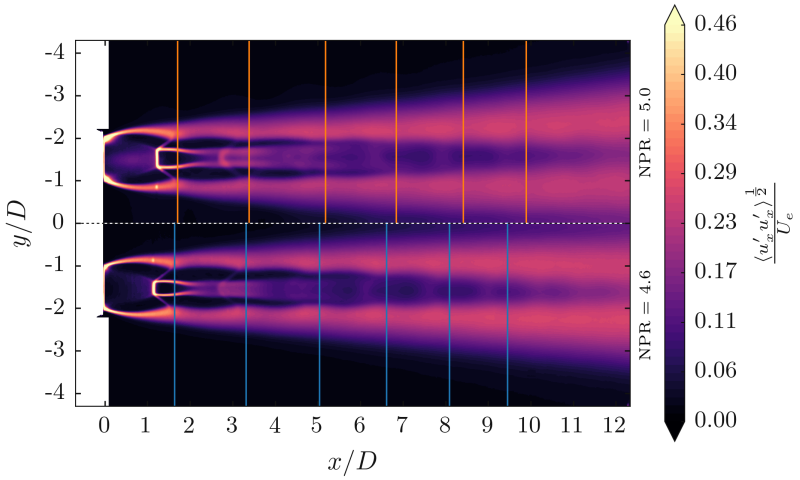

Figure 9. Standard deviation of axial velocity for lower jet in both cases.

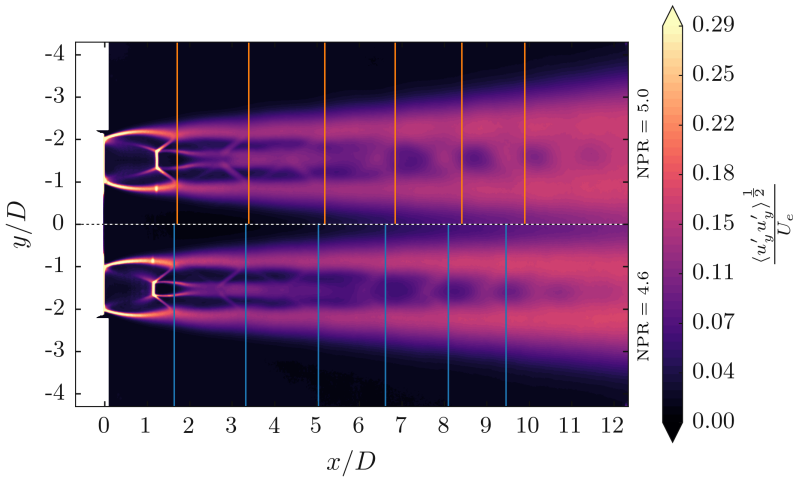

Figure 10. Standard deviation of transverse velocity for lower jet in both cases.

B. Shear-Layer

Shear-layer thickness is calculated for each jet on both shear-layers facing the external jet near-field (denoted as **E** in figures) and the interior inter-nozzle region (denoted **I**). Shear-layer thickness is estimated as a function of axial position but could not be reliably detected far downstream. The thickness is defined as the spatial jet spanwise distance between maximum u_x standard deviation to a 30 % threshold level of the respective axial maximum. The **I** and **E** external jet shear-layer thicknesses were found to be symmetrical and the mean thickness is provided in figure 11.

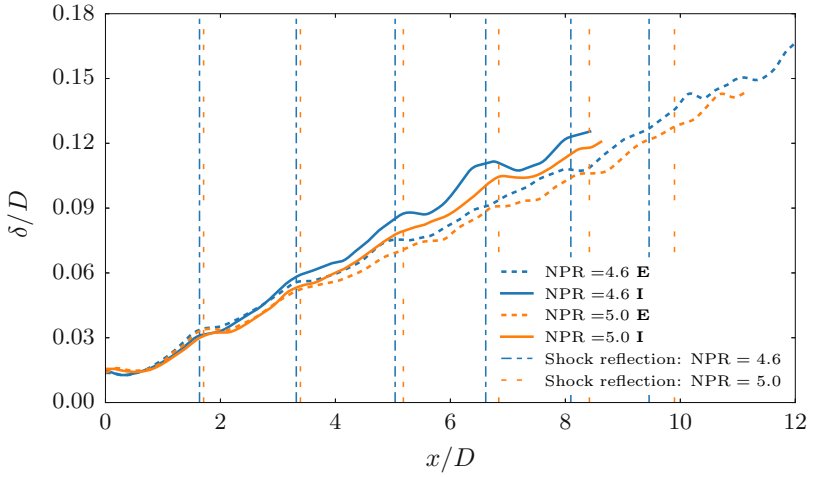

Figure 11. Averaged shear layer thickness estimate.

Shear-layer growth-rates in the **I** region are found to be consistently higher than those in the **E** region. This suggests that the coupled interaction, regardless of its modal shape, produces greater mixing in the inter-nozzle region. The NPR = 5.0 case also produces higher shear-layer growth rates for both the internal and external near fields than NPR = 4.6. A proposed explanation is provided later when examining mode shape.

C. Standing-Wave

The standing-wave structure is the result of the fluctuating pressure field caused by downstream convecting CVSs and upstream propagating acoustic waves.[14] Panda[15] was among the first to provide a quantification for the banded pattern through schlieren photography when measuring temporal variance. He was able to deduce that these bands were the interference pattern between upstream convecting CVSs and downstream propagating acoustic waves. He described the structure as a 'standing-wave' and the term has remained in usage within the jet aeroacoustics community since. Common usage of 'standing-wave' implies that the resulting interference pattern between two waves is fixed and spatially stationary to the naked eye. In this case, however, the naked eye is unable to see the interference pattern as the waves have different propagation speeds and hence the interference pattern moves spatially. The two waves, however, do have the same frequency and produce an interference pattern visible in measures of amplitude fluctuation.

The standard deviation of axial velocity for both cases was presented in figure 9. The same figure with a logarithmic scale is now used in figures 12 and 13 to simultaneously resolve the jet core and the smaller fluctuations of the standing-wave structure.

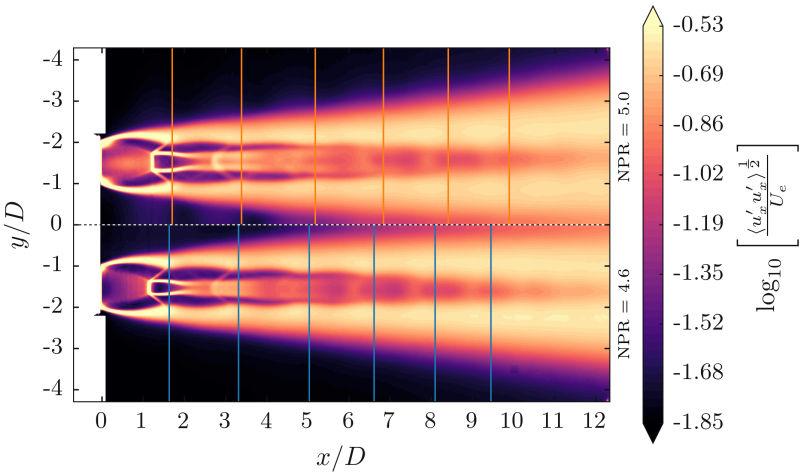

Figure 12. Half-half contour of standard deviation of axial velocity with logarithmic scale. Standing-wave is visible in NPR = 5.0 **half only as lobed structures adjacent to the jet.**

The standing-wave structure is observed in the NPR = 5.0 case as lobes of higher fluctuation in axial velocity and the structure is visible both in the **I** and **E** regions of the jets. No modulation is apparent in the transverse velocity fluctuations. This implies that the interference between hydrodynamic coherent structures and acoustic waves is predominantly in the axial direction. To the authors' knowledge, this is the first time the standing-wave produced by a shock containing supersonic jet has been recorded in the velocity field. The standing-wave was not observed in the studies of Alkislar et al.[17] For clarity, figure 14 presents axial profiles of fluctuating axial velocity for the jets' **I** and **E** regions. These profiles have been detrended to remove the monotonic increase in velocity fluctuations associated with shear layer growth, which dominated the sinusoidal modulation due to the standing-wave. The detrending was accomplished using a 1D Gaussian filter.

Figure 14 a contains the detrended line plots for the NPR = 4.6 case. There is a weak sinusoidal modulation of the axial fluctuations in the inter-nozzle region. No modulation is evident on the jet exterior. Figure 14 b, for the higher pressure ratio, shows a consistent sinusoidal modulation for both the inter-nozzle and jet exterior profiles. The fluctuation in the crest of the standing-wave at $x/D \approx 1.5$ is a velocity artifact caused by the refraction of laser light from the Mach disk. The discrepancy between the standing-wave for the two cases may be linked to three-dimensionality in the coupling of the plumes. Schlieren path integrated density gradient fluctuations performed by Edgington-Mitchell et al.[16] showed no standing-wave in the major axis for an under-expanded elliptical jet flapping about the minor axis. This may provide an explanation for the weak or non-existent standing-wave for the NPR = 4.6 case. The standing-wave wavelength and shock spacing are provided in table 2. Within this work, for the case where the standing-wave is present,

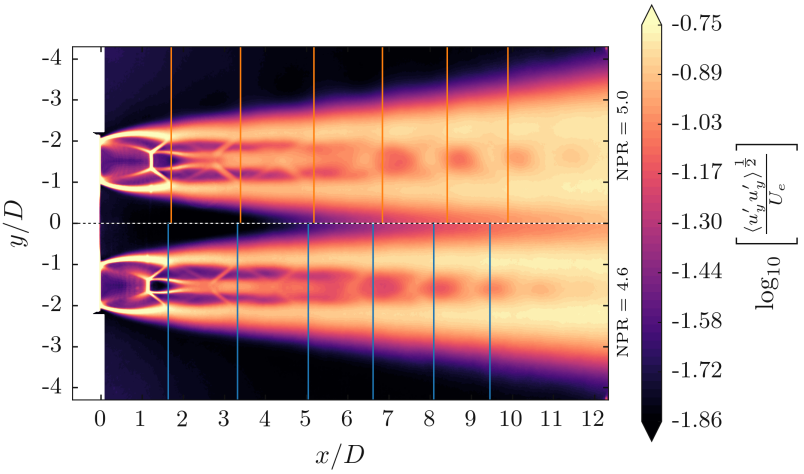

Figure 13. Half-half contour of standard deviation of transverse velocity with logarithmic scale. No standing-wave is visible.

the standing-wavelength was found to be greater than the shock-cell spacing. It is unknown whether a predominantly out-of-plane standing-wave exists for the NPR = 4.6 case, which cannot be resolved with an in-plane planar measurement. Within the two cases examined by Panda,[15] he found that the standing-wavelength was less than the shock-cell spacing in both cases. Conversely, Edgington-Mitchell et al.[16] found a standing-wavelength that was greater or equal to the shock-cell spacing for all cases considered.

Table 2. Screech metrics

	NPR	
	4.6	5.0
Screech Strouhal number	0.22	0.19
Screech wavelength, ($a \approx 345\,\mathrm{m/s}$, temp $= 293\ K$)	$3.38\,D$	$3.88\,D$
Average shock reflection point spacing (first 4)	$1.61\,D$	$1.68\,D$
Average symmetry standing-wave spacing	$1.56\,D$	$1.73\,D$
Average shear-layer standing-wave spacing	$1.56\,D$	$1.67\,D$

In the NPR = 5.0 case, the fluctuation modulation pattern produced by the standing-wave is larger in the **I** region. The standing-wave strength will be linked to both the amplitude of the upstream propagating acoustic waves and the downstream convecting hydrodynamic waves. Seiner[1] demonstrated that for symmetric coupling modes, the overall sound pressure level in the interior region was greater than the sum of two non-interacting single jets. Morris[24] predicted that the increased pressure fluctuations caused by passing coherent hydrodynamic structures drops off exponentially with increasing distance from the shear layer. It is suggested in the present work that the amplitude discrepancy between the interior and exterior regions derives from two factors. Firstly, the difficulty of defining a consistent measurement location between the inner and outer jet edges may hinder direct comparison. Secondly, the stronger acoustic field present in the interior region due to the synchronized summation of both jet's acoustic waves should result in a stronger standing-wave as suggested by Seiner.[1]

A strong local minima in fluctuating magnitude is visible at an axial location of $x/D \approx 4$ within the inter-nozzle region. This was determined not to be an artifact from the Gaussian filter subtraction. Low

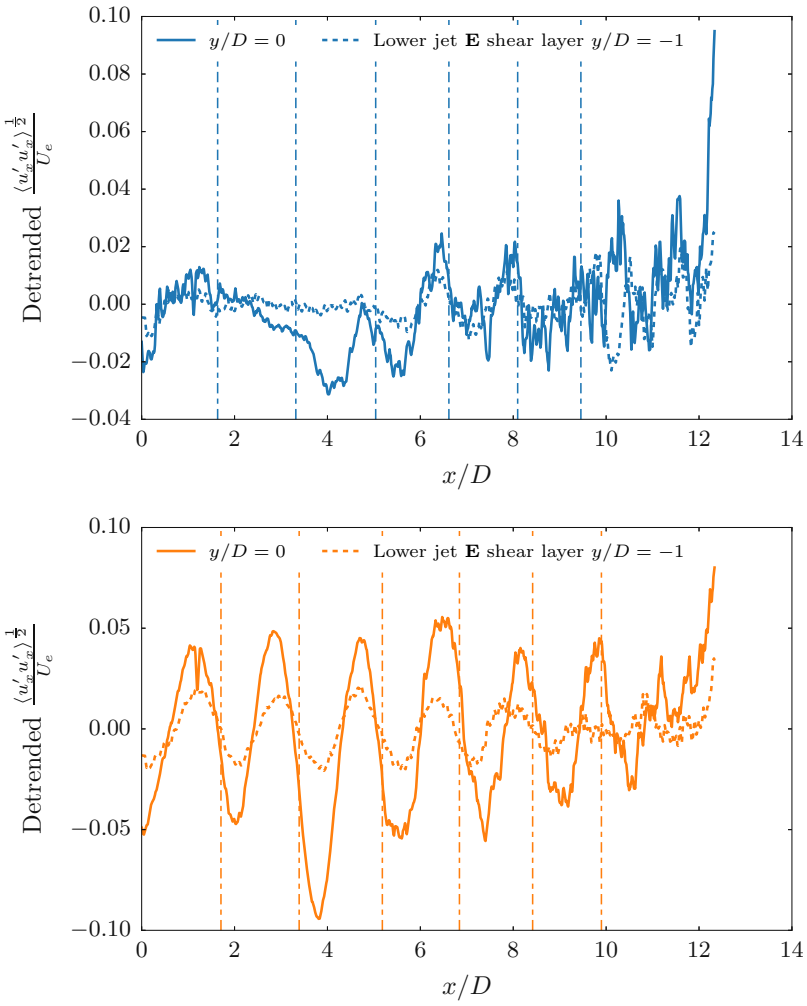

Figure 14. Detrended standard deviation of axial velocity showing standing-wave modulation.

fluctuation indicates a nodal position in the standing-wave. The root-mean-square acoustic results of Panda[15] show a stronger crest at the 3rd standing-wave. Further investigation of the acoustic wave propagation and subsequent interference is required to explain this behavior.

D. Characterization of Dominant Modal Behavior

Despite the relatively similar mean-field structure, the standing-wave pattern observed in the two NPR cases was markedly different. Given the standing-wave is produced by the interaction between periodic CVSs and acoustic waves, to further examine this discrepancy we now consider the dominant periodic modal behavior of the flow. To characterize the periodic dominant modal behavior of the coupled twin-jets, a snapshot proper orthogonal decomposition (POD) of 9,000 instantaneous velocity fields is performed. POD constructs a set of basis functions that optimally represent the ensemble of fluctuating velocities.[25–27] The decomposed modes are orthogonal and ranked by eigenvalue. The corresponding eigenvalues are correlated to the specific kinetic energy of each mode and the eigenvectors provide the mode shape.

NPR = 5.0 will be presented first as the interpretation of the POD results is more straightforward. The eigenvalue energy cascade for the higher NPR is presented in figure 15. Only approximately 15 % of the cumulative specific mode energy is contained in the first 4 modes. After the 4th mode, however, the energy contribution is small ($\leq 1\,\%$).

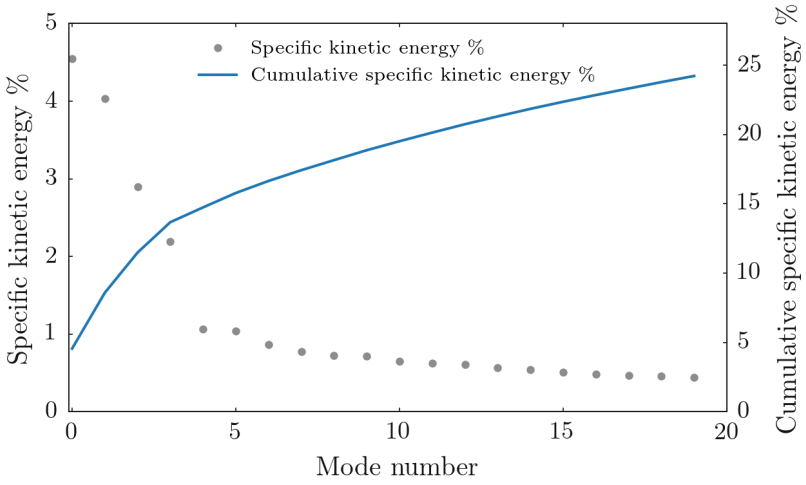

Figure 15. POD mode energy distribution, NPR = 5.0

Examining the first two mode shapes (mode 0, figure 16 and mode 1, figure 17) reveals a pattern along each jet of symmetric fluctuating positive and negative mode value. Oberleithner et al.[28] provides a method to observe the temporal relationship between the modes. Mode coefficients of each snapshot are plotted for mode 0 against 1 (plot omitted for brevity). The exercise results in a phase portrait, as the instantaneous velocity fields are randomly sampled over time. The phase portrait for mode 0 and mode 1 produce a neat circular shape indicating that the modes are oscillating as pair and are at an angle $\pi/4$ out-of-phase. In contrast, the mode shapes for modes 2 and 3 do not appear to form a modal pair by inspection or by phase portrait and have been omitted.

The mode 0 and 1 modal pair form a symmetric mode about the streamwise symmetry line between the jets. This is most apparent in the transverse velocity component, which consists of alternating bands of positive and negative value within the jet plumes that are out-of-phase with respect to one another. The interpretation of planar jet centerline measurements to 3D twin-jet coupling modes is limited by no knowledge of the out-of-plane component. Considering this, the symmetric modes suggested by the mode 0, 1 pair could be azimuthally helical or flapping in nature. The symmetric mode is in agreement with previous analysis that examined two-point velocity correlations.[29] Proposed symmetric coupling mode allows for the superposition of simultaneously emitted acoustic waves and explains the larger standing-wave amplitude observed in the inter-nozzle region.

The sinusoidal pattern produced by the POD mode shapes of the 0 and 1 modes corresponds to the hydrodynamic wavelength of the CVSs.[30] Measurement to link the coupling mode and standing-wavelength can be provided by the derivation performed by Panda[15] resulting in equation , which links the standing-

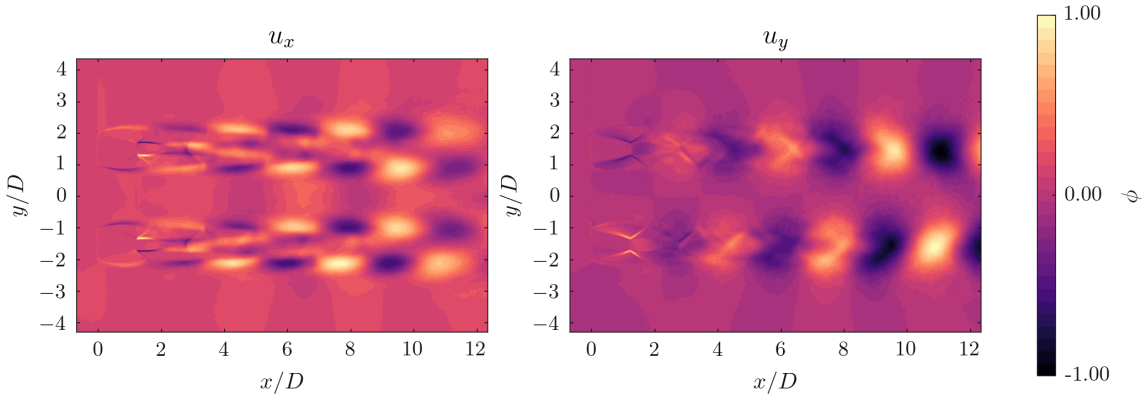

Figure 16. POD mode 0 shape in the axial and transverse directions, NPR = 5.0**.**

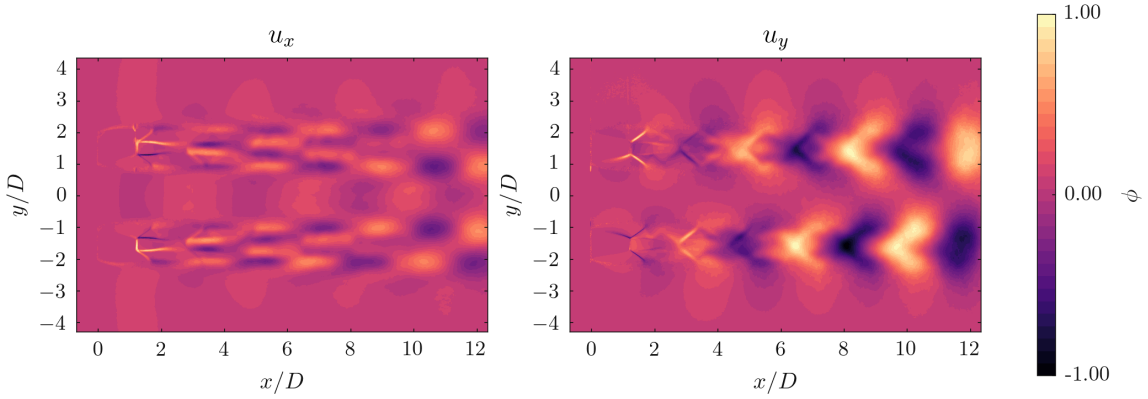

Figure 17. POD mode 1 shape in the axial and transverse directions, NPR = 5.0**.**

wavelength (L_{sw}), the screech acoustic wavelength (λ_s), and the hydrodynamic wavelength (λ_h).

$$\frac{1}{L_{sw}} = \frac{1}{\lambda_s} + \frac{1}{\lambda_h} \tag{1}$$

The average hydrodynamic wavelength was measured from the POD mode shapes 0 and 1 to be 1.62 D. The standing-wavelength is equal to twice the standing-wave spacing, as the variance provides an absolute measurement. The screech wavelength was provided in table 2 as 3.88 D. When substituted into the right-hand side of equation 1, the values of L_{sw} and λ_s result in a screech wavelength of 1.76 D. This value is within 2 % of the measured standing-wavelength and provides evidence that the relationship between standing-wave and jet instability mode developed by Panda[15] applies to twin-jets as well.

The mode energy distribution for NPR = 4.6 is presented in figure 18. In this case, at least 6 modes have greater than 1% relative energy. The two highest energy modes, mode 0 and 1, do not form a mode pair as determined by their asymmetric mode shapes (figures 16 and 17) and phase portrait, which shows a randomly distributed cloud of snapshot coefficients. The lack of high energy mode shapes associated with an obvious in-plane coupling mode is currently under investigation. Maps of two-point velocity correlations also found no coherent mode pattern for the lower NPR = 4.6 case.[29]

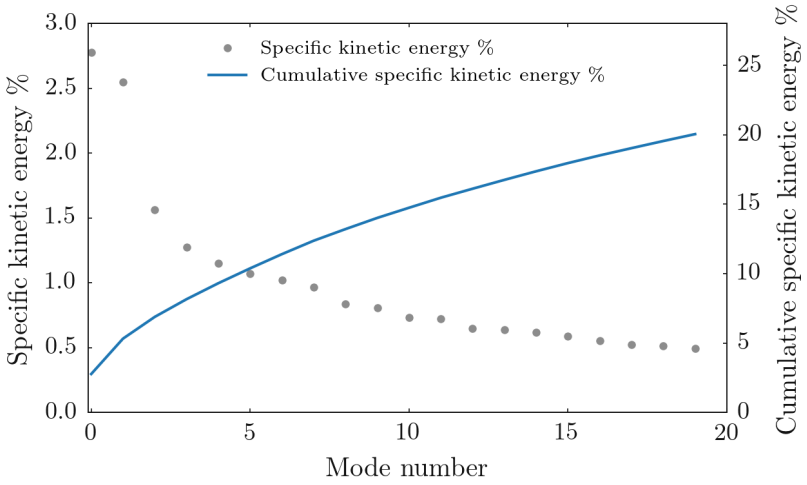

Figure 18. POD mode energy spectrum, NPR = 4.6

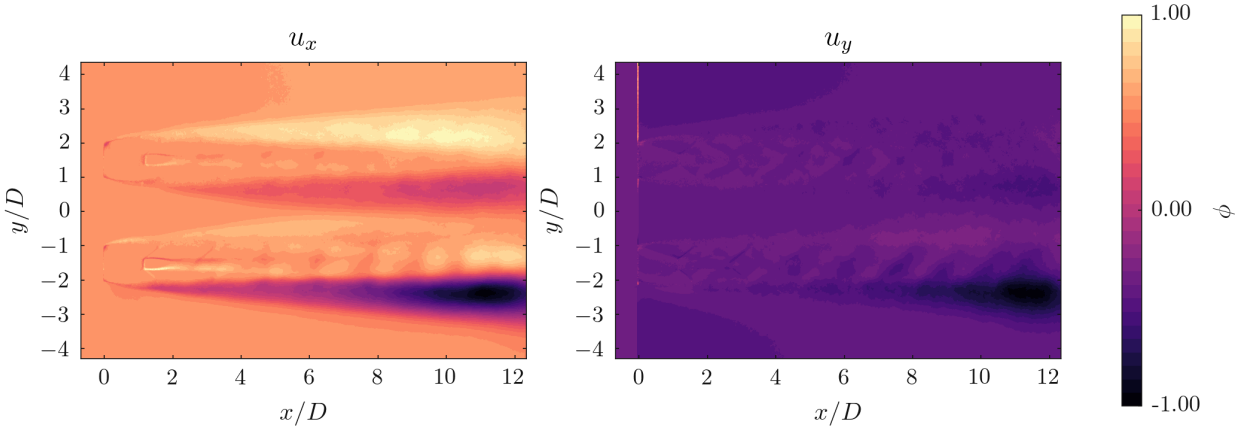

Figure 19. POD energy in the axial and transverse directions: mode 0, NPR = 4.6**.**

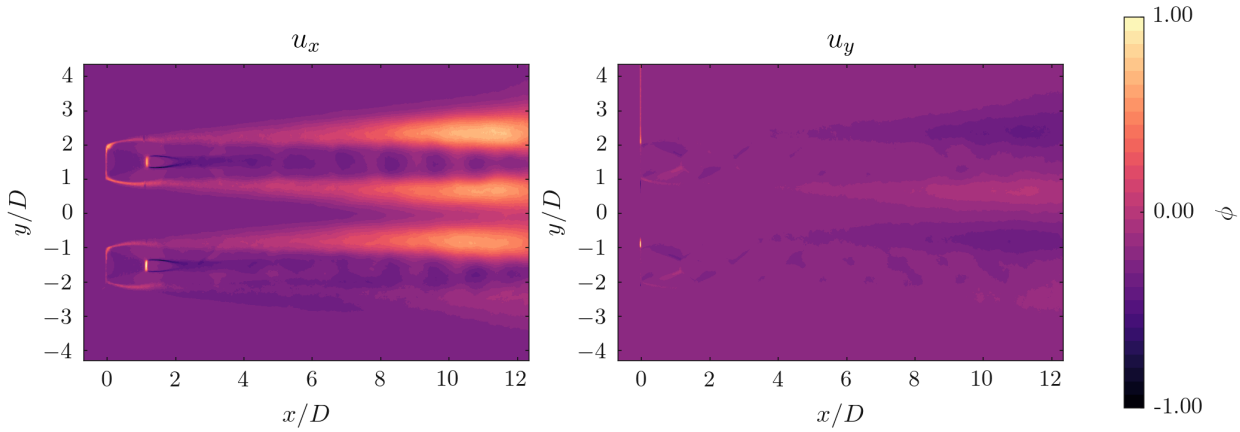

Figure 20. POD energy in the axial and transverse directions: mode 1, NPR = 4.6**.**

IV. Conclusion

PIV measurements and analysis of turbulent flow properties and modality of coupled under-expanded twin-jets has been presented. Two cases have been recorded that are separated by a discontinuous jump in screech frequency. The screech frequency jump is thought to be the result of a change in screech feedback mechanism, accompanied by a change in supersonic twin-jet coupling mode. A strong standing-wave is evident in the velocity fluctuations for the NPR = 5.0 but is much weaker in the NPR = 4.6 case. Proper orthogonal decomposition was performed on both cases to reveal the dominant modes of the flow. NPR = 5.0 revealed a symmetric POD mode within the first two most energetic modes. The symmetric mode pair was suggested to be associated with a symmetric azimuthal helical or symmetric flapping coupling mode. The symmetric coupling mode allows for the superposition of simultaneously emitted acoustic waves and explains the larger standing-wave amplitude in the inter-nozzle region. The NPR = 4.6 case showed few high energy modes, and none were found to be applicable with azimuthal helical or flapping modes as they are currently understood. The lack of an in-plane mode was consistent with previous research of the flow, and assists the explanation of a very weak in-plane standing-wave.

References

[1]Seiner, J. M., Manning, J. C., and Ponton, M. K., "Dynamic Pressure Loads Associated with Twin Supersonic Plume Resonance," *AIAA Journal*, Vol. 26, No. 8, 1988, pp. 954–960.

[2]Powell, A., B, B. G., R, H., M, L. G., P, S., M, W. R., and G, L., "On the Mechanism of Choked Jet Noise," *Proceedings of the Physical Society. Section B*, Vol. 66, No. 12, dec 1953, pp. 1039–1056.

[3]Tam, C. K. W., "Supersonic Jet Noise," *Annu. Rev. Fluid Mech*, Vol. 27, 1995, pp. 17–43.

[4]Raman, G., "Advances in understanding supersonic jet screech: Review and perspective," *Progress in Aerospace Sciences*, Vol. 34, No. 1–2, 1998, pp. 45–106.

[5]Raman, G., Panickar, P., and Chelliah, K., "Aeroacoustics of twin supersonic jets: a review," *International Journal of Aeroacoustics*, Vol. 11, No. 7, 2012, pp. 957–984.

[6]Kuo, C.-W., Cluts, J., and Samimy, M., "Exploring Physics and Control of Twin Supersonic Circular Jets," *AIAA Journal*, Vol. 55, No. 1, jan 2017, pp. 68–85.

[7]Kuo, C.-W., Cluts, J., and Samimy, M., "Effects of excitation around jet preferred mode Strouhal number in high-speed jets," *Experiments in Fluids*, Vol. 58, No. 4, apr 2017, pp. 35.

[8]Wlezien, R., "Nozzle geometry effects on supersonic jet interaction," *AIAA Journal*, Vol. 27, No. 10, oct 1989, pp. 1361–1367.

[9]Shaw, L., "Twin-jet screech suppression," *Journal of Aircraft*, Vol. 27, No. 8, aug 1990, pp. 708–715.

[10]Morris, P. J., "Instability waves in twin supersonic jets," *Journal of Fluid Mechanics*, Vol. 220, No. 1, nov 1990, pp. 293.

[11]Kuo, C.-W., Cluts, J., and Samimy, M., "Effects of excitation around jet preferred mode Strouhal number in high-speed jets," *Experiments in Fluids*, Vol. 58, No. 4, apr 2017, pp. 35.

[12]Raman, G. and Taghavi, R., "Coupling of twin rectangular supersonic jets," *Journal of Fluid Mechanics*, Vol. 354, 1998, pp. 123–146.

[13]Tam, C. K. W. and Thies, A. T., "Instability of rectangular jets," *Journal of Fluid Mechanics*, Vol. 248, No. -1, mar 1993, pp. 425.

[14]Westley, R. and Woolley, J., "The near field sound pressures of a choked jet when oscillating in the spinning mode," *2nd Aeroacoustics Conference*, American Institute of Aeronautics and Astronautics, Reston, Virigina, mar 1975, pp. 1–8.

[15]Panda, J., "An experimental investigation of screech noise generation," *Journal of Fluid Mechanics*, Vol. 378, jan 1999, pp. 71–96.

[16]Edgington-Mitchell, D., Honnery, D., and Soria, J., "Staging behaviour in screeching elliptical jets," *International Journal of Aeroacoustics*, Vol. 14, No. 7, 2015, pp. 1005–1024.

[17]Alkislar, M. B., Krothapalli, A., Choutapalli, I., and Lourenco, L., "Structure of Supersonic Twin Jets," *AIAA journal*, Vol. 43, No. 11, 2005, pp. 2309–2318.

[18]Mitchell, D. M., Honnery, D. R., and Soria, J., "Near-field structure of underexpanded elliptic jets," *Experiments in Fluids*, Vol. 54, No. 7, jul 2013, pp. 1578.

[19]Tan, D. J., Edgington-Mitchell, D., and Honnery, D., "Measurement of density in axisymmetric jets using a novel background-oriented schlieren (BOS) technique," *Experiments in Fluids*, Vol. 56, No. 11, nov 2015, pp. 204.

[20]Weightman, J. L., Amili, O., Honnery, D., Soria, J., and Edgington-Mitchell, D., "Supersonic Jet Impingement on a Cylindrical Surface," *22nd AIAA/CEAS Aeroacoustics Conference*, 2016, pp. 2016–2800.

[21]Soria, J., "An investigation of the near wake of a circular cylinder using a video-based digital cross-correlation particle image velocimetry technique," *Experimental Thermal and Fluid Science*, Vol. 12, No. 2, 1996, pp. 221–233.

[22]Yoo, J., Mitchell, D., Davidson, D. F., and Hanson, R. K., "Planar laser-induced fluorescence imaging in shock tube flows," *Experiments in Fluids*, Vol. 49, No. 4, oct 2010, pp. 751–759.

[23]André, B., Castelain, T., and Bailly, C., "Investigation of the mixing layer of underexpanded supersonic jets by particle image velocimetry," *International Journal of Heat and Fluid Flow*, Vol. 50, dec 2014, pp. 188–200.

[24]Morris, P. J., "Flow Characteristics of the Large Scale Wave-Like Structure of a Supersonic Round Jet," *Journal of Sound and Vibration*, Vol. 53, No. 2, 1977, pp. 223–244.

[25]Edgington-Mitchell, D., Oberleithner, K., Honnery, D. R., and Soria, J., "Coherent structure and sound production in the helical mode of a screeching axisymmetric jet," *Journal of Fluid Mechanics*, Vol. 748, jun 2014, pp. 822–847.

[26]Weightman, J. L., Amili, O., Honnery, D., Soria, J., and Edgington-Mitchell, D., "An explanation for the phase lag in supersonic jet impingement," *J. Fluid Mech*, Vol. 815, 2017.

[27]Sirovich, L., "Turbulence and the dynamics of coherent structures part I: Coherent structures*," *Quarterly of Applied Mathematics*, Vol. 45, No. 3, 1987, pp. 561–571.

[28]Oberleithner, K., Seiber, M., Nayeri, C. N., Paschereit, C. O., Petz, C., Hege, H.-C., Noack, B. R., and Wygnanski, I., "Three-dimensional coherent structures in a swirling jet undergoing vortex breakdown: stability analysis and empirical mode construction," *Journal of Fluid Mechanics*, Vol. 679, jul 2011, pp. 383–414.

[29]Bell, G., Soria, J., Honnery, D. R., and Edgington-Mitchell, D., "PIV Analysis of Coupled Supersonic Twin-Jets," *23rd Australasian Fluid Mechanics Conference*, 2016, pp. 1–4.

[30]Tan, D. J., Soria, J., Honnery, D., and Edgington-Mitchell, D., "Novel Method for Investigating Broadband Velocity Fluctuations in Axisymmetric Screeching Jets," *AIAA Journal*, apr 2017, pp. 1–14.

Appendix G

Individual Microphone Responses of OASPL Estimates Under Jet Forcing

Figure G.1a shows the response of the individual microphones at NPR = 3.25 with mode E forcing. Figure 7.8d shows the mean response of these microphones' OASPL estimate. The mean estimate at this condition shows a clear peak at approximately St = 0.36. A strong peak is also observed within the individual responses contained in figure G.1a. The variation in baseline response between microphones is relatively significant (approximately 15 dB) but all microphones show an increase in OASPL. The microphone pairs generally show responses of approximately the same amount. The in-plane microphone pair 0-1 shows a very strong increase of approximately 25 dB. The out-of-plane pairs show a lower amplification from their respective baseline value. Figure 7.9 shows the changes in amplification from the baseline for each microphone pair, which gives an indication of amplification or damping direction under jet forcing. Sub-figure 7.9b shows the change between the microphone pairs for this condition.

Figures G.1b and G.1c show the individual responses for NPR = 3.50 with mode C and NPR = 3.00 with mode C respectively. The individual responses within Figure G.1b show the same general trends of amplification for NPR = 3.50 with amplification trends between microphone pairs. Figure G.1c shows the most significant case of OASPL reduction against the baseline case. It is observed that microphones 0-1 do not show a significant dampening of OASPL, but the out-of-plane microphones do. The trends between pairs are approximately equal, except for microphone 4.

The mean microphone OASPL estimate figures are used to highlight the overall response of the jet over the parameter space and provide a general indicator of jet OASPL behaviour with reference to the unforced jet.

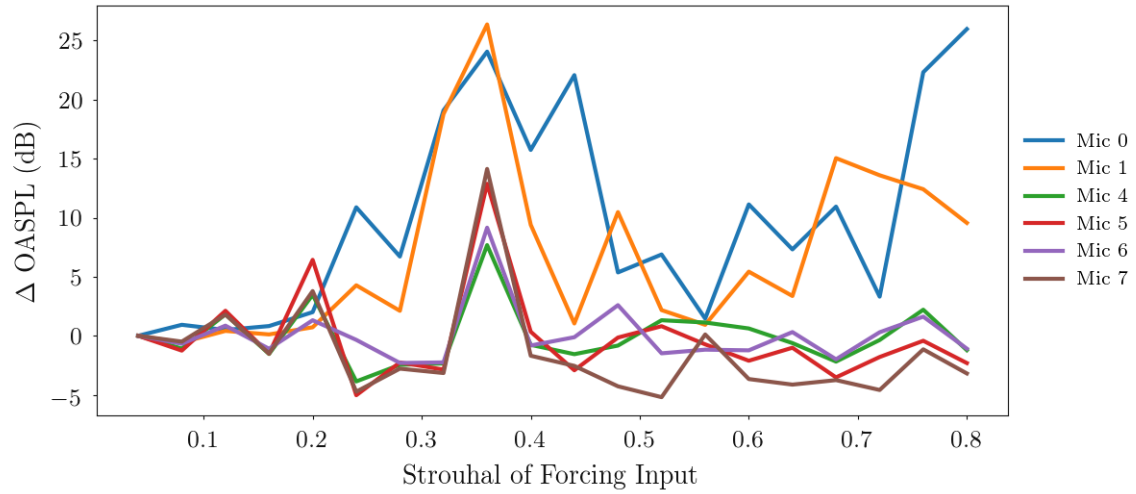

(a) NPR = 3.25 with mode E forcing.

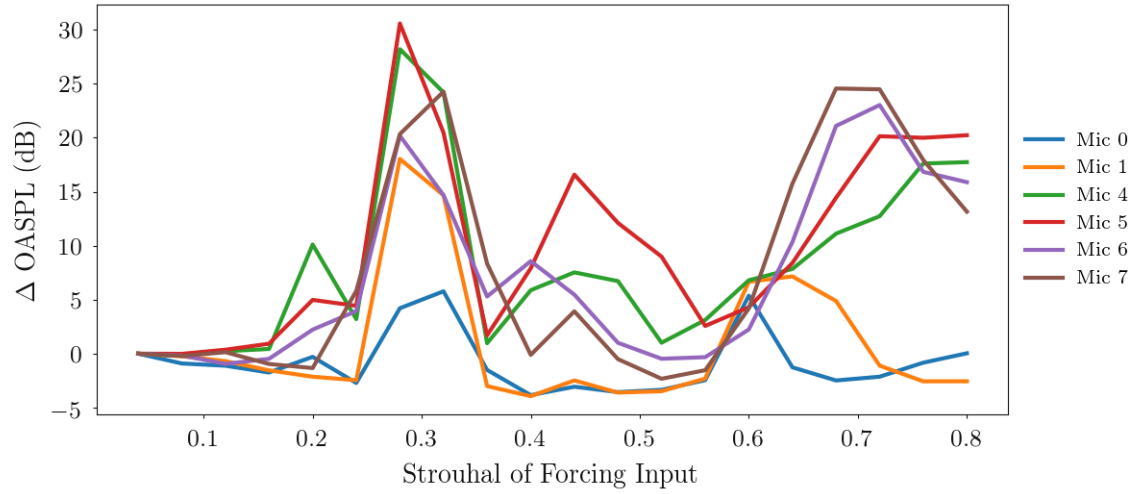

(b) NPR = 3.50 with mode C forcing.

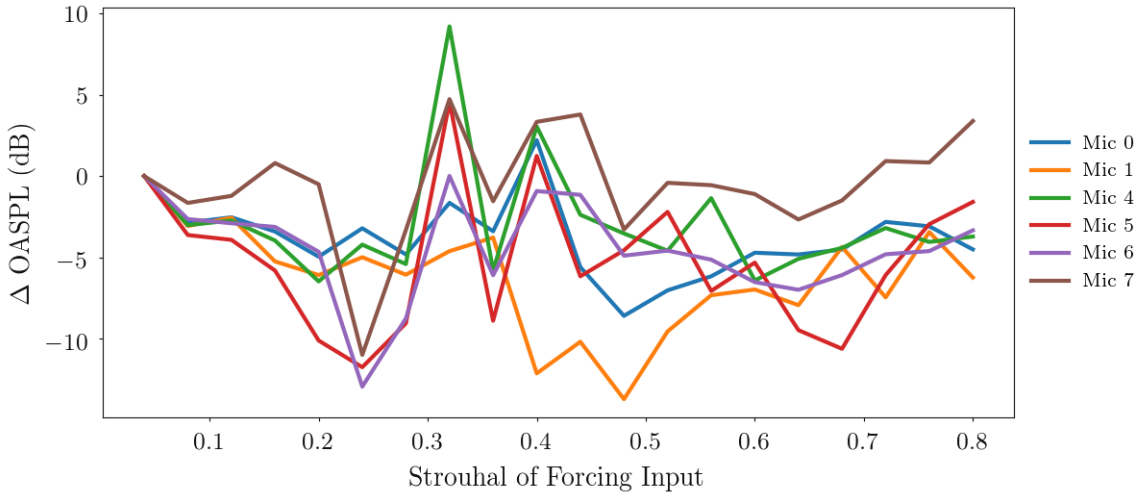

(c) NPR = 3.00 with mode C forcing.

Figure G.1: Individual microphone OASPL estimates with jet forcing. This figure is discussed within section 7.2.5.